THE UNIVERSITY *of* EDINBURGH

Development and Characterisation of Microelectrode and Nanoelectrode Systems

Helena Louise Woodvine

The University of Edinburgh
PhD Thesis
July 2011
Supervisor Dr. A.R. Mount

Declaration

I declare that this thesis has been entirely composed by myself.

I declare that as a member of a small research group I have made a substantial contribution to the work contained within this thesis. The majority of work is my own but relevant acknowledgment is given to any person/persons who aided in the development of this research.

I declare that the work has not been submitted for any other degree or professional qualification.

Signed,

Helena Woodvine

I would like to dedicate this work to my Mum, Ailsa and my Dad, Keith for I would not have been here to write it, if it wasn't for them.

"Small is Beautiful"
Leopold Kohr

And … I just couldn't resist slipping one in by Einstein …
he was my idol as a child after all

"Any Intelligent fool can make things bigger, more complex, and more violent. It takes a touch of genius - and a lot of courage – to move in the opposite direction"
Albert Einstein

0. Abstract

Micro- and nano-electrodes have distinct advantages over large electrodes, including their decreased iR drop and enhanced mass transport due to radial diffusion characteristics which leads to the ready establishment of a steady state (or near steady-state) signal without convection. This enhanced mass transport also leads to increased current densities and signal to noise ratios. However, there is a need for fabrication techniques which reproducibly give micro- and nano-electrodes of controlled size and shape. The optimisation of systematic arrays on the nano-scale, open up possibilities for developing highly sensitive electrode devices, for use in physical chemistry and the determination of fast electrode kinetics and rates of reaction, as well as to provide highly sensitive electroanalytical devices, able to detect very low concentrations of substrates.

This thesis first presents work involving the fabrication and characterisation on silicon substrates of square platinum microelectrodes. There is already an established theory for the behaviour of microdisc electrodes however, it is easier to make microsquares reproducibly using pixellated photomasks. The voltammetric and ac impedance characteristics of these electrodes in background electrolyte and in the presence of ferri/ferrocyanide redox couple are presented and the response is theoretically analysed. A combination of computer simulation, theory and experimentation show that these electrodes have increased current densities (14% greater) compared with a microdisc of equivalent radius and an alternative theoretical expression is presented to calculate the limiting current of microsquares at all dimensions.

This thesis then discusses the development and optimisation of novel nano-band cavity array electrodes (CaviArE), using standard photo-microlithographic techniques. The resulting architecture encloses a Platinum nanoband of 50 nm width within each array element that is positioned half way up the vertical edges of shallow square cavities (depressions), with a total depth of 1050 nm. The width of the square cavity and the separation of the array

elements can be controlled and systematically altered, with great accuracy. Figure 0.1 shows a schematic diagram depicting this architecture.

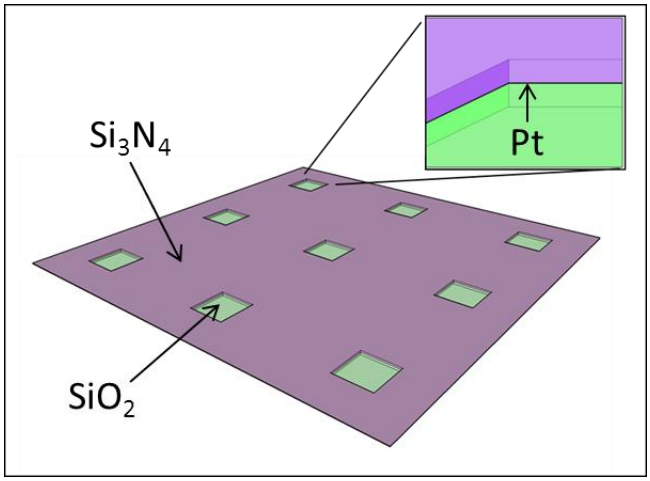

Figure 0.1: Schematic diagram of the nanoband electrode array architecture used in this work, with Si_3N_4 and SiO_2 insulation sandwiching the black Platinum nanoband in each depression (inset). The square separation depicted in this figure has a spacing of 3d (3 times the square length) and a cavity depth of 1050 nm.

The CaviArE devices are shown to give quantitative pseudo-steady-state responses characteristic of multiple nanobands, whilst passing overall currents consistent with a macroelectrode. The array has a much enhanced signal-to-noise ratio compared with an equivalent microsquare array, as it has 0.167% of the area and is therefore markedly less affected by non-Faradaic currents, while it passes comparable Faradaic currents. At high sweep rates the response is also virtually unaffected by solution stirring. The impedammetric characteristics presented show different diffusional regimes at high, medium and low frequencies, associated with diffusion within individual square cavities, outside of the cavity and finally across the whole array as the diffusional fields of the neighbouring array elements overlap. Justification and fitting of equivalent circuits to these frequency regions provide details about the charge transfer, capacitance and diffusional processes occurring. The results show that these systems are highly sensitive to surface transfer effects and a rate constant for ferricyanide of 1.99 cm s^{-1} was observed, suggesting fast kinetic processes can be detected. Together, these characteristics make nanoband electrode arrays, with this architecture, of real interest for sensitive electroanalytical applications, and development of devices for industrial application is currently being undertaken.

Table of Contents

1. Introduction

1.1. Outline

Electrochemistry is the study of the inter-conversion of electrical and chemical energy. Reaction typically occurs by electron exchange at the interface between a conducting electrode and ionic solution[1]. Exchange of electrons across this interface is known as a charge transfer reaction[2].

Electrolytic chemistry uses applied electrode potentials to force chemical reactions and thus allows the use of electricity (and therefore possible renewable energy sources), to synthesise or detect the presence of different analytes through reaction. Only very low voltages need be applied to manufacture reactive materials and the synthesis of valuable chemicals can be extremely energy efficient. At present electrochemistry is prominently used for industrial technologies such as the electroplating of metals[1] and large scale production of aluminium and chlorine[1]. Electrochemical techniques provide a method for the sensitive detection of chemical species since measurements of very low currents and hence low concentrations can be achieved. The technology is also used in devices such as electrochromic displays, electroanalytical sensors, batteries, and fuel cells[1].

It has been known for over 60 years that size and geometry of electrodes can have massive effects on electrochemical processes occurring within electrochemical experiments[3]. However, only recently have fabrication methods been developed that enable manufacture of small electrode systems on the micro- and nano-scale, at reasonable cost and size control[4]. The focus of this thesis is to look at the reproducible fabrication of such micro- and nanoelectrode systems using standard photolithographic techniques and to study the responses of these electrode systems, using a combination of electrochemical techniques such as cyclic voltammetry and impedance spectroscopy, and computer simulation. This chapter outlines the relevant literature regarding microelectrode and nanoelectrode systems, describing their electrochemical behaviour, common fabrication processes and typical

applications. This chapter also discusses how the use of digital, numerical simulation has aided in the study of the diffusive flux towards these micro- and nanoelectrode systems.

1.2. Microelectrodes

1.2.1. Electrochemistry at Microelectrodes

Microelectrodes, often referred to in the literature as ultramicroelectrodes (UME)[2,5] are defined as electrodes whose critical (at least one) length is on the micron scale. As the dimensions of a working electrode reach the micron scale, the behaviour begins to depart from that of a large (macro) electrode. As the diffusion-controlled current depends on the electrode dimension the currents observed at microelectrodes are many magnitudes smaller than those observed at macroelectrodes, typically within the nanoamp (nA) range. However, the current densities per unit area are larger. There is also a significant decrease in iR drop (section 2.1) associated with these electrodes. In the past many electrochemical measurements were restricted due to the resistance of the solution between the working and reference electrodes, limiting the precision with which the applied potential could be controlled. The invulnerability of microelectrodes to iR drop allows the research of previously inaccessible samples such as non-polar solvents, supercritical fluids, solids and gases[6].

The origins of this behaviour lie in the markedly different transport regime. The mass transport from the bulk of the solution toward a microelectrode differs from that toward a macroelectrode and the former has several advantages[6]. This was first demonstrated in the 1960s, when experiments performed on very small disk electrodes did not agree with the theory of planar diffusion and it was found that the current responses became time-independent and stationary[2]. The diffusional mass transport to a microelectrode is extremely efficient and comparable to those of a conventional macroelectrode rotated at several thousand revolutions per minute, r.p.m[5] (a regime which is usually practically inaccessible). Due to the small size of microelectrodes, the dimensions of the diffusion layer exceed the radius of the

microelectrode on time scales comparable to those used during ordinary electrochemical experiments. Thus the originally planar diffusion field transforms into a radial diffusion field, which provides more efficient mass transport[5]. This therefore allows the fast establishment of steady-state or near steady-state responses and high current densities, proportional to the redox concentration[5]. Microelectrodes also have increased signal-to-noise ratio compared to macroelectrodes. This is true for individual microelectrode systems and microelectrode arrays[6,7].

Analysis of microelectrodes is simpler than macroelectrodes as mass transport is usually the most dominant factor and steady-state (or near steady-state) currents are readily established on the time scales of normal experiments without the need for additional stirring[5]. The system is also less sensitive to external convective transport (e.g. thermal transport) within the bulk solution. This efficient radial mass transport means that microelectrodes also have very high reaction rates[2,4-6].

When the applied potential at the electrode surface is changed, the interface does not attain the necessary potential drop for electrochemical reaction until the charging of the double layer (at the electrode/electrolyte interface) is complete[1,4]. This capacitive charging, when relatively slow, can hinder studies of electron transfer reactions since both the Faradaic and charging current are convolved with time. Minimising both the relative magnitude of the charging current compared to the Faradaic current and the time it takes for the double layer to charge, is therefore desirable. The capacitive charging current, i_c, falls exponentially with time according to the expression

$$i_c = \frac{\Delta E}{R_U} \exp\left(\frac{-t}{R_U C_{CL}}\right) \qquad \textbf{Eqn. 1.1}$$

where R_U is the uncompensated electrolyte resistance, C_{DL} is the double layer capacitance and t is the time. For a macroelectrode the charging time, $R_U C_{DL}$ is

independent of electrode size, whilst for a microelectrode, R_UC_{DL} is proportional to the electrode radius, r^2. The charging time for microelectrodes therefore decreases with r, making smaller microelectrodes progressively more useful for the study of high-speed electron transfer reactions[2,5]. For macroelectrodes i_c and the Faradaic current, i_f, are often comparable on time scales of ordinary experiments, especially when the concentrations of redox active species are low[2]. When microelectrodes are used, the current ratio i_f/i_c hugely improves as the Faradaic component of the current density increases linearly with decreased radius, whereas the capacitive charge decreases with C_{DL}, in proportion to electrode area[6].

1.2.2. Microelectrode applications

The principal advantages of microelectrodes are their reduced R_uC_{dl} value, negligible iR drop and of course the fast establishment of steady-state or near steady state currents due to the enhanced mass transport rates. Most microelectrode applications make the use of one or all of these characteristics.

Microelectrodes are used for determination of electrochemical reaction mechanisms. Under steady-state conditions, kinetic and thermodynamic data can be accurately evaluated due to the absence of iR drop and decreased R_uC_{dl}[2]. The improved i_f/i_c ratio also enables trace chemical analysis since the limits of detection are reduced[4,5]. The small iR drop often permits measurement on samples with very low ion concentrations often without additional background electrolyte, which makes measurement from unadulterated samples possible[2,4,5]. Microelectrodes also make fantastic analytical sensors[8]. The small size of the electrodes permits multi-sensor arrays with improved signal to noise ratio, fast charging currents and fast establishment of a steady-state (or pseudo-steady-state) currents, improves the sensor response rate over macroelectrodes[6]. Due to their small size, microelectrodes are also ideal for in vivo biological measurements[5]. Microelectrodes can be used for monitoring local redox-active cell signalling and metabolic agents important in cells of living organisms, without destroying cell structures[9]. Microelectrodes, in recent years have also been utilised for scanning electrochemical microscopy

(SECM)[10-12]. SECM provides information on the redox activity of different surfaces and is used for imaging a variety of surfaces for electrochemical activity, e.g. the redox centres present in thin solid films. The small dimensions of microelectrodes give good spatial resolution of these surface images.

Other specialised uses of electrochemical systems involve coating electrode surface with a redox or π-conductive polymer film and monitoring the transport of electrons and ions through the polymer layer[13]. Modifying electrodes in this manner has promising applications in a variety of industries including the active film in organic electronic devices[14]; biosensors, for example *in vivo* monitoring of biologically important species such as catecholamines and adsorbic acid[15]; and for charge storage and amplification[6,13]. These applications may be enhanced by the use of microelectrodes, particularly where mass transport is an important factor in the measurement.

1.2.3. Microelectrode Fabrication

In electrochemistry it is not necessary for all dimensions of a microelectrode to be small. As long as one dimension is on the micron scale, desirable, enhanced radial diffusion characteristics can be achieved[5]. Figure 1.1 shows common types of single microelectrodes used and Figure 1.2 shows common microelectrode arrays.

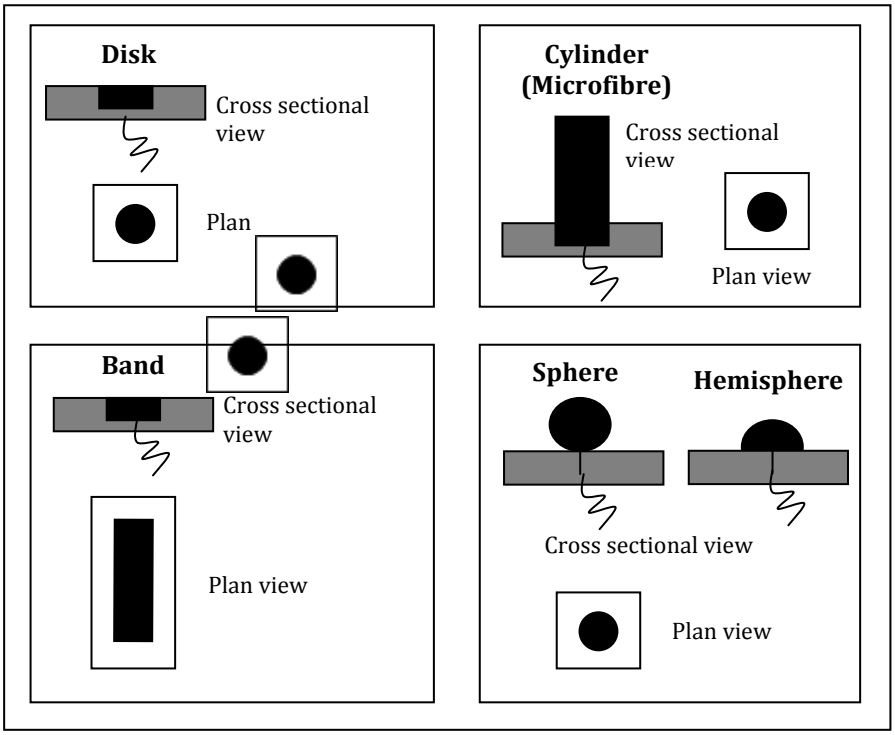

Figure 1.1: Schematic diagram of the most common types of single microelectrodes[5,6]

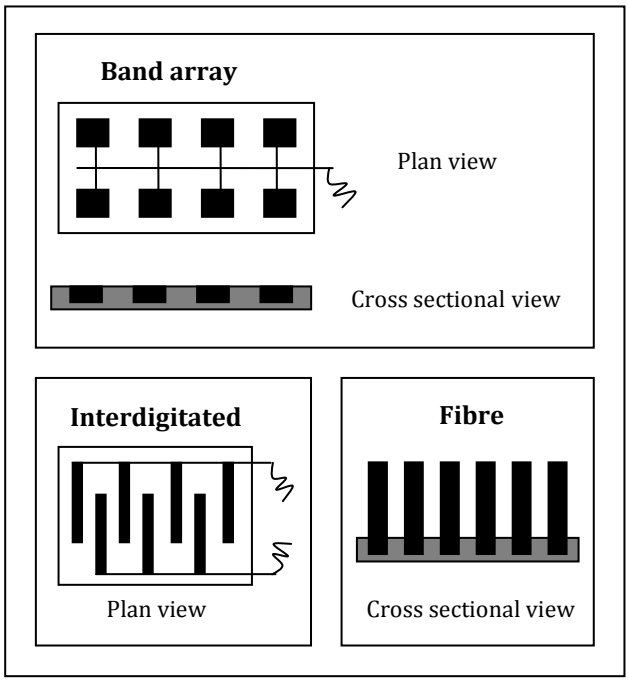

Figure 1.2: Schematic diagram of the most common form of microelectrode arrays[6]

Microdiscs are usually fabricated by fusing metal wires or carbon fibres into tapered glass or plastic capillaries[2,6] The end of the wire is exposed and cut flush to the surface whilst the rest of the wire is insulated inside the capillary. Microband electrodes are typically fabricated by fusing thin strips of metal foil

between sheets of glass or other synthetic insulator[2,6]. Fabrication of thinner microbands involves evaporation or sputtering of metals onto an insulating substrate, which is then covered with a second insulating layer to give a sandwich structure with the band electrode as the filling[16]. Microcylinders have been manufactured by sealing thin metal wires or carbon fibres in tapered insulating capillaries with the protruding wire cut to length[6]. For very small fibres the tips can be produced via electrochemical etching[2]. The seals around the exposed metal surface must be tight to ensure that there is no leakage around the edges. Epoxy resins are often used as they are easy to fabricate, are chemically resistant to attack and are non-contaminating[6]. Microspheres are commonly miniaturised hanging mercury drop electrodes[6] and hemisphere microelectrodes are typically produced by the electrolytic deposition of mercury on a planar metal or carbon disk microelectrode[6]. Although mercury has the desirable attribute of tending to produce electrodes with very uniform surfaces, a problem with mercury is that inter-metallic compounds can form by dissolution of the support metal into the mercury[6].

Microelectrode assemblies have been prepared by dispersing particles of conductive material such as graphite powder on to an insulating sheet. This is usually achieved by mixing the conductive powder with a two component epoxy resin in toluene. The resulting viscous mixture is then cast as a film, cured and cut into plates. Electrical contacts are made using silver paint[17]. These assemblies are easy to fabricate but electrode size, shape and array density is difficult to control[6]. Microelectrode arrays with more controlled pitch and spacing can also be produced by laser micromachining and subsequent screen-printing techniques. In this method, electrode array holes are first created in the polymer membrane, using an infra-red femptosecond (fs) laser ablation device. The screen-printing step utilises a manual screen printer and commercial carbon ink. The laser ablated thin polymer membrane is printed on the ablated side by forcing the conductive ink to penetrate through the array holes. An insulating layer is then pasted over the ink, leaving a square as the contact pad. The other side of the polymer membrane thus becomes the working electrode array[18]. Figure 1.3 gives an overview of this procedure.

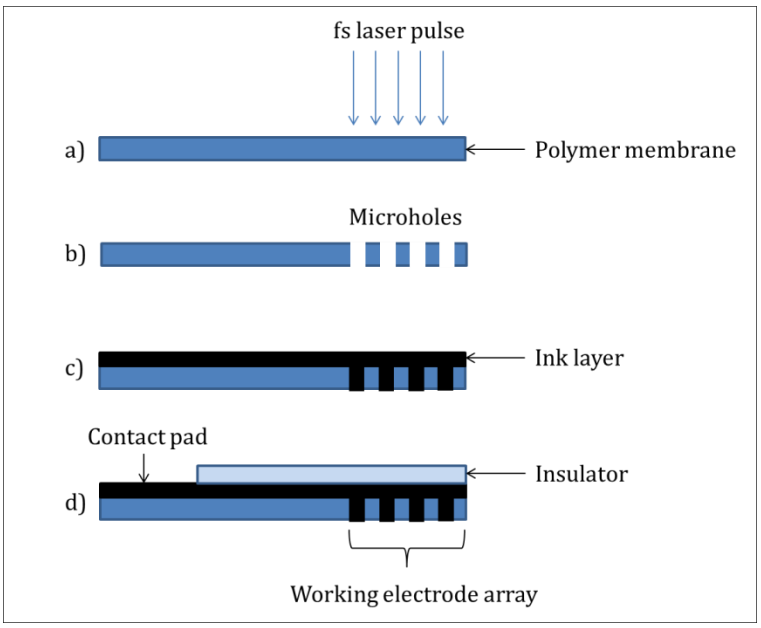

Figure 1.3: Side view of the different steps for the screen printed microelectrode array fabrication, showing **a)** the poly membrane and fs laser pulsing; **b)** the membrane after laser ablation; **c)** the ablated membrane after screen printing and **d)** the membrane after insulation showing the electrical contact and the working electrode surface[i]

Recent promising microelectrode fabrication processes utilise microlithographic techniques[19] (long used in the electronic and semiconductor industry) which have made the fabrication process of arrays and indeed single electrodes, more reproducible[8]. A popular process used for microelectrode manufacture is photolithography. This fabrication technique is more versatile than other methods and permits the preparation of electrodes with a broad range of shapes and sizes. The geometry of the electrodes can be more accurately controlled producing well defined electrode dimensions[2].

With the vast and varied analytical capabilities of microelectrodes it is not surprising that in recent years much research has been conducted on the reproducible fabrication of individual microelectrodes and microelectrode arrays and on the development of theoretical analysis in order to characterise, understand and ultimately utilise their enhanced attributes[8,20,21]. It is also useful or advantageous if the microelectrodes are reusable, easy to clean, and that their surface has uniform activity in order for redox processes to be accurately monitored[2]. This is a real challenge and there is a necessity therefore

[i] The schematic diagram shown in figure 1.5 is the authors own, but it has been adapted from a diagram given in reference 18

to develop fabrication techniques which reproducibly give microelectrodes of controlled size, shape and surface homogeneity, and also to develop sound methods for analysing the data. This is the subject of the work presented in chapter 4.

1.3. Nanoelectrodes

1.3.1. Electrochemistry at Nanoelectrodes

At least some of the benefits associated with microelectrodes (section 1.2), can be expected to be further enhanced as the electrode dimensions are decreased to the nanometre (nm) scale. Nanoelectrodes are defined as electrodes with a critical dimension (the dimension which controls electrochemical response) in the nanometre range, typically defined as between 1nm and 100 nm[22]. On such small scales, the electrodes themselves cannot be observed using ordinary optical microscopy and therefore imaging techniques such as scanning electron microscopy (SEM) must be employed, though even then it is difficult to image electrodes once they reach single nanometre dimensions[22,23]. Electrochemistry therefore is also an important tool for the characterisation of nanoelectrodes since the electrochemical response can be used to infer electrode dimensions. For nanoelectrodes with a critical dimension greater than 10 nm, the voltammetric properties observed have been reported to agree with classical diffusional theory, established for microelectrodes[24]. As with microelectrodes, steady-state (or pseudo-steady-state) voltammograms are observed for single nanoelectrodes, a result of the fast establishment of radial diffusion. The limiting current is directly proportional to the concentration of the electrolyte and can be related to the electrode dimension by applying the appropriate steady-state model. (e.g. Table 2.1), for the geometry of the electrode. However, as it is unlikely that the precise dimensions are known, due to the difficulties in controlling size and shape of nanoelectrodes (section 1.3.3) these steady-state models can only predict approximate sizes.

Microscale models are often also employed for very small nanoelectrodes (less than 10 nm). However, when the electrode's critical dimension is decreased to within the same order of magnitude as the thickness

of the electrical double layer, (established in response to the electrical charge on the electrode surface), or to molecular sizes, the experimental response has been seen to deviate from the behaviour observed at electrodes on the micrometre scale[22,25,26]. Numerous researchers[22-32] have shown that the application of traditional transport and kinetic theories to electrodes on this scale is largely inappropriate and can lead to erroneous voltammetric analysis.

In all electrochemical reactions, as the reaction proceeds, a thin depletion layer of thickness, δ, develops in the solution adjacent to the electrode, and in order for the reaction to continue, the redox analyte must be transported across this depletion layer to the electrode surface[25]. For single nanometre nanoelectrodes, the thickness of this depletion zone may be comparable to the thickness of the electrical double layer. The Debye length, κ^{-1}, which is typically used to characterise the thickness of this electrical double layer[25], is independent of electrode size. When δ and κ^{-1} are comparable, one postulate is that the electric field present in this regime may enhance or reduce the transport rate of charged ions to the electrode surface. For example it would be expected that the transport of a positively charged reactant to a negatively charged electrode would be increased in such a system due to the electrostatic attraction of oppositely charged species. However, if the electrode was positively charged, transport would be hindered[26]. Smith and White[28] use a simulation model based on the Poisson equation[ii] to discuss how significant changes to the voltammetric responses can occur at nanoelectrodes, explaining that limiting currents can be enhanced (or reduced) with increased charge, leading to erroneous estimation of the electrode size. Figure 1.4 shows one of the CVs obtained in the research by Smith and White to illustrate this point.

[ii] The Poisson equation is $\nabla^2 \emptyset = -\rho/\varepsilon\varepsilon_0$ where $\emptyset$ is the electric potential, ρ is the net charge density of in the solution, ε is the static dielectric constant and ε_0 is the permittivity of vacuum.

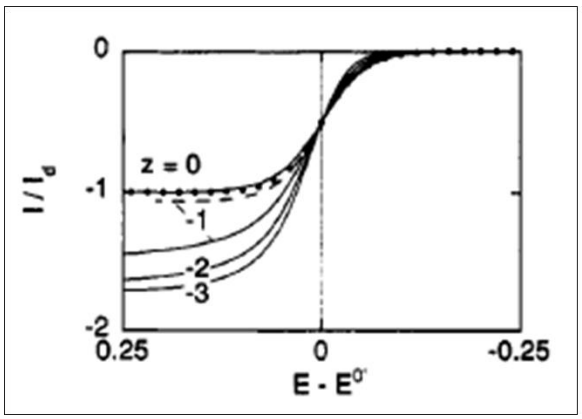

Figure 1.4: The CV responses of a single electrode oxidation at a 1 nm electrode (solid lines) of a neutral reactant (z=0) and negatively charged (-1, -2 and -3) reactants. The solid points (•) indicate the response predicted by typical microelectrode transport theory. Only the neutral reactant gives rise to a response approaching that expected by typical theory. The currents are significantly enhanced for the negatively charged species as a result of the electrostatic attraction between the negatively charged reactant and positively charged electrode. Smith and White say that by the use of the Possion equation can account for this change. The dashed line (- - -) shows the response of a 10 nm electrode with a charge of z = -1, normalised for electrode area, for comparison.[iii]

Smith and White also state that the voltammetry at very small electrodes can be affected by the formal potential $E^{0'}$ of a species, depending on whether it is more positive or more negative than the point of zero charge (PZC). The shifts in the CVs can often be mistaken for kinetic responses leading to erroneous estimation of rate constants. Figure 1.5 shows another CV recorded by Smith and White in their research to illustrate this behaviour.

[iii] This Figure has been taken from reference 28 to show effects of charge at very small (1 nm) electrodes in order to illustrate postulated electrostatic effects which may occur when dimensions reach single nanometre scales.

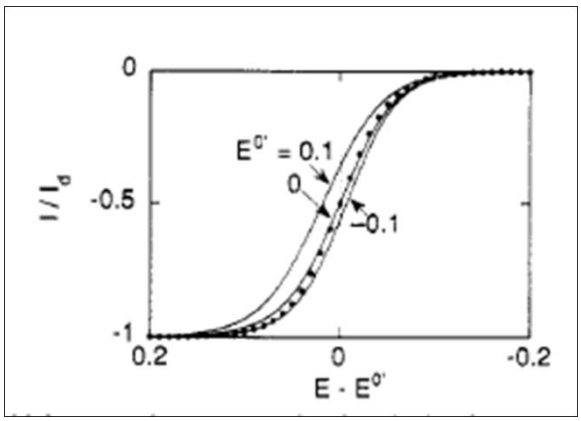

Figure 1.5: The CV responses of a single electrode oxidation at a 1 nm electrode of a neutral reactant (z=0) with different formal potentials $E^{0'}$, indicated on the graph. The solid points (•) indicate the response predicted by typical microelectrode theory. If the $E^{0'}$ value of the redox couple is positive of the PZC, then $E_{1/2}$ on the CV is shifted to more positive potentials due to electrostatic repulsion of electro-generated product. This shift could be mistakenly attributed to kinetic limitations which tend to shift the curve in the same direction. If $E^{0'}$ is negative of the PZC then $E_{1/2}$ shifts more negative due to the electrostatic repulsion of the positively charged product from the electrode surface. This shift towards cathodic potentials cannot be explained on the basis of slow heterogeneous kinetics, since CV waves for an oxidation reaction would never shift negative. However, negatives shifts may be able to cancel out positive shifts actually associated with kinetic limitations, making the response appear more reversible. As a consequence overestimations of rate constants may be calculated.[iv]

Chen and Kucernak[31] discuss the voltammetric responses of nanoelectrodes of varying sizes in several redox systems and describe the effects on these voltammetric responses in solutions with and without supporting background electrolyte. They show that deviations from typical behaviour occur at very small nanoelectrodes without the presence of background electrolyte and attribute these differences to migratory and electrostatic effects within the double layer.

Another postulate is that the observed effects are not due to electrostatics but to other physical changes in the double layer. For example White and co-workers[33] have also considered the effects when the depletion zone surrounding the nanoelectrodes are comparable to the region where changes in the viscosity and density of the medium occur. They propose that the diffusion coefficients of redox active species may be different from the bulk solution in this region, since the electrical field associated with the charged electrode surface will locally affect the ion-solvent interactions and the local

[iv] This figure has been taken from reference 28 to show the effect of formal potential at very small (1 nm) electrodes in order to illustrate postulated electrostatic effects which may occur when dimensions reach single nanometre scales.

solvent composition. Due to increased structure of the liquid in the vicinity near the electrode surface, it might be expected that the diffusivity will be slower in this region and hence smaller diffusion coefficients will be expected.

Despite the great attractiveness of nanometre-sized electrodes, for a long time experimental results from such systems were rare and unreliable. This is still an area where theory is being developed before experimental validation is achieved. One of main challenges in nanoelectrode research is the lack of technology for reproducible electrode fabrication with accurately control dimensions. Much research has been conducted in this area and single nanoelectrodes can be fabricated at reasonable cost and reproducibility (section 1.3.3). However, characterisation of these electrodes often assumes ideal geometries, when their shapes are likely to be non-ideal. Therefore the effective radius is often quoted[24,29-31] since the exact geometry is unknown. Another issue with single nanoelectrodes is that despite the high current densities, very low absolute currents are passed, commonly in the picoamp (pA) range[22,25]. This often requires development of and measurement with precision low current, low noise potentiostats, which require efficient electromagnetic shielding and whose use is limited because of these requirements.

One solution to this problem is to multiply the observed current by simultaneous measurement with multiple nanoelectrodes[22,34]. This offers many of the benefits of ultra-small electrodes, but with the output currents of a macroelectrode. When these multi electrode systems are randomly spaced they are known as nanoelectrode ensembles (NEE) and when the electrodes are evenly and systematically spaced they are known as nanoelectrode arrays (NEA)[22]. An advantage of both NEEs and NEAs is that charging current, i_c is proportional to the geometric area of the electrode elements but the Faradaic current, i_f, when the diffusional fields overlap is proportional to the total electrode area (that is the active electrode and inter-electrode spacing)[22].

Characterisation of these multi-electrode systems is possible via voltammetry, however, there are four kinds of diffusion regime which must be

considered[22,35]. Figure 1.6 shows a schematic diagram of the different diffusion regimes towards two adjacent nanoelectrodes in an array (this is discussed in more detail in section 2.4).

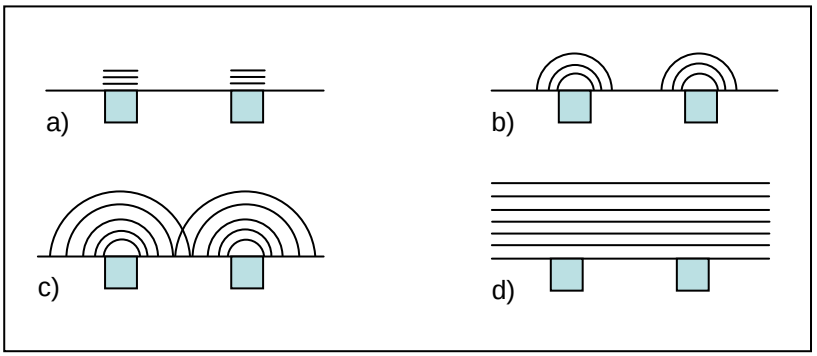

Figure 1.6: Schematic diagram showing the different diffusion regimes towards a multielectrode system where a)shows linear diffusion to each nanoparticle, b) shows radial diffusion towards each nanoparticle, c) shows overlapping diffusion zones and d) shows overall linear diffusion[v].

Randomly separated NEEs are more difficult to interpret electrochemically than NEAs because the variable neighbour separation means that the diffusion over the entire array is likely to show a combination of all four regimes at any given time. To avoid this, it is desirable to produce evenly spaced NEAs of controlled dimension, the preparation of which will marry the diffusional regimes with the time scale of the experiment and the distribution of electrodes on the surface[35]. However, these are typically harder to fabricate (see section 1.3.3).

1.3.2. Nanoelectrode Applications

Many of the microelectrode applications stated in section 1.2.2 are also suitable and indeed may be improved by the use of nanoelectrodes and nanoelectrode arrays. To date the main areas where nanoelectrodes have been used are in physical chemistry, imaging and analysis[22]. However, as mentioned in section 1.3.1, care must be taken when analysing data obtained for very small nanoelectrodes due to deviations from classical theory and effects of changes in local solution properties and electrostatic forces near the electrode surface.

[v] Figure 1.8 has been adapted from figure 1 in reference 35.

One of the main impetuses for the establishment of reproducible and robust methods for the preparation of nanoelectrodes is for their use in physical electrochemistry and in the measurement of fast electrode kinetics. This is because the mass transport rates towards nano-scale electrodes is extremely fast[22].

Nanoelectrodes are also desirable as SECM probes (see section 1.2.2), when electrochemical mapping of surfaces require greater resolution than is possible using micro-sized probes[22]. Although SECM probing had previously been used as a method of characterisation of new electrodes, Gray and Unwin[36] were the first to use nanoelectrode SECM probes for imaging. The probe was used to image Cl^- diffusion from a 50 μm pore.

Nanoelectrodes have also become very desirable for analytical applications, such as the detection of low concentrations of redox-active molecules, or in understanding initial stages of processes such as metal corrosion and heterogeneous nucleation which include formation of nanometre-sized transient structures[29]. Due to the enhanced current densities and small sizes of these electrodes, it is in fact possible to detect the reactions of very small numbers of molecules. Indeed one of the greatest challenges in electrochemistry has been the detection of single molecules. The first example of single molecule electrochemical detection was performed by Bard and co-workers using a 15-nm radius Platinum electrode[37]. The group measured the oxidation of [(trimethylammonio)methyl] ferrocene (Cp_2FeTMA^+) to Cp_2FeTMA^{2+} by trapping a small volume of dilute solution of electroactive species between the microelectrode tip and a conductive substrate. SECM was used to adjust the tip-substrate distance to approximately 10 nm. Anodic current peaks were observed as a single molecule moved into and out of the electrode-substrate gap.

Nanoelectrode arrays may also prove to be a valuable tool for multi-analyte sensing systems[38]. For example, nanoarrays fabricated using carbon microspheres coated with metal nanoparticles. This provides a method of

making a multi-metal nanoelectrode array, constructed using nano particles of more than one metal, or by functionalising the metal particles to be ion selective. Compton and co-workers describe the bulk surface modification of such glassy carbon microspheres used for the simultaneous detection of thallium(I), bromide and hydrazine[39].

1.3.3. Nanoelectrode Fabrication

As described in section 1.3.1, one of the major concerns of the use of nanoelectrodes is that they are difficult to fabricate with controlled dimensions[38], thus research on the use of nanoelectrodes is often closely linked to the research of their fabrication[38]. Advances in different fabrication methods have vastly increased the preparation and use of nanoelectrodes in physical chemistry, imaging science and analytical measurements, and has provided valuable information about electrochemical kinetics and chemical analysis. Further development of reproducible fabrication methods is required however, before widespread application of these electrode systems is available. This is the subject of Chapters 5 to 7.

Presently, there are a number of fabrication techniques employed in the preparation of nanoelectrodes and several widely used fabrication techniques are described below. Figure 1.6 shows a schematic diagram of the most common nanoelectrode geometries produced. Nanoband electrodes were the first type of nanoelectrode fabricated. These were produced by sputtering metal films (2-100 nm) onto cleaved mica insulator surfaces (figure 1.7 a), then coating the metal with epoxy insulator and fixing it within a tube. The end perpendicular to the metal film was then ground down to reveal the nano band[33,40].

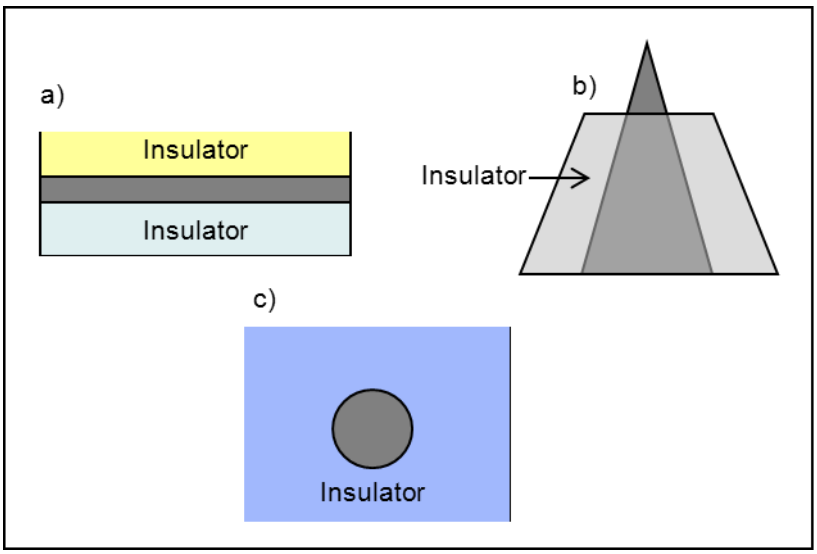

Figure 1.7: A schematic of the most common types of single nanoelectrodes[25]

Hemispherical nanoelectrodes have also been fabricated by adapting a method previously used for preparation of the conducting tips in scanning tunnelling microscopy (STM). The electrodes were fabricated by sequential electrochemical etching of microwires, then insulation of all but the tip of the electrode, using an insulating material[41-44]. These procedures actually produce a fine cone-shaped tip (figure 1.6 b), which is approximated as a hemisphere during characterisation. Nanodisc electrodes have been fabricated using a similar technique, but then the tip was electrochemically etched to produce a planar disc electrode[45].

Nanodisc electrodes have also been prepared in a similar manner to microdiscs (section 1.2.3) by sealing a microwire inside a glass capillary (figure 1.6 c). The system was then heated and pulled using a computer controlled pipette puller, which resulted in the reduction of the radius of both the capillary and wire inside and the establishment of a seal between the glass and the metal wire[46]. However, control of precise, reproducible dimensions, using these fabrication processes have been proved to be quite difficult to attain[22]. In particular as nanowires are often tapering, the fabrication procedure can lead to a change in disc radius, often producing oval shaped electrodes rather than true discs.

As mentioned in section 1.3.1, nanoelectrode arrays are desirable and so much research has been undertaken in the fabrication of nanoelectrode ensembles and arrays. A range of fabrication techniques have been adopted to produce ensemble devices. The technique used by Compton and co-workers to fabricate multi-analyte sensors[39] (section 1.3.2) produces nanoelectrode ensembles. The group utilised electroless deposition of gold nanoparticles onto the surface of glassy carbon microspheres, by mixing the glassy carbon, in a solution of $AuNa(S_2O_3)_2 \bullet xH_2O$ and L-ascorbic acid dissolved in water. The microspheres were then immobilised on the surface of a macroelectrode. This method provides a relatively easy procedure of producing ensembles.

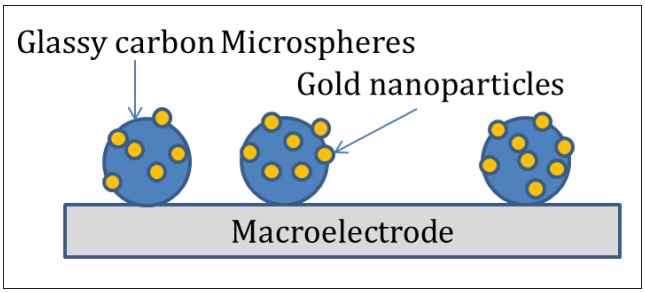

Figure 1.8: Schematic diagram representing gold coated glassy carbon microsphere ensemble immobilised on a macroelectrode

Ultrasound[47] can also be employed to open pores in insulating layers deposited over conducting materials, thereby exposing an ensemble of active electrode areas. This technique was used successfully by Barton and co-workers[47] to produce sonochemically fabricated ensembles via the ablation of polydiamenobenzene films at an ultra-sonic frequency of 25 kHz, exposing the underlying conductive substrate. Random NEEs can also be achieved by the use of ultrasound to drive suspended metal particles into a target electrode. This provides a simple method for sonochemical deposition via acoustically abrasive attachment, ultrasound powers of 50 W cm^{-2} are typically used[38].

Templated metal growth in the nanopores of membranes[48-50] has also been utilised. Evans and co-workers[48] have utilised commercially available nanopore membranes as templates and produced gold nanowell ensembles with a depth of 600 nm. The electrodes were prepared by first forming a copper film over the surface of the nanopore membrane, then electrodepositing gold

into the pores, before removing the copper film to reveal the nanowell arrays. The same group[49] has also fabricated gold nanowells of 50 nm depth by the electrodeposition of gold into porous alumina membranes, creating the well through a combination of electrochemical stripping and ion bombardment of the gold. Penner and Martin[50] were able to fabricate nanodisc assemblies by the electrodeposition of platinum into the pores of a porous polycarbonate membrane. Electroless deposition of gold into porous polycarbonate has also been achieved, using commercially available gold electroless plating solutions[27]. These are all areas of considerable research interest, but the challenge with these technologies is that it is currently not possible to produce large multiple nanoelectrode systems with systematic control of the size and separation of each electrode. Without this, there is heterogeneity of individual electrode responses and reactivity, with individual electrodes being affected by diffusional layer overlap from neighbouring electrodes to variable extents as a function of time and frequency.

Nanoelectrode arrays arranged in an ordered manner have been achieved to some extent by using controlled polymer deposition, orientation and selective dissolution[51,52]. Jeoung *et al*[51] fabricated nanoporous arrays by spin-coating a polystyrene (PS)/poly(methyl methacrylate) (PMMA) copolymer solution onto a gold-plated silicon film. The dried films were then annealed in the presence of strong electric fields to orient the PMMA cylinders perpendicular to the surface. UV exposure cross-linked the PS and degraded the PMMA. Rinsing in glacial acetic acid removed the PMMA, revealing the porous cross-linked template on the gold substrate. However, it is currently difficult to control the electrode size and spacing using this method.

Deposition of metals on to self-assembled monolayers (SAMs) has been utilized with reasonable success, Speets *et al*[53] fabricated gold-self assembled monolayer sandwich structures by gas-phase deposition of gold on alkylthiolate self-assembled monolayers on polycrystalline gold, using pulsed laser deposition (PLD) through a nanosieve (thin silicon nitride membrane). The nanosieve acted as a shadow mask and a pattern of gold islands were produced.

However, it is difficult to control deposition and the dimensions of the islands are usually quite large. When smaller electrodes are deposited, the number isolated deposits (not in contact with the bottom of the electrode increases.

Carbon Nanotube[54,55] (CNT) and boron-doped diamond[56] nanowire assemblies have also been explored. CNTs are typically grown via plasma-enhanced chemical deposition on to electrochemically deposited nanoparticles such as nickel[34]. This creates arrays of up to millions of CNTs (~100 nm in diameter), separated by only a few micrometers. However, CNT assemblies involve the lithographic production of metal catalyst centres on the sub-micron scale for templated nanotube growth. This requires extremely precise nanopatterning procedures and does not permit variety in the electrode material and size. Boron-doped diamond nanowire assemblies also require nanopatterned masking for selective etching and are typically fabricated by use of diamond nanoparticles as a hard mask and by the use of reactive ion etching to create vertically aligned boron-doped, nano-wires[56].

Another approach includes nanoskiving[57,58] which requires insulation of a thin metal deposit, then sectioning of the substrate producing encapsulated nanowires. Figure 1.9 depicts the concept of the preliminary stages of nanoskiving, showing a) a thin film of deposited metal sandwiched between two insulating layers, and b) several slices of the substrate, showing the nanowires encapsulated between the insulating substrate.

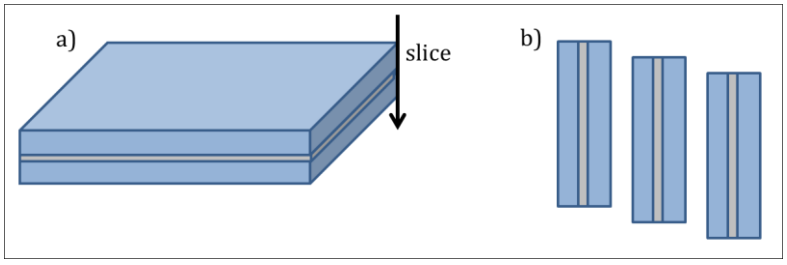

Figure 1.9: Schematic diagram representing the fabrication of nanowires via nanoskiving. Slicing of the substrate **a)** using a standard 45° diamond knife produces sections **b)** with thicknesses as small as 50 nm.

The encapsulated wires must then be mounted and connected on to a suitable support before the insulation is removed. Nanoskiving takes advantage

of thin film deposition techniques such as e-beam evaporation to deposit thin metal layers[57].

1.4. Modelling Diffusional Flux towards an Electrode Surface

The use of microelectrodes and nanoelectrodes in recent years has enhanced the capabilities of electrochemical analysis. As described above, not only do these electrodes have lower capacitance and reduced ohmic distortions, but they also provide an enhanced rate of mass transport over macroelectrodes, and hence have opened opportunities of studying fast electrochemical processes, previously inaccessible using voltammetric analysis. The enhanced rate of mass transport, over macroelectrodes arises from a difference in the diffusional domains[59]. As explained in section 2.4, mass transport is controlled by linear diffusion towards a macroelectrode, but for micro- and nanoelectrodes, with critical dimensions less than the scale of the diffusion layer, the edges of these electrodes contribute significantly to the diffusion, and radial, convergent diffusion is observed.

For these reasons micro- and nanoelectrodes are desirable for use in a variety of electroanalysis and electrochemical measurement applications. Since the diffusional regimes towards electrode surfaces have profound effects on the electrochemistry occurring, it is of interest to electrochemists to try and understand the diffusional regimes established during experimentation. The diffusion towards macroelectrodes can be approximated as linear over all time scales and this can be solved analytically. However, micro- or nanoelectrodes show linear diffusion at short times and radial diffusion at longer times. This is very difficult to solve analytically. In order to solve such diffusional regimes, transport equations in two and even three dimensions must be solved[60].

Digital, numerical simulation is now a well-established strategy for analysis of electrochemical experiments and is known to be an efficient method for studying complicated systems such as the diffusive flux towards a micro- or nanoelectrodes[61]. Recent advances in computational simulations have opened up the possibility of solving more complex problems in two dimensions

(2D)[20,62-65] and even three dimensions (3D)[59,66-69], and these approaches have been used extensively by research groups to monitor diffusion processes towards micro- and nanoelectrodes.

An electrochemical model typically involves simulation of the concentration distributions of chemical species involved in the electrochemical reaction under diffusional and/or convective control[70]. As long as the mechanism of the electrochemical process being studied, the electrode geometry and the experimental technique (steady state or transient) is known, the experiment can be described mathematically as a set of coupled partial differential equations (PDE)[71]. Many simulation techniques have been employed to simulate the concentration distributions within electrochemical reactions and John Alden[70] in his DPhil thesis, describes many of the techniques. Most commercially available simulation programmes are based on finite difference methods (FDM) or Finite Element methods (FEM)[63] and Fulian and Fisher[72] have shown the Boundary Element method (BEM) can also be a valuable tool for modelling electrochemical processes under diffusion control in 2 and 3 dimensions. This method reduces the processing memory and time in comparison to FEM.

Computational simulation of electrode systems has been used extensively to model the diffusional regimes for many different electrode geometries and designs. An example of some of the relevant literature is presented below. Some of the first microelectrode systems solved by digital simulation were those of planar microdiscs. Heinze[62], using FDM, solved 1D diffusion towards a planar microdisc and utilised an implicit alternating direction method (ADI) to build a 3D picture of the radial diffusion towards the disc electrode. Gavaghan utilised FDM to model 2D steady state diffusion towards a planar microdisc and presented strategies for refining the FDM mesh, for more accurate simulations. Later Gavaghan and co-workers[65,73] utilised FEM models to simulate 2D steady–state diffusion towards a range of microelectrode architectures including planar microdiscs, recessed microdiscs, and channel microband electrodes. In their study they used adaptive meshing methods to

refine the mesh over subsequent simulations and increase accuracy of the simulation. The group studied both continuous Galerkin FEM and discontinuous Galerkin FEM models, and suggested that the latter model provides a better method for modelling channel mircobands and convection-dominated problems[65]. They extended their model to time-dependent problems, but stated that the main drawback of this method was the mathematical complexity involved. The group hoped to implement the technique into a more user-friendly software package.

Guo and Lindner[20], have utilised a commercially available FEM software package, COMSOL Multiphysics, to model 2D time-dependent (transient) diffusion towards shallow recessed microdisc arrays. They were able to model isolated linear diffusion towards the individual electrodes, as well as both radial diffusion and different diffusional regimes associated with the overlapping arrays. They presented examples of the CV profiles associated with each diffusional regime. Their study showed good agreement between simulation and experiment.

Strutwolf and Williams[74] utilised FDM models to simulate the transient response of co-planar and interdigitated array electrodes in generator-collector mode and show that elevated electrodes have advantages over co-planar electrodes, since there is faster communication between neighbouring electrodes and thus shorter response times.

Alden and co-workers[75], have presented an alternative simulation method, the strongly implicit procedure (SIP) based on the Oldham equation[vi]. The 2D diffusional mass transport profiles associated with short-time chronoamperometric transients for elevated, recessed, platform and line microbands electrodes were solved by means of the simple analytical equations established by SIP.

[vi] $i = Fc^{\infty}w\left(\frac{A}{\pi^{1/2}\theta^{1/2}}+1\right)$ where w is the electrode length, $\Theta = Dt/x_e$ and x_e is the electrode width

(75) Alden, J. A., J. Booth, R.G. Compton *, R.A.W. Dryfe, G.H.W. Sanders *Journal of Electroanalytical Chemistry* **1995**, *389*, 45.

Beriet and co-workers[76] have also simulated 2D chronoamperometric responses of a regular array of micro-disc electrodes, over different potential steps. They show the ability of the FEM model to model different diffusional regimes established for arrays depending on the depth of recess of the arrays and current densities observed over short and medium timescales.

Several research groups have also performed 3D simulations for the diffusional transport towards different microelectrode geometries. Strutwolf[67] has utilised the FDM approach to model steady-state diffusion towards rectangular microelectrodes. He modelled one quarter of the electrode area, and utilised dynamic adaptive meshing to improve accuracy of his model.

Cuttress and Compton[59,68] have pioneered the development of an alternate Finite difference simulation method, using a Graphics processing unit (GPU) simulation, which was originally developed for graphics cards in PCs. GPU provides significant increase in speed over standard CPU (central processing unit) simulations, which are performed by writing programming code, as it enables many calculations to be run in parallel. Cuttress and Compton have used this modelling technique to simulate pseudo-3D steady-state diffusional profiles associated with elliptical electrodes, square and rectangular microelectrodes and microband electrodes amongst others.

Myland and Oldham[66] have performed 3D chronoamperometric simulations based on Fick's Law and the Cottrell's equation, at the interior walls of a hollow cube, following a potential step over short time regimes. They also developed the technique to measure the corresponding vertex of a solid cube.

Numerical simulation can also be used to model other electrochemical processes. FEM models have been utilised to simulate Faradaic impedance[61,77] and for modelling convective flow over electrodes contained within micro-channels[78]. FDM models have been shown useful for modelling the influence of electrode roughness on stripping voltammetry[79]. However, these techniques are less relevant for the work presented in this thesis.

The commercial software, COMSOL multiphysics, will be utilised in this thesis, to model 3D FEM steady-state concentration profiles of different microelectrode geometries. This software has proved to be a viable simulation method for modelling electrochemical diffusional regimes, at least in 2D[20]. The principles of FEM modelling are presented in section 2.7. However, it must be noted that Cuttress, Compton and co-workers[60], who carried out both 2D and 3D simulation of microdisc electrodes using this software, state that it should be used with some caution. They state that care must be taken when establishing the FEM mesh, to ensure accuracy of the simulation. They also show that often during adaptive mesh refinement, COMSOL simulations often fail to converge, leading to erroneous models.

1.5. Aims

The aims of the work in this thesis are to develop robust and reproducible fabrication and characterisation of micro- and nanoelectrode systems. Chapter 2 therefore describes the principles of the electrochemical and theoretical and simulation techniques utilised throughout this thesis for characterisation and discusses in more detail the diffusional characteristics of micro- and nanoelectrode systems. The commercially available Finite Element Method (FEM) simulation program, COMSOL will be utilised in this thesis and this numerical technique will also be outlined in Chapter 2.

Chapter 3 outlines the experimental methods used in this work and by the aid of two case studies, validates the voltammetric, impedimetric and simulation methods used. Chapter 4 presents the controlled fabrication and systematic characterisation of a single microsquare platinum electrode system. FEM analysis in Chapter 4 is used to simulate diffusional flux of ferricyanide towards microsquare electrodes of different sizes. With the aid of computer simulation, it is shown that the limiting current densities of these and other square systems are enhanced, with respect to microdiscs of equivalent dimension. The chapter also develops, by utilising FEM models, a theoretical expression to predict the limiting current densities of single microsquares of all dimensions through FEM

Chapter 5 presents the development of a novel nanoelectrode array. This shows that microfabrication methods similar to those outlined in chapter 4 can be used to reproducibly fabricate nanoband arrays of controlled dimensions. Chapter 6 shows the systematic voltammetric study and analysis of these nanoband arrays with specific dimensions and spacing, fabricated using the optimised processes developed in Chapter 5. This chapter discusses in detail the cyclic voltammetric data, showing that it fits well to microband theory, but with nanoband dimensions. It also quantifies the response in different concentrations as well as with different redox couples. Chapter 7 presents typical electrochemical impedance spectroscopy (EIS) data obtained for these nanoband arrays. Analysis of these data through equivalent circuits enables the fundamental response of these nanoband arrays to be established.

Chapter 8 draws together the important conclusions and findings of the work carried out for this thesis and is also used to discuss possible future research ideas which would enhance understanding and characterisation of the novel array architecture. Limitations of the simulation programme used for this work, when attempting to model complex nanoarray systems is also discussed, as well as the development of the novel array design, described in chapter 5, into a device which can be used in industrial applications.

1.6. References

(1) Bard, A. J.; Faulkner, L. R. *Electrochemical Methods, Fundamentals and Aplications*; Second ed.; John Wiley and Sons, Inc.: Hoboken, 2001.

(2) Heinze, J. *Angewandte Chemie International Edition in English* **1993**, 1268.

(3) Randles, J. E. B. *Discussions of the Faraday Society* **1947**, *1*, 11.

(4) Pons, S.; Fleischmann, M. *Analytical Chemistry* **1987**, *59*, A1391.

(5) Forster, R. J. *Chemical Society Reviews* **1994**, *23*, 289

(6) Stulik, K., C. Amatore, K. Holub, V. Marecek and W. Kutner *Pure and Applied Chemistry* **2000**, *72*, 1483.

(7) Weber, S. G. *Analytical Chemistry* **1989**, *61*, 295.

(8) Feeney, R.; Kounaves, S. P. *Electroanalysis* **2000**, *12*, 677.

(9) Ferapontova, E. E., T.G. Terry, A.J. Walton, C.P. Mountford, J. Crain, A.H. Buck, P. Dickinson, C.J. Cambell, J.S. Beattie, P. Ghazal, P. and A.R. Mount *Electrochemistry Communications* **2006**, *9*, 303.

(10) Bard, A. J.; Fan, F. R. F.; Kwak, J.; Lev, O. *Analytical Chemistry* **1989**, *61*, 132.

(11) Bard, A. J.; Denuault, G.; Lee, C.; Mandler, D.; Wipf, D. O. *Accounts of Chemical Research* **1990**, *23*, 357.

(12) Bard, A. J.; Fan, F.-R. F.; Pierce, D. T.; Unwin, P. R.; Wipf, D. O.; Zhou, F. *Science* **1991**, *254*, 68.

(13) Chidsey, C. E. D.; Murray, R. W. *Science* **1986**, *231*, 25.

(14) B. H. Hamadani; Richter, C. A.; Suehle, J. S.; Gundlach, D. J. *Applied Physics Letters* **2008**, *92*, 3.

(15) Wightman, R. M.; May, L. J.; Michael, A. C. *Analytical Chemistry* **1988**, *60*, 769A.

(16) Wehmeyer, K. R.; Deakin, M. R.; Wightman, R. M. *Analytical Chemistry* **1985**, *57*, 1913.

(17) Corb, I.; Manea, F.; Radovan, C.; Pop, A.; Burtica, G.; Malchev, P.; Picken, S.; Schoonman, J. *Sensors* **2007**, *7*, 2626.

(18) Cugnet, C.; Zaouak, O.; René, A.; Pécheyran, C.; Potin-Gautier, M.; Authier, L. *Sensors and Actuators B* **2009**, *143*, 158.

(19) May, G. S.; Sze, S. M. *Fundamentals of Semiconductor fabrication*; Wiley International Esdition ed.; John Wiley ans Sons.: Hoboken, 2004.

(20) Guo, J.; Lindner, E. *Analytical Chemistry* **2009**, *81*, 130.

(21) Koster, O., W. Schuhmann, H. Vogt and W. Mokwa *Sensors and Actuators* **2001**, *B*, 573.

(22) Arrigan, D. W. M. *Analyst* **2004**, *129*, 1157.

(23) Murray, R. W. *Chemical Reviews* **2008**, *108*, 2688.

(24) Wang, C.; Hu, X. *Talanta* **2006**, *68*, 1322.

(25) Watkins, J. J.; Zhang, B.; White, H. S. *Journal of Chemical Education* **2005**, *82*, 712.

(26) White, H. S.; Bund, A. *Langmuir* **2008**, *24*, 2212.

(27) Menon, V. P.; Martin, C. R. *Analytical Chemistry* **1995**, *67*, 1920.

(28) Smith, C. P.; White, H. S. *Analytical Chemistry* **1993**, *65*, 3343.

(29) Shao, Y.; Mirkin, M. V.; Fish, G.; Kokotov, S.; Palanker, D.; Lewis, A. *Analytical Chemistry* **1997**, *69*, 1627.

(30) Conyers, J. L.; White, H. S. *Analytical Chemistry* **2000**, *72*, 4441.

(31) Chen, S.; Kucernak, A. *The Journal of Physical Chemistry B* **2002**, *106*, 9396.

(32) Caston, S. L.; McCarley, R. L. *Journal of Electroanalytical Chemistry* **2002**, *529*, 124.

(33) Morris, R. B.; Franta, D. J.; White, H. S. *Journal of Physical Chemistry.* **1987**, *91*, 3559.

(34) Tu, Y.; Lin, Y. H.; Ren, Z. F. *Nano Lett.* **2003**, *3*, 107.

(35) Belding, S. R.; Dickinson, E. J. F.; Compton, R. G. *The Journal of Physical Chemistry C* **2009**, *113*, 11149.

(36) Gray, N. J.; Unwin, P. R. *Analyst* **2000**, *125*, 889.

(37) Fan, F. R. F.; Bard, A. J. *Science* **1995**, *267*, 871.

(38) Compton, R. G.; Wildgoose, G. G.; Rees, N. V.; Streeter, I.; Baron, R. *Chemical Physics Letters* **2008**, *459*, 1.

(39) Dai, X.; Wildgoose, G. G.; Salter, C.; Crossley, A.; Compton, R. G. *Analytical Chemistry* **2006**, *78*, 6102.

(40) Seibold, J. D.; Scott, E. R.; White, H. S. *Journal of Electroanalytical Chemistry and Interfacial Electrochemistry* **1989**, *264*, 281.

(41) Penner, R. M.; Heben, M. J.; Longin, T. L.; Lewis, N. S. *Science* **1990**, *250*, 1118.

(42) Merkin, M. V.; Dekker, M. *Journal of Electroanalytical Chemistry* **1992**, *328*.

(43) Slevin, C. J.; Gray, N. J.; Macpherson, J. V.; Webb, M. A.; Unwin, P. R. *Electrochemical Communications* **1999**, *1*, 282.

(44) Chen, S.; Kucernak, A. *Electrochemical Communications* **2002**, *4*, 80.

(45) Woo, D. H.; Kang, H.; Park, S. M. *Analytical Chemistry* **2003**, *75*.

(46) Kateman, B. B.; Schuhmann, W. *Electroanalysis* **2002**, *14*.

(47) Barton, A. C.; Collyer, S. D.; Davis, F.; Gornall, D. D.; Law, K. A.; Lawrence, E. C. D.; Mills, D. W.; Myler, S.; Pritchard, J. A.; Thompson, M.; Higson, S. P. J. *Biosensors and Bioelectronics* **2004**, *20*, 328.

(48) Evans, U.; Colavita, P. E.; Doescher, M. S.; Schiza, M.; Myrick, M. L. *Nano Lett.* **2002**, *2*, 641.

(49) Doescher, M. S.; Evans, U.; Colavita, P. E.; Miney, P. G.; Myrick, M. L. *Electrochemical and Solid-State Letters* **2003**, *6*, C112.

(50) Penner, R. M.; Martin, C. R. *Analytical Chemistry* **1987**, *59*, 2625.

(51) Jeoung, E.; Galow, T. H.; Schotter, J.; Bal, M.; Ursache, A.; Tuominen, M. T.; Stafford, C. M.; Russell, T. P.; Rotello, V. M. *Langmuir* **2001**, *17*, 6396.

(52) Thurn-Albrecht, T.; Steiner, R.; DeRouchey, J.; Stafford, C. M.; Huang, E.; Bal, M.; Tuominen, M.; Hawker, C. J.; Russell, T. P. *Advanced Materials* **2000**, *12*, 787.

(53) Speets, E. A.; Ravoo, B. J.; Roesthuis, F. J. G.; Vroegindeweij, F.; Blank, D. H. A.; Reinhoudt, D. N. *Nano Lett.* **2004**, *4*, 841.

(54) Koehne, J.; Li, J.; Cassell, A. M.; Chen, H.; Ye, Q.; Ng, H. T.; Han, J.; Meyyappan, M. *Journal of Materials Chemistry* **2004**, *14*, 676.

(55) Wang, K.; Fishman, H. A.; Dai, H.; Harris, J. S. *Nano Lett.* **2006**, *6*, 2043.

(56) Yang, N.; Uetsuka, H.; Osawa, E.; Nebel, C. E. *Nano Lett.* **2008**, *8*, 3572.

(57) Dickey, M. D.; Lipomi, D. J.; Bracher, P. J.; Whitesides, G. M. *Nano Lett.* **2008**, *8*, 4568.

(58) Xu, Q.; Rioux, R. M.; Dickey, M. D.; Whitesides, G. M. *Accounts of Chemical Research* **2008**, *41*, 1566.

(59) Cutress, I. J.; Compton, R. G. *Journal of Electroanalytical Chemistry* **2010**

645, 159.

(60) Cutress, I. J.; Dickinson, E. J. F.; Compton, R. G. *Journal of Electroanalytical Chemistry* **2010**, *638*, 76.

(61) Ferrigno, R.; Girault, H. H. *Journal of Electroanalytical Chemistry* **2000**, *492*, 1.

(62) Heinze, J. *Journal of Electroanalytical Chemistry* **1981**, *124*, 73.

(63) Nann, T.; Heinze, J. *Electrochemistry Communications* **1999**, *1*, 289.

(64) Gavaghan, D. J. *Journal of Electroanalytical Chemistry* **1998**, *456*, 1.

(65) Gavaghan, D. J.; Gillow, K.; Sűli, E. *Langmuir* **2006**, *22*, 10666.

(66) Myland, J. C.; Oldham, K. B. *Journal of Electroanalytical Chemistry* **1996**, *405*, 39.

(67) Strutwolf, J. *Electroanalysis* **2005**, *17*, 1547.

(68) Cutress, I. J.; Compton, R. G. *Journal of Electroanalytical Chemistry*, *643*, 102.

(69) Woodvine, H. L.; Terry, J. G.; Walton, A. J.; Mount, A. R. *Analyst*, *135*, 1058.

(70) Alden, J., Oxford University, 1998.

(71) Stephens, M. M.; Moorhead, E. D. *Journal of Electroanalytical Chemistry* **1987**, *220*, 1.

(72) Fulian, Q.; Fisher, A. C. *The Journal of Physical Chemistry B* **1998**, *102*, 9647.

(73) Harriman, K.; Gavaghan, D. J.; Houston, P.; Süli, E. *Electrochemistry Communications* **2000**, *2*, 163.

(74) Strutwolf, J.; Williams, D. E. *Electroanalysis* **2005**, *17*, 169.

(75) Alden, J. A., J. Booth, R.G. Compton *, R.A.W. Dryfe, G.H.W. Sanders *Journal of Electroanalytical Chemistry* **1995**, *389*, 45.

(76) Beriet, C.; Ferrigno, R.; Girault, H. H. *Journal of Electroanalytical Chemistry* **2000**, *486*, 56.

(77) Michel, R.; Montella, C.; Verdier, C.; Diard, J. P. *Electrochimica Acta*, *55*, 6263.

(78) Stevens, N. P. C.; Fisher, A. C. *The Journal of Physical Chemistry B* **1997**, *101*, 8259.

(79) Menshykau, D.; Compton, R. G. *The Journal of Physical Chemistry C* **2009**, *113*, 15602.

2. Background

2.1. Electrochemical Studies

The investigation of electrode reactions requires studies of the electrode kinetics and electrochemical thermodynamics at a single electrode surface. For this a three-electrode system is usually necessary. The electrochemical cell comprises a working electrode (w.e.) which is the electrode of study, a reference electrode (r.e.) of known potential, and counter electrode (c.e.), typically platinum gauze[1]. For aqueous solutions the reference electrode is typically a Saturated Calomel Electrode (SCE) or a silver / silver chloride electrode.

A potential voltage, E, is applied between the w.e. and r.e. but as the potential of the r.e. is constant, only the potential of the w.e. changes. E is therefore the potential of the w.e. with respect to the r.e. The reactivity of the w.e. is controlled by changing this applied voltage. Current passes between the w.e. and c.e. which is of large enough area to ensure the current at the w.e. is limiting and that this current is a measure of the w.e. reaction rate. Figure 2.1 is a schematic diagram representing a typical three-electrode cell set up.

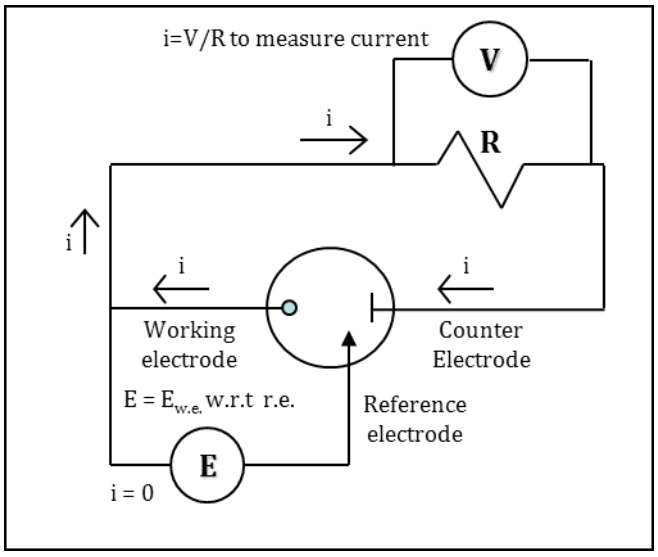

Figure 2.1: Schematic diagram representing the three-electrode cell set up. The voltage is applied between the w.e. and the r.e. and is therefore the potential with respect to the r.e. and the current passes between the w.e. and the c.e.

The Nernst Equation can be used to provide a linkage between the applied or measured electrode potential and the concentrations of the oxidised and reduced forms of the electro active species at equilibrium. For a general charge transfer reaction in which *n* electrons are transferred, Nernst showed that the potential E, at the electrode related to the concentrations of the oxidized and reduced species by

$$E = E^{\Theta\prime} + \frac{\mathbf{R}T}{n\mathbf{F}} ln \frac{c_O}{c_R} \qquad \textbf{Eqn. 2.1}$$

where, E is potential (in V), $E^{\Theta\prime}$ is the formal potential, **R** is the universal gas constant (8.314 $JK^{-1}mol^{-1}$), n is the number of electrons transferred in the redox reaction, T is the temperature (in K), **F** is Faraday's constant (96845 $Cmol^{-1}$); and c_O and c_R are the concentrations of the oxidised and reduced species at the electrode surface, respectively. The formal potential is equal to the half-cell potential when the concentration ratio c_O/c_R is unity and all other concentrations are fixed. $E^{\Theta\prime} \sim E^{\Theta}$, the standard potential, when the activities of the oxidized and reduced species remain constant.

In order to induce charge transfer, the applied potential induces an electric field at the electrode/solution interface as a result of the difference in electrical potential between the two phases. In order for the interface to maintain electrical neutrality the charge on the electrode must be matched in solution by ions of equal and opposite charge. This gives rise to electrostatic redistribution of ions at the interface. The electrode/solution interface then acts like two oppositely charged plates of a capacitor (known as a double layer). Its capacitance is a measure of the amount of electric charge stored for a given potential difference. (Figure 2.2)

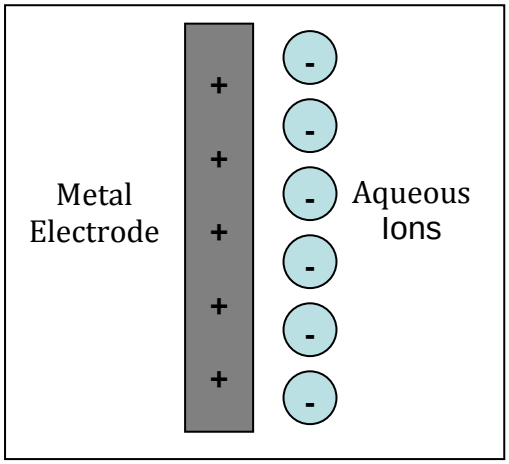

Figure 2.2: Schematic diagram of aqueous anions lining up against a positively charged metal electrode creating a double layer.

The change in concentration of ionic species caused by charge transfer can result in a change in charged species in the solution, and thus alter the electric field distribution close to the electrode. This will then cause a change in migratory flux and hence the rate of mass transport of electroactive material to and from the electrode. This interrelation of ion migration, diffusional mass transport and charge transfer at the electrode surface during the electrochemical reaction is complex and can be very difficult to control and interpret.

To avoid these problems, experiments are therefore typically performed under conditions where migration can be neglected. This is achieved by the presence of high concentrations of chemically and electrochemically inert ions in solution, in a solution known as the background electrolyte. The background electrolyte often has ions of concentration around or in excess of 0.1 M. This should be at least 100 times the concentration of the reactant for the measured current not to be perturbed by migration effects[2]. The double layer thickness is then on the molecular scale, comparable to the electron transfer distance between electrode and redox species and the absence of potential gradients outside this region prevents migration of ions from the bulk becoming important. Since the background electrolyte is added in such high concentrations and is not involved in any Faradic process, the redistribution of cations or anions close to the interface has little effect on the overall

concentration in the bulk. As the electrolytic reaction proceeds, the background electrolyte is therefore readily able to maintain electrical neutrality in the interfacial region and prevent build-up of electric fields in solution during electrolysis.

The very high concentration of background electrolyte compared to that of the redox active species also has the added advantage that the ionic strength of the solution effectively stays constant during electrolysis. This means that the activity coefficients of the oxidised and reduced species are also kept constant and thus both thermodynamics and kinetics can be described in terms of concentration. Even with added ~0.1 M inert ions however the solution has a finite resistance, R, and at high currents a component of the applied potential E is often required to drive the current through the solution. This component is termed iR drop[1].

2.2. The Standard Redox Couple - Ferri/ferrocyanide

The simplest electrochemical reaction involves a fully electrochemically reversible redox couple. Electrochemically reversible redox reagents are those where the oxidation and reduction reactions are kinetically rapid, such that the reaction is under thermodynamic control and the Nernst equation (Eqn. 2.1) always applies. A common standard redox couple for this purpose is ferri/ferrocyanide, ($[Fe(CN)_6]^{3-}/[Fe(CN)_6]^{4-}$), sold commercially in both oxidised and reduced forms[3-7].

$$[Fe(CN)_6]^{3-} + e^- \rightleftharpoons [Fe(CN)_6]^{4-} \qquad \textbf{Eqn. 2.2}$$

The $[Fe(CN)_6]^{3-}$ complex has O_h symmetry and consists of a Fe(III) centre, bound to six cyanide ligands. ^-CN molecules have strong ligand fields, creating a low-spin configuration in the Fe d-orbitals. $[Fe(CN)_6]^{3-}$ can easily be reduced to $[Fe(CN)]^{4-}$ in a one electron transfer process[8] with only a very small configuration change to form the Fe(II) centre. The large, strongly bound ^-CN molecules prevent strong interaction with water. The diffusion coefficients of both oxidised ($6.98*10^{-6}$ cm^2s^{-1}) and reduced ($6.61*10^{-6}$ cm^2s^{-1}) complexes at

298 K in 0.1 M KCl, are well documented in literature[4], as are the electrochemical responses at both macroelectrode and microelectrode surfaces. The Standard potential of 0.001 M ferri/ferrocyanide in 0.1 M KCl vs. the Normal hydrogen electrode (NHE) is ~0.436 V[9]. The standard redox potential of the saturated Calomel electrode (SCE) vs. NHE is 0.244 V. This then gives an approximate oxidation potential for ferri/ferrocyanide of 0.192 V vs. SCE.

2.3. Cyclic Voltammetry

Cyclic Voltammetry is a commonly used technique in electrochemistry, since it provides a fast and simple method for initial characterisation of a redox-active system, able to provide an estimate of the redox potential as well as information about the rate of electron transfer between the electrode and the analyte. Cyclic voltammetric measurements are performed in a stagnant solution and thus (except at very slow seep rates and/or very long times) rely only on diffusion to transport material to the surface of the electrode. Ferri/ferrocyanide is an example of a one-electron (n=1) redox system that can be can be represented by the simple general equation:

$$A + e^- \underset{k_{ox}}{\overset{k_{red}}{\rightleftharpoons}} B \qquad \textbf{Eqn. 2.3}$$

Where A (ferricyanide) is the oxidised form of the electroactive species, B (ferrocyanide) is the reduced form of the electroactive species, k_{ox} is the oxidation rate constant and k_{red} is the reduction rate constant.

In a cyclic voltammetric experiment the potential, E, applied to the w.e. is linearly changed with time between two potential limits, first sweeping E in the forward direction from E_1 to E_2 and then in the reverse direction back to E_1. The applied potential, E, with time is a function of the potential sweep rate (v) at which the potential is swept and also upon the time[2]. The change in E with time is therefore controlled by the potential sweep rate (v). Figure 2.3 represents the potential waveform.

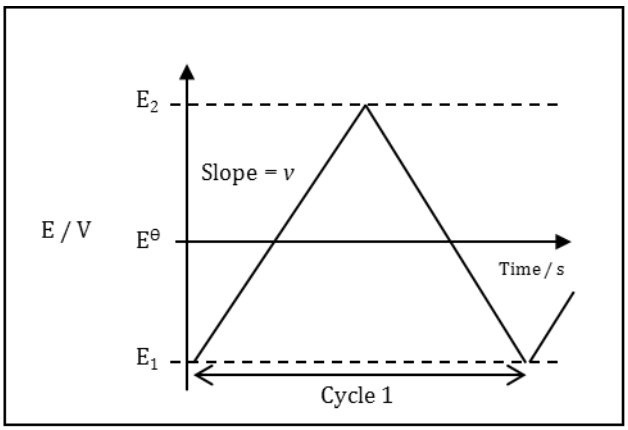

Figure 2.3: Diagram representing the potential sweep waveform as the time of the experiment progresses

This data is then plotted as potential (*E*) vs. current (i), giving a cyclic voltammogram (CV). Figure 2.4 represents a typical CV obtained during a fully reversible redox reaction, where only the oxidised species, A is present in solution at the beginning of the experiment.

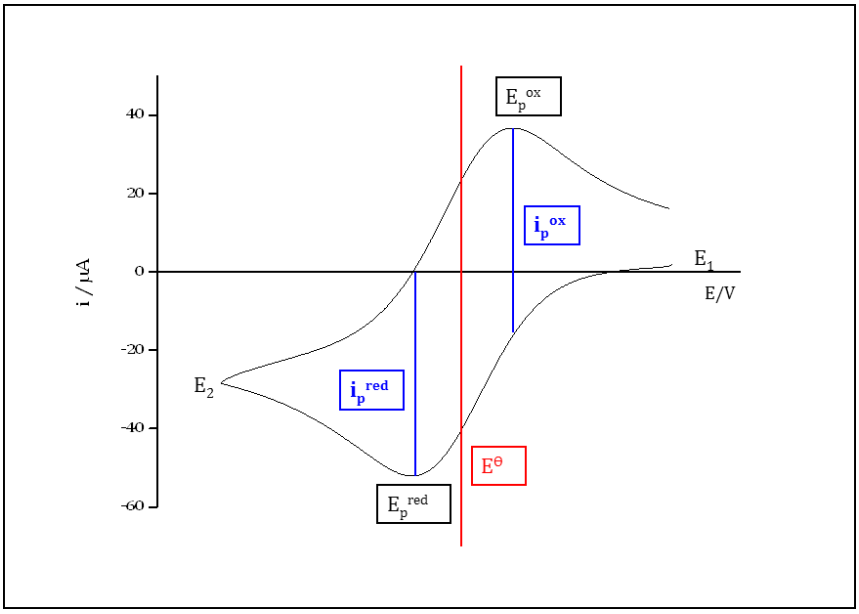

Figure 2.4: A typical Cyclic Voltammogram for a fully reversible redox system. E_1 is the start potential; E_2 is the limiting potential, i_p^{ox} is the anodic (oxidation) peak current, i_p^{red} is the cathodic (reduction) peak current, E_p^{ox} is anodic (oxidation) peak potential and E_p^{red} is the cathodic (reduction) peak potential[1].

For the reduction of A, it is normal to start at a potential E_1, where only the oxidised species, A is present and then decrease *E* until the reduction reaction occurs, when a characteristic negative current starts to flow. The current magnitude rapidly increases, becoming more negative (for a reduction reaction) since the reaction rate constant increases with decreasing potential[1]. When *E*<<

E^{θ} all of A at the electrode is converted to B and the concentration of A at the electrode surface falls to zero. The magnitude of the current falls in this region even with decreasing potential, as mass transfer of A to the electrode becomes limiting since progressive depletion from further and further away from the electrode surface, leads to less and less efficient mass transport. In the reversible case, B can be oxidised back to A. When reversing the scan from E_2, a more positive current is passed with increasing potential as the product oxidation reaction occurs. The current falls to zero, in this case, when all of B at the electrode surface is converted back to A.

The peak potential, E_p and the peak shape, with respect to E^{θ}, are characteristic of the reversibility of the A/B redox couple. For a fully electrochemically reversible system the magnitudes of the forward and reverse peaks are the same, the peak positions are independent of sweep rate, v and the peak separation depends on the number of electrons, n involved in the transfer process. The peak separation is given by

$$E_p^{ox} - E_p^{red} = 2.218\frac{\mathbf{R}T}{n\mathbf{F}} \qquad \textbf{Eqn. 2.4}$$

where E_p^{ox} is the anodic (oxidation) peak potential and E_p^{red} is the cathodic (reduction) peak potential. Therefore a reversible electron transfer at 298K will have a peak separation of approximately $59/n$ mV, independent of scan rate[1]. Since the peak separation is independent of scan rate for fully reversible systems, the half wave potential, $E_{1/2}$ can be found from the mid-point between the oxidation and reduction peak potentials at all scan rates, v.

$$E_{1/2} = \frac{\left(E_p^{ox} - E_p^{red}\right)}{2} \qquad \textbf{Eqn. 2.5}$$

$E_{1/2}$ is related to E^{θ} by

$$E^{\Theta} = E_{1/2} + \frac{\mathbf{R}T}{n\mathbf{F}} ln\left(\frac{D_O}{D_R}\right)^{1/2} \qquad \textbf{Eqn. 2.6}$$

where D_R is the diffusion coefficient of the reduced species (in cm^2s^{-1}) and D_O is the diffusion coefficient for the oxidised species[1]. The magnitude of the second term is usually small, so an estimate of the standard potential can be obtained from the cyclic voltammogram of a fully reversible process if one assumes that $D_O = D_R = D$ and therefore $E_{1/2} \approx E^{\theta}$.

The peak current, i_p for an electrochemically reversible system is related to scan rate, v (in Vs^{-1}), and can be given by the Randles-Sevcik equation[10]

$$i_p = 0.4663AFD^{1/2}v^{1/2}c^{\infty}\left(\frac{F}{RT}\right)^{1/2} \qquad \textbf{Eqn. 2.7}$$

where A is the electrode area (in cm^2), D is as above and c^{∞} is the bulk concentration of the electroactive species (in mol cm^{-3}). From this equation it can be seen that i_p is proportional to $v^{1/2}$. If equations 2.4 to 2.7 are satisfied then the system is termed Nernstian or fully reversible.

As mentioned in section 2.1 there is always a finite resistance arising from the electrolyte solution and also from the electrical wires. Collectively this is known as uncompensated resistance (R_u). This means that the true surface potential, E' will differ from the applied potential by an amount $E' = E - iR_u$. This often means that unless the uncompensated resistance is corrected for, the peak potentials will be shifted from their true value and reversible couples may not appear Nernstian. Then increasing peak separations with increasing current (increasing v), may then be misinterpreted as due to quasi-reversible or even irreversible behaviour if care is not taken to consider the uncompensated resistive effects[1,11,12], especially for macroelectrodes.

2.4. Hemispherical (Radial) Diffusion

When the appropriate potential is applied to a stationary electrode, immersed in an unstirred electrolytic solution, oxidation or reduction of the redox active species at the electrode surface generates a concentration gradient in the

solution near the electrode. Diffusive mass transport is required to bring redox species to the surface from the bulk[11].

There are two distinct limiting cases of diffusion and they are dependent on the size of the electrode. For macroelectrodes of millimetres or greater length, the thickness of the diffusion layer (the layer at the electrode depleted of reactant) is much smaller than the electrode dimension during the time scale of normal experiments. The electrode therefore appears to be an infinite planar surface (Figure 2.5), mass transport is dominated by linear diffusion and the current response decays with time.

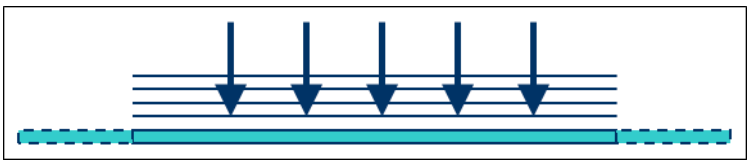

Figure 2.5: Diagram representing the planar diffusion field experienced by macroelectrode

For a disc microelectrode, if the radius is sufficiently small that during normal experimental timescales, the dimensions of the diffusion layer exceed the radius of the electrode, the mass transport process becomes dominated by hemispherical diffusion (figure 2.6). Even though the rate of diffusion for redox species decreases with time as depletion occurs, this is counterbalanced by an increase in the number of redox species diffusing to the electrode as the surface area of the hemisphere grows. These effects exactly counterbalance at steady-state and so the diffusion rate reaches a steady state at some finite time which means that the current also attains a time-independent, steady-state value.

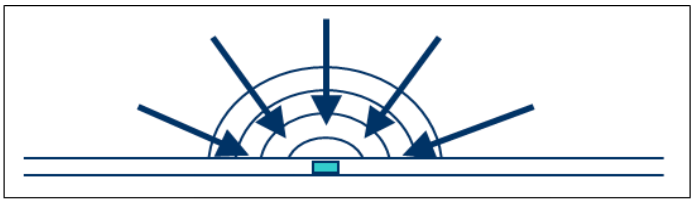

Figure 2.6: Diagram representing the hemispherical diffusion field experienced by microelectrodes

The current for both limiting cases can be derived analytically for many electrode shapes[11]. The simplest derivations involve spherical electrodes which can be solved using circular coordinates since the surface is uniformly accessible. For a macroelectrode of any shape, experiencing a linear diffusion field, the time-dependent current, i_t obeys the Cottrell equation[11,12]

$$i_t = \frac{nAFD^{1/2}c^{\infty}}{\pi^{1/2}t^{1/2}} \qquad \textbf{Eqn. 2.8}$$

where t is the time and at t =0 the bulk concentration, $c^{\infty} \rightarrow 0$ at the electrode surface. This shows that i_t is inversely proportional to $t^{1/2}$. Conditions of planar diffusion are only properly fulfilled if the electrode is sufficiently large.

As the electrode radius decreases, semi-infinite planar diffusion transforms into spherical diffusion and the current attains a time-independent, steady-state value given by[12]

$$i_L = \frac{nAFDc^{\infty}}{r} \qquad \textbf{Eqn. 2.9}$$

where r is the electrode radius, and i_L, the mass-transport limited current is independent of time. The modified Cottrell expression[11,12], derived from equations 2.8 and 2.9 was developed to model the electrode current, i at all times, t.

$$i = \frac{nAFD^{1/2}c^{\infty}}{\pi^{1/2}t^{1/2}} + \frac{nAFDc^{\infty}}{r} \qquad \textbf{Eqn. 2.10}$$

From this equation we can see that at very short time scales, for all geometries, planar diffusion dominates and the second term can be neglected, resulting in the limiting case, modeled by the Cottrell equation. At longer times the first term in equation 2.10 will have decayed to the point where its contribution to the overall equation is negligible and thus the mass transport is then dominated by hemispherical diffusion, resulting in a limiting current. From this it can be

seen that the smaller the electrode, the shorter the time for establishment of hemispherical diffusion. It can be noted that for very long timescales, hemispherical diffusion will theoretically be established even at macroelectrode surfaces. Indeed, so called 'edge effects' are often detected during long experimental times[11]. Unavoidable convective processes, however, typically prevent macroelectrodes from ever reaching true steady state situations.

In general, the diffusion at microelectrodes is governed by time-dependent changes in mass transport, where one-dimensional diffusional fields are transformed into multidimensional spatial fields, when an additional radial component is introduced. Heinze[11] describes this mathematically using Fick's laws of diffusion for several microelectrode geometries (table 2.1). As with the microsphere case described above, once radial diffusion becomes the predominant diffusional process, the currents become time independent or insensitive. The attainable steady state or quasi-steady state limiting currents for these different geometries are also given in Table 2.1. These limiting current expressions were determined through Oldham's theoretical studies[11,13], by introducing a surface diameter, d ($i_L = 2n\mathbf{F}c^{\infty}Dd$) which can be applied to all geometries[11].

Type of electrode	Diffusion towards electrode	Limiting current
Large (macro) electrode	$\frac{\delta c}{\delta t} = D\frac{\delta^2 c}{\delta x^2}$	N/A for macroelectrode
Micro-cylindrical electrode	$\frac{\delta c}{\delta t} = D\left(\frac{\delta^2 c}{\delta r^2} + \frac{1}{r}\frac{\delta c}{\delta r}\right)$	Approximate: $i = \frac{2n\mathbf{F}Dc^{\infty}A_{surf}}{\ln\left[\frac{4(Dt)}{r^2}\right]}$ where A_{surf} = cylinder surface area and r = electrode radius
Micro-spherical electrode	$\frac{\delta c}{\delta t} = D\left(\frac{\delta^2 c}{\delta r^2} + \frac{2}{r}\frac{\delta c}{\delta r}\right)$	$i_L = 4\pi n\mathbf{F}Dc^{\infty}r$
Micro-disc electrode	$\frac{\delta c}{\delta t} = D\left(\frac{\delta^2 c}{\delta r^2} + \frac{1}{r}\frac{\delta c}{\delta r} + \frac{\delta^2 c}{\delta z^2}\right)$	$i_L = 4n\mathbf{F}Dc^{\infty}r$
Micro-band electrode	$\frac{\delta c}{\delta t} = D\left(\frac{\delta^2 c}{\delta x^2} + \frac{\delta^2 c}{\delta z^2}\right)$	Approximate: $i = \frac{2\pi n\mathbf{F}Dc^{\infty}l}{\ln\left[\frac{4(Dt)}{r^2}\right]}$ where l = length of band and r is related to band width, w by $r = w/\pi$ [14]

Table 2.1: Table to show the diffusional schemes towards electrodes of different geometries and the limiting currents associated with these electrodes, adapted from ref. (10).

For microelectrodes under diffusional control, the current density is larger the smaller their diameter, width or dimension. This effect is greatest for spherical diffusion fields and current densities can be up to two orders of magnitude greater than at a normal macroelectrode[11]. Table 2.1 shows that cylindrical and band microelectrodes attain only quasi-steady states, as their currents contain time-dependent terms. On the other hand, the current response can be increased by altering the band length without changing the diffusion field. The equation for a microband electrode will be discussed in more detail in chapter 6.

2.5. Modified Tafel Analysis

An accurate picture of any dynamic process must yield a thermodynamic equation at the limit of equilibrium. For an electrode reaction, equilibrium is characterised by the Nernst Equation (Eqn. 2.1), which links the electrode potential to the bulk concentration.

A theory is also required to explain the observed dependence of current on potential under specific cirumstances. For example current is often limited wholly or partially by the rate at which redox reagents are transported to the electrode surface. This kind of limitation does not affect interfacial kinetics. This is especially true in the case of low currents and efficient stirring, in which mass transport is not the limiting factor affecting current. In these cases the current is controlled by interfacial dynamics and is dependent upon the potential driving the reaction. Early studies by Tafel[1] showed that in such a case current is often related exponentially to the over potential, η.

$$\eta = a + b\log|i| \qquad \textbf{Eqn. 2.11}$$

where i is the current and the constants and for a reduction reaction, a and b can be determined by theory as:

$$a = \frac{+2.3\mathbf{R}T}{\eta\alpha_{red}\mathbf{F}}\log i \quad \text{and} \quad b = \frac{+2.3\mathbf{R}T}{\eta\alpha_{red}\mathbf{F}} \qquad \textbf{Eqn. 2.12}$$

where α_{red} is the electrochemical transfer coefficient for reduction and $\alpha_{ox} = 1 - \alpha_{red}$

A plot of log i vs. η known as a Tafel plot is a useful device for evaluating kinetic parameters. In general, there is an anodic (oxidation) branch with a slope $\frac{(1-\alpha_{red})n\mathbf{F}}{2.3\mathbf{R}T}$ and a cathodic (reduction) branch with a slope $\frac{(1-\alpha_{red})n\mathbf{F}}{2.3\mathbf{R}T}$. The linear segments of the graph extrapolate to yield i^0, but the plots deviate sharply from linear behaviour as η approaches zero when the back reactions can no longer be regarded as negligible.

The original Tafel analysis was developed for macroelectrodes and did not take into account the effects of mass transfer or relate to experiments with very facile kinetics and reversible behaviour. It also could not be applied over the entire data range, therefore modified Tafel equations were developed which took into account both mass transfer effects and reversible reactions[1]. The modified Tafel equation used for analysis of data in this thesis was originally developed for a rotating disk electrode[15]. For this type of electrode, currents are steady-state (time-independent) and mass transport rates are constant at a constant rotation speed. The Tafel analysis can be applied here to microelectrodes, since steady-state currents are also reached. On considering a reaction at an electrode where the transfer limited flux, *J*, to the electrode is given by:

$$J = k_{mt}(c^{\infty} - c^{0}) \qquad \textbf{Eqn. 2.13}$$

where k_{mt} is the mass transport rate constant and c^{0} is the concentration of analyte at the electrode surface. The current of a reaction is then related to this flux by:

$$i = n\mathbf{F}AJ = n\mathbf{F}Ak_{mt}(c^{\infty} - c^{0}) \qquad \textbf{Eqn. 2.14}$$

The limiting current, i_L of a reaction is therefore:

$$i_L = n\mathbf{F}Ak_{mt}c^{\infty} \qquad \textbf{Eqn. 2.15}$$

Combing these equations gives

$$\left(\frac{i_L}{i} - 1\right) = \frac{n\mathbf{F}Ak_{mt}c^{\infty}}{n\mathbf{F}Ak_{mt}(c^{\infty} - c^{0})} \qquad \textbf{Eqn. 2.16}$$

Thus

$$\left(\frac{i_L}{i} - 1\right) = \frac{c^{0}}{(c^{\infty} - c^{0})} = \frac{c^{0}}{c^{0}_{prod}} \qquad \textbf{Eqn. 2.17}$$

where c^0_{prod} is the concentration of the redox product and this equation holds true since the sum of the of the concentration of reactants and products is equal to the bulk concentration.

For example, in a reversible reaction: $A + e^- \leftrightarrow B$ where $c^0 = c^0_A$ and $c^0_{prod} = c^0_B$ the applied potential can be related back to the Nernst equation as follows:

$$E = E^\theta + \frac{RT}{nF} \ln \frac{c^0_A}{c^0_B} \qquad \textbf{Eqn. 2.18}$$

If, in the case of a fully electrochemical reversible reaction where $E^\theta = E_{1/2}$ combining equations 2.17 and 2.18 gives:

$$E = E^\theta + \frac{RT}{nF} \ln \left(\frac{i_L}{i} - 1 \right) \qquad \textbf{Eqn. 2.19}$$

A plot of $\ln\left(\frac{i_L}{i} - 1\right)$ vs. E therefore will yield a Tafel plot with a slope $\frac{nF}{RT}$.

If the reaction is kinetic, one could still plot a Tafel slope, though the gradient would be equal to $\frac{\alpha_{red} nF}{RT}$(ref [15]).

2.6. Electrochemical Impedance spectroscopy (EIS)

2.6.1. Nyquist Plots and Equivalent Circuits

AC impedance spectroscopy (EIS) imposes on the w.e. of the three electrode system, an oscillating sinusoidal potential, E_{ac} (of c.a. 5 – 10 mV rms amplitude) superimposed on a fixed dc potential, E_{dc}. The dc potential is used to set the mean surface concentrations of A and B at the electrode surface. The measured response is the ac component of the current, i_{ac} at differing applied frequencies, ω (in radians s^{-1})[1]. The impedance, Z is then calculated as

$$Z = \frac{E_{ac}}{i_{ac}} \qquad \textbf{Eqn. 2.20}$$

The impedance is split into two parts, a real component, Z_{Re} corresponding to the in-phase response and an imaginary component, Z_{Im} corresponding to the out-of-phase response.

$$Z(\omega) = Z_{Re} - jZ_{Im} \qquad \textbf{Eqn. 2.21}$$

where j is $\sqrt{-1}$.

The variation of impedance with frequency is often presented as a Nyquist plot which displays Z_{Re} on the x-axis and $-Z_{Im}$ on the y-axis for different values of ω. Nyquist plots are extremely useful in electrochemistry as they are able to show the kinetics and diffusional processes occurring in the system under investigation. Theoretical analysis leads to appropriate equivalent circuits which are able to model these observed results.

Typical shapes for Nyquist plots of ac impedance as a function of frequency are most easily explained by first considering electrical analogue circuits. A pure resistor gives a purely real impedance of Z_{Re} = R, the value of which is independent of frequency. A Nyquist plot of resistance will therefore appear as a fixed point, R on the Z_{Re} axis[2] (figure 2.7), giving the resistance in Ohms.

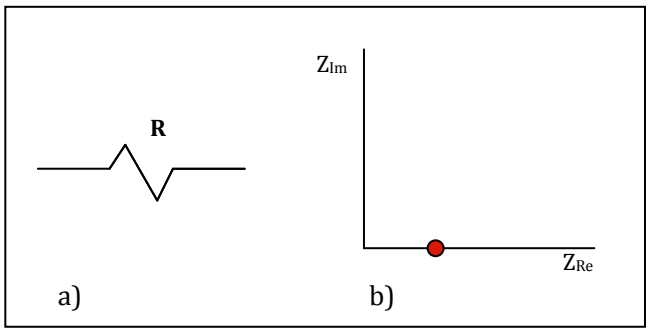

Figure 2.7: Schematic diagram representing the Nyquist plot of a pure resistor, R where **a)** is the electrical representation of a resistor and **b)** is the corresponding Nyquist plot.

For a capacitor, the impedance is purely imaginary and $-Z_{Im} = 1/\omega C$, where C is the capacitance. There is no real resistance and therefore no offset on

the Z_{Re} axis. However, the impedance is inversely proportional to the frequency and therefore at low frequencies the impedance is large and at high frequencies the impedance is small. Thus the Nyquist plot will appear as in figure 2.8.

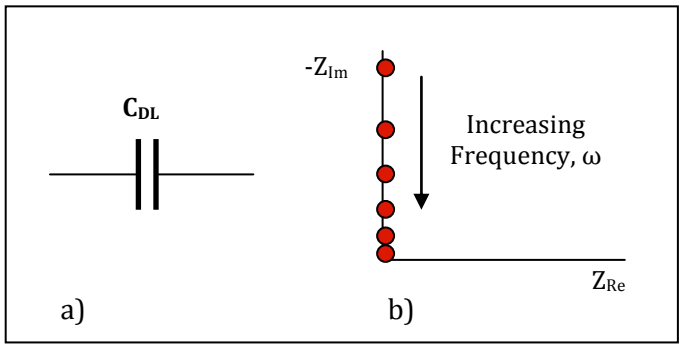

Figure 2.8: Schematic diagram representing the Nyquist plot of a pure capacitor, where **a)** is the electrical representation of a double layer capacitor and **b)** is the corresponding Nyquist plot.

When a resistor and a capacitor are placed in series, the Nyquist plot will appear as a vertical line with $Z_{re} = R$ and $-Z_{Im} = 1/\omega C$, [2] (figure 2.9).

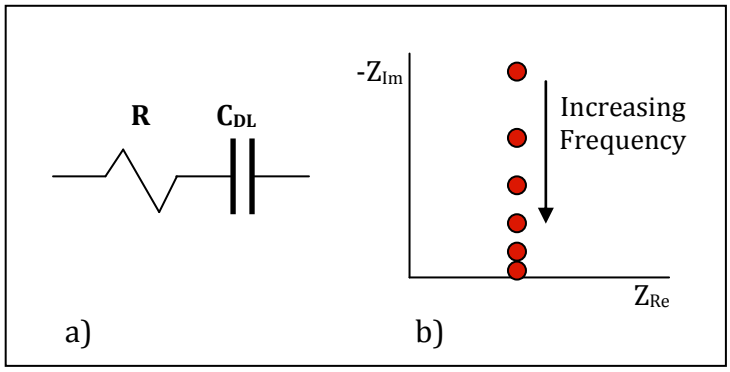

Figure 2.9: Schematic diagram representing the Nyquist plot of a pure resistor and pure capacitor in series, where **a)** is the electrical representation of a resistor and capacitor in series and **b)** is the corresponding Nyquist plot.

A capacitor and resistor in parallel is a little more complicated because the current can pass through either component. High frequencies favour passage of current through the capacitor and lower frequencies favour passage of current through the resistor. In this case the Nyquist plot appears as a semicircle (figure 2.10). At the high frequency limit current flows only through C_{DL} and $Z_{Re} = 0$. As the frequency decreases, the capacitor starts to charge and current flow is impeded, when current begins to pass through the resistor, leading to an increasing Z_{Re}. At the lowest frequencies once C_{DL} is fully charged, the current flows only through the resistor[2] and $Z_{Re} = R - Z_{Im} = 0$.

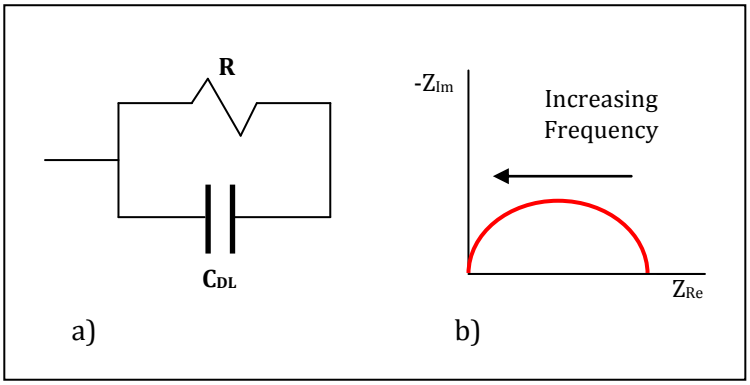

Figure 2.10: Schematic diagram representing the Nyquist plot of a pure resistor and pure capacitor in parallel, where **a)** is the electrical representation of a resistor and capacitor in parallel and **b)** is the corresponding Nyquist plot.

The general equivalent circuit used for redox active electrochemical systems was developed by Randles in 1947[16]. The circuit is made up of a combination of resistors and capacitors, which represent physical processes occurring in the reaction. This model also includes a Warburg impedance component, used to model the diffusional transport of electroactive species in the system. Figure 2.11 shows the Randles equivalent circuit which is still used effectively today for fitting impedance data and which is a valuable tool for understanding different systems under investigation.

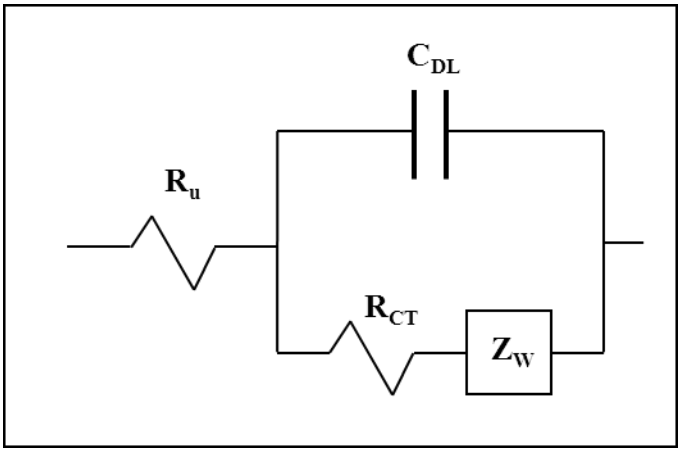

Figure 2.11: Schematic diagram representing Randles equivalent electrical circuit used to describe redox active electrochemical systems; R_u is the uncompensated electrolyte resistance, R_{CT} is the charge transfer resistance, Z_W is the Warburg impedance and C_{DL} is the double layer capacitance.

Figure 2.12 shows a typical Nyquist plot obtained during a reversible electrochemical process at a macroelectrode[1].

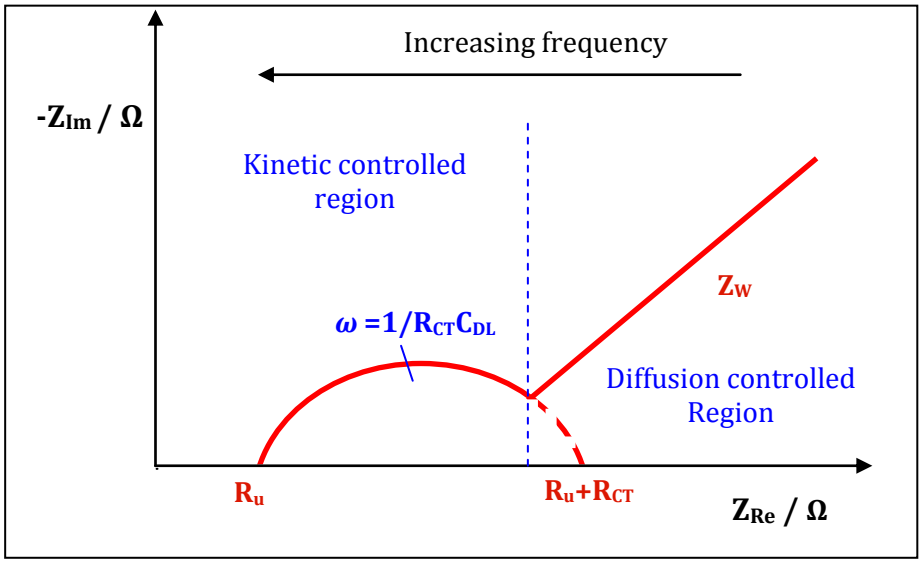

Figure 2.12: Schematic representation of a typical Nyquist plot obtained from reversible electrochemical systems; R_u is the uncompensated resistance, R_{CT} is the charge transfer resistance, Z_w is the Warburg impedance, ω is the angular frequency and C_{DL} is the double layer capacitance

At very high frequencies the dominant contribution to the total impedance is the uncompensated resistance, R_U (section2.3), determined on the plot by the intercept of the semicircle on the Z_{Re} axis. The charging of the electrode/electrolyte double layer (the origin of the electrical capacitor) provides a path of negligible resistance to non-Faradaic current at high frequencies. As the frequency decreases however, C_{DL} charges, the correct potential profile for electrochemistry is established and a redox reaction occurs whose rate is governed by $1/R_{CT}$. By extrapolating the semicircle to the x-axis an accurate value for R_{CT} can be obtained. As the reaction continues and the electrode/electrolyte interface becomes depleted of analyte, a diffusion gradient is established which produces mass transport of analyte from the bulk to the surface, modeled by Z_W. At low frequencies this mass transport becomes a significant limiting factor. This is modeled by the Warburg impedance Z_W,

$$Z_W = \frac{\sigma}{\omega^{1/2}} - j\frac{\sigma}{\omega^{1/2}} \qquad \textbf{Eqn. 2.22}$$

where σ is the Warburg coefficient, j is $\sqrt{-1}$ and ω is the radial frequency. This gives the typical Z_W 45^0 line on the Nyquist plot. Since a macroelectrode appears as an infinite surface during typical reactions, depletion becomes

progressively greater with time (lower ω) and the Warburg impedance, Z_W will continue to rise.

Since the development and subsequent interest in the different physical nature of microelectrodes, much research has been conducted in the advancement of theories and equivalent circuits, attempting to explain and analyse the unusual impedance plots observed when working with microelectrodes.

Figure 2.13 shows the now established modified Randles equivalent circuit used to model microdisc behaviour[5,17].

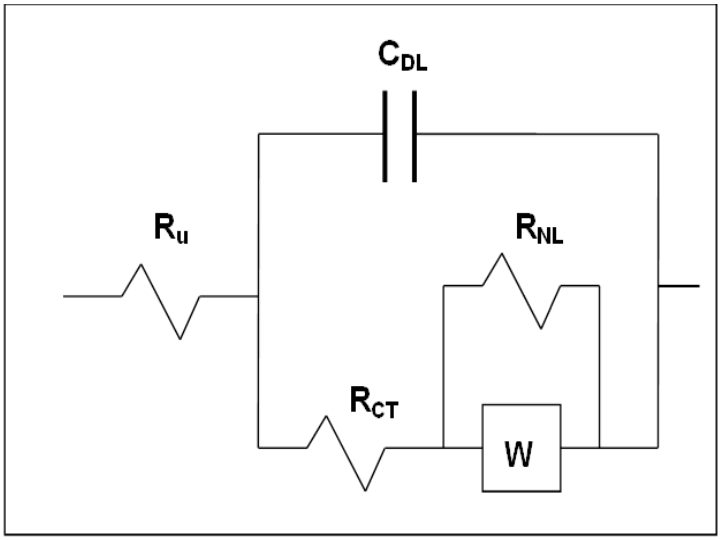

Figure 2.13: Schematic representation of the modified Randles' Circuit frequently used to model the EIS response of microdisc electrodes; R_u is the uncompensated (electrolyte) resistance, C_{DL} models the charging of the double layer, R_{CT} is the charge transfer resistance, Z_W - is the Warburg impedance and R_{NL} models the non-linear resistance which corresponds to steady-state diffusion.

In this case, R_{NL} describes the non-linear resistance which determines the steady state current obtained, once under hemispherical diffusion. Bruce and co-workers state that, although this equivalent circuit is only an approximation to impedance of a microdisc, the 'hemispherical approximation', it provides a method of extracting the different parameters with reasonable accuracy across the whole range of ω[17]. Figure 2.14 is a schematic diagram representing a typical Nyquist plot obtained at a microdisc.

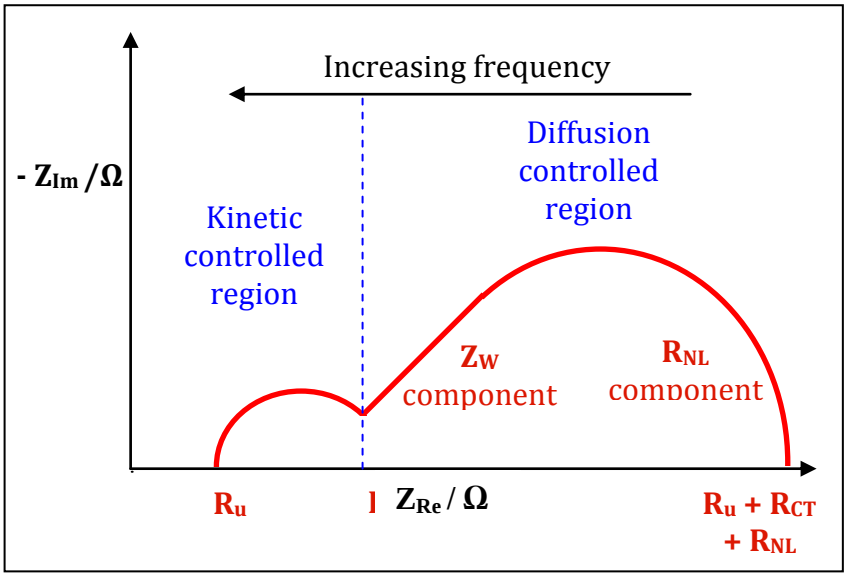

Figure 2.14: Schematic representation of a typical Nyquist plot obtained from reversible electrochemical system at a microelectrode; R_u is the uncompensated resistance, R_{CT} is the charge transfer resistance, Z_w is the Warburg impedance and R_{NL} is the non-linear resistance.

Figure 2.14 shows a small, initial semicircle again attributed to the charge transfer resistance in parallel with the double layer capacitance attributed to electric charge transfer. It will be discussed later, however, that for microelectrodes, where hemispherical diffusion is attained very quickly and coupled with the fact that fully reversible reactions have very facile kinetics, this initial charge transfer semicircle is often very small and the resistance may not be measurable[5,18]. The most interesting feature of a microelectrode Nyquist plot is that the Warburg impedance does not continue as a 45^0 line. The plot instead, returns to the Z_{Re} axis at very low frequencies, indicating a steady state current as $Z_W \rightarrow 0$.

2.6.2. Transmission Line Theory

Although the Randles equivalent circuit enables us to reasonably fit and interpret data from Nyquist plots, physically it is not clear why it is an accurate representation of electrochemical reaction. The Warburg impedance component is placed in parallel with the double layer capacitor, suggesting that the Warburg element can be short circuited by passing current when charging the double layer. However, the Warburg impedance is a diffusion parameter and describes the mass transport in the bulk solution at medium frequencies not at the electrode surface at high frequencies. Without understanding the

fundamental principles, it is difficult to see why these two components can be related in this way. Transmission line theory, based on a model originally used to represent power lines in engineering can be used to justify the use of the Randles' circuit[19,20]. The transmission lines are constructed by examining the fundamentals of charge and species movement within the electrochemical system which then can be reduced to describe the system in terms of the physical properties of electronic circuit elements[20].

Research by Albery, Mount and others, in their work on ion and electron transport through polymer films[15,19-22] has shown that both ion and electron transport always produce a finite rather than a zero resistance. The transmission line they proposed therefore has two resistive rails. They also show that the current is driven not only by the voltage (or field) but also by diffusion gradients[19-22]. They proposed a modified Transmission rail with distributed Capacitance, as shown in figure 2.15[20].

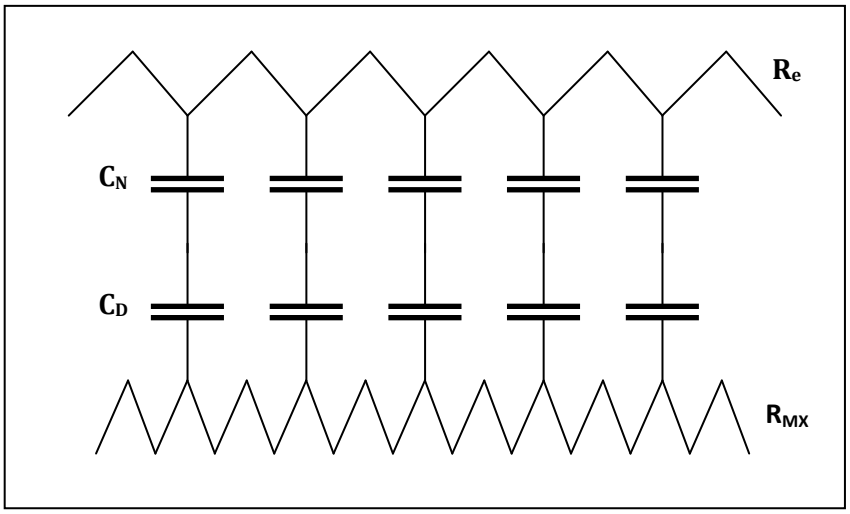

Figure 2.15: Schematic diagram of the Modified Transmission Line, proposed by Albery and Mount; Re represents the resistive line of ferri/ferrocyanide, R_{MX} represents the resistive line of the inert background ions in the electrolyte, C_N is the modified Nernst capacitance and C_D is the modified Donnan capacitance.

Consider the flux, J_e of electrons at the electrode interface in the z-direction, for a simple one electron transfer process. ($A^+ + e^- \leftrightarrow B$)

$$J_e = D_e \left\{ \frac{\delta b}{\delta z} + \left[\frac{ab}{a+b} \right] \left(\frac{F}{RT} \right) \left(\frac{\delta E}{\delta z} \right) \right\} \qquad \textbf{Eqn. 2.23}$$

where a and b are the concentrations of A and B respectively, D_e is the diffusion coefficient of the analyte electrons and E is the potential of the electrode. In previous work many authors ignored the first term and assumed that the flux was driven only by the second term, by the applied potential. This is incorrect and it has been shown that when both terms are taken into account, the modified driving potential is given by

$$E_N = E + \left(\frac{\mathbf{R}T}{\mathbf{F}}\right)\ln\left(\frac{\mathrm{a}}{\mathrm{b}}\right) \qquad \textbf{Eqn. 2.24}$$

where, the modified potential, E_N is known as the Nernst potential. This is because the electron flux driven by the modified potential is reminiscent of the Nernst equation (Eqn. 2.1). This in fact gives the expected Nernst equation when E_N is zero. This occurs when the oxidised and reduced forms of the analyte are in equilibrium, and therefore there is no resulting flux, even if E and a are varying[20].

The flux, J_X of counter ions from the bulk solution is given by the Nernst-Planck equation[20].

$$J_{mx} = D_{mx}\left[\frac{\delta c}{\delta \mathrm{z}} \pm c\left(\frac{\mathbf{F}}{\mathbf{R}T}\right)\left(\frac{\delta E}{\delta z}\right)\right] \qquad \textbf{Eqn. 2.25}$$

Where D_{mx} is the diffusion coefficient of the electrolyte counter ions, c is the concentration of electrolyte, z is the distance through the diffusion layer and E is the potential of the solution. The first term describes ion motion induced by diffusion, the second term describes the motion induced by migration in the electric field. The driving potential for a singly charged anion is given by[19,20].

$$E_D = E + \left(\frac{\mathbf{R}T}{\mathbf{F}}\right)\ln\left(\frac{\mathrm{a}}{\mathrm{s}}\right) \qquad \textbf{Eqn. 2.26}$$

where s is the concentration of the specific counter ion in solution and the modified potential, E_D is known as the Donnan potential as it is related to the electric potential arising at Donnan equilibrium[19,20]. Equation 2.25 shows that a

gradient in the field $\left(\frac{\delta E}{\delta z}\right)$ can be balanced by a gradient in the concentration term $\frac{\delta \ln(c)}{\delta z}$. Under these conditions the Boltzman distribution law is obeyed, resulting in no flux when E_D is zero.

By applying Laplace transforms to these fundamental equations, Albery and Mount[20] were then able to calculate the response to small step potentials used in AC Impedance measurements. They found that

$$E_N^* \approx E^* + \left(\frac{RT}{F}\right) a^* \left[\left(\frac{1}{\bar{a}}\right) + \left(\frac{1}{\bar{b}}\right)\right] \qquad \textbf{Eqn. 2.27}$$

and

$$E_D^* \approx E^* - \left(\frac{RT}{F}\right) \frac{a^*}{\bar{a}} \qquad \textbf{Eqn. 2.28}$$

where starred terms (*) are used to indicate small perturbations induced by the small potential step and barred terms (-) are used to indicate the mean concentration of species at the electrode surface. The equations hold when c* << $\bar{c}$.

This difference in driving force leads to the distributed capacitance being adapted. The observed capacitance C_Σ is given by

$$\frac{1}{C_\Sigma} = \frac{1}{C_N} + \frac{1}{C_D} \qquad \textbf{Eqn. 2.29}$$

Where C_N is the Nernst capacitance due to the electrochemical reaction ($A^+ + e^- \leftrightarrow B$) and transfer of electrons, and C_D is the Donnan capacitance due to diffusion of electrolyte ions.

The Nernst capacitance is calculated using

$$C_N = \left(\frac{ALF^2}{RT}\right)\left(\frac{\bar{a}\,\bar{b}}{c}\right) \qquad \textbf{Eqn. 2.30}$$

where A is the electrode area, L is the length of the transmission line, F is Faraday's constant and c is the total redox ion concentration.

The Donnan capacitance is given by

$$C_D = \left(\frac{ALF^2}{RT}\right)\bar{a} \qquad \textbf{Eqn. 2.31}$$

The Resistances along both the R_e transmission line and R_{MX} transmission line can then be calculated through equations

$$R_e = \left(\frac{RT}{F^2}\right)\left(\frac{1}{\bar{a}} + \frac{1}{\bar{b}}\right)\left(\frac{L}{AD_e}\right) \qquad \textbf{Eqn. 2.32}$$

and

$$R_{MX} = \left(\frac{RT}{F^2}\right)\left(\frac{L}{AD_x\bar{a}}\right) \qquad \textbf{Eqn. 2.33}$$

This modified transmission line and corresponding theoretical mathematics can then be used as a basis to model real electrochemical systems. This transmission line theory was originally developed to model transport of ions and electrons through a polymer film at decreasing ac frequencies, however the transmission line can also be applied to aqueous solutions to model the Warburg impedance and the transport of background electrolyte and redox species through the growing depletion zone[21]. Figure 2.16 shows the Randles' circuit above the transmission line developed to explain the impedance plots observed for fully reversible redox processes occurring at macroelectrodes. Note that as the double layer is charged by the potential it is not charged through either C_N or C_D.

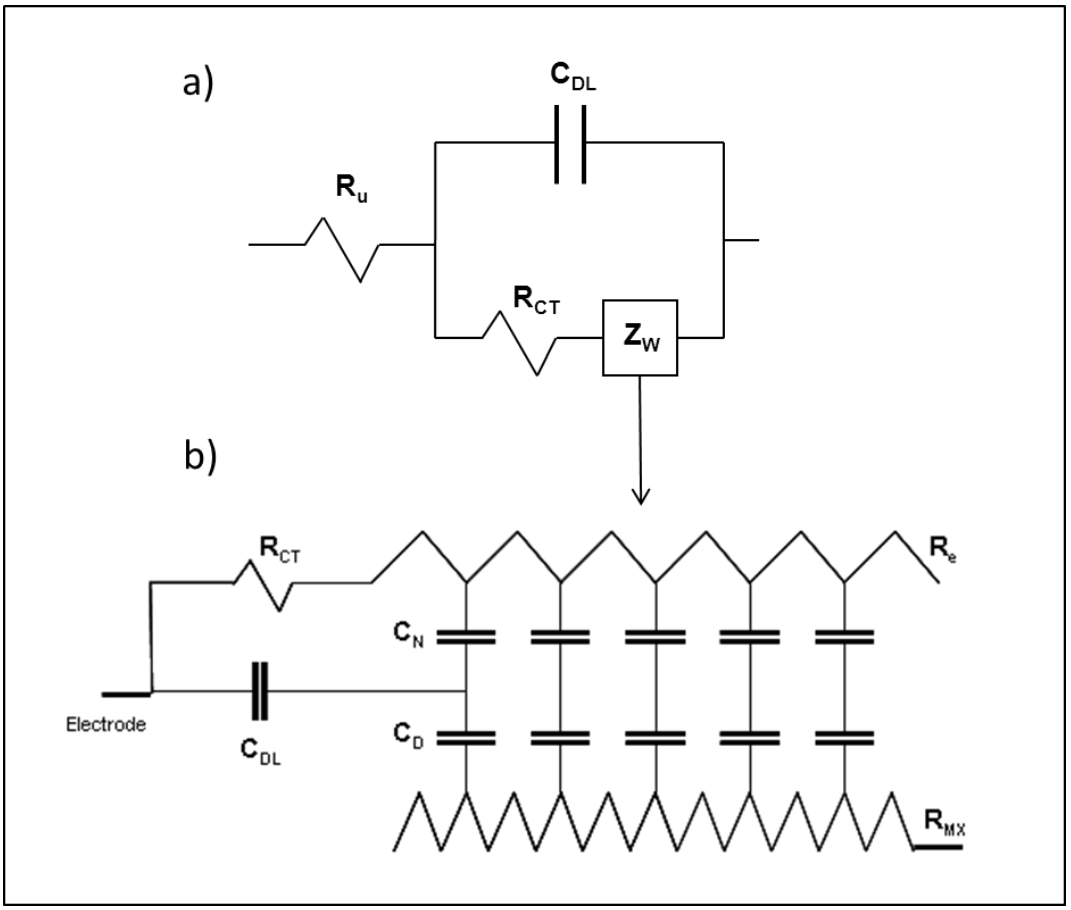

Figure 2.16: Schematic diagram of a) the Randles' circuit and b) the modified transmission Line proposed by Albery and Mount, extended to model real electrochemical experiments in aqueous solution. R_e represents the resistive line corresponding to electron transfer and transport of redox active ions in the analyte, R_{MX} represents the resistive line corresponding to the transport of inert M^+ and X^- ions in the backround electrolyte, R_{CT} is the charge transfer resistance, C_N is the modified Nernst capacitance, C_D is the modified Donnan capacitance and C_{DL} is the double layer capacitance. Charging of this transmission line represents the Warburg component of the Randles' circuit in a) and growth of the depletion zone with time.

In electrochemical aqueous systems, the concentration of background electrolyte is always much greater than the concentration of the analyte being studied. Therefore the concentration of inert ions in the background electrolyte, $[M^+, X^-]$ will be much greater than the concentration of the redox ions in the analyte, ferri/ferrocyanide in this case. Thus $R_{MX} << R_e$ and since current always travels along the path of least resistance, it is understood that current will flow most easily through R_{MX}. In this case, detailed analysis shows that the Randles circuit is obtained, where R_u the uncompensated electrolyte resistance is given by R_{MX} and the Warburg impedance Z_W is given by the charging of the transmission line[20].

The Nyquist plot obtained for a macroelectrode can be fully explained with transmission lines. At very high frequencies capacitors are uncharged and the current will flow easily through the transmission line of lowest resistance, R_{MX}. As the frequency decreases the double layer will charge, the electrochemical reaction will take place and the resistance, R_{CT} of charge transfer at the electrode/electrolyte interface will start to affect the plot. The semicircular section of the Nyquist plot is thus formed by R_{CT} in parallel with C_{DL}. Following transfer, an increasing depletion zone will be set up, requiring analyte to travel further through the solution before reaching the electrode. The Warburg impedance can be explained as progressive charging of the transmission line which gives the observed 45^0 slope.

By analogy for microelectrodes, the modified Randles circuit applies with R_{NL} in parallel with the transmission line.

2.6.3. Theoretical Variation of Circuit Elements with E_{dc}

Ac impedance is a valuable tool in electrochemistry as it allows one to keep E_{dc} constant, fixing the redox composition, which enables circuit elements to be measured at different E_{dc} values by performing repeated EIS measurements. We therefore use Transmission Line Theory to determine how these parameters should vary with E_{dc}. For a fully reversible reaction, as shown in equation 2.3:

$$A + e^- \underset{k_{ox}}{\overset{k_{red}}{\rightleftharpoons}} B \qquad \textbf{Eqn. 2.3}$$

the kinetic charge transfer resistance, $R_{CT,K}$ at the electrode surface is given by[15]

$$R_{CT,K} = \frac{RT}{AF^2c}\left(\frac{1}{k_{ox}} + \frac{1}{k_{red}}\right) \qquad \textbf{Eqn. 2.34}$$

where A is the electrode area and c is the total concentration of the analyte redox couple. The electrochemical rate constants k_{ox} and k_{red} are given by

$$k_{ox} = k^{\theta} \exp\left(\frac{\alpha_{ox}\mathbf{F}(E_{dc}-E^{\theta})}{\mathbf{R}T}\right) \quad \textbf{Eqn. 2.35}$$

and

$$k_{red} = k^{\theta} \exp\left(-\left(\frac{(1-\alpha_{ox})\mathbf{F}(E_{dc}-E^{\theta})}{\mathbf{R}T}\right)\right) \quad \textbf{Eqn. 2.36}$$

Where α_{Ox} is the electrochemical transfer coefficient of the oxidised species and is related to the kinetics of the reaction and therefore to the reversibility of the redox process taking place. It is a constant between 0 and 1, since $\alpha_{Ox} + \alpha_{Red} = 1$. By substituting Equations 2.35 and 2.36 into equation 2.34 we find that

$$R_{CT,\,K} = \frac{\mathbf{R}T}{k^{\theta}A\mathbf{F}^2c}\left[\exp\left(\frac{-\alpha_{ox}\mathbf{F}(E_{dc}-E^{\theta})}{\mathbf{R}T}\right) + \exp\left(\frac{(1-\alpha_{ox})\mathbf{F}(E_{dc}-E^{\theta})}{\mathbf{R}T}\right)\right] \quad \textbf{Eqn. 2.37}$$

When $E_{dc} = E^{\theta}$, $k_{ox} = k_{red} = k^{\theta}$. Experimentally, a plot of E vs. $R_{CT,\,K}$ should give a minimum value of resistance $R^{min}_{CT,K}$ when $E = E^{\theta}$ as

$$R^{min}_{CT,\,K} = \frac{\mathbf{R}T}{A\mathbf{F}^2c}\left(\frac{2}{k^{\theta}}\right) \quad \textbf{Eqn. 2.38}$$

By substituting equation 2.38 into equation 2.37, a global expression for $R_{CT,\,K}$ is obtained.

$$R_{CT,\,K} = \frac{R^{min}_{CT,\,K}}{2}\left[\exp\left(\frac{-\alpha_{ox}\mathbf{F}(E_{dc}-E^{\theta})}{\mathbf{R}T}\right) + \exp\left(\frac{(1-\alpha_{ox})\mathbf{F}(E_{dc}-E^{\theta})}{\mathbf{R}T}\right)\right] \quad \textbf{Eqn. 2.39}$$

Values of $R_{CT,\,K}$ and E_{dc} for each EIS spectrum can therefore be fitted to assess the applicability of this equation and to obtain values for $R^{min}_{CT,\,K}$, α_{ox} and E^{θ}.

For a fully reversible system electrochemical processes often happen so quickly that the kinetics of the reaction is not observed. Equilibrium is reached rapidly and therefore the kinetic α-terms cannot be determined.

Previous work in this area always assumed that R_{CT} was measurable due the semicircular charge-feature observed on the Nyquist plot at high

frequencies [5,23,24]. We believe, however, that the observed R_{CT} semicircle may not necessarily be a kinetically controlled charge transfer resistance but could also a thermodynamic feature. In a fully reversible reaction k_{ox} and k_{red} are no longer the limiting parameters and instead the reaction is controlled by thermodynamic properties and thus must be modeled by Nernstian mathematics. We can use Transmission Line theory to explain this conviction.

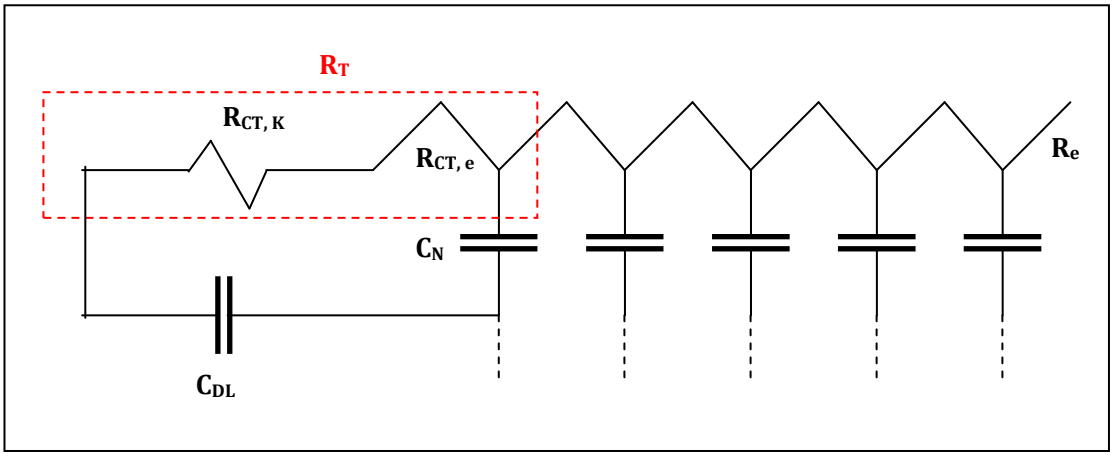

Figure 2.17: Schematic diagram of the Transmission Line, proposed for this report, to explain the impedance observations for fully reversible redox processes. R_e represents the resistive line corresponding to redox active ions in the analyte, R_{MX} represents the resistive line corresponding to the transfer of M^+ and X^- ions in the electrolyte, $R_{CT,\,K}$ is the kinetic charge transfer resistance, $R_{CT,\,e}$ is the thermodynamic charge transfer resistance caused by a small amount of R_e charging, C_N is the modified Nernst capacitance, C_{DL} is the double layer capacitance and R_T is the combined resistance of $R_{CT,\,K}$ and $R_{CT,\,e}$

Normally the double layer charges at high frequency and then at lower frequencies, this charge is injected into the R_e rail. We propose, however, that if there is negligible kinetic charge transfer resistance, there would still be the first part of the transmission line, $R_{CT,\,e}$, near the electrode which could be shunted by C_{DL} at high frequency. Mathematically we can therefore derive an expression for $R_{CT,\,e}$ using the form of resistance of R_e (Eqn. 2.32) from the transmission line. Utilising this expression to model thermodynamically hindered charge transfer gives:

$$R_{CT,e} = \frac{RTL}{AD_e F^2 c}\left(\frac{c}{\bar{a}\,\bar{b}}\right) \qquad \textbf{Eqn. 2.40}$$

where $R_{CT,\,e}$ is the small amount of R_e shunted by C_{DL}, $\bar{a}$ and $\bar{b}$ are the mean concentrations of oxidised and reduced species at the interface respectively, *c* is the total concentration of analyte in solution, D_e is the diffusion coefficient of ferri/ferrocyanide and *L* is the length of transmission rail shunted by C_{DL}.

It is then easy to show (Appendix A1.1) that

$$R_{CT,\,e} = \frac{R_{CT,\,e}^{min}}{4}\left[2 + \exp\left(\frac{F(E_{dc}-E^{\theta})}{RT}\right) + \exp\left(-\left(\frac{F(E_{dc}-E^{\theta})}{RT}\right)\right)\right] \qquad \textbf{Eqn. 2.41}$$

In fact $R_T = R_{CT,\,K} + R_{CT,\,e}$. For fully reversible systems the kinetic charge transfer resistance is very small and the reaction is extremely facile. However, one still observes a current output due to charging of a small portion of R_e shunted by C_{DL} at high frequency.

When $R_{CT,\,e} >> R_{CT,\,K}$, $R_T \approx R_{CT,\,e}$ and the EIS values will fit to equation 2.41. When $R_{CT,\,K} >> R_{CT,\,e}$, $R_T \approx R_{CT,\,K}$ and the EIS values will fit to equation 2.39. Fitting of equations 2.39 and 2.41 therefore enables the determination of the relative importance of kinetics and thermodynamics to charge transfer.

The modified Randles' circuit applied to a microdisc has an additional circuit element, R_{NL}, added to the Randles' circuit to account for the effects of hemispherical diffusion seen at these micron scale disc electrodes; this enables the onset of a steady-state current at longer times (low frequencies). It can be argued that charge transport in this resistive circuit element is driven by the same processes as in R_e, which means the same dependency of R_{NL} on E_{dc} as R_e, and that a similar equation to eqn. 2.41 will also apply to R_{NL}, with R_{NL} replacing R_{CT}.

Because the same processes drive the non-linear resistance, R_{NL} of a microelectrode, the same functional form is found for the variation of R_{NL} with E_{dc}.

$$R_{NL} = \frac{R_{NL}^{min}}{4}\left[2 + \exp\left(\frac{F(E_{dc}-E^{\theta})}{RT}\right) + \exp\left(-\left(\frac{F(E_{dc}-E^{\theta})}{RT}\right)\right)\right] \quad \textbf{Eqn. 2.42}$$

The equation which defines the Warburg impedance, (the charging of the transmission line) in the real and imaginary plane can be defined as

$$|Z_W| = \frac{\sqrt{2}\sigma}{\omega^{1/2}} \quad \textbf{Eqn. 2.43}$$

Mathematically (Appendix A1.2), it can be shown that the Warburg coefficient also takes exactly the same form as the $R_{CT,e}$ and R_{NL}.

$$\sigma = \frac{\sigma^{min}}{4}\left[2 + \exp\left(\frac{F(E_{dc}-E^{\theta})}{RT}\right) + \exp\left(-\left(\frac{F(E_{dc}-E^{\theta})}{RT}\right)\right)\right] \quad \textbf{Eqn. 2.44}$$

It should be noted that the FRA equivalent circuit modeling program used in this work (as with many others) doesn't actually return Z_W, from the fit but Y_0, which is the magnitude of the admittance, Y (1/Z) at ω =1 rad s^{-1} (~0.16 Hz), Y_0 is related to Y by:

$$Y_0 = \frac{Y}{(j\omega)^{1/2}} \quad \textbf{Eqn. 2.45}$$

Y_0 is therefore related to σ by:

$$\sigma = \frac{1}{\sqrt{2}\cdot Y_0} \quad \textbf{Eqn. 2.46}$$

2.6.4. The Constant Phase Element (CPE)

The equivalent circuit and transmission line models discussed in this report up to now include only resistors and pure capacitors in their design. Although much simplified, these models provide accurate fitting and interpretation of most electrochemical responses. However, real-world electrochemical systems are imperfect, and sometimes the assumption of pure double capacitor behaviour does not model the true response. A Constant Phase Element (CPE)

is a non-intuitive equivalent circuit element that models the behaviour of a double layer as an imperfect capacitor.

One physical explanation for CPE behaviour is electrode roughness[25]. A perfect double layer capacitor response requires a completely planar two-dimensional surface. For a rough, fractal surface the fractal dimension, D of the surface is between 2 and 3. Translated this means that some of the surface fills three dimensions. It has been shown theoretically[26] that for rough electrode surfaces the capacitance can be modified by a parameter, n, the fractal roughness factor. In this case

$$n = \frac{1}{D-1} \qquad \textbf{Eqn. 2.47}$$

Mathematically, the CPE's electrical impedance is given by

$$Z_{CPE} = \frac{1}{Q_0(\omega)^n} \exp\left(\frac{\pi}{2} n j\right) \qquad \textbf{Eqn. 2.48}$$

with $Q_0 = 1/|Z|$ at $\omega = 1$ radian s^{-1}

From this equation it can be seen that the phase angle of the CPE impedance is independent of frequency and has a constant value of (90*n) degrees. This gives the CPE its name[6].

For a smooth surface the fractal dimension, D = 2.0 and n = 1.0. The impedance is unchanged and the phase angle of capacitance is 90^0, the same as a pure capacitor and $Q_0 = C_{DL}$. For a highly contorted surface where $D \rightarrow 3.0$, then $n \rightarrow 0.5$ and the angle of the CPE is thus 45^0.

Near planar electrodes will have a phase angle near 90^0, that is a roughness factor between 0.9 and 1.0 and hence near 2D dimensionality. However rougher electrodes may have increased dimensionality and therefore n values may be much less than 1.0. For a solitary CPE, symbolised by Q in

figure 2.18, the Nyquist plot is just a straight line which makes an angle, θ of (n*90)

When the CPE capacitance is in parallel with a charge-transfer resistance, the Nyquist plot is the arc of a circle, but with the centre of the circle below the x-axis, giving a depressed semi-circle.

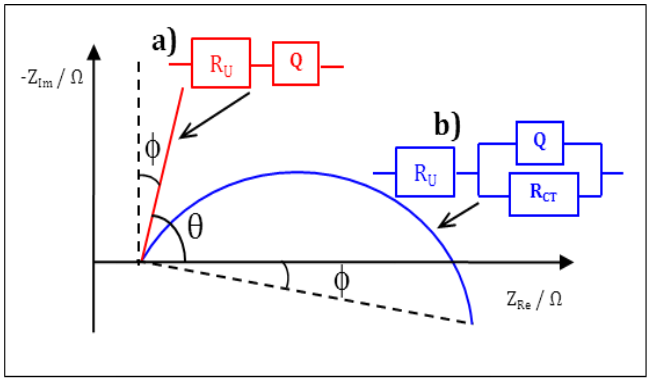

Figure 2.18: Schematic diagram showing effect of the CPE the on a Nyquist plot in equivalent circuits. For a solitary CPE, in series with R_U, **a)** the Nyquist plot obsereved is a line which makes an angle, $\theta = (n*90^0)$ with the x-axis, (depressed by $\phi = (1\text{-}n)*90^0$). The plot for a CPE in parallel with the Charge Transfer Resistance ($\mathbf{R_{CT}}$), **b)** is a semicircle with its centre again depressed by an angle,ϕ of $(1\text{-}n)*90^0$

The roughness of a microelectrode surface may be substantial in comparison with its surface area and therefore represent an increased dimensionality surface. The data may thus be modeled better using a CPE circuit component rather than a pure double layer capacitor. The roughness factor and CPE determined from the model fit can be used to calculate the equivalent capacitance, C.

$$C = Q_0(\omega_{max})^{n-1} \qquad \textbf{Eqn. 2.49}$$

where ω_{max}, is the frequency at the top of the semi-circle.

Other physical factors as well as fractal roughness may contribute to deviations from perfect capacitor behaviour, such as electrode porosity, variation in electrode coating, slow adsorption reactions, or non-uniform potential and current distributions[25]. However, it has been shown that even though the physical factor may not show exactly CPE behaviour, very often CPEs will still fit to the experimental data. This is increasingly true as the complexity

of a circuit model grows. Since CPE has two parameters Q_0 and n, whilst C_{DL} only has one, the use of a CPE, adds an extra variable and therefore, if possible it is better to fit to C_{DL}, particularly for complicated circuits. A CPE should only be used therefore when an extra parameter is required for good fit to the data. Also, if possible Q_0 and n should ideally relate to the physical model of the system. It should be noted that to avoid additional parameters to an equivalent circuit used to model redox behavior, the roughness factor of an electrode can be determined prior to experimentation, by running EIS experiments in background electrolyte only.

2.7. Principles of Finite Element Method

As with many solution method simulation models, the finite element method (FEM) is a technique for finding approximate numerical solutions to partial differential equations (PDE). The solution approach is based either on eliminating the differential equation completely (steady state problems), or rendering the PDE into an approximating system of ordinary differential equations, which are then numerically integrated.

Rather than approximating the differential operator itself, as in the finite difference method, in FEM, the differential equation is converted to an integral equation in which a stationary point corresponds to the solution of the differential equation and instead, it is the 'function space' within which the solution is sought which is approximated[27]. The principles of FEM are discussed briefly below, in relation to diffusional flux towards an electrode surface. For a more in depth overview of the principles and applications of FEM in electrochemistry please refer to references ([27-34]).

In FEM, the space over which the problem is formulated is divided into a number of sub-regions known as elements, which join at points known as nodes. The choice of element geometry depends on the dimension of the problem[30], in one dimension there is no freedom of choice, in two dimensions, triangles are chosen (figure 2.21), and in three dimensions, tetrahedrons are chosen (Figure 3.9).

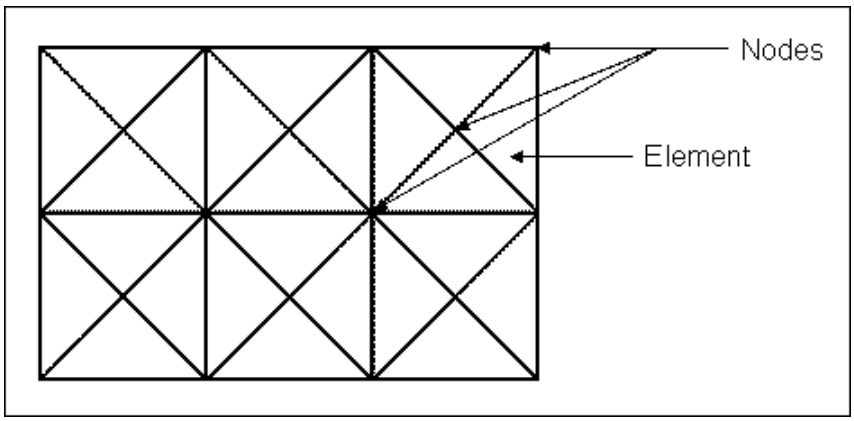

Figure 2.19: Pictorial representation of a FEM bounded domain, separated into triangular elements and connected by nodes

In solving PDEs, the primary challenge is to create an equation that is an approximation of the equation to be studied, but is also numerically stable, in that errors during input and intermediate calculation steps, do not accumulate and cause the resulting output to be meaningless. In FEM, the weighting functions employed are those used in the assumed solution itself, minimising the error in a global sense over the entire domain[27].

The basis of many electrochemical simulation programs and indeed the focus of simulations in this thesis is diffusional mass transport of an electroactive species towards an electrode surface. This can be described by Fick's second Law [27,30] which in one dimension is:

$$\frac{\delta c}{\delta t} = D\frac{\delta^2 c}{\delta x^2} \qquad \textbf{Eqn. 2.50}$$

where D is the diffusion coefficient of the species in question, c is the concentration of the species and t is the time. The concentration, c can be given in vector formulation by

$$\vec{c} = \vec{c}(t\vec{x}) \qquad \forall \vec{x} \in \Omega \qquad \textbf{Eqn. 2.51}$$

where Ω is a bounded subdomain of the model, with a continuous differentiable boundary. From this, a generalised form of Equation 2.50, in all directions is given as

$$\vec{c} = D\nabla^2\vec{c}$$ **Eqn. 2.52**

Provided that all the programmer wishes to obtain, is the flux of a species towards and at an electrode, this equation will suffice. When monitoring flux towards an activated electrode it is necessary to consider three types of boundary condition. The first is the semi-infinite boundary limit, represented as the concentration far from the electrode surface and is simply set as the bulk concentration, $\vec{c}^{\infty}$

$$\vec{c}(t^0) = \vec{c}^{\infty}$$ **Eqn. 2.53**

This holds true since at time zero, t^0 no reaction has yet occurred in these simulations and therefore the concentration at all points is equal to the bulk concentration

The second boundary condition is given at inert walls (i.e. insulating material) or at symmetry axes. In these cases there is no flux, normal to the surface at any time, *t* and hence

$$\nabla_n\vec{c}(t) = 0$$ **Eqn. 2.54**

Where ∇_n is the gradient normal to the surface.

The third boundary condition is the condition at the electrode surface at time zero, t^0 and for a simple flux simulation the surface is initially set with a concentration of zero, c^0:

$$\vec{c}(t^0) = \vec{c}^0$$ **Eqn. 2.55**

One major advantage of the finite element method, over the finite difference method, is the fact that non-uniform meshes are automatically created, whereby the mesh density is increased in regions where sharp

gradients exist. In the case of diffusive flux, the mesh will be greatest where the concentration gradient is changing most rapidly (i.e. initially at the electrode surface and boundary interfaces). Figure 2.22 is a schematic diagram to represent the concept of FEM mesh density increasing as it approaches the electrode surface.

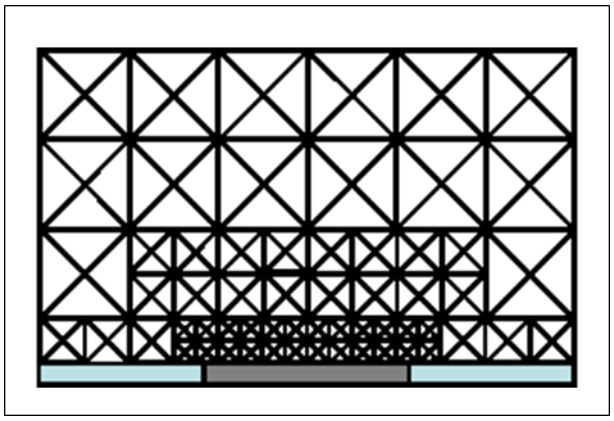

Figure 2.20: schematic diagram illustrating a FEM mesh density increasing towards the electrode surface where the largest changes in concentration gradient will be observed.

This form of meshing ensures that there is adequate information in the regions where concentration gradients are changing most rapidly, and therefore enables construction of an accurate, continuous solution[27]. The numerical calculations are then solved by calculating the differences between movements between all the mesh elements. In the case of diffusive flux of an electroactive species, the concentration distribution is approximated within in each element by a weighted sum of a set of trial (interpolating) functions of the nodal values; based on Fick's second law of diffusion and established by the chosen boundary conditions[35]. Thus for the special case at steady-state, where $\vec{c} = D\nabla^2\vec{c} = 0$, the concentration distribution within each element must be calculated to satisfy zero flux in and out of all elements.

In many simulation models, dynamic adaptive mesh refinement is often also used [36,37], where the mesh is refined after each computation to optimise the grid and ensure the differential parameters are accurately calculated. This does however translate into more memory and storage needs as well as increased simulation time[27]. This can be somewhat overcome by selectively packing the

mesh in regions where known sharp gradient changes will occur and then allowing very sparse meshing in regions of very little gradient change.

2.8. References

(1) Bard, A. J.; Faulkner, L. R. *Electrochemical Methods, Fundamentals and Aplications*; Second ed.; John Wiley and Sons, Inc.: Hoboken, 2001.

(2) Fisher, A. C. *Electrode Dynamics*; Oxford University Press: New York, 1996.

(3) Feldberg, S. W. G. H. A., J.A. Bell, C.K Chang, C.B. Wang *Biophysical Journal* **1981**, *34*, 149.

(4) Koster, O., W. Schuhmann, H. Vogt and W. Mokwa *Sensors and Actuators* **2001**, *B*, 573.

(5) Los, P.; Bruce, P. G. *Polish Journal of Chemistry* **1997**, *71*, 1151.

(6) Rosvall, M. *Electrochemistry Communications 2* **2000**, *2*, 4.

(7) Shaffer, P. A.; Williams, R. D. *The Journal of Biological Chemistry* **1935**.

(8) Granger, M. C.; Swain, G. M. *Journal of the Electrochemical Society* **1999**, *146*, 4551.

(9) Kolthoff, I. M.; Tomsicek, W. J. *The Journal of Physical Chemistry* **1935**, *39*, 945.

(10) Randles, J. E. B. *Transactions of the Faraday Society* **1948**, *44*, 327.

(11) Heinze, J. *Angewandte Chemie International Edition in English* **1993**, 1268.

(12) Forster, R. J. *Chemical Society Reviews* **1994**, *23*, 289

(13) Zoski, C. G., A.M. Bond, E.T. Allinson, and K.B. Oldham *Analytical Chemistry* **1990**, *62*, 37.

(14) Kovach, P. M.; Caudill, W. L.; Peters, D. G.; Wightman, R. M. *Journal of Electroanalytical Chemistry* **1985**, *185*, 285.

(15) Albery, W. J. *Electrode Kinetics*; Clarendon Press: Oxford, United Kingdom, 1975.

(16) Randles, J. E. B. *Discussions of the Faraday Society* **1947**, *1*, 11.

(17) Christie, l.; Los, P.; Bruce, P. G. *Elecrrochimica Acta* **1995**, *40*, 2159.

(18) Fleischmann, M., S. Pons and J.Daschbach *Journal of Electroanalytical Chemistry* **1991**, *317*, 1

(19) Albery, W. J.; Mount, A. R. *Journal of the Chemical Society-Faraday Transactions* **1993**, *89*, 2487.

(20) Albery, W. J.; Mount, A. R. *Electroactive Ploymer Electrochemistry, Part 1: Fundamentals, Chapter 4: Transmission Lines for Conducting Polymers*; Lyons. PLenum press: New York, 1994.

(21) Albery, W. J., C. Zeng, B.R. Horrocks, A.R. Mount, P.J. Wilson, D. Bloor, A.T. Monkman and C. M. Elliott *Faraday Discussions of the Chemical Society* **1989**, *88*, 247.

(22) Albery, W. J.; Mount, A. R. *Journal of the Chemical Society-Faraday Transactions* **1993**, *89*, 327.

(23) Fleischmann, M. *Journal of Electroanalytical Chemistry* **1988**, *250*, 277.

(24) Hepel, T.; Osteryoung, J. *Journal of Electrochemical Society: Electrochemical Science and Tecnology* **1986**, *133*, 752.

(25) Jorcin, J.-B.; Orazem, M. E.; Pébère, N.; Tribollet, B. *Electrochimica Acta* **2006**, *51*, 1473.

(26) Bruce, N. C.; Garcia-Valenzucia, A. *Revista Mexicana De Fisica* **2007**, *53*, 296.

(27) Stephens, M. M.; Moorhead, E. D. *Journal of Electroanalytical Chemistry* **1987**, *220*, 1.

(28) Moorhead, E. D.; Stephens, M. M. *Journal of Electroanalytical Chemistry* **1990**, *282*, 1.

(29) Stevens, N. P. C.; Fisher, A. C. *The Journal of Physical Chemistry B* **1997**, *101*, 8259.

(30) Nann, T.; Heinze, J. *Electrochemistry Communications* **1999**, *1*, 289.

(31) Beriet, C.; Ferrigno, R.; Girault, H. H. *Journal of Electroanalytical Chemistry* **2000**, *486*, 56.

(32) Penczek, M.; Stojek, Z.; Osteryoung, J. *Journal of Electroanalytical Chemistry* **1984**, *181*, 83.

(33) Penczek, M.; Stojek, Z.; Osteryoung, J. *Journal of Electroanalytical Chemistry* **1984**, *170*, 99.

(34) Gavaghan, D. J. *Journal of Electroanalytical Chemistry* **1998**, *456*, 1.

(35) Alden, J., Oxford University, 1998.

(36) Strutwolf, J. *Electroanalysis* **2005**, *17*, 1547.

(37) Gavaghan, D. J.; Gillow, K.; Sűli, E. *Langmuir* **2006**, *22*, 10666.

3. Global Experimental

3.1. Electrolytes

All aqueous solutions reported were prepared using Milli Q deionised water and were degassed using an argon stream for a minimum of 20 minutes prior to investigation. An argon blanket was blown over the surface of the solutions during experimentation, unless otherwise stated.

3.1.1. Ferri/ferrocyanide Redox Couple

Unless otherwise specified, the electrolyte used for analysis of the electrode systems in this study, was aqueous potassium ferricyanide, $K_3[Fe(CN)_6$ [10 mM] (Sigma Aldrich, ACS reagent ≥ 99%), in aqueous potassium chloride [0.1 M] (Fisher Scientific, lab reagent grade, > 99% purity) background electrolyte.

3.1.2. Sulphuric Acid Microelectrode Cleaning

The acid cleaning solution was aqueous sulfuric acid, H_2SO_4 [0.05M] (VWR/BDH/Prolabo, 98-100 %, purity)

3.1.3. Potassium Chloride Microelectrode Cleaning

The potassium chloride cleaning solution was aqueous KCl [0.1M] (Fisher Scientific, lab reagent grade, > 99% purity).

3.2. Working Electrodes

3.2.1. Platinum Macrodisc Electrode

The macroelectrode used in Case Study 1 (section 3.5) was a platinum disc electrode with co-planar insulation, normally used for rotating disc experiments (Oxford Electrodes, area = 0.387 cm^2).

3.2.2. Platinum Single (50 µm)² Microsquare Electrodes

The (50 µm)² platinum electrodes were fabricated at the Scottish Microelectronics Centre (SMC), specifically for this research. The microlithographic fabrication process is described in section 4.2.

3.2.3. Platinum Microsquare Arrays and Nanoband Cavity Array Electrodes

The platinum microsquare arrays and nanoband cavity array electrodes (CaviArE) were also fabricated at the SMC. The development of their design and fabrication method is described in chapter 5.

3.3. Reference and Counter Electrode

The reference electrode (r.e.) used for all experiments was a commercial Saturated Calomel Electrode ($Hg/Hg_2Cl_2/sat^d$ KCl, SCE, Russel Electrodes). It was stored in saturated aqueous potassium chloride, KCl solution. The reference was regularly tested against other SCEs by recording the voltage between them, to ensure that the reference potential remained constant to within a few millivolts. The potassium chloride solution within the r.e. was also regularly changed to prevent shifting of the SCE potential. All potentials stated throughout this work, are therefore quoted with respect to this SCE electrode. The counter electrode (c.e.) was based on a platinum gauze (Sigma-Aldrich 52 mesh, 425mg = 25 mm X 25 mm, 99.9% metals basis). It was produced in house, by spot welding to a piece of platinum wire.

3.4. Electrochemical Instrumentation and Control

3.4.1. Cyclic Voltammetry

Electrochemical data were measured using a computer controlled potentiostat (Autolab, PGSTAT 30). These data were collected and analysed using Autolab General Purpose Electrochemical Software (GPES), ecochemie, version 4.9 for windows on a Dell Pentium 4 processor PC, using windows XP. The cyclic voltammogram (CV) plots were produced using Origin software, version 7.5 and 8 on the same PC. All subsequent data manipulation and analysis, was carried out in Microsoft Office EXCEL and/or in Origin (version 7.5 and 8.5)

3.4.1.1. Cleaning of Electrode Systems

The aqueous electrochemical cleaning used throughout this thesis was performed by continuous voltammetric cycling of the electrode systems in either sulphuric acid or potassium chloride solution. The potential range and

current magnitudes were selected to obtain optimal cleaning conditions. For both sulphuric acid cleaning and KCl cleaning, the potential window was chosen to cycle between oxide formation at positive potentials and hydrogen gas formation at negative potentials, to provide both chemical and mechanical cleaning of the electrode surface. The voltages were selected to control the current and hence the amount of oxide and hydrogen formation. This enabled gentle cleaning to reduce the risk of damaging the electrode (see section 4.3.2). As well as physical cleaning, sulphuric acid is a strong acid and, even in very low concetrations, may induce chemical cleaning of the electrode surface. KCl is pH neutral and therefore is a much gentler cleaning agent, however it must be remembered that pH changes will still occur at the electrode surface in the un-buffered solution upon electrochemical cleaning (section 4.3.2).

These cleaning cycles were adjusted in order to optimise cleaning for specific experiments (as indicated by characteristically clean CVs) and therefore the potential window and current limits are quoted as necessary throughout the report. Table 3.1 shows the optimized GPES cleaning input parameters used for the majority of cleaning of the microelectrode systems under investigation. It should be noted that the total number of scans varied considerably between different electrodes which indicates variation in initial cleanliness and therefore cleaning was continued until the CV response no longer changed and was characteristic of clean platinum. For single microsquares, typically 25-40 scans were required (section 4.3.4) whilst for microsquare arrays and CaviArE, typically 40-60 scans were carried out (section 5.3.3).

Electrode system	Cleaning solution	Preconditioning potential / V (10s)	Oxidizing Potential limit / V	Reducing potential limit / V	Sweep rate / mVs^{-1}	Current Cap / A
$(50\ \mu m)^2$ Pt electrode	$H_2SO_{4\ aq}$ [0.05 M]	0.00	+2.00	-0.40	100	$1x10^{-6}$ (current limit $1x10^{-5}$)
$(50\ \mu m)^2$ Pt electrode	$KCl_{\ aq}$ [0.1 M]	0.00	+2.40	-1.80	100	$1x10^{-8}$ (Current limit $1x10^{-7}$)
Microsquare arrays	$H_2SO_{4\ aq}$ [0.05 M]	+0.05	+1.60	-0.37	100	Dependent on total electrode area
CaviArE	$H_2SO_{4\ aq}$ [0.05 M]	+0.05	+1.60	-0.37	100	Dependent on total electrode area

Table 3.1: Table of typical GPES input parameters required to clean the different microelectrode systems under investigation. It should be noted that the parameters were adjusted to optimize cleaning for specific experiments but the table gives an overview of the most commonly used protocol.

3.4.1.2. Analysis of Electrode Systems

Unless otherwise stated, the cyclic votammetry waveform for analysis of all the platinum electrodes in ferricyanide was to sweep from +0.35 V to 0.00 V and back to +0.35 V for each cycle. An initial conditioning potential of +0.35 V was applied for 10 seconds before CV study to ensure all the ferricyanide remained oxidized before data collection. 1-3 CV scans were recorded for each experiment and CVs were recorded at a variety of scan rates, between 1 mVs^{-1} and 30 Vs^{-1}[i].

3.4.2. Electrochemical Impedance Spectroscopy (EIS)

Impedance data were collected and analysed using Autolab Frequency Response Analysis (FRA), ecochemie, NOVA software, version 4.9 for windows on a Dell Pentium 4 processor PC, using windows XP. Equivalent circuits were fitted to the collected data using the in-built circuit components in the FRA software. The equivalent circuit models could be manipulated manually to produce the models required for data Analysis. The graphs of the impedance data were

[i] GPES utilizes a cyclic staircase, with a default step potential of 0.00244 V. This step is small enough to create a linear sweep. For the higher sweep rates of 10, 20 and 30 Vs^{-1} this step potential was increased to 0.01, 0.02 and 0.03 V respectively, in order to obtain CVs.

presented in Origin (version 7.5 and 8.5). Values of $R_{CT,}$ R_{NL} and Z_W at each dc potential were obtained directly from iterative fitting to the required equivalent circuit in FRA, for analysis of the variation of parameters with E_{dc} (section 3.5, 4.3 and 7.3). The Advanced Fitting Tool function in Origin was used to iteratively fit these experimental data to the theoretical expressions derived in section 2.6.3.

In order to run sets of impedance experiments at different dc potentials, batch files were created using the 'Project' tool in FRA. In a 'new project' window, sets of procedure were stored and run in sequence. The ac frequency range was kept constant for each procedure in the batch file, with a start frequency of either 1000 Hz (single microsquares and microsquare arrays) or 61 x 10^3 Hz (CaviArE) and an end frequency of 0.01 Hz. 50 different data points, logarithmically spaced in frequency, were collected for each of the single platinum microsquares and the microsquare array experiments and 68 data points were collected for CaviArE. The dc potential was systematically changed for each procedure and therefore a set of impedance plots at different dc potentials were recorded automatically in batch. The dc potentials typically ranged from +0.150 V to +0.230 V to encompass E^{θ} for ferri/ferrocyanide. The rms amplitude for single microsquares and microsquare arrays was maintained at 0.001 V, whilst the rms amplitude for the CaviArEs was increased to 0.01 V as increased signal to noise was required. Appendix A2 gives tables of the optimized impedance input parameters for the single microsquares, microsquare arrays and CaviArE as well as the input parameters for the macrodisc used in Case Study 1 (section 3.5)

As well as cyclic cleaning of electrodes in KCl [0.1 M], EIS experiments were performed in background electrolyte alone to determine the constant phase element parameters and thus the deviation from a pure double layer capacitor. Such experiments were performed at a dc voltage of +0.25 V, between frequencies of 1000 Hz and 1 Hz with an rms amplitude of 0.001 V for all electrodes.

3.5. Case Study 1 – Validation of analysis: Platinum macroelectrode response

Initial experiments were carried out using a platinum macrodisc w.e. (0.387 cm^2) in order to examine the measured reversibility of the ferri/ferrocyanide couple, determine the standard redox potential and test the theoretical expressions for fitting impedance data. The electrode surface was cleaned before and after each experiment by polishing with an α-alumina micropolish (Buehler, 1.1μm) slurry with deionised water on a microcloth pad (Buelher, PSA). Figure 4.1 represents a typical first scan cyclic voltammogram obtained using this electrode.

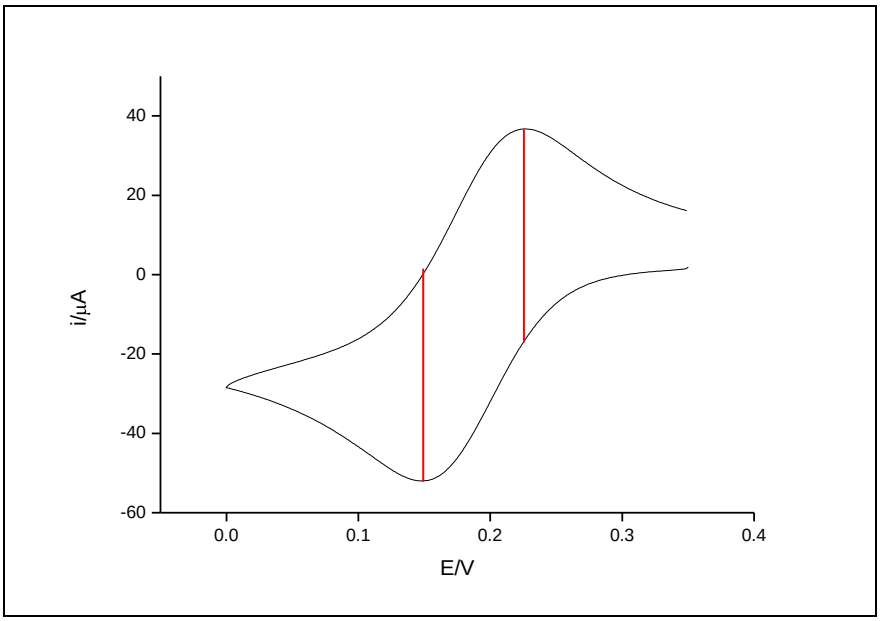

Figure 3.1: Cyclic voltammogram showing the redox behaviour of 10 mM potassium ferricyanide in 0.1 M KCl background electrolyte, at a sweep rate v = 100 mVs^{-1}. The measured oxididation peak current amplitude is 39.6 μA and reduction peak current amplitude is -45.4 μA.

The oxidation peak potential is +0.226 V and the reduction peak potential is +0.148 V, which gives a measured $E_{1/2}$ value of +0.187 V. As explained in section 2.3 $E_{1/2}$ can be related to the standard potential, E^{θ} using equation 2.5. Since $\frac{RT}{nF}\ln\left(\frac{D_O}{D_R}\right)^{1/2} = 2.87 \times 10^{-3}$ for ferri/ferrocyanide redox couple at 298 K[1], E^{θ} was therefore calculated to be +0.190 V when taking into account the small difference in diffusion coefficients of ferricyanide and ferrocyanide. This is within 2 mV of the calculated literature value. The peak separation calculated

from this CV is 0.078 V which is greater than the 0.059 V expected for a fully reversible, one electron process.

After taking sets of impedance measurements at different dc potentials and fitting the data to a Randles' equivalent circuit model, (e.g. see Figure 3.4), a value of the uncompensated resistance was obtained as 95 Ω. Inserting this value into the iR drop correction tool in GPES, the peak separation was reduced to 0.062 V which is within 5% of the theoretical value. This suggests that the reaction is indeed fully reversible but that there is significant uncompensated resistance within the system.

The original Randles' circuit which is often used to fit a macrodisc electrode response is shown in figure 2.11 (section 2.6.1). However the Nyquist plots obtained during this research fitted better to an equivalent circuit with a CPE replacing the C_{DL} component (Figure 3.2).

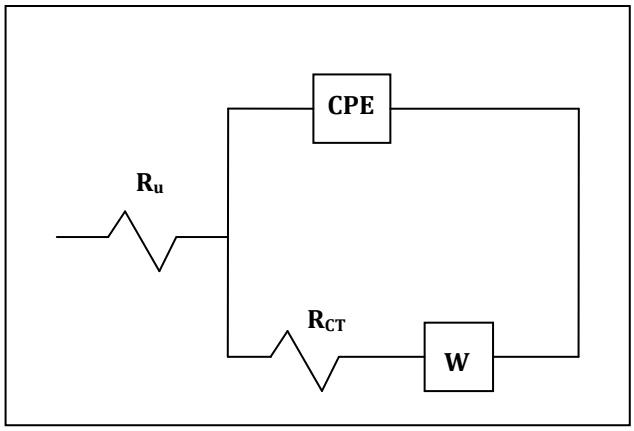

Figure 3.2: Schematic diagram of a modified Randles circuit incorporating a constant phase element CPE, where R_u is the uncompensated resistance and CPE is in parallel with the charge transfer resistance, R_{CT} and the Warburg impedance, W.

Figure 3.3 shows a typical Nyquist plot obtained from the macroelectrode at +0.190 V. The plot was iteratively fitted to the CPE modified Randles' circuit until tolerance was reached.

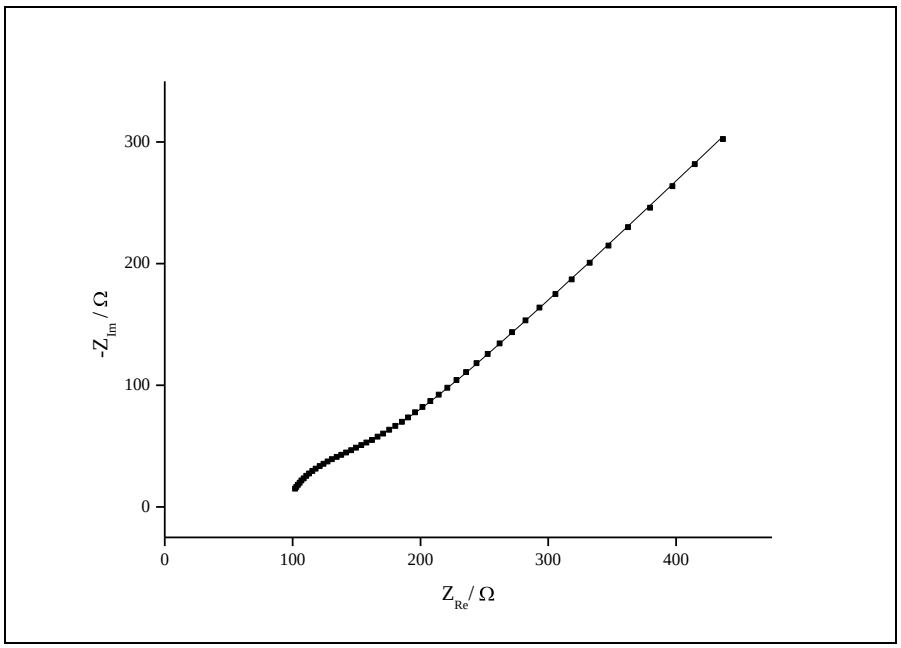

Figure 3.3: Nyquist plot of 10 mM ferricyanide in 0.1 M KCl background electrolyte on a Pt macrodisc electrode at a dc potential of +0.190 V. Black squares represent experimental data and black line represents equivalent circuit to the CPE modified Randles' circuit fit with a χ^2 value of $6.8X10^{-4}$.

The χ^2 value is extremely small which confirms the observation that this is an accurate model fit to the data.

Table 3.2 shows the corresponding output data recorded after iteratively fitting the CPE modified Randles' Circuit to the data.

Element	Value
R_u / Ω	(94.8 ±0.2)
Q_0 / $Ω^{-1}$	(2.9 ± 0.1) $x10^{-5}$
n	(0.860 ± 0.006)
R_{CT} / Ω	(65 ± 1)
Z_W / $Ω^{-1}s^{1/2}$	(9.46 ± 0.001) $x10^{-4}$

Table 3.2: Table of the values obtained from fitting the experimental data shown in Figure 3.3 to the CPE modified Randles' equivalent circuit using the fitting tool in FRA. All parameters were allowed to vary in the iterative fit.

The roughness factor, n for this experiment is 0.86 which would give a phase angle of 77.4^0 (from Eqn. 2.48) which indicates a significant depression of the charge transfer semicircle.

From the relationship between the true double layer capacitance, C_{DL} and the charge transfer resistance, R_{CT}[ii]:

$$C_{DL} = \frac{(Q_0 R_{CT})^{1/n}}{R_{CT}} \qquad \textbf{Eqn. 3.1}$$

the value of C_{DL} for this electrode (with a geometric area of 0.386 cm^2) at E_{dc} = 0.19 V, is 10.44 µF, which corresponds to a capacitance of 27 µF cm^{-2}. However since the CPE calculates a 13^0 shift in phase angle from 90^0, the active surface area may be larger than the geometric area, due to increased surface roughness and hence increased dimensionality.

A graph of charge transfer resistance against dc potential obtained at each potential, was plotted and these data were fitted to both kinetic and thermodynamic fitting equations:

$$R_{CT,K} = \frac{R_{CT,K}^{min}}{2}\left[\exp\left(\frac{-\alpha_{ox}\mathbf{F}(E_{dc}-E^{\Theta})}{\mathbf{R}T}\right) + \exp\left(\frac{(1-\alpha_{ox})\mathbf{F}(E_{dc}-E^{\Theta})}{\mathbf{R}T}\right)\right] \qquad \textbf{Eqn. 2.39}$$

and

$$R_{CT,e} = \frac{R_{CT,e}^{min}}{4}\left[2 + \exp\left(\frac{\mathbf{F}(E_{dc}-E^{\Theta})}{\mathbf{R}T}\right) + \exp\left(\frac{\mathbf{F}(E_{dc}-E^{\Theta})}{\mathbf{R}T}\right)\right] \qquad \textbf{Eqn. 2.41}$$

Figure 3.4 shows a typical plot of R_{CT} vs. E_{dc} calculated from iterative fitting of the CPE modified Randles' citcuit to the EIS data obtained at different dc potentials. Equation 2.39, (which assumes charge transfer is limited by kinetics) was fitted to the data and shown by the red line.

[ii]The equation was obtained from the electrochemistry resources website, accessed on 17/07/2011: http://www.consultrsr.com/resources/eis/cpecalc.htm

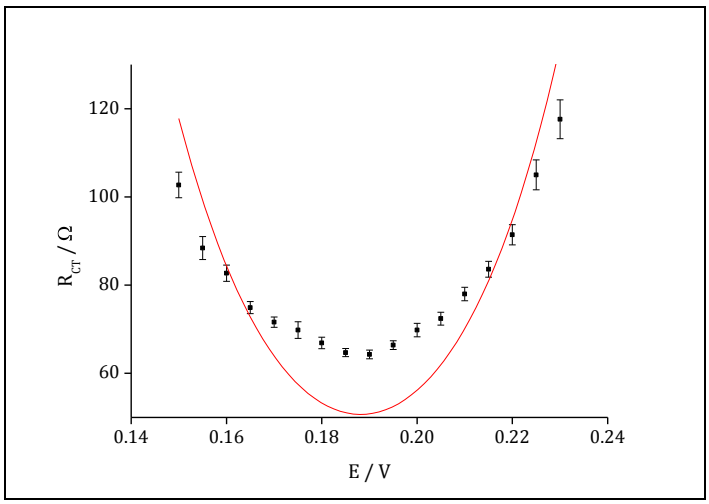

Figure 3.4: Graph of the charge transfer resistance, R_{CT} against dc potential, E_{dc}, The curve was fitted using eqn. 2.39 and gives a correlation coefficient of 0.702. The minimum charge transfer resistance, $R^{min}_{CT,\,K}$ is 50.68 ± 1.77 Ω, giving a standard potential, E^{Θ} of 0.188 ± 0.001 V; α_{Ox} was fxed at 0.5 in this case, although letting α_{Ox} vary did not produce better fits.

It is clear that this model does not produce a good fit to the data. Figure 3.5 shows the fitting curve obtained using equation 2.41 for the same data set, and is typical of all charge transfer data obtained from the macrodisc electrode.

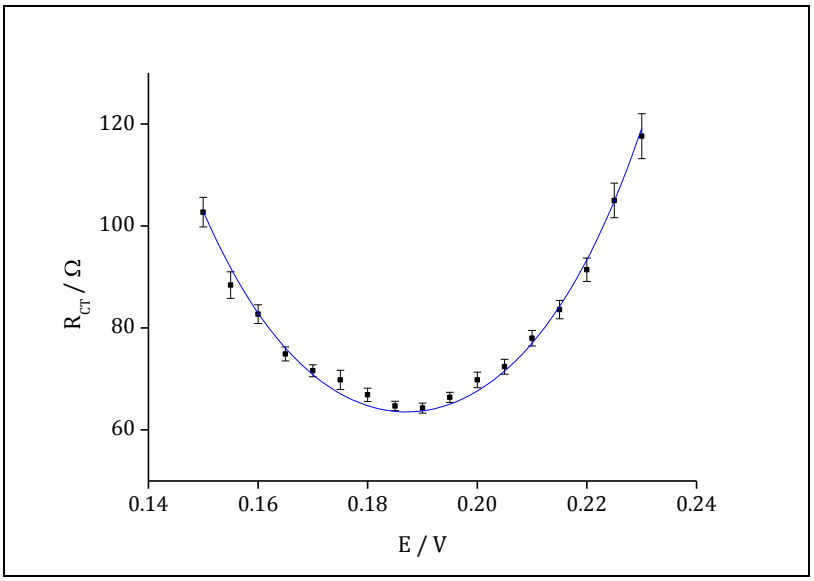

Figure 3.5: Graph of the charge transfer resistance, R_{CT} against dc potential, E_{dc}, The curve was fitted using eqn. 2.41 and gives a correlation coefficient of 0.994. The minimum charge transfer resistance, $R^{min}_{CT,\,K}$ is 63.53 ± 0.32 Ω, and standard potential, E^{Θ} of 0.187 ± 0.001 V.

These results show that, as expected, kinetically controlled charge transfer resistance for the ferricyanide redox couple is not observed at a macroelectrode, since $R_{CT,\,e} >> R_{CT,\,K}$ and thus $R_T = R_{CT,\,e}$ (see section 2.6.3). The results also record a standard potential of + 0.187 ± 0.001 V wrt SCE for the macroelectrode,

which correlates very well with the $E_{1/2}$ value obtained from the CVs (Fig. 3.1). This indicates that this method of analysis can be used to measured ferri/ferrocyanide electrochemical kinetics and/or thermodynamics.

3.6. FEM Simulation of Ferricyanide Reduction

Three-dimensional FEM steady-state electrochemical diffusion simulations of ferricyanide reduction were carried out using COMSOL Multiphysics version 3.2b for Linux (COMSOL, Inc., Burlington, MA), run remotely from a Dell Pentium 4 PC using the Xfce 4 Desktop Environment interface (Xfce 4.4.2, Oliver Fourden©). One quarter of a microsquare electrode and of a microdisc electrode were simulated in the space domain, utilising the symmetry associated with square and disc.

Previous experiments and 2D simulations on microdisc array electrodes have established negligible interaction between neighbouring array elements at steady-state when electrodes are separated by more than 24 times the disc radius[2,3]. This suggests the steady-state diffusion is established for each microdisc before the diffusion layer extends to the order of 12 times the electrode radius. It must be noted that in fact the diffusion layer actually increases with time, even when there are steady-state currents[4,5], but this establishes that a steady-state current is first found when the diffusion layer has reached this distance. To avoid boundary effects due to concentration depletion at the edges of the space domain, a cube of 500 μm edge dimension (20 times the electrode radius) was used for simulation, with the electrode microdisc located as a quarter circle in the x-y plane at z = 0 and the disc centre at x = 0, y = 0 (figure 3.6 b). It was intially unclear if the same separation would be required for microsquare electrodes, but the microsquare electrode simulation was carried out using a cube of the same dimension, with the quarter square of electrode of edge length 25 μm again located in the x-y plane at z = 0, with full square centre at x = 0, y = 0 (Figure 3.6 a).

These simulations assumed transport solely by diffusion, consistent with stagnant solution measurements; in 3-D, the transport equation for ferricyanide diffusion in the cube for a steady-state simulation is:

$$\nabla \cdot (-D\nabla \bar{c}) = 0 \qquad \textbf{Eqn. 3.2}$$

where c is the concentration (set throughout to an initial value of 10 mM) and D is the isotropic diffusion coefficient of ferricyanide which is 6.98 x 10^{-10} m^2s^{-1} at 298 K in 0.1 M KCl electrolyte[6]. Equation 3.2, which is Fick's second Law of diffusion in three dimensions can also be written as:

$$\frac{\delta c}{\delta t} = -D\left(\frac{\delta^2}{\delta x^2} + \frac{\delta^2}{\delta y^2} + \frac{\delta^2}{\delta z^2}\right) = 0 \qquad \textbf{Eqn. 3.3}$$

Where *t* is the time is seconds and *x, y* and *z* are coordinates on the x, y and z-axis respectively.

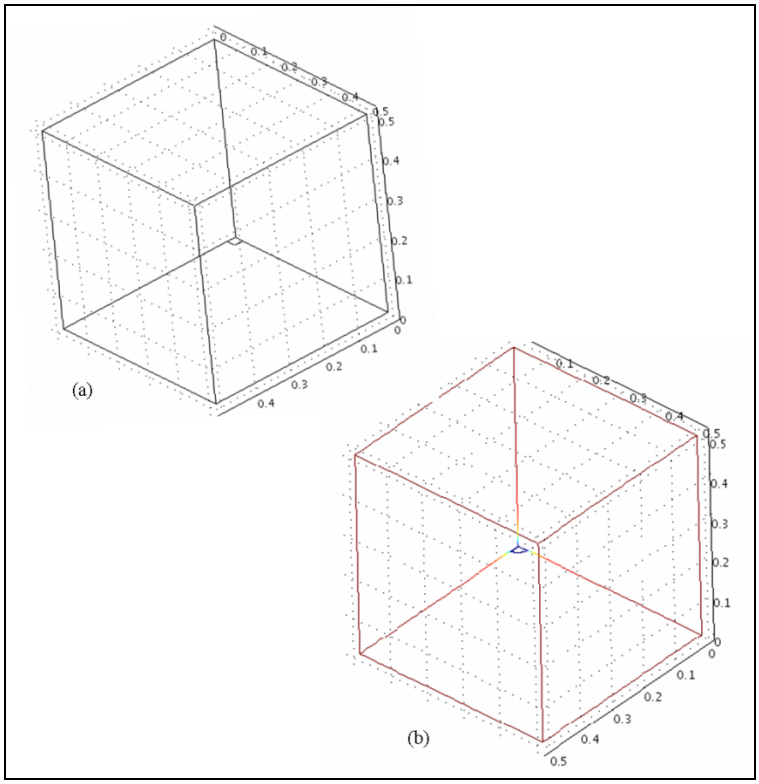

Figure 3.6: The three dimensional model produced to simulate diffusion towards the activated electrode surface of a) a microsquare and b) a microdisc. The large 3D cube represents the simulation space and the small square in the corner of the x,y-plane represents a quarter of the active microsquare electrode. For microdisc simulation this was replaced by a quarter of the microdisc. Dimensions shown are in millimetres.

Table 3.3 shows the COMSOL input parameters used for the model bounded subdomain.

Physics – Subdomain Settings (Subdomain 1)	
Equation	$\nabla \cdot (-D\nabla c) = R = 0$ Where c is the concentration and R is the reaction rate (mol $m^{-3}s^{-1}$).
Diffusion Coefficient, D / m^2 s^{-1}	$6.98x10^{-10}$
Initial concentration, $c(t_0)$ / mol m^{-3}	10
Predefined Elements	Lagrange - Quadratic
Shape Function	Shlag(2'c')
Integration Order	4
Constraint Order	2

Table 3.3: Table of the COMSOL subdomain parameters used to model diffusive flux towards th microdisc and microsquare electrode at t = 0.

Conservation of symmetrical boundary conditions were applied to the x = 0 and y = 0 planes (symmetry faces), with the ferricyanide concentration set to zero on the active electrode surface (to ensure the calculation of the mass transport limiting current) and the ferricyanide flux, normal to the face set to zero across the rest of the z = 0 plane (insulating face). This is consistent with an insulated surface. At all other cube boundaries the concentration of ferricyanide was fixed at the bulk value of 10 mM (outer sub-domain faces). Table 3.4 therefore gives a list of the COMSOL boundary settings:

Physics – Boundary Settings			
Boundary Selection	**Type of Boundary**	**Equation**	**Parameters**
Symmetry Faces	Insulation/Symmetry	$\mathbf{n}\cdot\mathbf{N}=0$ where n is the normal vector and $\mathbf{N} = -D\nabla c$	$N_0 = 0$ / mol m^2s^{-1}
Active Electrode	Concentration	$c=c_0$ where c_0 is initial concentration	$c_0=0$ / mol m^{-3}
Insulating face	Flux	$\mathbf{n} \cdot \mathbf{N} = N_0 + k_c + (c_b - c)$ where N_0 is the inward flux, k_c is the mass transfer coefficient and c_b is the bulk concentration	$N_0=0$ / mol m^2s^{-1} $k_c=0$ / m s^{-1} $c_b=0$ / mol m^{-3}
Outer sub-domain faces	Concentration	$c=c_0$	$c_0=10$ / mol m^{-3}

Table 3.4: Table of the COMSOL boundary settings used to model diffusive flux towards a microdisc and microsquare electrode.

COMSOL readily enables the integrated flux across the electrode area, *JA*, to be evaluated from the double integral of the local concentration gradients normal to the electrode surface[7]:

$$JA = D \int_0^{l/2} \int_0^{l/2} \left.\frac{\delta c}{\delta z}\right|_{z=0} \delta y \delta x \qquad \textbf{Eqn. 3.4}$$

where *l* is the length of the square edge or disc diameter for microsquare or microdisc as appropriate. Table 3.5 shows the post processing parameters selected in COMSOL in order to calculate the normal diffusive flux towards the electrode surface.

Post Processing – Boundary Integration	
Boundary selection	Active Electrode
Predefined quantities	Normal diffusive flux, c
Expression	ndflux_c_di
Unit of integral	Mol s^{-1}
Solution at angle (phase)	0^0

Table 3.5: Table to show the post processing boundary integration parameters in COMSOL

This normal diffusive flux can be readily converted to the limiting current, i_L at the electrode through

$$i_L = 4n\mathbf{F}JA \qquad \textbf{Eqn. 3.5}$$

where *n*, the number of electrons transferred, is unity for ferri/ferrocyanide and **F** is Faraday's constant.

Following a similar approach to Strutwolf, who computed the response of rectangular microelectrodes[6], dynamic adaptive mesh refinement (DAMR) was used to refine the current densities calculated from these simulations and ensuring that the grid is more dense at the electrode edges to accurately model the greatest rate of change of concentration gradients (section 2.7). The 'meshinit' option in COMSOL was selected to prevent physically unrealistic

mesh overlap and five refinements were carried out for each computational step. Table 3.6 shows the input parameters required for DAMR in COMSOL.

Solver Parameters			
General	**Linear system solver**	Conjugate gradients	
	Preconditioner	Algebraic multigrid	
	Quality of multigrid hierarchy	3	
	Matrix symmetry	Automatic	
Advanced	**Constraint handling method**	Elimination	
	Null space function	Automatic	
	Assembly block size	Automatic	
	Stop if error due to undefined dimension?	Yes	
	Solution form	Automatic	
	Type of scaling	Automatic	
	Row equilibrium	On	
Stationary Solver	**Linearity**	Automatic	
	Relative Tolerance	$1x10^{-6}$	
	Maximum number of iterations	25	
	Damped Newton?	Yes	
Adaptive Mesh refinement	**Use refinement in geometry:**	Current geometry	
	Error method	**L2 Norm**	
		Scaling factor	1
		Stability estimate derivative order	2
		Element selection method	Rough global minimum
		Increase number of elements by?	1.1
	Residual method	weak	
	Maximum number of refinements	1-5	
	Maximum number of elements	$1x10^{7}$	
	Refinement method	Meshinit	
	Residual order	Auto	
	Weights of eigenmodes	1	

Table 3.6: Table of the solver paramters selected in COMSOL, to adaptively refine with meshinit meshing during simulations of the microdisc and microsquare arrays.

3.7. Case Study 2 - Validating COMSOL: Simulation of a microdisc electrode

In order to validate the COMSOL FEM method of simulation a microdisc electrode was chosen. This is because there is a well-established analytical expression, which enables calculation of the steady-state current at a microdisc electrode, when the redox agent completely reacts at the electrode surface and a

steady-state mass transport limited current is established[8-10] . The expression is:

$$i_L = 4n\mathbf{F}Dc^{\infty}r \qquad \textbf{Eqn: 3.6}$$

Where c^{∞} is the bulk solution concentration and *r* is the radius of the microdisc in question. As initial electrochemical studies were performed on a microsquare with a square length of 50 μm, a comparable microdisc of 50 μm diameter was modeled and simulated as described in section 3.6 to validate this approach. For the one electron transfer of potassium ferricyanide (10 mM) in aqueous solution and a diffusion coefficient of 6.98×10^{-6} cm^2 s^{-1} (at 298 K), the limiting current calculated using equation 3.6 is 67.3 nA.

After refining the FEM model several times using DAMAR, the limiting current calculated from the simulation asymptotically reached a steady value. Ideally the simulation should end when the tolerance is reached, however the refinement (performed on the lynux system) often fell down before this, when the mesh was too dense to insert more element nodes. Initial experiments were performed on a pc version of COMSOL, which often ran out of processing memory before the mesh refinement was complete.

Figure 3.7 shows a close up image of the adaptively refined mesh attained for the simulated quarter microdisc electrode before the mesh failed to insert more element nodes.

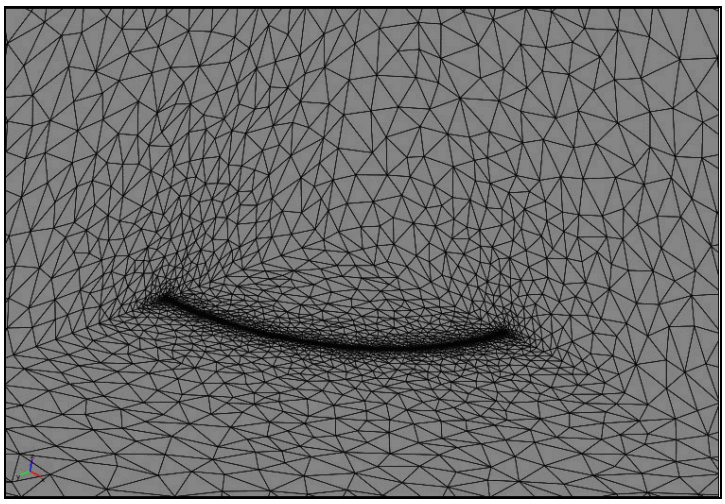

Figure 3.7: Image of the final mesh density obtained using DAMR during the FEM simulation. The number of degrees of freedom = 564154

It should be noted that the highest mesh density occurs around the circumference of the electrode, and since the mesh density scales with diffusive flux, a very dense mesh represents high diffusive flux thus the highest ferricyanide transport rate and hence current density occurs around the circumference.

Figure 3.8 shows the graph obtained when plotting simulated current against increasing mesh density. The red line is the limiting current calculated using expression 3.5.

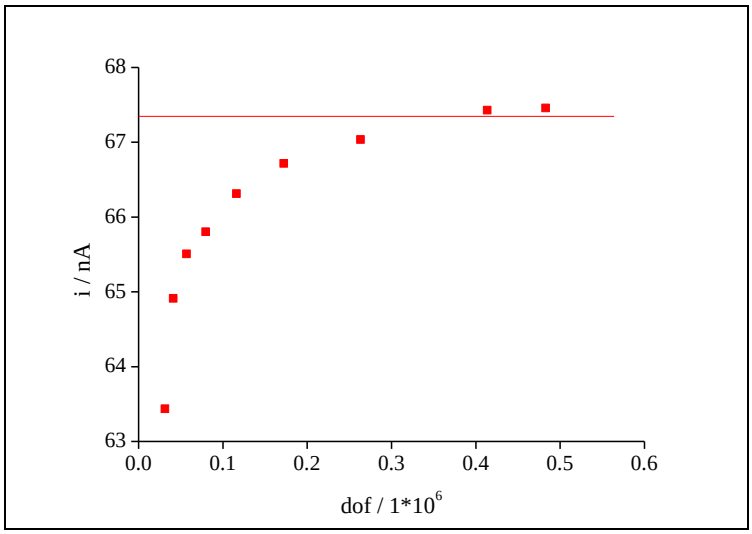

Figure 3.8: Plot of COMSOL calculated limiting currents for simulated microdisc (r =25.0 μm, red spots) at increasing degrees of freedom (dof). Also shown is the theoretical limiting microdisc current obtained from eqn 3.7.1 (red line).

It is highly satisfying that these values asymptotically approach the established analytical value calculated from equation 3.4, which supports the accuracy of this method for calculations on electrodes of this dimension.

For further validation that the computer model is able to accurately determine limiting currents which correspond to the theoretically derived microdisc expression and, in order to obtain an estimate of the accuracy of the FEM model used, microdiscs of several other disc diameters (100 μm, 30 μm, 20 μm, 10 μm, 5 μm, 3 μm, 2 μm and 1 μm) were also simulated. The graph below shows a plot of limiting current calculated by FEM simulation and that obtained from the theoretical expression (Eqn. 3.6).

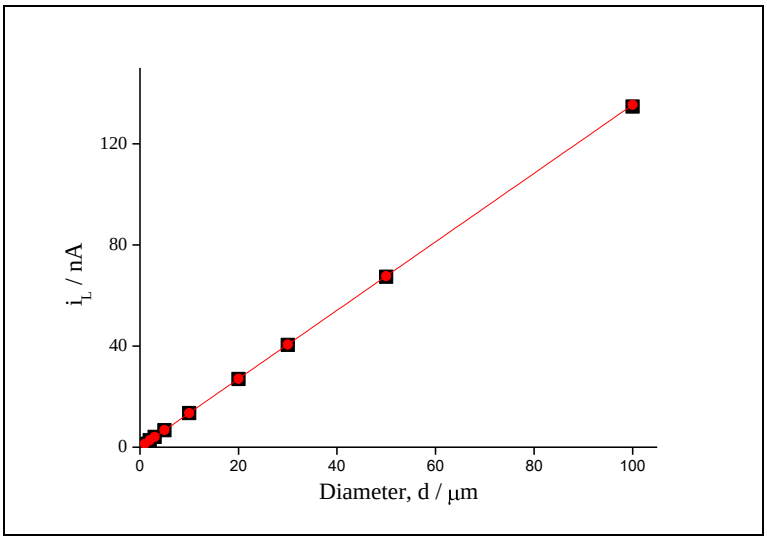

Figure 3.9: Plot of the theoretical limiting current (black squares) for each of the microdisc sizes. For all sizes the gradient of theoretically derived limiting current is -1.3469×10^{-9} and an intercept of zero. The COMSOL simulated limiting currents (red circles) for microdiscs of increasing size are plotted as an overlay. The linear regression line for this data has an intercept of $(-9 \pm 10) \times 10^{-12}$ A and a gradient of $(1.3537 \pm 0.0003) \times 10^{-9}$.

The gradient of slope for theoretical limiting current against diameter is 1.3469×10^{-9} and the gradient of slope for the COMSOL simulated limiting current against diameter is $(1.3537 \pm 0.0003) \times 10^{-9}$. The data shows that limiting currents calculated via the FEM simulation are consistently and systematically very slightly larger than the theoretically derived limiting currents and at this accuracy have an error of just 0.5%. However the two values are the same to two significant figures which confirms that the COMSOL simulations can

accurately predict microdisc limiting currents. This work gives confidence in the ability to simulate the response of microsquares of similar dimension.

3.8. Imaging

3.8.1 Optical Microscopy

Optical images were obtained on three different microscopes. The microsquare electrodes in Chapter 4 were viewed under a Reichert Jung Polyvar microscope in the clean room at the SMC. The images were captured with a Leica, DC-300 digital camera attached to the optical microscope and rendered using Leica IM50 Image acquisition software. The CaviArE and microsquare arrays in Chapter 5 were viewed under an Olympus BH-2 microscope. The images were captured with a Sony MVC-FD200 digital camera. The CaviArE and microsquare arrays in Chapters 6 and 7 were viewed under a Zeiss Axiotron microscope. The images were captured with a Diagnostics Instruments Spot Insight QE digital camera and rendered using the Diagnostics Instrumentation Spot v3.5 for Windows image software. Any deviations from this will be detailed as required.

3.8.2. FIB (Focused Ion Beam) sectioning followed by Scanning Electron Microscopy

In order to examine the device and its composition of deposited, patterned and etched layers, a focused ion beam (FIB) system (FEI FIB 200) was used to cut a channel into the device thereby revealing a cross section through the deposited layers. The system uses a Gallium ion beam to sputter material from the surface of the chip. Once a channel has been cut in the device, the cross section was imaged using a scanning electron microscope (Philips, L40FEG).

3.8.3. Photographs

Photographs were taken using a Sony, Cybershot DSC P200 digital camera

3.9. References

(1) Bard, A. J.; Faulkner, L. R. *Electrochemical Methods, Fundamentals and Aplications*; Second ed.; John Wiley and Sons, Inc.: Hoboken, 2001.

(2) Guo, J.; Lindner, E. *Analytical Chemistry* **2009**, *81*, 130.

(3) Davies, T. J.; Compton, R. G. *Journal of Electroanalytical Chemistry* **2005**, *585*, 63.

(4) Amatore, C.; Saveant, J. M.; Tessier, D. *Journal of Electroanalytical Chemistry* **1983**, *147*, 39.

(5) Amatore, C.; Fosset, B. *Analytical Chemistry* **1996**, *68*, 4377.

(6) Koster, O., W. Schuhmann, H. Vogt and W. Mokwa *Sensors and Actuators* **2001**, *B*, 573.

(7) Strutwolf, J.; Williams, D. E. *Electroanalysis* **2005**, *17*, 169.

(8) Heinze, J. *Angewandte Chemie International Edition in English* **1993**, 1268.

(9) Britz, D.; Poulsen, K.; Strutwolf, J. *Electrochimica Acta* **2004**, *50*, 107.

(10) Oldham, K. B. *Electrochemistry Communications* **2004**, *6*, 210.

4. Characterisation of Single Microsquare Platinum Electrodes

4.1. Introduction

As discussed in Chapter 1, microelectrodes have well established analytical advantages over macroelectrodes[1-3]. Their enhanced radial mass transport diffusion leads to the rapid establishment of steady state currents without external convection. They also have reduced iR drop, increased Faradaic current densities and therefore higher signal-to-noise ratios, which greatly increases their detection sensitivity. Microelectrodes therefore are of considerable interest when developing highly sensitive electroanalytical systems. However, to achieve reproducible system enhancement, there is a need to employ fabrication techniques and develop processes that optimise microelectrode responses and provide devices with specific size, shape and pitch. Photolithographic techniques (long established in the electronic and semiconductor industries) have made possible the fabrication of microelectrodes of controlled dimension[4,5]. Berduque *et al*[6] have recently used this approach to fabricate and characterise microsquare and microdisc electrodes. Their conclusion is consistent with a previous approximation[7] that a microsquare electrode has an equivalent mass transport limited current to a microdisc when its side length is equal to the disc diameter. This is in contrast to Morita *et al*[5], who suggest an equivalent response from microdisc and microsquare electrodes of the same area. The resolution of whether a microsquare response can be readily related to that of a microdisc is important because microdisc electrodes have been well characterised, and their time-dependent and steady-state responses solved analytically[2,8,9]. However, microsquare electrodes are easier to fabricate accurately on the micron scale with standard pixelated photomasks.

This chapter describes work carried out in collaboration with a research group at the Scottish Microelectronics Centre (SMC), located on The University of Edinburgh's science and engineering campus. The group have utilised photolithographic techniques to produce microsquare electrodes of highly

reproducible dimensions and fundamental microsquare electrode response. This has enabled a systematic study of these systems. In addition, the fabrication of these microsquare electrodes has been achieved using a biocompatible insulating layer, parylene, which is compatible with their use in biosensing and biodetection applications[10].

This fabrication of these microsquare electrodes is first outlined, followed by systematic analysis of their electrochemical response using a combination of cyclic voltammetry, electrochemical impedance spectroscopy (EIS) and computer simulation. The results are compared and contrasted to the well-established behaviour of microdisc electrodes of a similar dimension and a theoretical expression is established for determining the limiting currents of these electrode systems.

4.2. Specific Experimental procedure

4.2.1. Microsquare Fabrication

Square platinum microelectrodes of edge dimension 50 μm were fabricated on 3-inch <100> n-type Silicon wafers (IDB Technologies) on which surface silicon dioxide insulation (500 nm thickness) was grown using wet oxidation (1100 ^{0}C for 35 minutes in an O_2/H_2 atmosphere). Patterned electrodes were then fabricated by using a lift-off process (Figure 4.1).

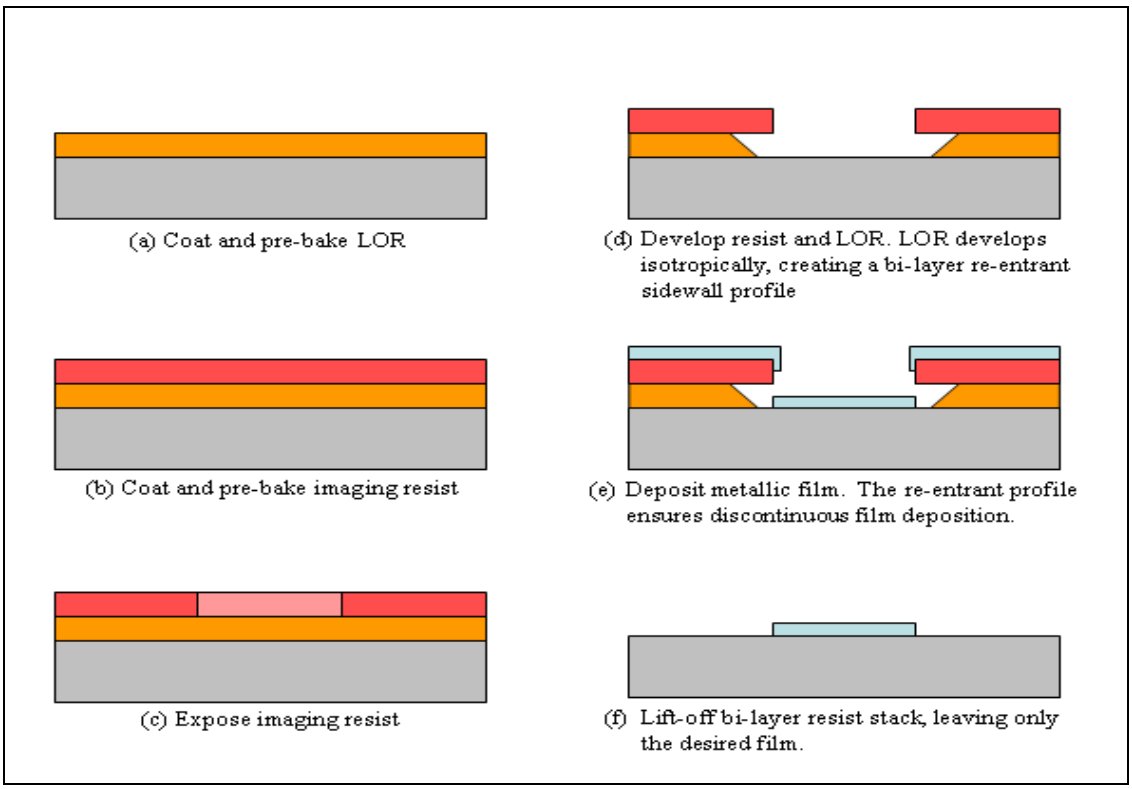

Figure 4.1: Schematic diagram of the platinum array patterning lift off process[i]

A 450 nm layer of lift-off resist, (LOR, LOR-5B, Microchem, Chestech) was spun onto the wafer and baked for five minutes at 190°C (Fig. 1(a)). This was followed by spin deposition of positive photoresist (Megaposit SPR350, Microchem, Chestech), at 4000 rpm to give of a 1 µm layer, which was baked for 60 seconds at 90°C (Fig. 1(b)). Following UV exposure of the resist through a metallisation mask plate (Fig. 1(c)), the resist was developed by submersion in a developer solution (Microposit MF319 Developer, Microchem) with agitation for 60 seconds before rinsing in de-ionised water, to give the required microelectrode pattern complete with an undercut to facilitate the lift-off process (Fig. 1d). The electrode film consisted of a 200 nm layer of sputter deposited Platinum on a 5 nm sputter deposited chrome adhesion layer performed, each deposited using a Denton Vacuum Desktop 3 sputter tool (Fig. 1e). The undercut ensured a discontinuous metal film, which enabled successful lift-off of the excess material during stripping using a resist remover (Megaposit SPR350, Microchem, Chestech). This was performed by submersion in two subsequent baths of resist remover for 45 minutes each, before a final 15

[i] This diagram was provided for this thesis by Dr Jonathan Terry, who fabricated the electrodes.

minute rinse in isopropyl alcohol (IPA), (Fig. 1(f)). For biocompatible insulation of all but the active electrode areas and contact pads, a 1 μm layer of parylene was deposited. Parylene C dimer (741-767 mg) (FW 277.19, SCS Coatings Cas: 28804-46-8) was vaporised under vacuum on a hot plate and pyrolised in a room temperature deposition chamber to enable reaction and deposition of the monomer gas as a transparent, insulating polymer film. Patterning of this parylene using standard photolithography, followed by reactive ion etching in oxygen plasma, was used to open up defined electrode (Figure 4.2) and contact pad areas.

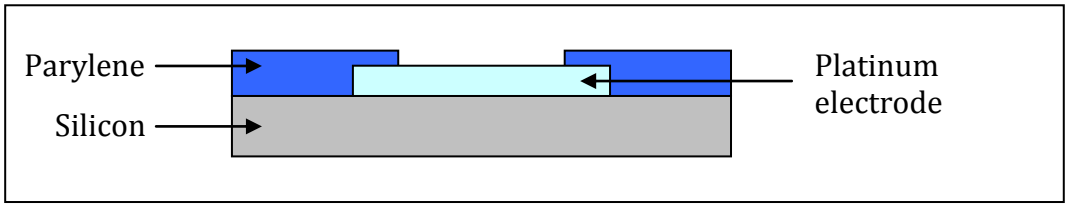

Figure 4.2: Schematic diagram showing the cross section of the final microsquare electrode.

It should be noted that to ensure effective edge insulation and pattern matchimg, the deposited Platinum microsquare was of 60 μm edge dimension, whilst the exposed hole in the parylene area had a 50 μm edge dimension. It should also be noted that parylene insulator generaterates a small, (~ 800 nm) lip around the the edge of the electrode. Berdque *et al*[6] in their study of recessed electrodes state a theoretical equation for the calculation of the limitng current of an inlaid microdisc electrode.

$$i_L = 4n\mathbf{F}Dcrd \qquad \textbf{Eqn. 4.1}$$

where d, in this case, is the thickness of the insulating recess. However the thickness of the recess defined by the Parylene layer, in this study, is less than 2% of the square edge dimension and it has been established for microdiscs that the response of these electrodes can be considered as essentially equivalent to planar electrodes, thereby simplifying simulation[11]. The metalisation mask template for the single platinum square electrode was manufactured to pattern eight electrodes on one silicon chip, each connected to an individual platinum wire and contact pad. Figure 4.3. shows a

schematic of these microsquare electrode devices.

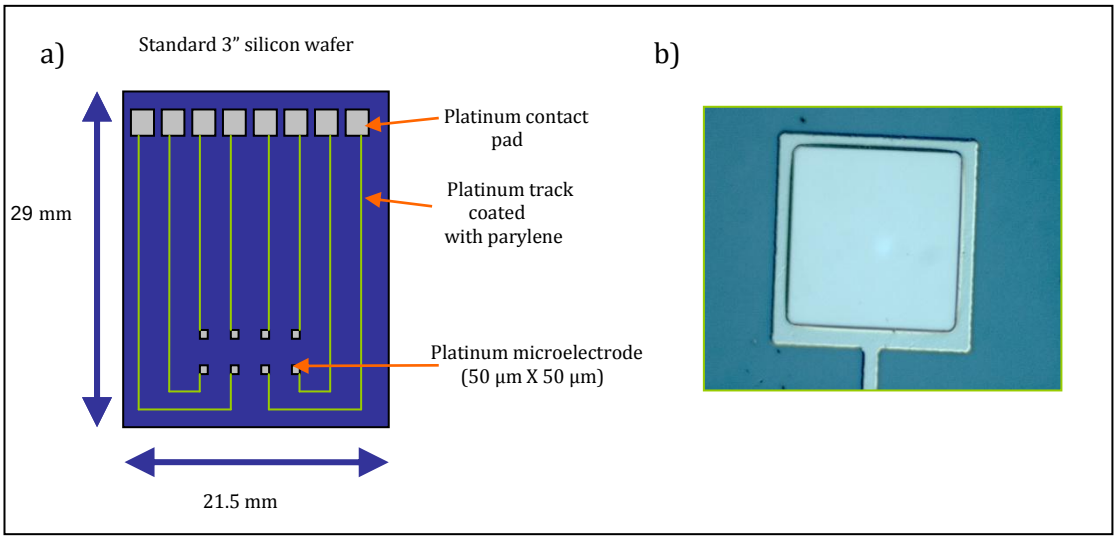

Figure 4.3: Schematic diagram of the layout of a multiple Platinum electrode chip, showing the platinum contact pads, the insulated platinum tracks and eight individual platinum microsquare electrodes; alongside is a photograph of a typical electrode produced by the described process.

4.2.2. Ferri/Ferrocyanide Solutions

For experiments performed in section 4.3.1, aqueous potassium ferricyanide, $K_3Fe(CN)_6$ [5 mM] (FISONS, SLR reagent grade, > 99% purity) and potassium ferrocyanide, $K_4Fe(CN)_6.3H_2O$ [5.0 mM] (Sigma-Aldrich, ACS reagent grade, > 99% purity) were prepared in aqueous solution with potassium chloride [0.1 M] background electrolyte.

For experiments performed in sections 4.3.2 – 4.3.4, aqueous potassium ferricyanide, $K_3Fe(CN)_6$ [10.0 mM] (Sigma-Aldrich ACS reagent ≥ 99% purity) in potassium chloride [0.1 M] was used. All other solution are as those outlined in section 3.1

4.2.3. Apparatus and Setup

Analysis of the 50 µm platinum electrodes had to be carried out in a Faraday cage (Autolab) to shield the experiments from external electrical noise interference. To assist these experiments a connection system was created in house, using standard components including ribbon cable, IDC sockets and header, and an IC test clip, which enabled simultaneous interrogation of all the eight electrodes on a chip. Figure 4.4 shows a diagram of the connecting device.

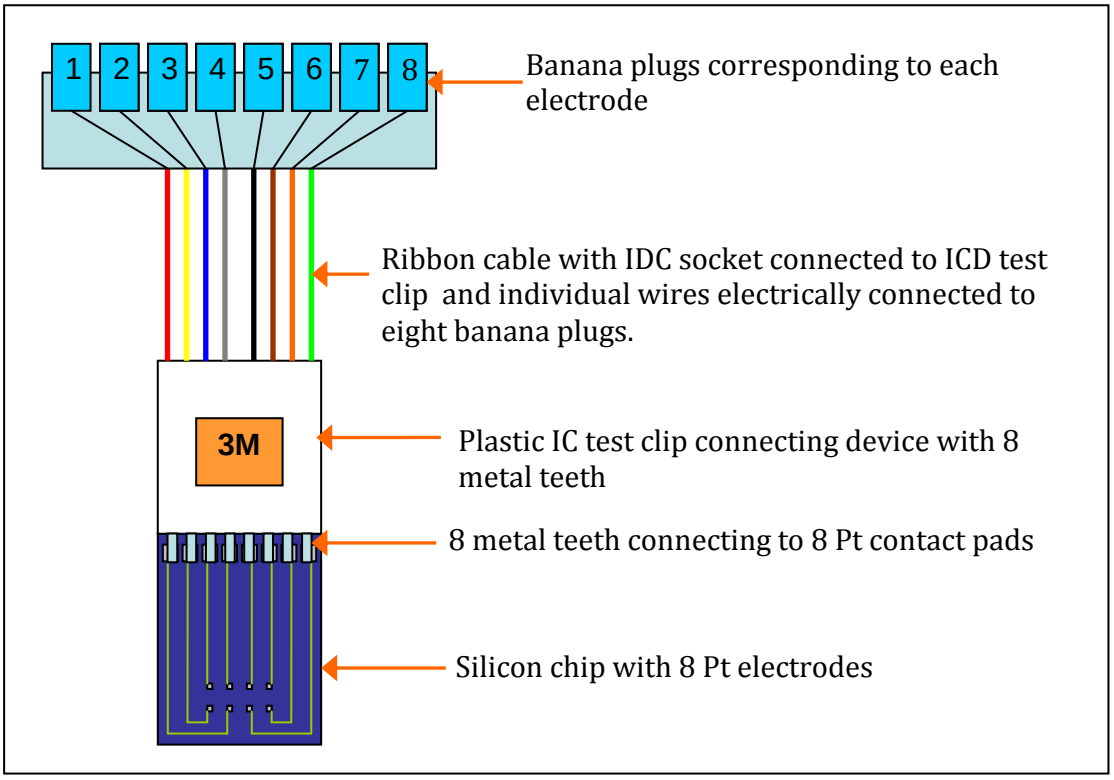

Figure 4.4: Diagram representing the connection device modified at the SMC, to enable connection to each individual electrode on the silicon chips. The banana plugs have been numbered on the diagram, to coincide with the numbering scheme of electrodes on the chip.

The test clip has a spring opening mechanism allowing easy insertion and removal of the silicon chips under test, and the banana plug sockets at the other end of the connection system, enable rapid connection to each of the electrodes. The ribbon cable connection was held at a fixed height using a clamping stand. The reference and counter electrodes were immersed in the solution of interest and the beaker height adjusted by means of a labjack until the electrodes were immersed in the solution, ensuring that the contact pads were not wetted. Figure 4.5 is a photograph of the experiment set up used.

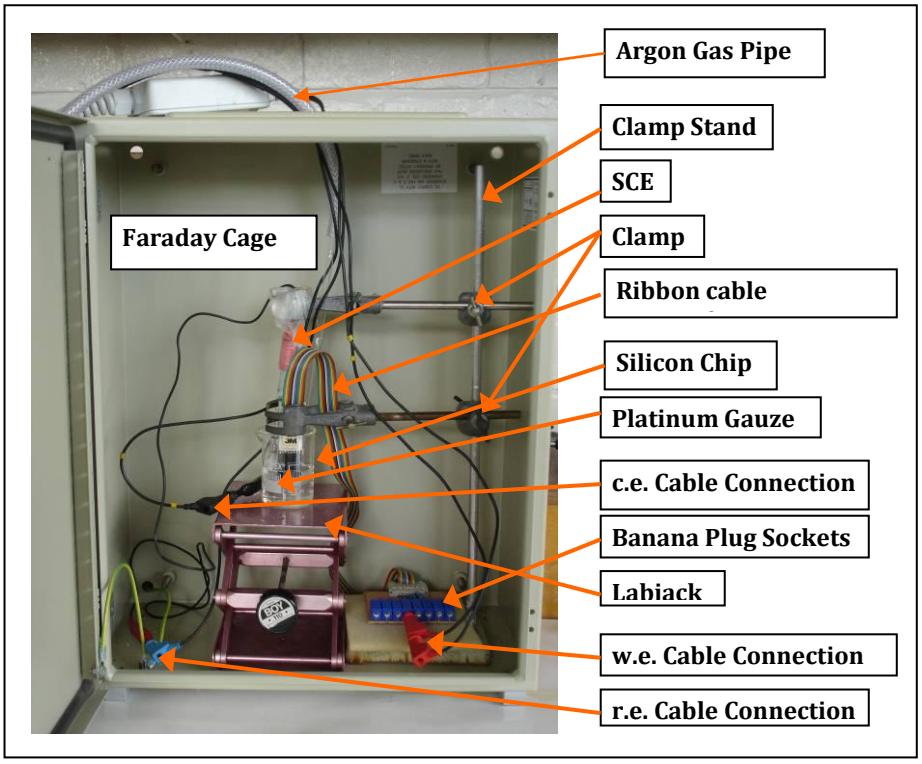

Figure 4.5: Photograph of the experimental set up used to analyse the response of platinum microsquare electrodes

4.2.4. Finite Element Modelling (FEM)

FEM models were set up as described in section 3.6 and simulations of the response of the (50 μm)^2 platinum single electrodes (denoted S50μ), in ferricyanide were performed. Similarly to microdiscs simulations, described in section 3.7, microsquares of varying lengths were also modelled and compared both to the responses of microdiscs and to the corresponding theoretical expressions.

4.3. Results and Discussion

4.3.1. Preliminary Sulfuric Acid Cleaning

The cyclic voltammograms obtained for the S50μ electrodes showed that their surfaces required extensive cleaning before experiments could be carried out. Figure 4.6 presents a typical cyclic voltammogram obtained for such an S50μ electrode, in the potential range expected for characteristic oxidation and reduction of ferri/ferrocyanide before the surface was cleaned.

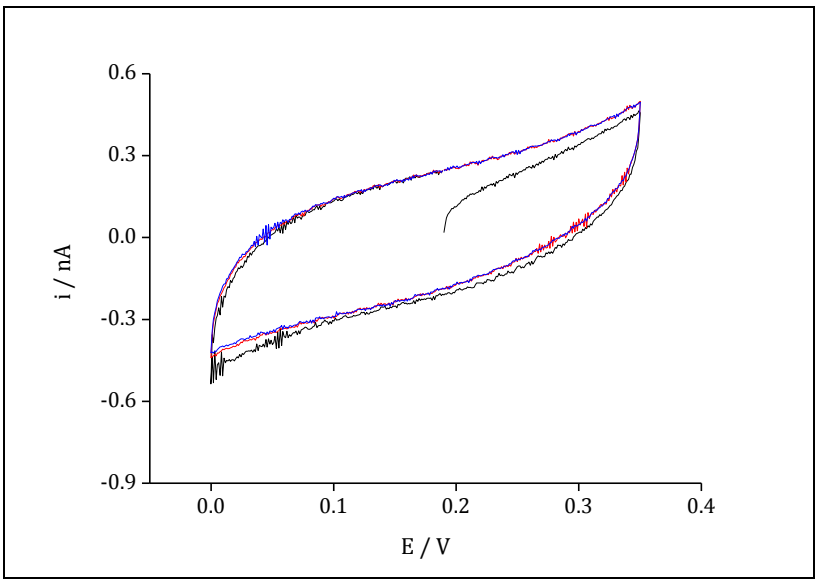

Figure 4.6: Cyclic voltammogram (CV) of a 1:1 aqueous solution of 5 mM ferricyanide, 5 mM ferrocyanide, in 0.1 M KCl background electrolyte at an S50µ Pt electrode prior to cleaning in H_2SO_4. The potential in ferri/ferrocyanide was held at + 0.19 V, (the approximate standard potential for the ferri/ferrocyanide couple vs. SCE), for 10 seconds and then swept from + 0.19 V through the oxidising potentials, to + 0.35 V and then through the reducing potentials to + 0.00 V and back to +0.19 V at a sweep rate is $100mVs^{-1}$. The potential in this CV and all following CVs is recorded with respect to a standard calomel electrode (SCE).

Figure 4.7 shows a corresponding cyclic voltammogram (CV) obtained with an increased potential window.

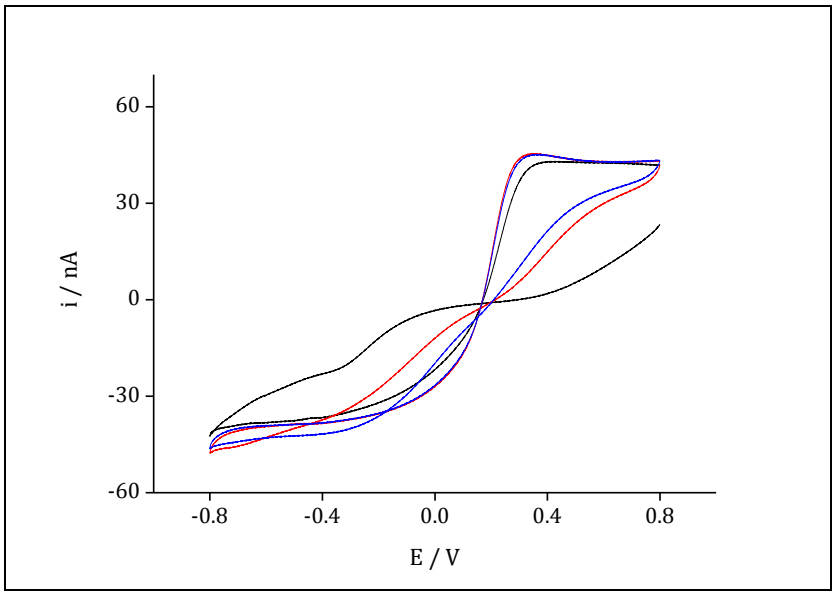

Figure 4.7: Cyclic voltammogram of a 1:1 aqueous solution of ferri/ferrocyanide at a S50µ Pt electrode prior to cleaning in H_2SO_4, at a sweep rate of $100mVs^{-1}$ between +0.8 V and -0.8 V.

The lack of distinct redox peaks in Fig. 4.7 and nucleation loops observed as well as changes in the CV with cycle number are due to surface passivation and changes in surface reactivity with potential and CV cycling. This passivation

layer may be a thin layer of parylene which was not etched off completely or remnants of the organic photoresist stripper used during fabrication.

An established protocol for cleaning platinum microelectrodes[12,13], which utilises cyclic voltammetry, is to place the electrode in an aqueous solution of sulfuric acid (H_2SO_4) and continuously cycle between oxidation and reduction potentials to generate O_2 and H_2 respectively (see section 3.4.1.1 for all details) until the CV no longer changes and is characteristic of pure platinum. Figure 4.8 shows a typical CV obtained for the S50µ electrodes under investigation when cycled 20 times in 0.05 M H_2SO_4. The potential window and current cap was optimised in prior experiments. The current was restricted to a maximum current of 1 µA magnitude, to limit gas production so as not to cause damage to the electrode.

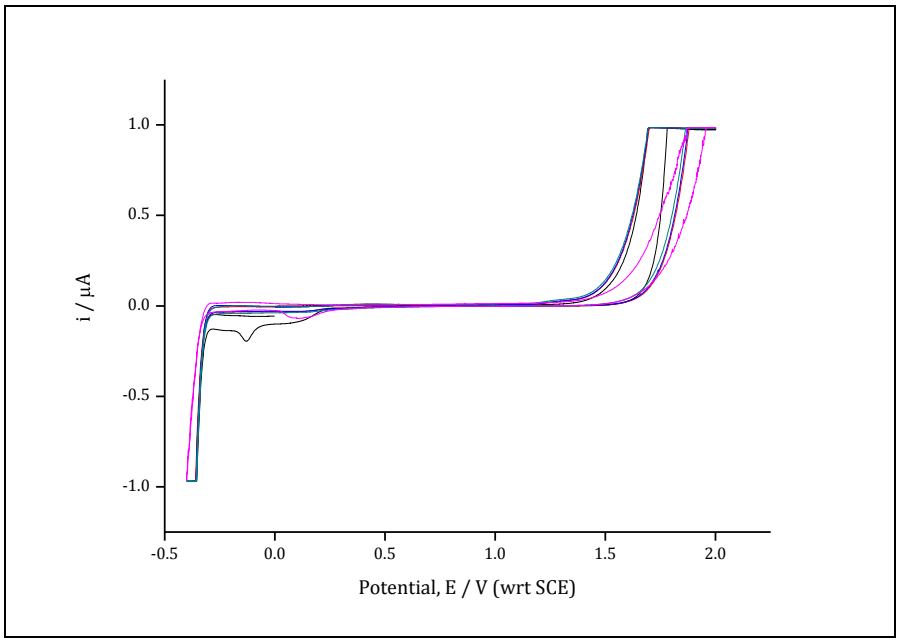

Figure 4.8: Cyclic voltammogram showing scans 1, 5, 10, 15 and 20 of the cleaning cycling on a S50µ Pt electrode in 0.05M H_2SO_4 at a sweep rate of 100 mVs^{-1} between +2.00 V and -0.50 V.

Optical images of the S50µ electrodes were taken before and after cleaning in sulfuric acid. Figure 4.9 shows one such electrode before and after acid cleaning.

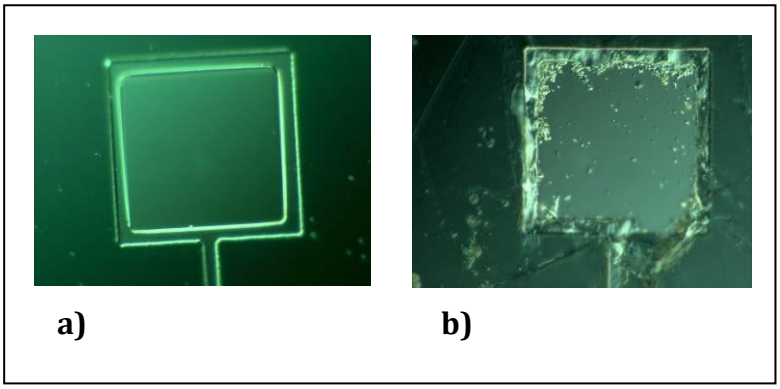

Figure 4.9: Optical images at 50X magnification of a S50µ Pt electrode where a) shows a contrast image of the electrode before experimentation, b) shows a contrast image of the same electrode after cleaning in H_2SO_4 and CV analysis in ferri/ferrocyanide.

The contrast image, figure 4.9 a) shows that before cleaning the parylene layer is smooth and appears homogeneous, and the edges of the parylene coating the electrode are sharp along all sides. However, after cleaning (Figure 4.9 b)) the parylene layer seems to have begun to strip from the edges of the electrode.

Industrially, parylene is said to be resistant to solvent attack, although swelling of the parylene film has been observed to varying extents in different organic and inorganic solvents[14]. In regards to sulfuric acid, the parylene C film has been shown to swell by 0.3 % and 0.4 % in sulfuric acid concentrations of 10% and 95-98% respectively at room temperature[15]. Discoloration of the parylene, suggesting some chemical attack and more significant swelling of 5.1 % has been shown in the concentrated acid at elevated temperatures[ii], though this is arguably in much harsher conditions than those used during experimentation in this research. This dilute concentration of acid was therefore not expected to affect the parylene insulation layer without electrochemical activity. In order to confirm this, a number of acid immersion experiments were carried by placing an electrode in a solution of sulfuric acid (0.05 M) for several hours, followed by imaging of the electrode. In line with the technical report (ref. ii), little or no change to the parylene insulator was observed suggesting that acid immersion alone is not a sufficient cause of the observed parylene degradation, and that stripping of parylene from the parylene/electrode interface is only observed after electrochemical cleaning in acid. Although no literature has been found on

[ii] Information obtained from a technical report on parylene: http://www.vp-scientific.com/solvent.htm accessed on 12/05/2011

this subject regarding parylene, electrochemical cycling of electrodes in strong acids between oxidizing and reducing potentials is designed to remove organic impurities from the electrode surface through oxidation and/or reduction followed by product dissolution. As parylene is an organic polymer, it would not be surprising that attack of parylene is observed. This effect may have been caused not only by the oxidation and/or reduction reactions leading to soluble polymer species but also by the oxygen and hydrogen gas released causing mechanical lifting. The fact that parylene stripping was only observed at the electrode interfaces and not elsewhere on the silicon chip, further supports this argument. In a study of polymer insulator adhesion to platinum electrodes, Nichols *et al*[16] reported detachment of parylene from the surface of platinum electrode during CV cycling and observed formation of gas on the metal underneath the parylene film. If a similar effect occurs during acid cleaning, with gas bubbles forming on the platinum underneath the parylene lip, this may also increase the amount of parylene stripping observed.

In addition to the parylene stripping observed, surface contaminants were also shown, optically, to build up on the electrode, after experimentation in ferri/ferrocyanide. Figure 4.10 shows another electrode where a blue-coloured residue can be clearly observed congregating around the edges of the electrode.

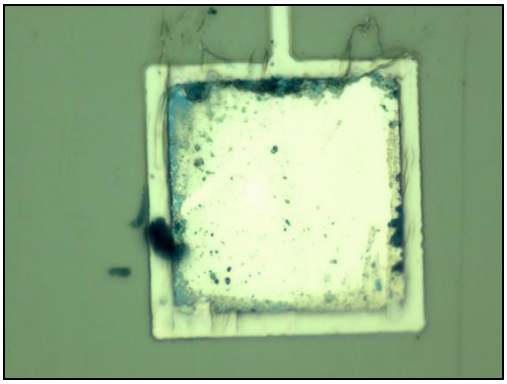

Figure 4.10: Optical image at 50X magnification of a 50 μm Pt electrode after experimentation, showing signs of a blue solid around the edges of the electrode.

The optical images therefore have not only shown damage to the parylene insulator layer caused by acid cleaning but also seem to suggest that a

passivation film may form on the edges of the Platinum electrode during experimentation. In Figure 4.10 it also looks as though some of the solid has actually formed under the lip of the parylene coating the electrode surface, perhaps due to lifting of the parylene from the surface due to swelling or mechanical lifting.

It is interesting to consider the nature of this blue product. Granger and Swain[17] have proposed several arguments suggesting that the $[Fe(CN)_6]^{-3/-4}$ redox couple may not always undergo electron transfer via a simple outer-sphere mechanism. Firstly they argue that the electron-transfer rate constant is dependent on the nature and concentration of the supporting electrolyte and propose that a dimeric species can be formed consisting of the oxidized and reduced forms of the analyte anion, coupled through a bridging cation. Secondly they say there is evidence that a semi-passivation layer of $[Fe(CN)_6]^{-3/-4}$ can also form on electrode surfaces. This irreversible adsorbate on Platinum was postulated to be redox active Prussian blue ($KFe^{II}[Fe^{III}(CN)_6]$). The blue coloured solid observed in this work may then be a complex such as Prussian Blue or a similar Fe(III)/Fe(II) product. In another publication, Pharr and Griffiths[18] performed experiments on a Platinum electrode and demonstrated that at potentials between 0.02 and 0.42 V *vs.* SCE, a decrease in k^{θ} with time was observed for the ferri/ferrocyanide system which they postulate to be due to adsorption of the ferrocyanide ion.

Figure 4.11 shows representative CVs obtained in an equimolar solution of ferricyanide [5 mM] and ferrocyanide [5 mM] at a)100 mVs^{-1} and b) 5 mVs^{-1} after the electrode has been cycled 20 times in sulfuric acid.

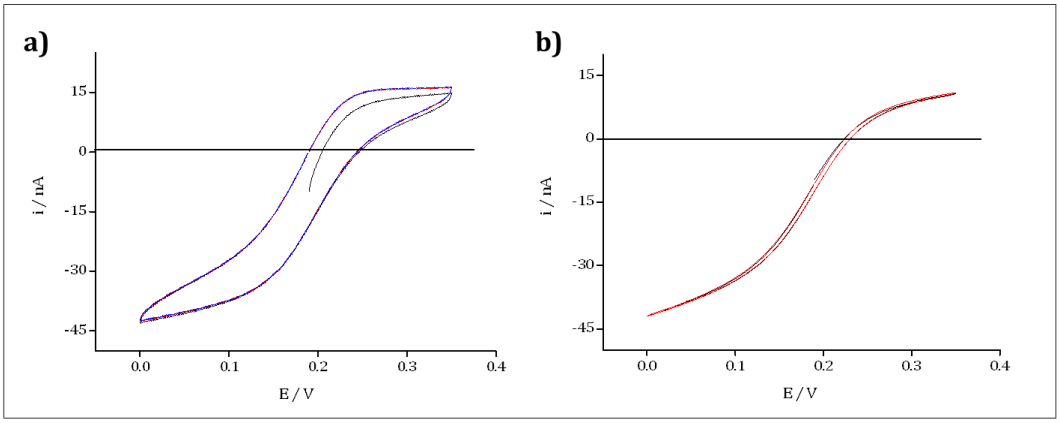

Figure 4.11: Typical CVs for an 1:1 aqueous solution of ferricyanide (5 mM), ferrocyanide (5 mM) in KCl (0.1 M) background electrolyte at a 50 µm Pt electrode after cleaning in H_2SO_4 for 20 cycles at a scan rate of **a)** 100 mVs^{-1} and **b)** 5 mVs^{-1} The scan rate is 100 mVs^{-1} between 0.35 V and 0.00 V.

At 100 mVs^{-1} the microelectrode response does not show steady-state characteristics, but at 5 mVs^{-1} the CV shows an essentially sigmoidal response, characteristic of a microelectrode. It must be noted however that the CV is sloping at either end of the cycle and the response is not even close to symmetrical about zero current. Given that the concentrations of ferricyanide and ferrocyanide were equal and that their diffusion coefficients are similar (section 2.2), this is unexpected. It is not clear why the electrode responses during these experiments were typically similar to those in Figure 4.11, although a combination of a build-up of a solid passivation layer and degradation of the parylene insulating layer could have an influence on the electrochemistry occurring at the surface of these electrodes.

In order to combat the problem of parylene degradation a new, milder cleaning technique needed to be developed. In addition as there were issues with insoluble products being obtained in a mixed ferri/ferrocyanide redox solution, experiments in ferricyanide [10 mM] only were carried out instead. The development of a potassium chloride cleaning protocol is discussed below in section 4.3.2 and the experimental results obtained in 10 mM ferricyanide are discussed in section 4.3.3.

4.3.2. Development of the Potassium Chloride Cleaning Technique

A new cleaning protocol was developed using 0.1 M potassium chloride which is pH neutral and therefore should reduce acid attack problems. It must be noted that in an un-buffered aqueous solution, significant pH changes will still be observed during electrochemical oxidation and reduction:

$$H_2O \rightarrow \tfrac{1}{2}O_2 + 2H^+ + 2e^- \qquad \text{pH decreases} \qquad \textbf{Eqn. 4.2}$$

$$H_2O + e^- \rightarrow \tfrac{1}{2}H_2 + OH^- \qquad \text{pH increases} \qquad \textbf{Eqn. 4.3}$$

However this pH change will only occur during electrochemical reaction and the overall mean pHs are likely to be more neutral than those observed in sulfuric acid.

It should be noted that Köster *et al*[19] also used a KCl cleaning protocol prior to experimentation on their microelectrode arrays. Utilising a similar technique, the protocol in this work cycled the electrodes in KCl between potentials that purposefully created bubbles of O_2 and H_2 which could chemically react with and/or physically dislodge any impurities coating the electrode surface. To establish this milder cleaning process, the potential window was initially set between -1.8 V and +2.5 V and the current was capped at 10 µA to limit the current magnitude to 100 µA. Figure 4.12 shows a typical CV response observed during three cleaning cycles using this protocol.

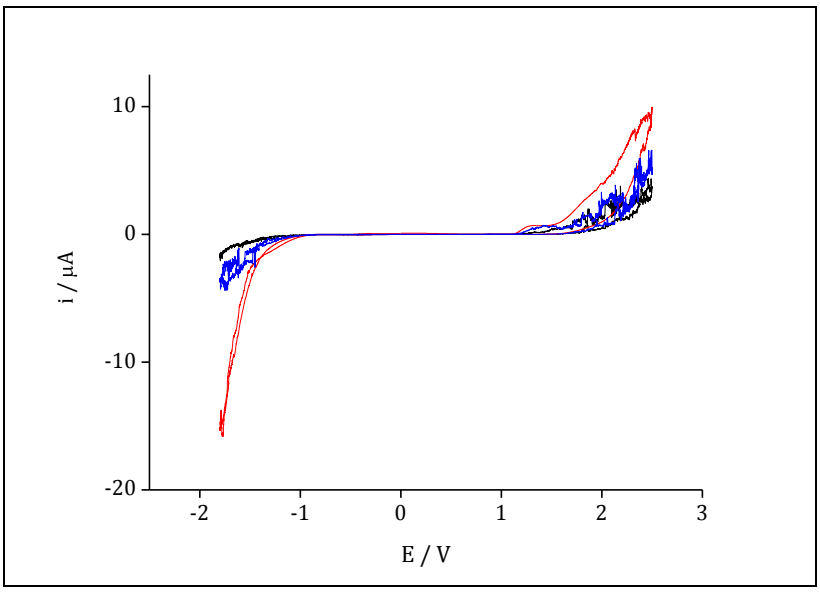

Figure 4.12: Cyclic voltammogram showing three cleaning cycles of a S50µ Pt electrode in KCl (0.1 M) at 100 mVs^{-1} between 2.5 V and -1.8 V. In this and subsequent figures, black is cycle 1, red is cycle 2 and blue is cycle 3.

Rather than showing smooth limiting currents of oxygen and hydrogen evolution at the oxidising and reducing ends respectively, the CVs show progressive spikes in the current. Such spikes are characteristic of bubbling on the surface of the electrode and can be attributed to growth of bubbles trapped on the electrode surface with time. These trapped bubbles would cause a progressive decrease in the total electrode area and hence a reduction in the current as the bubble grew. When the bubble becomes dislodged, the electrical connection is re-established causing a sharp increase in current again (a spike). This happens successively as bubbles are formed at the electrode surface. Figure 4.13 presents photographic evidence of such a large bubble becoming trapped on the surface of an electrode during cleaning.

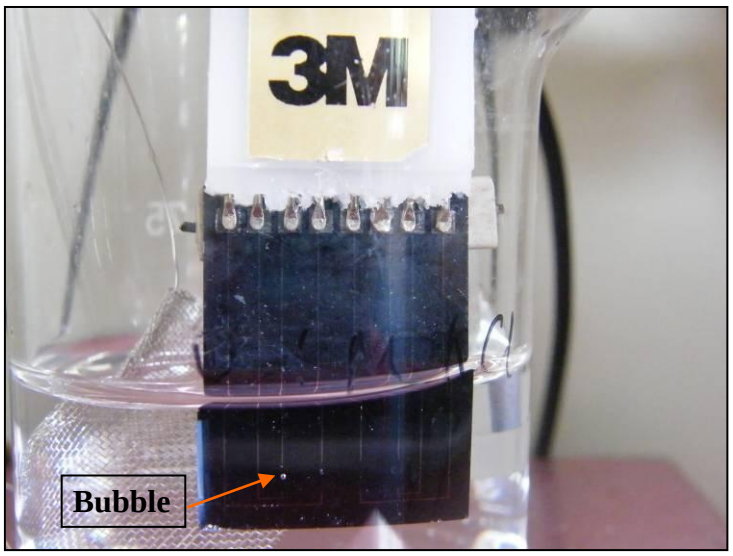

Figure 4.13: Photograph of a visible bubble which formed over the electrode during cyclic cleaning in KCl (0.1 M).

In the extreme case, a bubble can become permanently trapped on the surface, as shown in figure 4.14 in which case the current signal is lost completely.

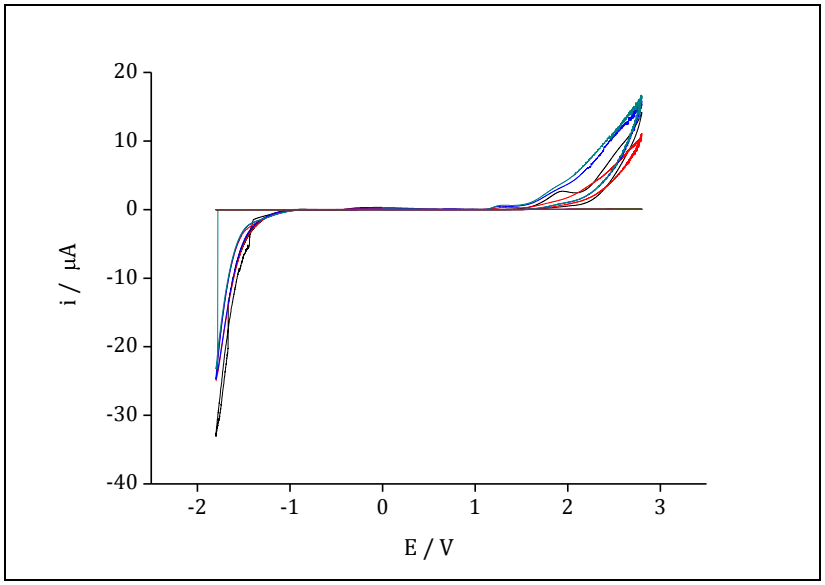

Figure 4.14: Cyclic voltammogram showing scans 1 to 10 of the cleaning cycling on a S50µ Pt electrode in KCl (0.1 M) at 100 mVs^{-1}, where pink is cycle 4 and green is cycle 5.

In this case the current signal was lost after five scans (green line), represented by a sudden sharp decrease to zero at a potential near -1.8 V. This loss of signal was observed in other experiments performed with this cleaning protocol. As expected, tapping of the beaker, to remove these bubbles, restored the current. Bubbling effects were detected in most experiments both visually on the chip

itself and graphically by irregular spiked peak shapes at the oxidising and reducing potentials.

Figure 4.15 shows the optical images of the same electrode before and after cleaning using this cleaning method.

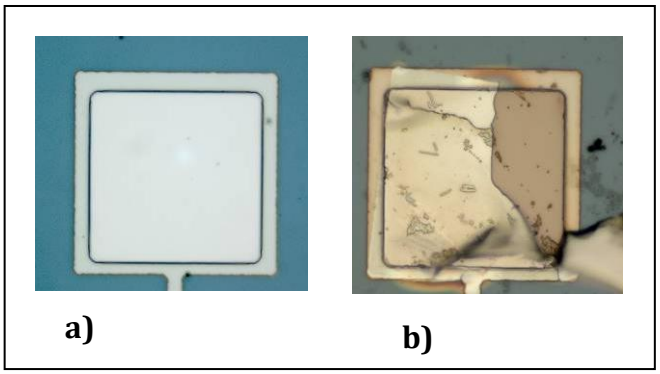

Figure 4.15: Optical images of a S50µ electrode **a)** before cleaning and **b)** after the cleaning in aqueous KCl, using a potential window between +2.5 V and – 1.8 V and a maximum current of 100 µA.

The optical images revealed major problems following this KCl cleaning process, in that most of the electrodes cleaned in the manner described above were cracked after experimentation. In fact, although the current range was manually capped at 100 µA this is still a relatively large current density (4 A cm^{-2}). This allowed very large amounts of gas bubble formation at both the oxidizing and reducing potentials. During cycling many surface layers of the deposited platinum would also be converted into platinum oxide and then back to platinum. Both of these effects could induce stress in the films, which may explain this cracking.

In order to avoid cracking whilst maximising cleaning, the amount of electrochemical reaction was limited by reducing the potential window from +1.20 V to -0.80 V and the current range was limited to a magnitude at 100 nA (4 mA cm^{-2}) to ensure smaller current densities. Figure 4.16 shows the cyclic voltammogram obtained for five cycles in KCl using this modified protocol.

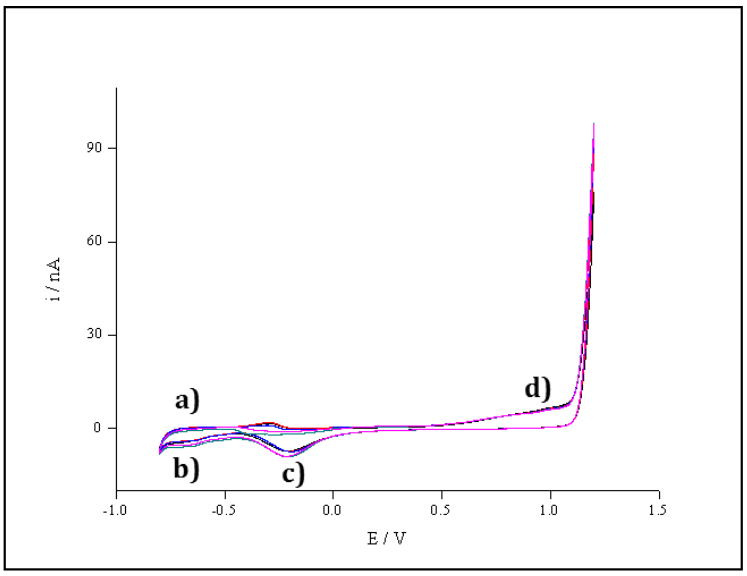

Figure 4.16: Cyclic voltammogram showing a 0.1 M KCl solution cleaning cycle of a (50 μm)^2 electrode at 100 mVs^{-1} with a potential range between +1.2 V and -0.8 V wrt SCE and a current is limit of 100 nA. Peak a) corresponds to H_2 gas oxidation, b) to adsorbed H_2, c) is platinum oxide reduction, and d) corresponds to O_2 adsorption and platinum oxide formation.

The CV in figure 4.16 shows a profile characteristic of clean platinum. The distinctive peaks at around -0.7 V labeled b) and a) on the graph are adsorbed Hydrogen gas evolution and re-oxidation hydrogen respectively. The oxidation peak at about -0.2 V labeled c) is distinctive of platinum oxide reduction[20] and the peak labeled d) at around 1.0 V is indicative of platinum oxide formation due to oxygen adsorption.

Studies, using this modified protocol showed that the parylene stripping problem was markedly reduced and electrode cracking was not observed. Figure 4.17 shows the optical image of the same electrode before and after cleaning in 0.1 M KCl, using this reduced potential window and current range.

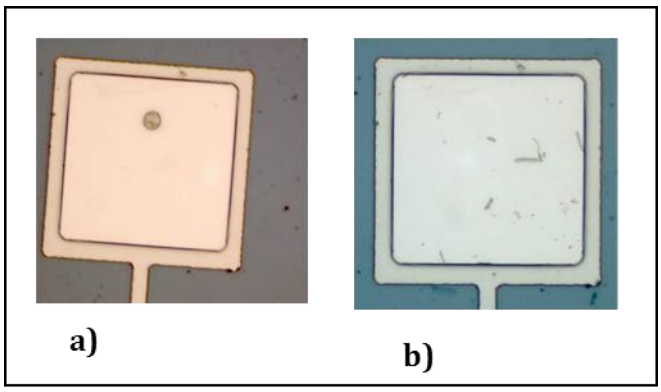

Figure 4.17: Optical images of the same electrode a) before and b) after cleaning in 0.1 M KCl, using the milder protocol shown in Fig. 4.16. It should be noted that the pink/purple colour observed in figure 4.17a) is due to a photoresist layer which has been spun deposited onto the electrode surface after fabrication as a protective coat prior to experimentation. The photoresist is removed by soaking the electrode in acetone for several minutes before electrochemical cleaning. This optical microscope image was taken before this process and so the photoresist is still coating the electrode.

Figure 4.17 a) is an image of a typical $(50\ \mu m)^2$ single electrode prior to removal of the photoresist layer and experimentation. This particular electrode appears to have a small impurity on the electrode surface. 4.17 b) shows that neither cracking of the electrode nor stripping of the parylene from the edges of the electrode is observed during this cleaning process. It also shows that the unknown impurity observed on the electrode surface in figure 4.17 a) was effectively removed during cleaning.

At this stage an interesting observation should also be made, which occurred on most of the electrodes analysed. This is the appearance of 'worm-like' fragments which were often seen on the active electrode surface and which covered many areas of the chip after experimentation. It is postulated that these fragments may be strips of parylene which have become detached from the exposed parylene edges, either during cleaning or perhaps during dicing of the silicon substrate. Further research into this effect was beyond the scope of this thesis, however problems with parylene lifting and stripping, when using it as an insulator for other electrode systems are discussed in Chapter 5 of this thesis.

Once the electrochemical cleaning protocol was optimised, it was found that electrochemical impedance spectroscopy (EIS) provided a very sensitive technique for determining the cleanliness of the Platinum electrode

surface by analysis of the charge transfer resistance. Figure 4.18 shows a typical impedance plot obtained from a platinum microsquare in aqueous ferricyanide solution after an intial 0.1 M KCl cleaning of 8 cycles and then again after a further 8 cycles.

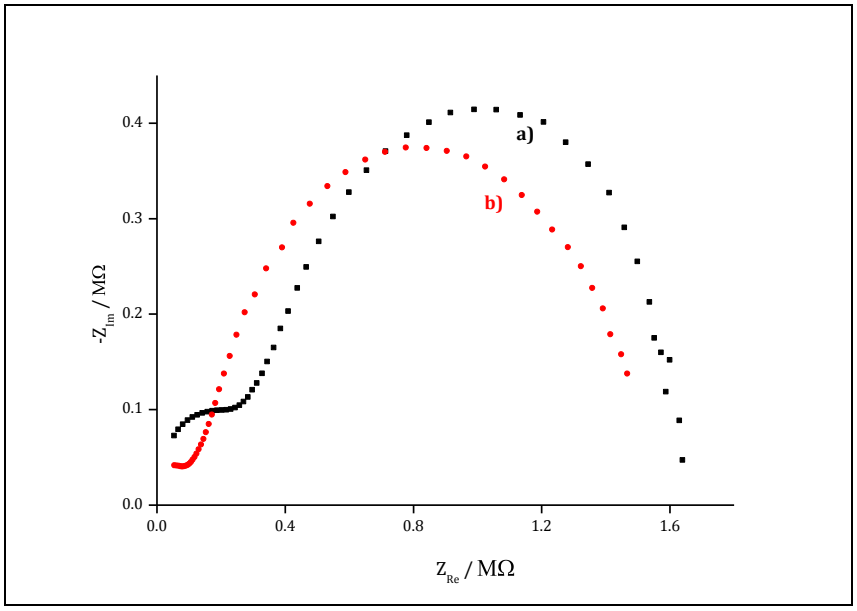

Figure 4.18: Nyquist plot of a 1:1 aqueous solution of 5 mM ferricyanide, 5 mM ferrocyanide with 0.1 M KCl background electrolyte on a 50 µm Pt electrode at a dc potential of 0.190 V and an ac perturbing potential between the frequencies 1000 Hz – 0.1 Hz. graph **a)** shows the EIS data obtained after cleaning the electrode 8 times in 0.1 KCl (black dots). Graph **b)** shows the EIS data obtained after cycling the same electrode a further 8 times in 0.1M KCl (red dots).

In chapter 2.6.1, it was discussed how EIS responses of microdiscs can be closely approximated to the modified Randles' circuit, (Figure 2.13)[21-23]. As described in chapter 2.6.3 and mathematically in further detail in appendix A1, if Nyquist plots are obtained at different dc potentials (E_{dc}), a range of values for the charge transfer resistance (R_{CT}), can be obtained by fitting this equivalent circuit to the data. A plot of R_{CT} vs E_{dc} yields a parabolic curve where the minimum resistance (bottom of the bowl) represents the standard potenital. Since the electron charge transfer can only be thermodynamically (concentration) or kinetically controlled, these curves should fit to to either the thermodynamic (eqn 2.39) or kinetic (eqn. 2.41) expressions derived. As also discused in detail in section 2.6.3, for very facile reactions such as the one-electron transfer reduction of ferricyanide to ferroccyanide, the charge transfer resistance is very small and the reaction is expected to be dominated by thermodynamics.

Figure 4.19 shows a plot of R_{CT} vs E_{dc} obtained from fitting the modified Randle's circuit to the high frequency EIS data values obtained at different dc potetnials after the first eight (Fig 4.18 a) 0.1 M KCl cleaning cycles.

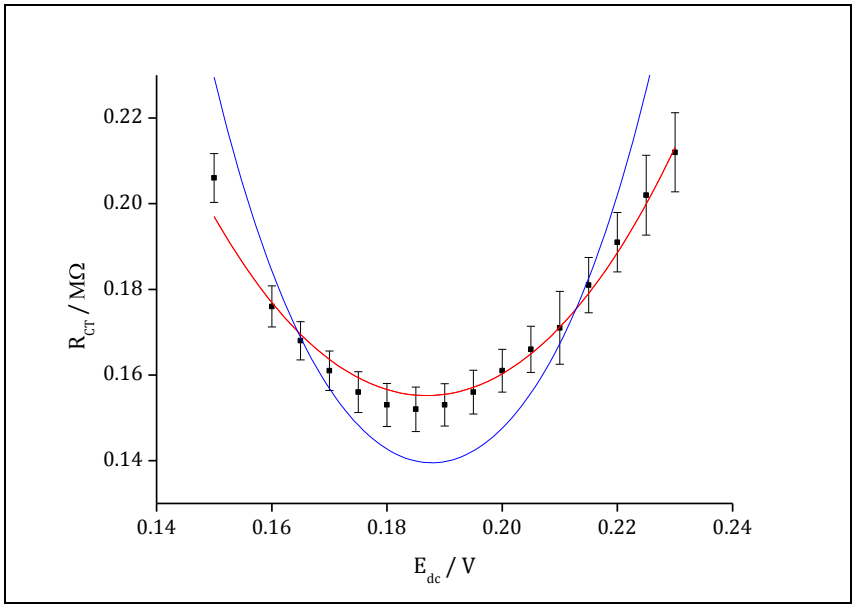

Figure 4.19: Plot of R_{CT} vs. E_{dc} found by fitting the EIS data obtained after initially cleaning the electrode in KCl for 8 cycles (Fig. 4.18 a)). The red line is the fit to the kinetic expression (eqn. 2.39) which gives a correlation coefficient of 0.989 and a value of 155.6 ± 2.16 kΩ for R_{CT}^{min}, a standard potential of 0.183 ± 0.008 V and an electrochemical transfer coefficient α_{Ox} of 0.5 ± 0.7. The blue line is the fit to the thermodynamic expression (eqn. 2.41) with a correlation coefficient of 0.553, and R_{CT}^{min} value of 139 ± 3 kΩ giving a standard potential of 0.188 ± 0.001 V.

It is clear from Figure 4.19 that the kinetic expression fits most accurately to the EIS data obtained after only eight cleaning cycles. The reaction rate, k^{Θ} calculated (eqn. 2.22) for the kinetic data above was 6.732×10^{-5} cm s^{-1} which is extremely slow in comparison to other values measured on clean platinum surfaces. From the literature k^{Θ} values of around 0.12–0.18 cm s^{-1} might be expected[22,24,25]. These results suggest that the impedance response shows kinetic limitation due to impurities on the surface of the electrode. The electrode was therefore then cleaned again a further eight times. As displayed in figure 4.18 b), the initial charge transfer semicircle then became much smaller. The graph below shows a plot of R_{CT} vs. E_{dc} obtained from fitting the modified Randles' circuit to the EIS plot obtained at different dc potentials after this second set of cleaning cycles.

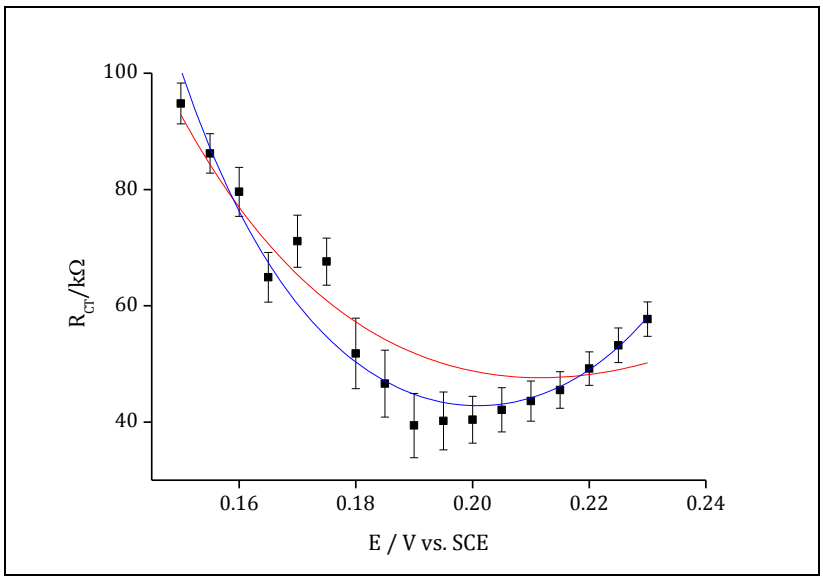

Figure 4.20: Plot of R_{CT} vs. E_{dc} found by fitting the EIS data obtained after a second set of cleaning in KCl for a further 8 cycles (4.18 b)). The red line is the fit to the kinetic (eqn. 2.39) which gives a correlation coefficient of 0.935 and a value of 50 ± 14 kΩ for R_{CT}^{min}, a standard potential of 0.195 ± 0.046 V and an electrochemical transfer coefficient α_{Ox} of 0.7 ± 0.4. The blue line is the fit to the thermodynamic expression (eqn. 2.41) which gives a correlation coefficient of 0.964, an R_{CT}^{min} value of 42.8 ± 0.9 kΩ and a standard potential of 0.195 ± 0.001 V.

As the charge transfer semicircle was much smaller after the second set of cleaning cycles, it became more difficult to use the modified Randles circuit to obtain accurate R_{CT} values, as reflected in the error bars. Never-the-less, reasonable values were obtained and both kinetic and thermodynamic models were again fitted to the data.

Although the correlation coefficient recorded for the kinetic fit was 0.935. It is clear that the kinetic curve does not follow the data points accurately and indeed most of the data do not lie on the curve within experimental error. The thermodynamic expression fits most accurately to the EIS data obtained after a second set of cleaning cycles. This suggests that upon further cleaning, the surface impurities have been removed and that the very small (almost non-existent) initial semicircle now observed is not kinetically limited. It should be noted that the resistance calculated after the second cleaning cycle is an order of magnitude smaller than after the initial cleaning, another indication that there were indeed resistive impurities hindering the charge transfer of ferricyanide on platinum. Although the response is modeled using the thermodynamic expression, a lower limit of k^{Θ} can be estimated by

inserting the minimum value of $R_{CT,e}$ into equation 2.38. Using this method a lower limit k^{θ} value of 0.049 cm s^{-1} was determined, further indicating that it is hard to measure kinetics using these microelectrodes.

For the experiments undertaken in this work on clean platinum, the kinetics were too fast to be observed and instead what one observes in this case, is a shunting of the first part of the $R_{CT,e}$ rail by C_{DL} at high frequency (Chapter 2.6.3). This corresponds to a charge transfer resistance, R_{CT}, controlled by thermodynamics. The charge transfer is so rapid that in a thin layer of solution, *L*, at the electrode surface, the Nernstian relationship between the concentrations of ferri/ferrocyanide and the applied potential applies even at these high frequencies. Since in the reversible case, at high frequencies:

$$R_{CT,e}^{min} = \frac{4RTL}{ADF^2c} \qquad \textbf{Eqn. 4.4}$$

one can obtain an estimate for *L* of around 650 nm. This can be considered to be the thickness of the solution at the electrode surface where rapid thermodynamically-controlled charge transfer occurs and Nernstian equilibrium is established (see appendix 10.1). Given that at these high frequencies this layer thickness is small compared to the electrode dimensions, planar diffusion will be occurring, and A should simply be the area of the microsquare electrode.

These results were invaluable in showing that the modified 0.1 M KCl cleaning protocol was able to produce clean platinum surfaces and that the EIS data is a very sensitive technique for determining the cleanliness by the size and potential dependence of R_{CT}. The standard potential in the aqueous ferri/ferrocyanide solution, by fitting to the R_{CT} semicircle, was +0.195 V. This is within 3 mV of the value calculated from the literature (section 2.2) which further supports the validity of this fitting. The fundamentals of the EIS response of the microelectrode will be discussed in more detail in section 4.3.5, where it will be used to describe the diffusion processes occurring with time.

For this study, the 0.1 M KCl cleaning protocol was therefore found to be sufficient to clean the electrode surface without hindering the electrode function, reducing the insulating properties of parylene or exposing unwanted areas of platinum. It was therefore used for the remainder of the research on the platinum microsquares and provided the opportunity for systematic study of these electrodes.

4.3.3. Micro-Square Redox Electrochemistry

Figure 4.21 shows a typical clean microsquare experimental cyclic voltammogram (CV) in 10 mM potassium ferricyanide for the 1-electron reduction of potassium ferricyanide at a sweep rate of 5 mVs^{-1}. The potential was again swept between +0.35 V and 0.00 V, (as described in section 3.4.1)

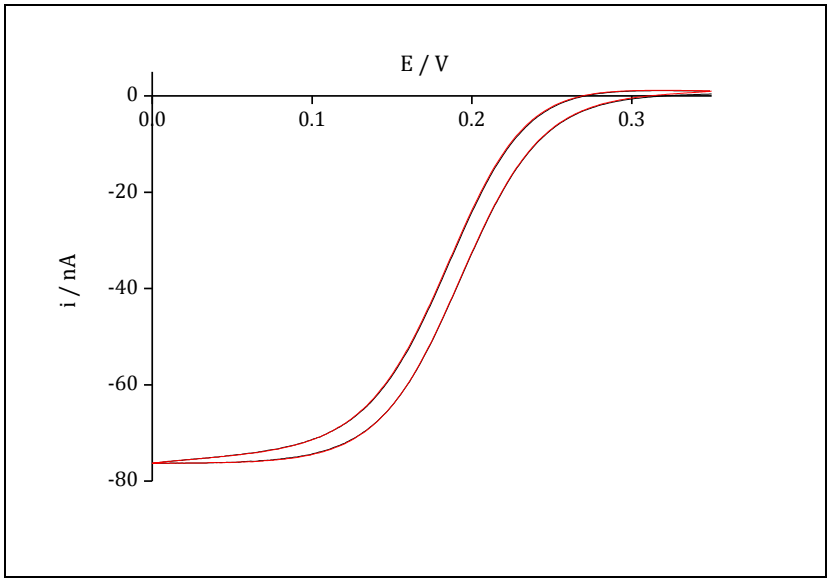

Figure 4.21: Graph to show a typical cyclic voltammogram obtained at a sweep rate of 5 mVs^{-1} of an S50µ Pt electrode in ferricyanide (10 mM) and KCl (0.1M) background electrolyte. The potential was swept between +0.35 V to 0.00 V wrt SCE.

As previously seen for microdiscs[21] and microsquares[6,26], a sigmoidal wave is observed, characteristic of a steady-state voltammetric response. Unlike the CVs obtained after acid cleaning and in an equimolar solution of potassium ferri/ferrocyanide (figure 4.10), the CV does not slope and flat experimental limiting currents are observed. Also, as with microdiscs, the mass-transfer corrected Tafel plot (Fig. 4.22) shows good straight lines for both the forward and reverse scans of the CV.

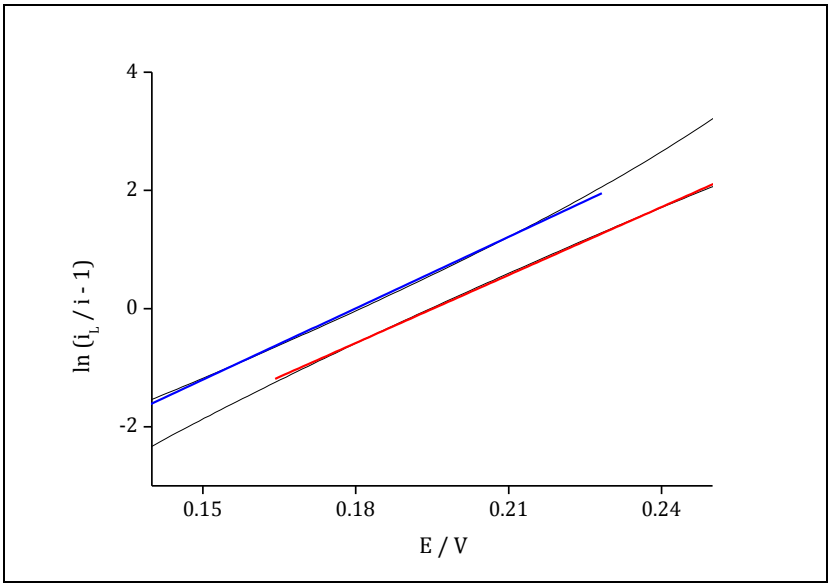

Figure 4.22: Plot showing the corresponding modified Tafel plots generated from Figure 4.18. The linear fits to the reducing (blue) and oxidising (red) data are shown. These give gradients of 40 and 38 V^{-1} respectively, in good agreement with the theoretical value of 40 V^{-1} for a fully reversible one electron reaction at 293K.

The Tafel plot fits well to theory developed for a microdisc, with gradients of 40 V^{-1} and 38 V^{-1} respectively. These are both in good agreement with the expected value of F/RT = 40 V^{-1} at 293K for a reversible one electron redox reaction at a microdisc, indicating the fabrication of clean Platinum microelectrodes and also suggests that at steady state, a microsquare does indeed have similar Tafel characteristics to a microdisc. This also suggests that 10 mM ferricyanide alone does not suffer from product formation.

The mass transport limiting current was measured experimentally on numerous microsquare electrodes. During early work, there was a large scatter in limiting current densities due to variation in electrode surface area. However, after the establishment of the reliable 0.1 M KCl cleaning protocol (section 4.3.2), there was much less variation in the current densities observed. An average value of 77.6 nA was obtained from these seven electrodes, with a standard deviation of approximately 1nA.

There are two frequently used theoretical expressions for calculating the limiting currents of planar microsquare electrodes. One theory assumes

the square can be treated like a microdisc in that the same expression (eqn. 3.6) may be used but with, the disc radius, *r*, replaced by *l*/2, where *l* is the length of the square side to give[6]:

$$i_L = 4nFDc\frac{l}{2} \qquad \textbf{Eqn. 4.5}$$

This expression yields a limiting current of 66.8 nA, and is 14% below that obtained experimentally.

An alternative theory which has been postulated, which is to assume that the microsquare behaves like a microdisc of equivalent area[5]. Since the square area is l^2 and the disc area is πr^2, this gives $r = \frac{l}{\sqrt{\pi}}$ and hence

$$i_L = 4nFDc\frac{l}{\sqrt{\pi}} \qquad \textbf{Eqn. 4.6}$$

This expression yields a limiting current value of 76.0 nA which is still 2% lower than the average experimental value. This data shows that the current densities of these microsquare electrodes appear consistently larger than those calculated by the microsquare limiting-current theoretical expressions outlined in the literature[5-7]. However it needs to be established whether this difference is significant.

4.3.4. FEM simulation of microsquare limiting currents

FEM models of the electrolyte flux and concentration gradients at the electrode surface have been developed in order to compare simulated currents to the responses observed experimentally. As outlined in section 3.7, microdisc simulations were also carried out in order to verify the model being used. Figure 4.23 a) shows the adapted microsquare mesh at the most dense refinement, typically produced after seven or eight computational steps, and figure 4.23 b), shows the corresponding adapted mesh for a microdisc.

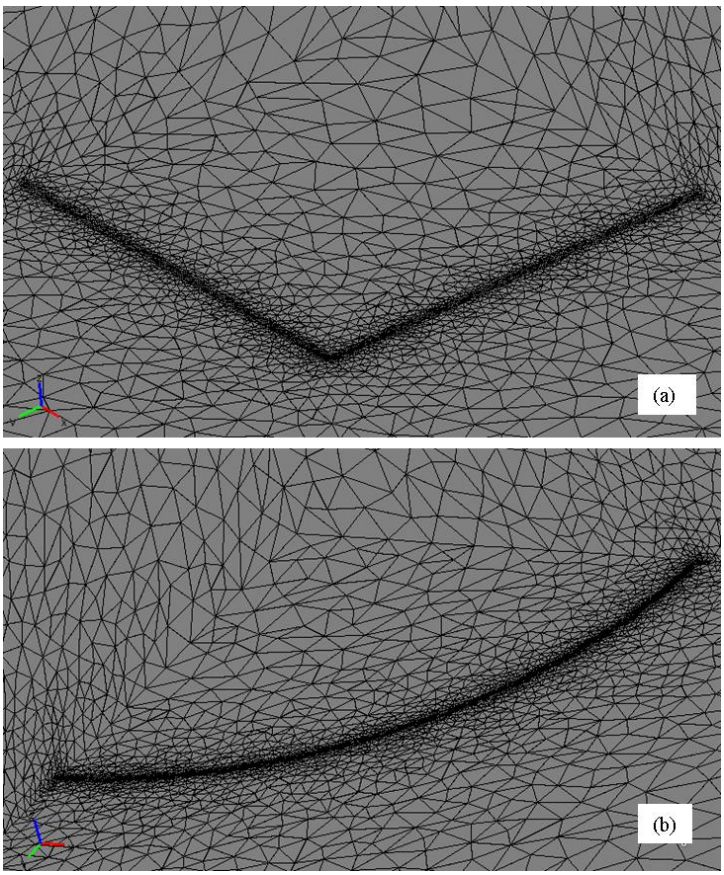

Figure 4.23: The finite element mesh generated for and a) a quarter microsquare electrode simulation at a mesh density corresponding to 461779 degrees of freedom (dof) shown with a vertical electrode x, y-plane orientation and b) a quarter microdisc electrode simulation with a mesh density corresponding to 512576 dof shown with a horizontal electrode x,y plane orientation

The markedly increased mesh density at the electrode edge can clearly be seen in each case. This is consistent with the expectation of steep concentration gradients and thus a large contribution of the edge current density to the overall limiting current.

Figure 4.24 a) and b) show the corresponding calculated steady-state diffusive flux profiles obtained with the high mesh density shown above for square and disc electrodes respectively.

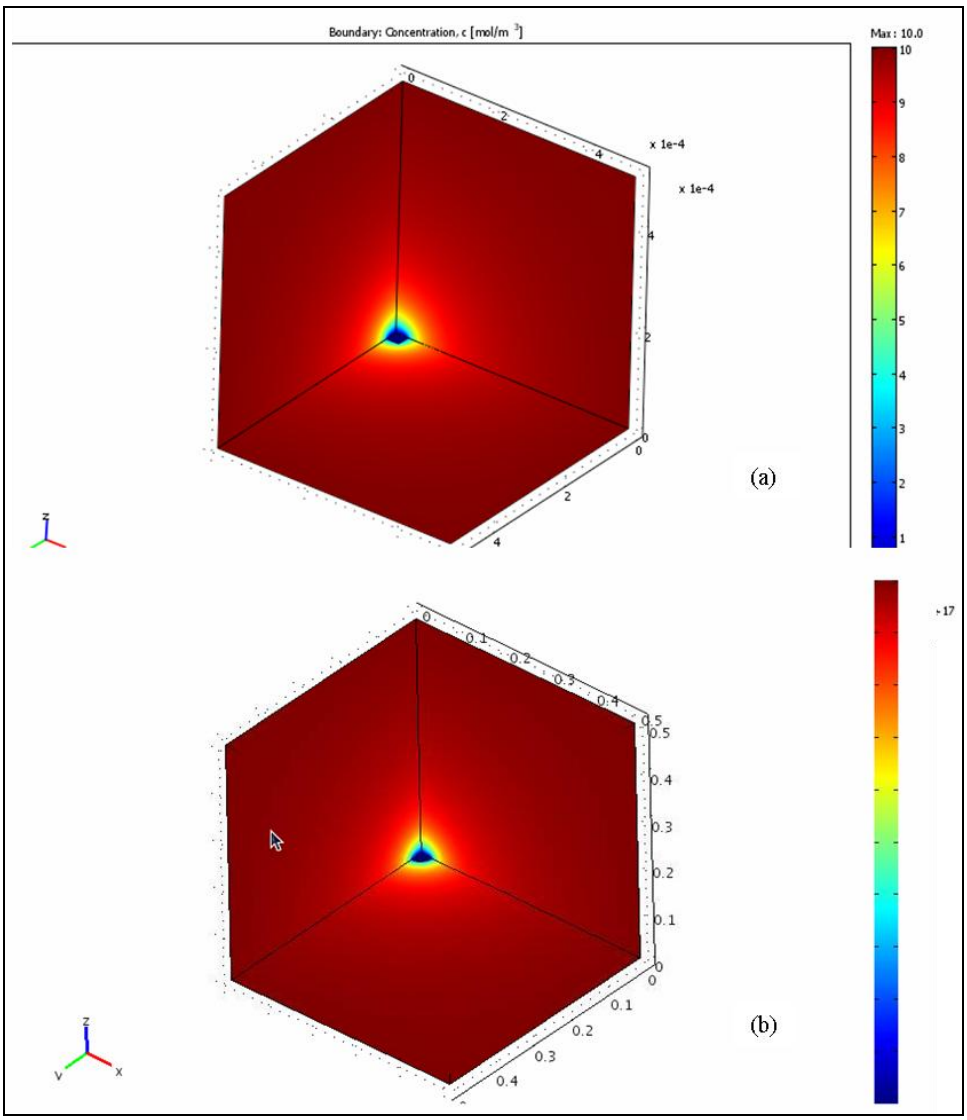

Figure 4.24: Typical steady-state concentration profiles for (a) microsquare and (b) microdisc electrodes. The concentration of ferricyanide is shown in roygb format, with red corresponding to 10mM (bulk) concentration and blue to 0mM. The increasing depletion of ferricyanide can be clearly observed upon approaching the electrode surface.

It is clear from these data that in each case the diffusion layer is similarly hemispherical for both the microdisc and microsquare and that the diffusion fields do not extend to the box edge, confirming that the space domain is sufficiently large to ensure accurate simulation.

Figure 4.25 below shows an overview of the limiting currents obtained for these simulations results. The red scattered plot and red line represent the simulated and theoretically calculated limiting current of a disc respectively. As shown in section 3.7, the simulated limiting currents of a microdisc correspond well to the analytical values obtained using eqn. 3.5,

which is known to accurately represent microdisc limiting currents. This gives confidence in the COMSOL modeling approach. The black scattered plot represents the simulated current values obtained from the FEM model of a S50μ microsquare electrode at increasing mesh densitites.

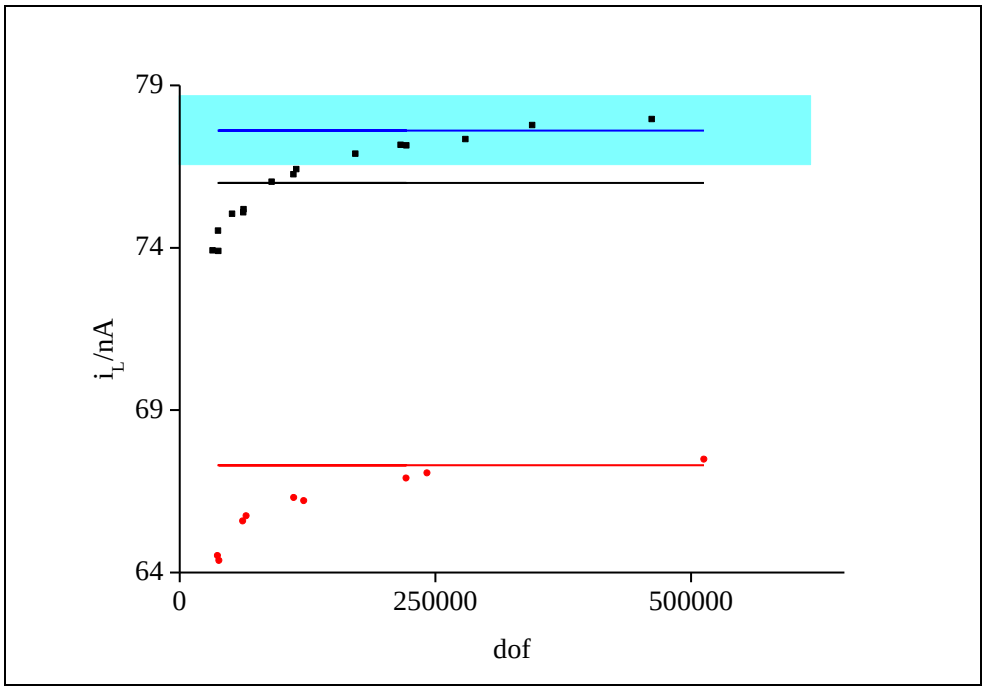

Figure 4.25: Plot of COMSOL calculated limiting currents for simulated microdisc (r =25.0 μm, red spots) and microsquare (l = 50.0 μm, black squares) at increasing degrees of freedom (dof). Also shown is the theoretical microdisc limiting current obtained using Eqn. 3.7.1 (red line). This is also the theoretical limiting current calculated for the microsquare from eqn. 4.1 when using $r = l/2$, whilst that using $r = l/\pi^{1/2}$ (eqn. 4.2) is shown as a black line. The blue line shows the average experimental current obtained for 7 microsquares, along with the standard deviation for these measurements (shaded blue box).

The average experimental mass transport limiting current and standard deviation of these measurements is shown as a blue line and shaded box respectively in Fig. 4.25. These data are seen to correspond well and are the same, within experimental error, to the simulated value obtained for microsquares at higher degrees of freedom.

The red line also represents the estimated limiting current of a microsquare if it is assumed to behave like a disc of the same equivalent radius (66.8 nA). These data clearly show that this value is systematically below both experimental and simulated microsquare values.

The black line represents the limiting current value calculated when assuming a microsquare behaves like a disc of the same equivalent area (Eqn. 4.6). This value although a much better estimate is also below both the mean experimental and simulated microsquare limiting current values. Therefore both theories underestimate the limiting currents of these microsquare electrodes, suggesting a more accurate expression is required to be developed.

Although the FEM simulations were able to accuratly predict the experimental limiting currents within experimental error, it is not able to provide the answer as to whether this deviation of microsquare limiting current response from the microdisc response is simply due to a difference in effective microelectrode area, as the previous treatments have assumed, or whether there is a fundamental difference between the microsquare and microdisc electrode response. To address this question, section 4.3.5 uses EIS to look at the electrode response as it evolves with time.

4.3.5. Electrochemical Impedance Spectroscopy (EIS)

The question still remains as to whether there is a fundamental difference between the evolution of microsquare and microdisc diffusion layers with time (and hence diffusion layer thickness). EIS is a valuable method for probing this, as it measures electrode response as a function of frequency, which is inversely related to time and therefore diffusion layer thickness.

Figure 4.26 shows the typical EIS profile produced after an appropriate number of cleaning cycles (as in Fig, 4.18). It is reassuring that the charge transfer semicircle is extremely small on this scale, consistent with reversible electron transfer. The EIS response is therefore dominated by the double layer capacitance, the Warburg impedance and the non linear resistance. The modified Randles' circuit (Figure 2.11) has been established as fitting accurately to a microdisc response (section 2.5). Figure 4.26 shows the fitting of this modified Randles' circuit to the high frequencies ($1x10^3$ Hz to 11.5 Hz), low frequencies (0.17 Hz to 0.01 Hz) and across the entire

frequency range.

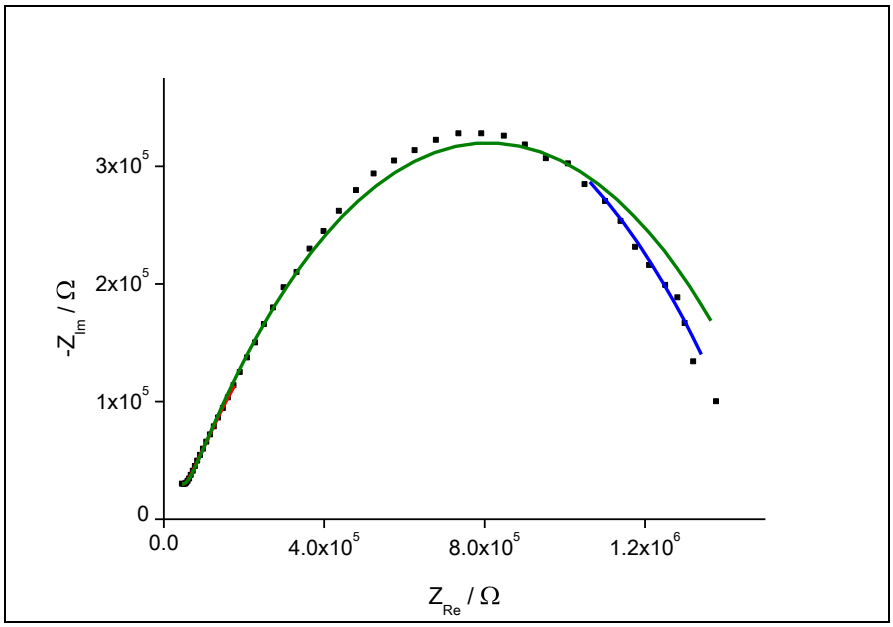

Figure 4.26: A typical Nyquist plot of the EIS response of a Platinum microsquare (l = 50.0 μm) in aqueous ferricyanide solution [10 mM] and KCl [0.1 M] background electrolyte. The spectrum was measured at a dc potential, Edc of + 0.19 V, ac amplitude 1 mV rms and frequency range 1000 Hz (low Z_{Re}) to 0.01 Hz (high Z_{Re}). Fits using the modified Randle's circuit (Figure 2.13) are shown to the high frequency data (red line), the low frequency data (blue line) and all data (green line).

It is clear that the modified Randles' equivalent circuit, developed for fitting microdisc EIS responses[22] fits well to the very high frequency plots (red line), which suggests that over these very fast time scales, linear diffusion is occurring similarly to a microdisc. In fact in this region, linear diffusional regimes would be expected for electrodes of any shape. The equivalent circuit also fits very well to the low frequency data, which suggests that at least at steady state, radial diffusion is likely established. This also supports the Tafel analysis (Fig. 4.22). However, it is clear that it is not possible to fit the entire frequency range accurately using this circuit. It is at medium frequencies, then in the portion of the Nyquist plot that cannot be fitted, when deviation from microdisc diffusion must occur.

The uncompensated resistance (R_U), the double layer capacitance (C_{DL}) and the Warburg impedance (Y_0) have been determined from the high frequency ($1x10^3$ Hz to 11.5 Hz) fit. The average uncompensated resistance

recorded for a range of data is 115 ± 6 kΩ, which corresponds to a value of 3 Ωcm^{-2}. The average double layer capacitance recorded is 1.1 ± 0.2 nF which corresponds to a value of 44 μFcm^{-1}. These are both reasonable for an electrode of this size.

As discussed in 2.6.3, values of the Warburg coefficient, σ and hence the corresponding Warburg parameter, $1/Y_0$ as a function of dc potential, E_{dc}, should yield a plot which fits to the thermodynamic expression given in equation 2.44. Figure 4.27 shows the variation of $1/Y_0$ as a function of E_{dc}.

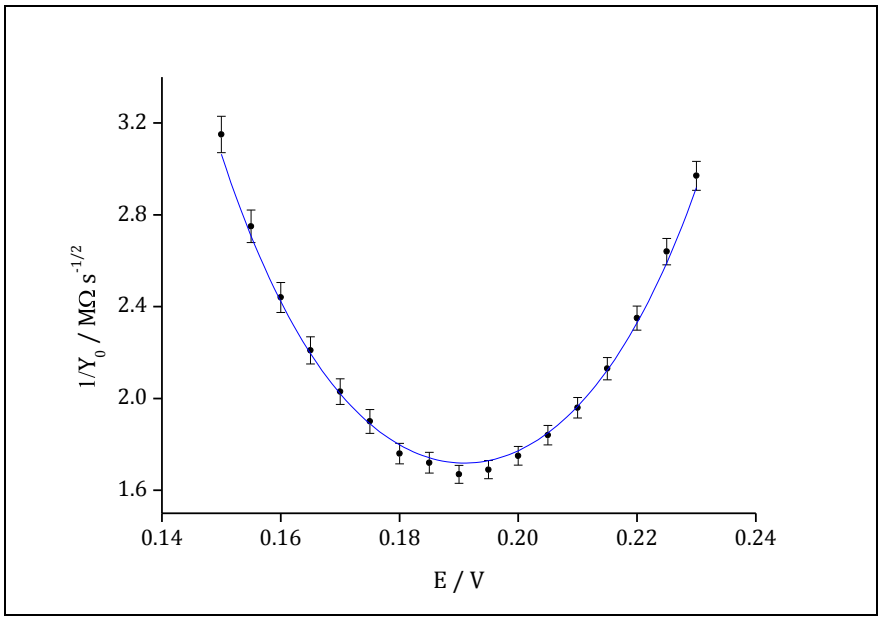

Figure 4.27: Plot of the non-linear resistance, σ obtained from EIS fits at low frequency, against dc potential, E_{dc}. The blue line shows the fit to thermodynamic expression (Eqn. 2.44) with a correlation coefficient of 0.989, a minimum Warburg parameter ($1/Y_0^{min}$) of 1.723 ± 0.007 MΩ $s^{-1/2}$ and a standard potential of 0.1914 ± 0.0002 V.

As expected the thermodynamic expression given by equation 2.44 fits with good aggreement and within experimental error, to the Warburg parameter data obtained from high frequency fits to the Nyquist plots obtained for this electrode at different dc potentials. The average $1/Y_0^{min}$ value obtained over a range of experiments is 1.5 ± 0.1 MΩ $s^{-1/2}$.

To further validate the fitting of these curves, σ^{min} values can be calculated theoretically using the expression[27]:

$$\sigma^{min} = \frac{\mathbf{R}T}{n^2\mathbf{F}^2A\sqrt{2}}\left(\frac{2}{D_O^{1/2}c^{\infty}} + \frac{2}{D_R^{1/2}c^{\infty}}\right) \qquad \textbf{Eqn. 4.7}$$

where D_O is 6.98x10^{-6} cm^2 s^{-1}, the diffusion coefficient of ferricyanide, D_R is 6.61x10^{-6} cm^2 s^{-1} the diffusion coefficient of ferrocyanide, c^{∞} is 1 x10^{-5} mol cm^3, the bulk concentration and the temperature, T is 298 K. The value calcuated for σ^{min} using Eqn. 4.7 is 1.15x10^6 Ω s$^{-1/2}$. The corresponding $1/Y_0^{min}$ value (Eqn. 2.46) is $2^{1/2}$ x 1.15x10^6 = 1.63x10^6 Ω s$^{-1/2}$ which is the same within experimental error as the value of $1/Y_0^{min}$ recorded experimentally. This shows that a good fit at high frequency is obtained and indicative of planar diffusion in this region.

The variation of R_{NL} as a function of E_{dc} can also be obtained by fitting the modified Randles' circuit to the low frequency (0.17 Hz to 0.01 Hz) data. In order to obtain reasonable fits to the data, the uncompensated resistance, R_U, capacitance, C_{DL}, and the charge transfer resistance, R_{CT} are fixed at the values obtained for the high frequency fit. Figure 4.28 shows a typical graph obtained for values of R_{NL} as a function of E_{dc}.

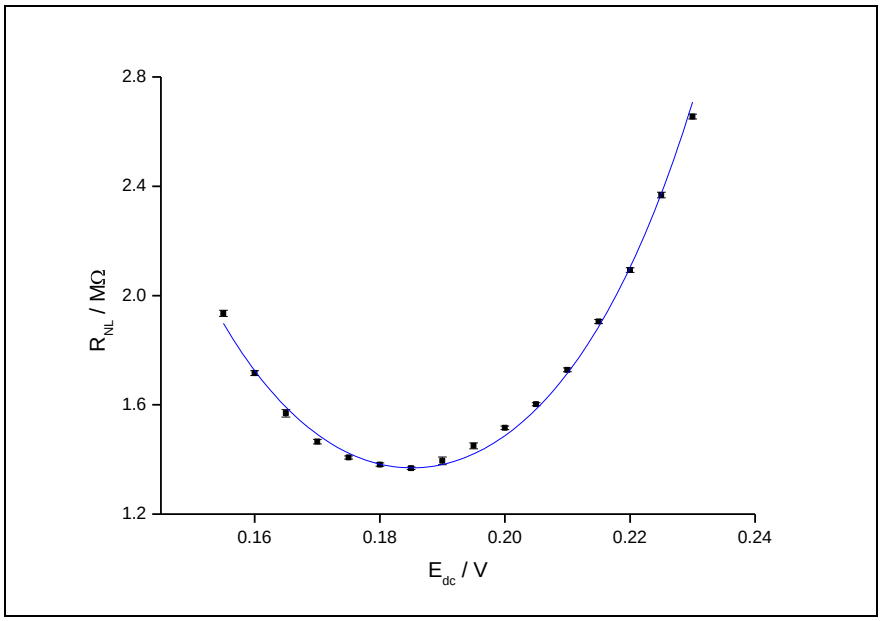

Figure 4.28: Plot of the non-linear resistance, R_{NL} obtained from EIS fits at low frequency, plotted against dc potential, E_{dc}. The blue line is the fit to the thermodynamic expression (eqn. 2.42) which has a correlation coefficient of 0.997, a minimum non-linear resistance, R_{NL}^{min} of (1.377 ± 0.005)x10^6 Ω and standard potential, E^{Θ} of 0.1861 ± 0.0002 V.

Consistent with the theory that R_{NL} should be driven by the thermodynamic processes of the redox ions within the analyte (section 2.6.3) the data fits very well to the theoretical expression given in equation 2.42 for non-linear resistance under thermodynamic control. The good agreement with eqn. 2.42 for the variation of R_{NL} (found at low frequency) with E_{dc} is satisfying and entirely consistent with the observation of reversible modified Tafel behaviour (Figure 4.23), confirming that microsquare electrodes can be used to determine Tafel characteristics. The average value of R_{NL}^{min} for a range of electrodes is (1.373 ± 0.004)x10^6 Ω.

However, the inability to fit EIS data accurately with this equivalent circuit across the whole frequency range for any E_{dc} is telling. If the difference in the EIS response were simply due to a difference in real or effective area, the modified equivalent circuit would fit these data at all frequencies and the systematic deviation seen at medium to low frequencies would not be found. Thus the evolution of the electrode response with time (or frequency) for a microsquare can be seen to be different to a microdisc.

In particular, the decrease in the value of the experimental non-linear resistance at low frequency (obtained from the intercept of the blue line in Figure 4.28 with the Z_{re} axis) compared to that obtained from the fits to microdisc theory across all frequencies (obtained from the low frequency intercept of green line in Figure 4.28 with the Z_{re} axis) is indicative of a greater steady-state current for a microsquare over a microdisc of a similar size given that R_{NL} is inversely proportional to to i_L (appendix A3) this also confirms the experimental observation in Fig. 4.25.

4.3.6. FEM Simulations for Microsquares of Different Sizes

All of the results described in section 4.3.5 were obtained for one size, S50μ microsquare electrodes. However, it was interesting to know if a similar behaviour would be observed for microsquare electrodes of different sizes. The COMSOL Multiphysics graphics programme was again therefore used to simulate microdiscs and microsquares of different dimensions, in the same

manner as described in Chapeter 3.6. Simulations of discs and squares from 1μm diameter/length to 100 μm diameter/length were performed to monitor how the limiting current values are affected by the size of the electrode. As described in Chapter 3.7 and 4.3.4, microdisc electrodes have been extensively studied and an analytical fitting expression has been developed which accurately predicts the limiting current of any size microdisc at steady-state. Square electrodes have not been studied as extensively and there exist at present, two possible theoretical fitting expressions for calculating limiting current (eqn 4.5 and 4.6). Both the FEM simulations and experiments in section 4.3.4 show that neither of the expressions accurately predicts, within experimental error, the limiting current, at least for microsquares of 50 μm in length. It is therefore interesting to see if similar behaviour is observed at all microsquare sizes.

Figure 4.29 presents simulated limiting currents for a number of different sized microdiscs and microsquares, and then compares these results with the analytically calculated limiting currents. The values quoted in this figure, represent the diameter and length of the microdiscs and microsquares, respectively.

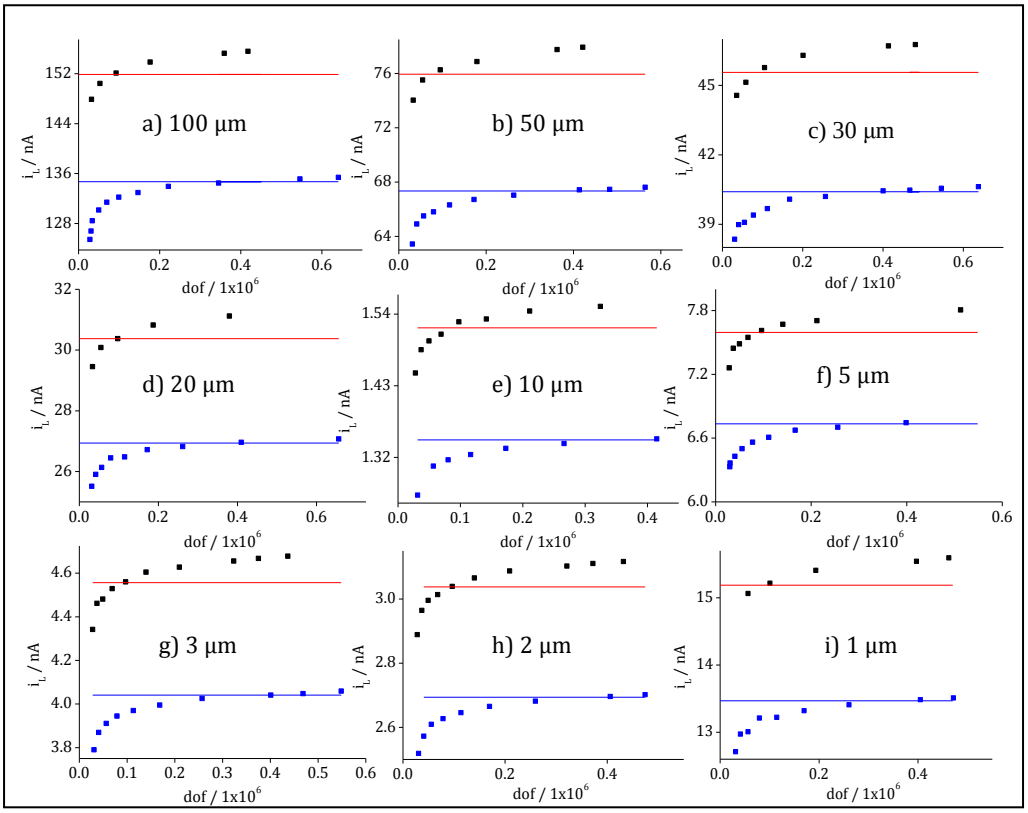

Figure 4.29: Plots of the limiting currents, i_L calculated as the adaptive mesh density increases (increasing dof) for different sized microsquare and micro-disc electrode simulations; **a)** to **i)** show data points for microdisc (blue scattered plot) and microsquare (black scattered plot) of length/diameter shown. The blue line shows the limiting current calculated using the expression $i_L = 4nFDcl/2$ and the red line shows the limiting current calculated using the expression: $i_L = 4nFDc\left(l/\sqrt{\pi}\right)$.

As can be clearly seen from the figure above, no matter what size electrode is simulated, the FEM simulation produces a similar pattern. The final limiting current calculated for the microdisc simulation at the highest degrees of freedom (dof) is the same, within experimental error, as the limiting currents calculated using the microdisc theoretical expression. However the FEM simulated microsquare limiting currents are systematically larger than the limiting currents of the equivalent microdiscs and neither of the postulated analytical expressions are able to accurately predict this current.

Figure 4.30 below shows a concentration slice obtained from a $(30\ \mu m)^2$ electrode (S30µ) steady-state diffusion simulation.

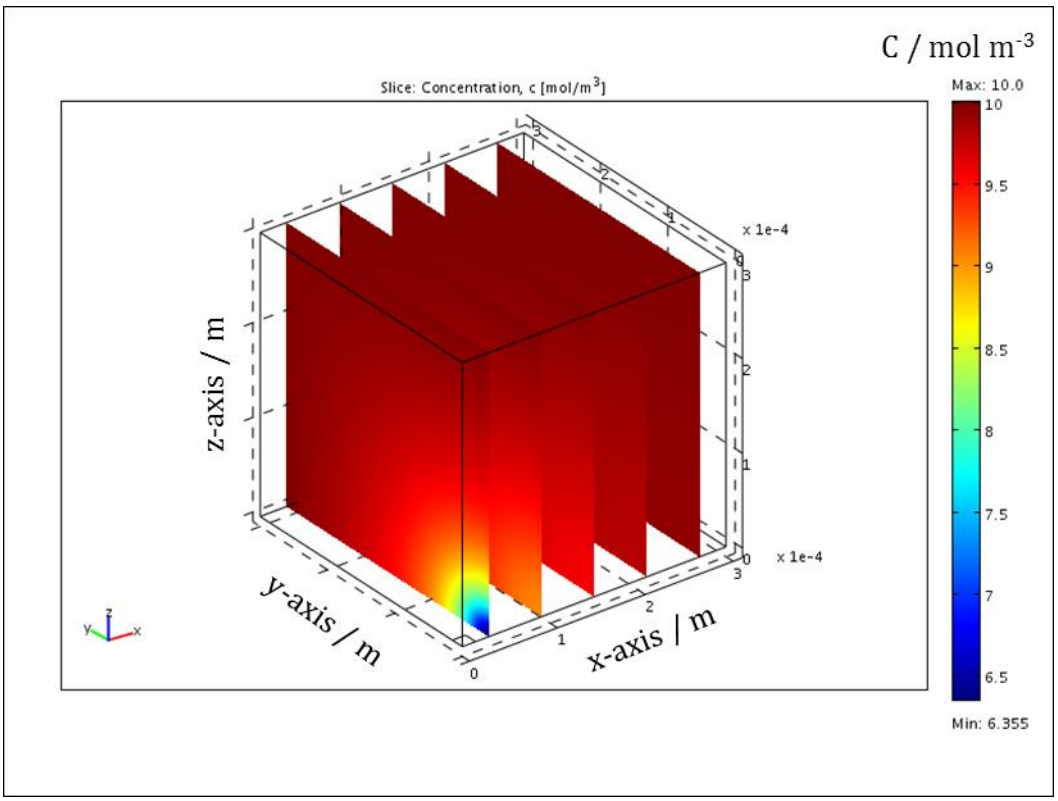

Figure 4.30: COMSOL image showing slices of the concentration gradient as it increases from the 30 μm^2 electrode surface in a 10 mM solution of ferricyanide with a diffusion coefficient of 6.98x10^{-6} cm^{2}s^{-1}.

As with the S50μ electrode this profile again shows hemispherical diffusional growth which again is consistent with similar microelectrode behaviour independent of electrode size.

Figure 4.31 shows the simulated plot of limiting current against microsquare length (black squares) along with the theoretically calculated limiting currents using the mathematical expressions, Eqn. 4.5 (red line) and Eqn. 4.6 (blue line).

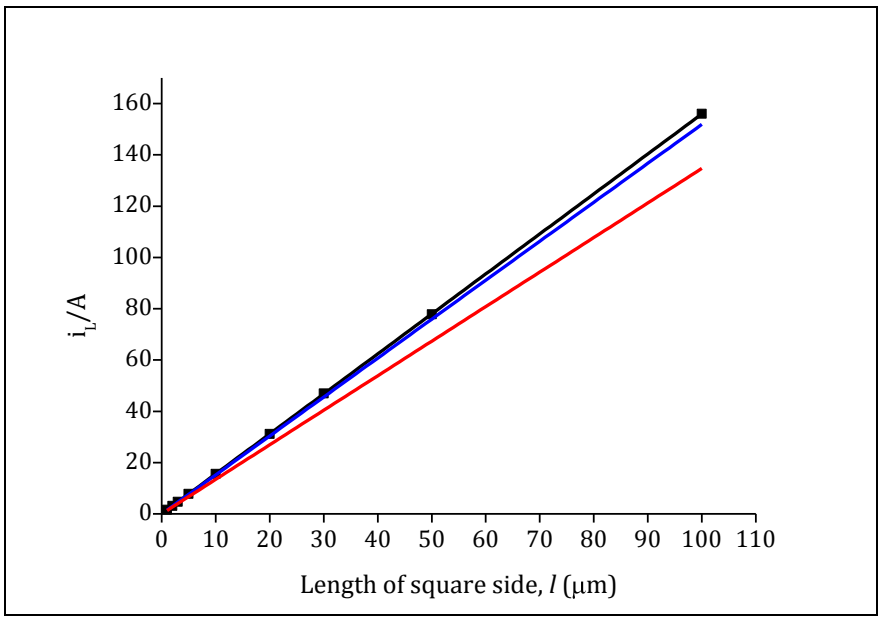

Figure 4.31: Graph to show the analytical limiting current calculated using $i_L = 4nFDcl/2$ (red line, Eqn. 4.5) and $i_L = 4nFDc\left(l/\sqrt{\pi}\right)$ (blue line) in comparison with the FEM simulated response and linear regression (black square/line) for microsquares of increasing square length. It can be clearly seen that the values for each size do not lie on top of one another in this instance. The linear regression of the FEM simulation had a correlation coefficient, r = 1 and a gradient of (1.559 ± 0.001)x10^{-9} A μm^{-1}. The gradient of the analytical Equation 4.5 is 1.346x10^{-9} A μm^{-1} and, the gradient of the analytical Equation 4.6 is 1.519x10^{-9} A μm^{-1}

The gradient of the FEM simulated plot is (1.559 ± 0.001)x10^{-9} A μm^{-1} which is 13.6% greater than that calculated using Equation 4.5 and 2.6 % greater than from that calculated using Equation 4.6. As shown in Case Study 2 (section 3.7), COMSOL Multiphysics was able to model the limiting currents of microdiscs of different radii to within 0.5% of the theoretically accepted values. Consistent with the results seen for S50μ, similar errors were seen in Figure 4.29 in modelling microdiscs of differing dimensions. It is likely therefore that the difference observed between microsquare simulation and analytical expression for the microsquares are statistically significant.

This figure shows that there is a linear relationship between the limiting current and edge dimension for these simulated responses, which suggests that the limiting current does indeed scale with electrode edge length at all dimensions. Thus, at least at steady-state and when utilising the FEM model developed for this thesis, it seems any corner diffusional effects are constant as the square decreases in size.

Since the COMSOL models establish a proportional current response with size at steady-state, an empirical limiting current expression can be developed to more accurately predict the limiting current of a microsquare. By considering the ratio of FEM simulation gradient and that of Eqn. 4.5 (red line, Figure 4.31) substitution of this ratio (0.864) into Equation 4.5 gives

$$i_L = 2.63n\mathbf{F}Dcl \qquad \textbf{Eqn. 4.8}$$

4.4. Conclusions

The results presented in this chapter have shown that square electrodes can be fabricated with very accurately controlled dimensions, using the photolithographic techniques described in section (4.2). Certainly, however, several materials issues arose during research including attack and/or lifting of the Parylene coating during sulfuric acid cleaning and cracking of the platinum electrodes during initial potassium chloride cleaning, thought to be caused by excessive bubbling. Optical microscope images showed this parylene degradation and cracking. A new, milder cleaning technique was thus developed to combat these problems. Also, although experimentally, initial CVs were sigmoidal in shape at low sweep rates, indicative of a microelectrode response, their sloping in shape and asymmetry about zero was indicative that other surface processes may have been occurring. Optical microscope images revealed that a blue-solid appeared to build-up around the electrode edge during experimentation. This layer may be a semi-passivation later similar to Prussian blue[17] which may have been affecting the electrochemistry at the electrode surface. It has also been suggested that potassium ferrocyanide may also adsorb onto platinum surfaces affecting the reaction rate[18]. A combination of these effects may have caused the unusual sloping and unequal distribution of the CV peaks about zero, observed during initial experiments (Figure 4.10). Thus care must be taken when performing ferri/ferrocyanide redox studies.

Since optimisation of the 0.1 M KCl cleaning protocol, experiments on different electrodes have reproducibly produced consistent results both in their CV limiting currents and EIS responses. This again indicates the reproducible

production of microelectrodes of controlled size and activity. The S50μ platinum electrodes do demonstrate microelectrode behaviour, particularly at low sweep rates, in that the steady-state cyclic voltammograms obtained at 5 mVs^{-1} show characteristic sigmoidal responses. These data also fits well to the modified Tafel analysis as previously shown for microdiscs. However this study has demonstrated that microsquare electrodes have increased mass transport limiting currents at steady-state compared with discs of comparable dimension, and hence that they have different limiting currents to those previously postulated theoretically. The very good agreement between FEM simulation and experiments on the S50μ electrodes further validates this observation. This was extremely important to establish, given the potential popularity of the use of microsquare electrodes due to their relative ease of construction using pixilated photomasks. Through a combination of simulation and experiment, the research has shown that in fact microsquare electrodes show systematically a 14 % greater limiting current density and different electrochemical impedance response as a function of frequency than a microdisc of comparable dimension. Indeed it has also been shown that microsquare electrodes have statistically higher limiting currents than predicted by either of the two previously postulated theoretical expressions (eqn. 4.5 and 4.6), and that in fact the empirical expression, Eqn. 4.8 better fits the simulated data and is consistent with experiment. This establishes the need for further fundamental microsquare characterisation.

The EIS measurements produced Nyquist plots with characteristic shapes simialr to to microdisc electrodes[19,22,23,28]. However the EIS experiments show that differences observed between microsquare and microdisc limiting currents are not simply due to a difference in actual or effective area, but that there is a distinct difference in the response of microdiscs and microsquares as a function of frequency, which indicates a difference in the evolution of the diffusion layer with time. The equivalent circuit (figure 2.11) extensively used to fit microdisc impedance data[22,23], and justified by Transmission Line Theory, does not accurately fit the entire frequency range of the microsquare EIS plots. This is postulated to be due to

the effects of enhanced diffusion at microsquare corners . If this is the case current densities will therefore be greater and the diffusion layer will be expected to increase more rapidly with time in this region compared to at the edge of a microdisc or long edge of a microsquare. Such effects (and the initial symmetry) will preclude the exactly hemispherical and symmetrical growth in diffusion layer seen for microdiscs at these time scales.

The modified Randles' circuit could however be used to fit the very high and very low frequencies separately, suggesting initial linear diffusion dependent on electrode area at short time scales and hemispherical diffusion at long time scales respectively, is still observed, similar to microdiscs. Values of charge transfer reistance, R_{CT}, the non-linear resistance, R_{NL} and the Warburg parameter, $1/Y_0$ were obtained in this manner and plotted against their corresponding dc potentials. The parabolic curves obtained for clean platinum surfaces fitted accurately to the expressions derived for thermodynamically controlled electron transfer (Equation 2.41, 2.42 and 2.44 respectively), as expected for a fully reversible system. The data in this chapter also shows that fits to the kinetic and thermodyanic expression (equation 2.39 and 2.41) can be used as a method to indicate if surface kinetic processes are occurring due to resitive films on the electrode surface.

FEM simulations of microsquare electrodes of different sizes show that, at steady-state the limiting current scales linearly with square length. It could be argued that as the square dimension is reduced; the corners will become more important, enhancing the current density of these electrodes due enhanced corner diffusion. These initial simulations suggest that this is not the case, however further experimental work in this area needs to be carried out in order to verify this. The microdisc simulations demonstrate that FEM simulation using COMSOL can model microdisc limiting current responses accurately at all dimensions, however the author understands that there are a number of limitations with this modelling program[29] (discussed in greater detail in chapter 8), and so it is essential that further experimental and theoretical studies are

carried out in order to better understand the microelectrode system under investigation.

These single microsquare electrodes have provided the opportunity for systematic study of microsquare response, and allowed the further development of microsquare theory. Microsquares have many of the favourable attributes seen in microdiscs; however the current output for these single squares is very low, in the nano-ampere range. The next chapter outlines the development of microelectrode and nanoelectrode arrays, which overcomes this issue.

4.5. References

(1) Forster, R. J. *Chemical Society Reviews* **1994**, *23*, 289

(2) Heinze, J. *Angewandte Chemie International Edition in English* **1993**, 1268.

(3) Stulik, K., C. Amatore, K. Holub, V. Marecek and W. Kutner *Pure and Applied Chemistry* **2000**, *72*, 1483.

(4) Alden, J. A., J. Booth, R.G. Compton *, R.A.W. Dryfe, G.H.W. Sanders *Journal of Electroanalytical Chemistry* **1995**, *389*, 45.

(5) Morita, M., M.L. Longmire, R.W. Murray *Anallytical Chemistry* **1988**, *60*, 2770.

(6) Berduque, A.; Lanyon, Y. H.; Beni, V.; Herzog, G.; Watson, Y. E.; Rodgers, K.; Stam, F.; Alderman, J.; Arrigan, D. W. M. *Talanta* **2007**, *71*, 1022.

(7) Caston, S. L.; McCarley, R. L. *Journal of Electroanalytical Chemistry* **2002**, *529*, 10.

(8) Britz, D.; Poulsen, K.; Strutwolf, J. *Electrochimica Acta* **2004**, *50*, 107.

(9) Oldham, K. B. *Electrochemistry Communications* **2004**, *6*, 210.

(10) Schmitt, G.; Schultze, J. W.; Fassbender, F.; Buss, G.; Luth, H.; Schoning, M. J. *Electrochimica Acta* **1999**, *44*, 3865.

(11) Guo, J.; Lindner, E. *Analytical Chemistry* **2009**, *81*, 130.

(12) Li, J.-T.; Chen, Q.-S.; Sun, S.-G. *Electrochimica Acta* **2007**, *52*, 5725.

(13) Chen, Y.-J.; Sun, S.-G.; Chen, S.-P.; Li, J.-T.; Gong, H. *Langmuir* **2004**, *20*, 9920.

(14) In *Encylcopedia of Chemical Technology, Supplement*; 4th Edition ed.; John Wiley and sons. Inc: 1998.

(15) *Solvent Resistance of the Parylene*, Speaciality Coating Systems, 2006.

(16) Nichols, M. F.; Hahn, A. W.; James, W. J.; Sharma, A. K.; Yasuda, H. K. *Biomaterials* **1981**, *2*, 161.

(17) Granger, M. C.; Swain, G. M. *Journal of the Electrochemical Society* **1999**, *146*, 4551.

(18) Pharr, C. M.; Griffiths, P. R. *Analytical Chemistry* **1997**, *69*, 4665.

(19) Koster, O., W. Schuhmann, H. Vogt and W. Mokwa *Sensors and Actuators* **2001**, *B*, 573.

(20) Priyantha, N.; Malavipathirana, S. *Journal of the Natural Science Council of Sri Lanka* **1996**, *24*, 237.

(21) Los, P., G. Zabinska, A. Kisza, L. Christie, A. Mount and P. G. Bruce *Physical Chemistry Chemical Physics* **2000**, *2*, 5449.

(22) Los, P.; Bruce, P. G. *Polish Journal of Chemistry* **1997**, *71*, 1151.

(23) Fleischmann, M., S. Pons and J.Daschbach *Journal of Electroanalytical Chemistry* **1991**, *317*, 1

(24) Winkler, K. *Journal of Electroanalytical Chemistry* **1995**, *388*, 151.

(25) Krulic, D.; Fatouros, N.; Khoshtariya, D., E. *Journal de Chimie Physique et de physico-Chimie Biologique* **1998**, *95*, 497.

(26) Strutwolf, J.; Williams, D. E. *Electroanalysis* **2005**, *17*, 169.

(27) Bard, A. J.; Faulkner, L. R. *Electrochemical Methods, Fundamentals and Applications*, 2001.

(28) Hepel, T.; Osteryoung, J. *Journal of Electrochemical Society: Electrochemical Science and Tecnology* **1986**, *133*, 752.

(29) Cutress, I. J.; Dickinson, E. J. F.; Compton, R. G. *Journal of Electroanalytical Chemistry* **2010**, *638*, 76.

5. Development of Platinum Microsquare Arrays and Nanoband Arrays

5.1. Introduction

There has been considerable interest in the fabrication and deployment of miniaturised electrodes for over 20 years. The potential benefits of these electrodes have been widely discussed in the literature[1-4]. As discussed in Chapter 1, the enhanced mass transport due to the hemispherical or radial diffusion that occurs on the micron scale gives high current densities and steady-state or near steady-state currents, reducing the effects of convection. Additionally, shorter RC time constants allow the investigation of faster electrode processes, while smaller iR drops enable the electrodes to work in a wide range of resistive electrolytes, with little or no added inert ions. As these effects are enhanced with decreasing electrode size, there has been real recent interest in taking electrodes from the micron[5] to the nanometer[6-14] scale. These electrode structures also offer the opportunity to exploit nanostructural effects such as enhanced surface catalytic activity[15,16]. Nanoelectrode systems have also been constructed for applications as diverse as enhanced thermal energy[17] and light harvesting[18]. However, there are two main issues with current nanoelectrode technology. The first is the lack of a technology for reproducible electrode fabrication with accurately controlled dimensions at reasonable cost and the second is the low absolute currents passed by nanoelectrodes (section 1.3.1).

Using the ideas developed in chapter 4, especially the idea of utilizing edge effects, this chapter presents the development of a novel electrode array architecture which offers the ability to control electrode material, size and spacing by the use of standard microfabrication techniques and tools. In this thesis the architecture is referred to as a Cavity Array Electrode (CaviArE), which consists of an array of ~ 1 μm depth microsquare holes (shallow cavities) of controlled size and spacing. Within each array element an enclosed platinum microband electrode of 50 nm width is positioned half way up the vertical edges of the cavities.

Since the fabrication process can easily be modified to produce micro-square arrays as an intermediate step, two types of array, (microsquare arrays and CaviArE) were fabricated in parallel, and the development of the design was carried out on both types of electrode array. The microsquare array responses were then used as a comparison for the nano-arrays. This chapter describes a number of materials issues encountered during preliminary analysis of these arrays and presents the steps and processes taken to overcome these issues. Section 5.2 describes the fabrication processes for each evolving generation and section 5.3 describes in detail the results obtained using each of the designs and the steps taken to improve the design.

5.2. Specific Experimental Procedure

5.2.1. Generation 1 - Parylene Insulated microsquare and Nano-band Arrays

Microsquare array electrodes were fabricated on 3-inch <100> n-type silicon wafers. The initial stage was the deposition of the films that make up the layers of the devices. Firstly, a 1000 nm layer of silicon dioxide was thermally grown on the wafer surface by a wet oxidation process. This involved heating the wafers in a quartz furnace tube to a temperature of 1100^{o}C for 150 minutes in a combined oxygen/hydrogen atmosphere. This layer isolates the devices from the silicon substrate and forms the bottom insulator. On to this insulator, a 5 nm titanium adhesion layer was deposited by e-beam evaporation and then on top of this a 50 nm platinum film was deposited, also by e-beam evaporation, to form the conductive electrode layer. The final layer of the device is the top insulator, which consists of a 1µm Parylene layer deposited in the same manner as described for single square arrays (Chapter 4.2.)

The device structures were fabricated by concurrent pattern and etch steps. A mask layout was designed in collaboration with the SMC and a mask set fabricated for the purpose of transferring the required patterns into the device layers. Figure 5.1 show details of the mask design.

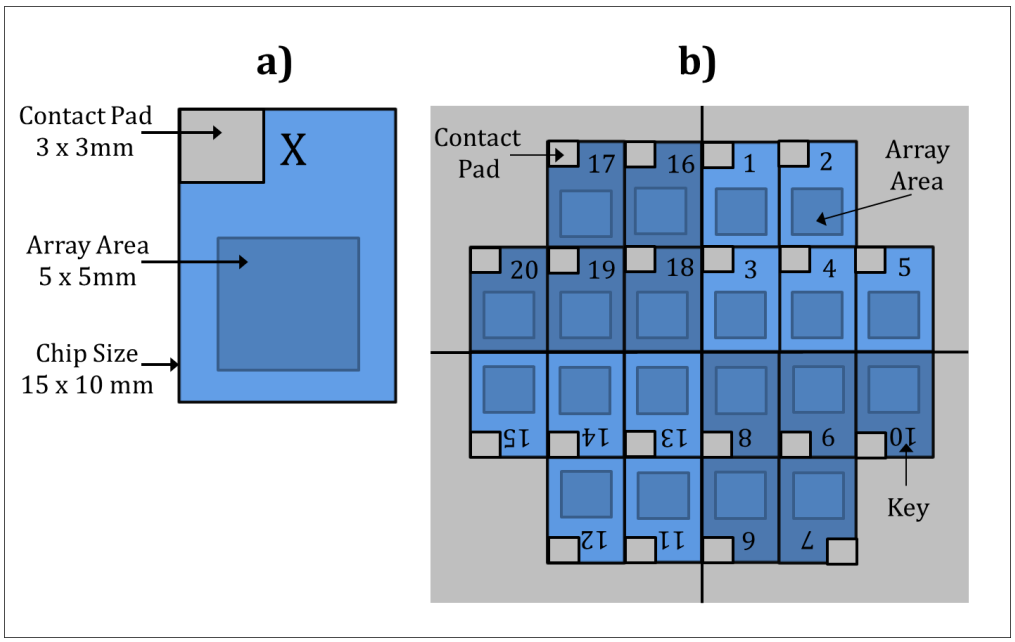

Figure 5.1: a) Device mask layout shows the dimensions of a single electrode array device; and **b)** shows the complete wafer mask of twenty devices.

The photolithography steps involved the spinning on of a 1500 nm layer of positive photoresist (Megaposit SPR350, Microchem), which was baked for 60 seconds at 90°C to dry the film and ensure a consistent, low level of solvent. After UV exposure of the resist through the photomask, the exposed resist was removed in a developing solution (Microposit MF319 Developer, Microchem) leaving the required pattern in the resist layer. The resist then acts as a mask layer for subsequent etch steps.

The first photolithography step defined the device areas and contact pads of the chips. Following patterning of the resist, the Parylene coating was removed from the required Platinum areas by reactive ion etching with oxygen plasma. The oxygen flow rate was 600 sccm (standard cubic centimetres per minute), with a power of 100 W and etch pressure between 60 and 62 mTorr. The resist layer was then stripped by successive rinses in acetone before a fresh 1600 nm thick layer of resist is applied for the second photolithography step.

The second photolithography step defined the microsquare/CaviArE arrays. Following patterning of the resist, the Parylene coating over the array of electrodes was again removed from the required areas by etching, in oxygen

plasma. Figure 5.2 shows a cross section of a small section of the microsquare array design.

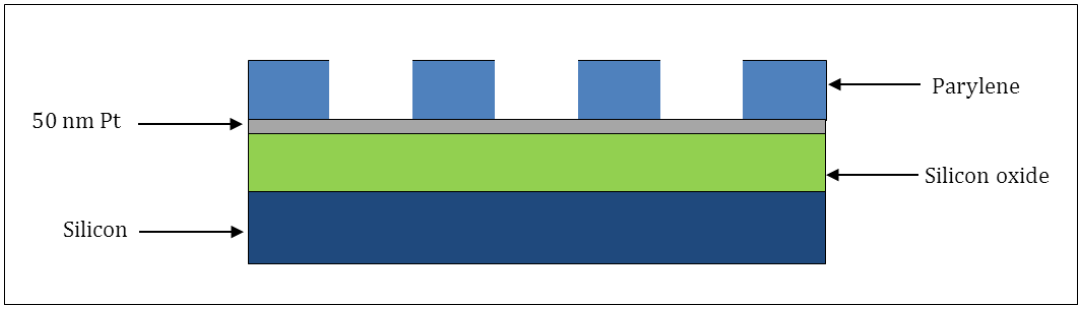

Figure 5.2: Schematic to show how the platinum square arrays are created (not to scale).

The CaviArE microfabrication approach was first described in the patent that protects this technology[19] and followed a similar procedure to that described above except that the second photolithography and etch step involved first etching the parylene in oxygen plasma as described above, then the platinum and titanium adhesion layer were argon milled (JLS RIE 80 system) using 25 sccm argon at a power of 200 W and 30 mT pressure. The etch time was 9 minutes. Finally 500 nm of the underlying thermal oxide layer was reactive ion etched (JLS RIE 80 system), using 46 sccm CHF_3, 4 sccm O_2 and 10 sccm Ar at a power of 100 W and pressure of 60 mT. The etch time was 20 minutes. This effectively created an array of 50 nm band electrodes in a square arrangement. Figure 5.3 shows a cross section of a small section of the CaviArE device.

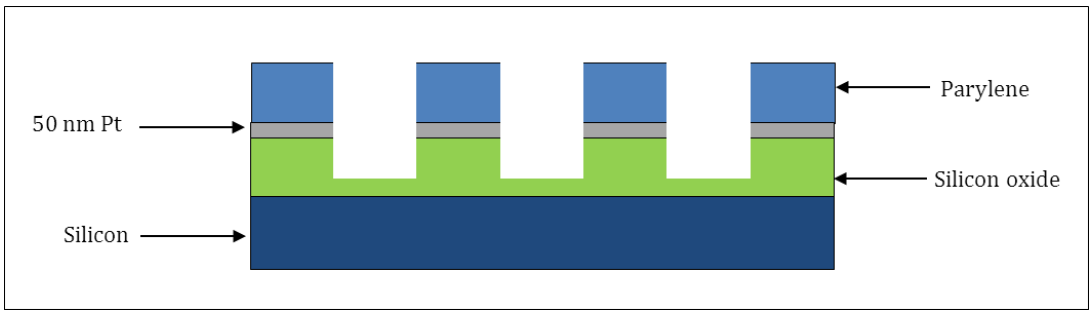

Figure 5.3: Schematic diagram representing the CaviArE nanoband design, (not to scale)

These electrode arrays were fabricated for a number of different square widths and spacing in order to facilitate a systematic study and determine fundamental electrode characteristics. Table 5.1 provides details of the different electrode arrays fabricated with this method, outlining the dimension and separation of

each electrode element. The total array footprint on the silicon substrate was kept constant at 5 x 5 mm; therefore the number of electrodes per substrate is dependent on their dimension and spacing. The total geometric area for both the microsquare arrays and CaviArE is also given in table 5.1.

Key	Square width, d /µm	Pitch	Number of electrodes per silicon substrate	Total area of square electrodes / cm^2	Total area of CaviArE electrodes / cm^2
1 (10µ1d)	10	d	62500	$6.25x10^{-2}$	$1.25x10^{-3}$
2 (20µ1d)	20		15625	$6.25\ x10^{-2}$	$6.25x10^{-4}$
3 (30µ1d)	30		6889	$6.2001\ x10^{-2}$	$4.1334x10^{-4}$
4 (50µ1d)	50		2500	$6.25\ x10^{-2}$	$2.5x10^{-4}$
5 (100µ1d)	100		625	$6.25\ x10^{-2}$	$1.25x10^{-4}$
6 (10µ2d)	10	2d	27889	$2.7889\ x10^{-2}$	$5.5778x10^{-4}$
7 (20µ2d)	20		6889	$2.7556\ x10^{-2}$	$2.7556x10^{-4}$
8 (30µ2d)	30		3136	$2.8224\ x10^{-2}$	$1.8816x10^{-4}$
9 (50µ2d)	50		1089	$2.7225\ x10^{-2}$	$1.089x10^{-4}$
10 (100µ2d)	100		289	$2.89\ x10^{-2}$	$5.78x10^{-5}$
11(10µ3d)	10	3d	15625	$1.5625\ x10^{-2}$	$3.125x10^{-4}$
12 (20µ3d)	20		3969	$1.5876\ x10^{-2}$	$1.5876x10^{-4}$
13 (30µ3d)	30		1764	$1.5876\ x10^{-2}$	$1.0584x10^{-4}$
14 (50µ3d)	50		625	$1.5625\ x10^{-2}$	$6.25x10^{-5}$
15 (100µ3d)	100		169	$1.69\ x10^{-2}$	$3.3x10^{-5}$
16 (10µ4d)	10	4d	10000	$1\ x10^{-2}$	$2x10^{-4}$
17 (20µ4d)	20		2500	$1\ x10^{-2}$	$1x10^{-4}$
18 (30µ4d)	30		1156	$1.0404\ x10^{-2}$	$6.936x10^{-5}$
19 (50µ4d)	50		400	$1\ x10^{-3}$	$4x10^{-5}$
20 (100µ4d)	100		100	$1\ x10^{-2}$	$2x10^{-5}$

Table 5.1: Parameters for the twenty microsquare array and CaviArE devices cavity on the mask layout

5.2.2. Generation 2 - PECVD Nitride Insulated Nanoband Array Electrodes

The electrode arrays were fabricated similarly to those described in section 5.2.1. However, instead of Parylene as the top insulator, the final layer of the device comprisesd a 500 nm silicon nitride layer deposited by plasma-enhanced

chemical vapour deposition (PECVD) using 40 sccm silane (SiH_4) and 55 sccm ammonia (NH_3) feed gases. The deposition time was 46.5 mins at a pressure of 900 mT, temperature of 573 K, and a power of 20 W (13.56 MHz). During the second photolithographic step, the layer of photoresist was increased to 2200 nm and the PECVD layer was reactive ion etched (JLS RIE80 system) using 60 sccm tetrafluoromethane (CF_4) and 4 sccm O_2 at a power of 150 W and pressure of 60 mT for 4 minutes. All other etch processes remained the same as previously.

The resulting architecture encloses a Platinum nanoband of 50 nm width within each array element that is positioned half way up the vertical edges of the shallow cavities (depressions), with a total depth of approximately 1050 nm. Figure 5.4 shows a schematic diagram depicting this architecture

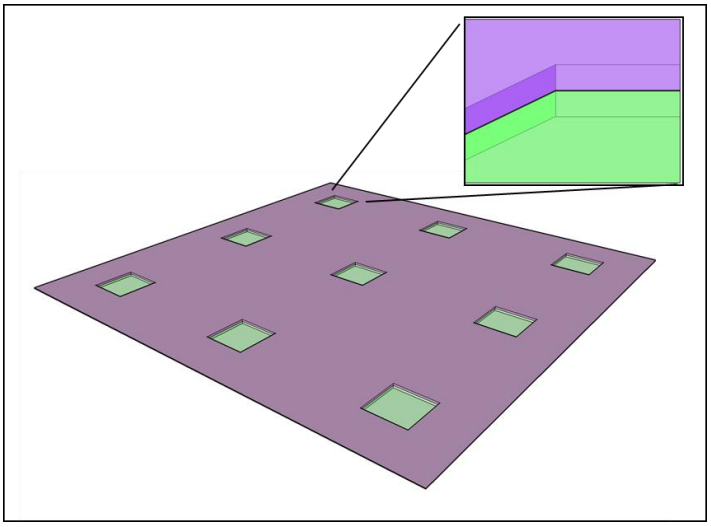

Figure 5.4: Schematic diagram of the nanoband electrode array architecture used in this work, with purple nitride and green oxide insulation sandwiching the black Pt nanoband in each depression (inset). The square separation depicted in this figure has a spacing of 3d (3 times the square length) and a cavity depth of 1050 nm.[i]

The spacing shown in Figure 5.4 depicts the 3d spacing architecture, but the electrode band was always positioned in the middle of the cavity

5.2.3. Generation 3 - LPCVD Nitride Insulated Microsquare and Nanoband Array Electrodes with Recessed Edges

The third generation of CaviArE devices were fabricated with an additional photolithography step, which employed a photomask developed to

[i] Figure provided by Dr Jonathon Terry, SMC

ensure that no platinum was exposed around the edges following dicing of the chips. The first two stages of the fabrication process, the silicon oxide growth and platinum deposition were the same as that described in section 5.2.1. After the platinum was deposited, a 1600 nm thick layer of photoresist was spun deposited on top and patterned using the new photomask, designed to ensure the edge of each chip was insulated. The excess platinum was then removed by argon milling to reveal the oxide layer beneath. Figure 5.5 a) shows a schematic diagram of one quarter of wafer chips to depict the oxide edges.

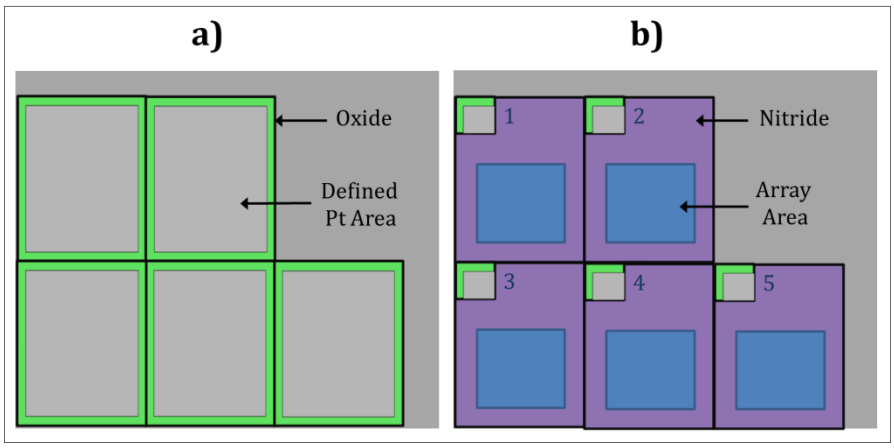

Figure 5.5: Depicting, schematically, **a)** One quarter of the wafer chips after the first photolithographic step, which uses a mask to define a small oxide boarder around each chip. After the photoresist has been developed, the platinum is removed by argon milling down to the oxide layer beneath; and **b)** shows the wafer chips upon completion of all fabrication steps. The diagram clearly shows the nitride top insulator and array area, and also shows the oxide edge visible around the contact contact pad.

The top insulator comprised of a 500 nm silicon nitride layer as in section 5.2.2, but deposited using low pressure chemical vapor deposition (LPCVD) rather than PECVD. The gases used were 15 sccm dichlorosilane (SiH_2Cl_2) and 10 sccm ammonia (NH_3). The LPCVD deposition time was 4.5 hours, at a pressure of 100 mT and temperature of 1073 K. After photo-patterning, the LPCVD layer was reactive ion etched in 60 sccm CF_4 and 4 sccm at a pressure of 60 mT and power of 150 W for 13 minutes. All other etching processes remained the same as previously. Figure 5.5 b) shows, schematically, the final array architecture, insulated with nitride and with the oxide edge clearly visible around the exposed platinum contact pad.

5.2.4. Collection of data

A specially designed lid, (designed by the author) made in house in the mechanical workshop at the University of Edinburgh from PTFE , was used in order to analyse multiple electrodes at the same time. Figure 5.6 shows schematic plan view of the lid and a photographic image of one of the Electrode chips connected to a crocodile clip by the contact pad in the corner. The crocodile clip has been soldered to a screw, which can be fastened into one of the holes in the lid.

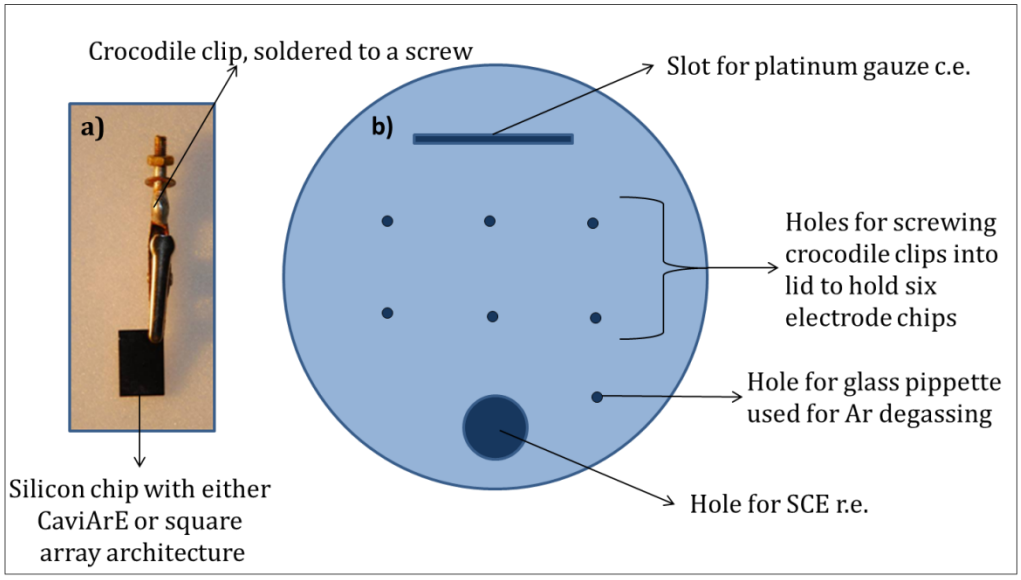

Figure 5.6: Showing **a)** a hotographic image (Sony, Cybershot DSC P200) of one of the electrode array chips, connected in one corner by the contact pad to a crocodile clip, which is soldered to a screw so that it can be fastened into the experiment lid. The back teeth of the crocodile clip are wound with Parafilm to prevent wicking of solution up the back of the silicon substrate; and **b)** shows a schematic diagram of the lid designed to fit over a Pyrex dish. The lid has specifically designed holes for six crocodile clips, an argon stream, the counter electrode and the reference electrode.

The lid enabled six different arrays to be experimented upon at the same time and by using a Multiplex module (Autolab, MUX.SCNR16), switching between the different working electrodes was simple and did not require any re-assembling of the equipment. Figure 5.7 shows a photograph of the experimental set up and top view of the experiment lid.

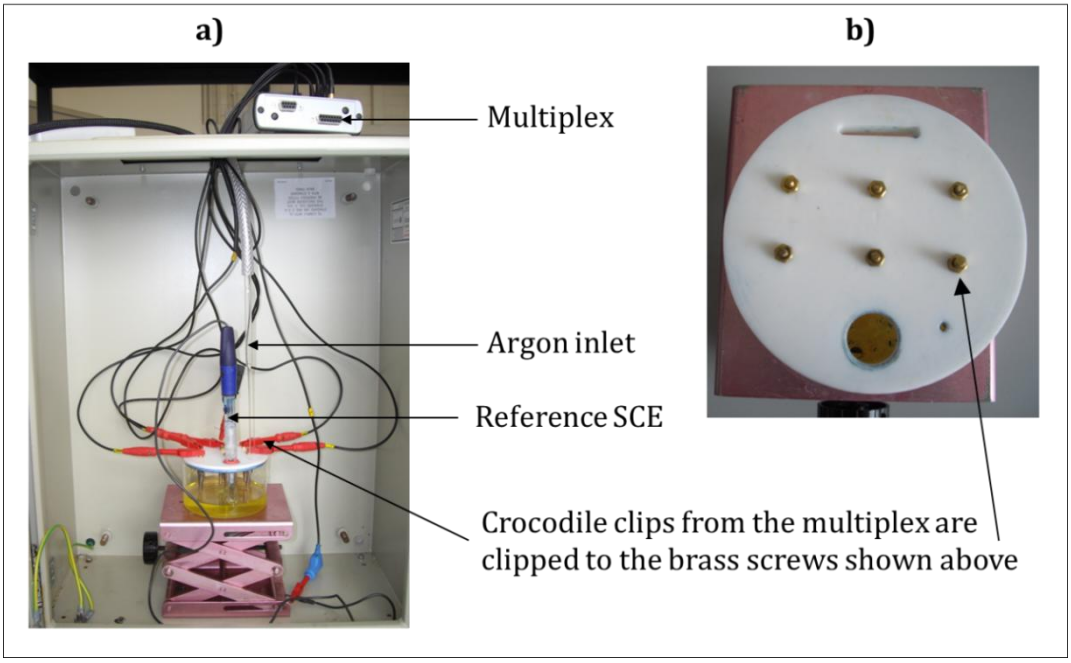

Figure 5.7: Showing **a)** a photographic image of the experimental set-up used in this research and **b)** a top view of the experiment lid with 6 crocodile clips screwed into the assigned slots ready for experimentation.

Unless otherwise stated, all experiments within this chapter utilized this set up and all electrochemical experiments followed the methodology described in sections 3.4.

During preliminary research (generations 1 and 2), before any experiments were undertaken, the edges of the chips needed to be insulated, since a platinum band was exposed around the entire edge of the chip. Nail varnish (clear, No. 7) was used for this initially and during latter experiments silicon rubber (Dow Corning, 3140 RTV coating) was used.

5.3. Results and discussion

5.3.1. Problems with Parylene.

5.3.1.1. Preliminary Studies

Initially, the electrode arrays were fabricated with a Parylene insulating layer, similar to the single microsquare electrodes and both the microsquare arrays and CaviArE devices were analysed as described in section 4.2.

Figure 5.8 show typical optical images of two microsquare array architectures obtained from different microscopes before experimentation.

Figure 5.8 a) shows the contrast image of a microsquare array with 100µ1d architecture ((100 µm)^2, 1d spacing), viewed on a Rechhert Jung Polyvar microscope and captured by a Leicha DC-300 camera in the clean room. For simplicity this architecture is denoted S100µ1d and where henceforth S or C denotes Square array or CaviArE respectively and xµyd denotes edge length, d of x µm and separation of yd. Figure 5.8 b) shows the optical image of a S50µ2d array ((50 µm)^2, 2d spacing) viewed on the Olympus BH-2 microscope and captured with the Sony MVC-FD200 digital camera.

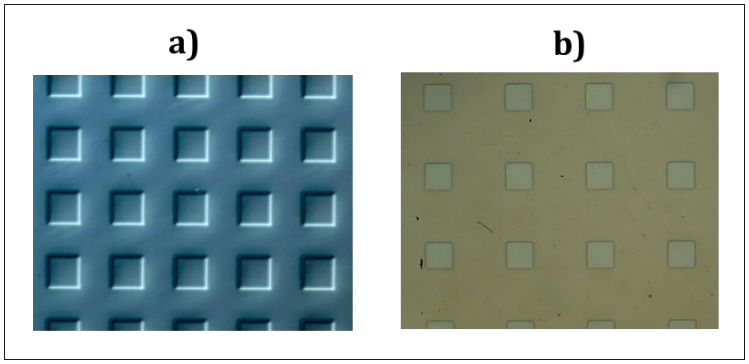

Figure 5.8: Showing **a)** the optical contrast image of a (100 µm)^2 microsquare array with a spacing of 100 µm (S100µ1d) viewed under the Reichert Jung Polyvar microscope and captured by the Leica, DC-300 camera; and **b)** the optical image of an S50µ2d array ((50 µm)^2, 2d spacing) viewed under the Olympus BH-2 microscope and captured with the Sony MVC-FD200 digital camera. NB: The black marks on b) are scratches on the microscope lens, not on the array.

Although the images obtained from the Reichert Jung Polyvar microscope and Leicha, DC-300 camera have a superior quality to the images from the Olympus BH-2 microscope and Sony MVC-FD200 digital camera the former was located in the clean room and access was limited. Therefore, during development, unless otherwise stated, the Olympus BH-2 microscope was used, as this was an open access microscope and multiple images could be acquired quickly. For the remainder of the chapter, images shown are obtained from this camera.

Figure 5.9 show typical CaviArE optical images for two different architectures, C10µ2d and C20µ3d.

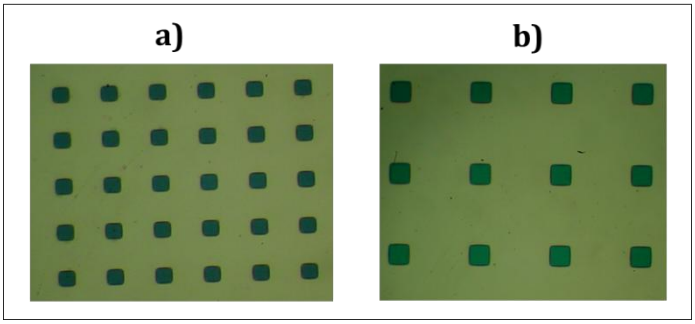

Figure 5.9: Showing **a)** the optical image of a C10µ2d array ((10 µm)^2 cavities, 2d spacing) viewed under the Olympus BH-2 microscope and captured with the Sony MVC-FD200 digital camera; and **b)** the optical image of a C20µ3d array ((20 µm)^2 cavities, 3d spacing) viewed under the Olympus BH-2 microscope and captured with the Sony MVC-FD200 digital camera.

It is satisfying that good images are again obtained, consistent with a well-defined fabrication process. The primary difference between these CaviArE image and the microsquare array images are that the square array elements are paler, due to light reflection from the platinum electrode surface. In contrast the optical images for the CaviArE substrates show dark microsquare regions. The individual electrodes cannot be imaged optically in this way as they are thin bands within the cavity, around the sides of the square edge. The hole images therefore are characteristic of the oxide floor at the base of the shallow cavity (in the case of parylene insulated electrode systems, this cavity is 1550 nm in depth).

As in chapter 4, the electrodes were initially cleaned in 0.1 M KCl, prior to experimentation and then analysed in 10 mM Ferricyanide. Figure 5.10 shows typical CVs obtained for both a microsquare array and CaviArE substrate in 10 mM potassium ferricyanide

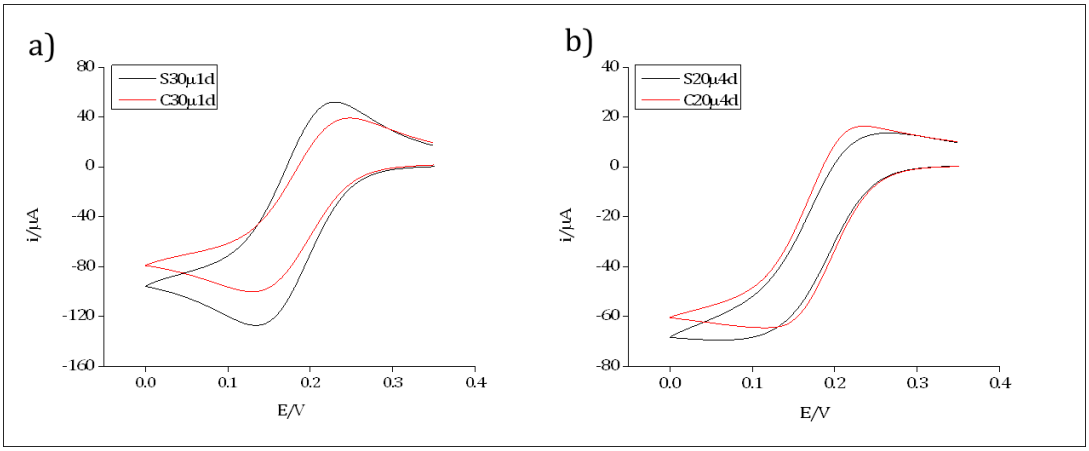

Figure 5.10: Typical 1st scan CVs obtained in 10 mM ferricyanide between 0.35 V and 0.00 V and a scan rate of 5mVs^{-1}; **a)** shows the CV comparison of an S30µ1d array, with a fabricated geometric area of 6.2001x10^{-2} cm^2 (black plot) and a C30µ1d array, with a fabricated geometric area of 4.1334x10^{-4} cm^2, (red plot); and **b)** shows the CV comparison of S20µ4d, with a fabricated area of 1x10^{-2} cm^2 (black plot) and C20µ4d, with a fabricated area of 1x10^{-4} cm^2 (red plot). This and all subsequent potentials are quoted relative to a saturated calomel (SCE) reference electrode unless otherwise stated.

Although it was expected, due to efficient mass transport, that the CaviArE substrates would have relatively high current densities, the current densities shown in Figure 5.10 a) and b) are almost as large as the corresponding microsquare array, even though their geometric areas should have been less than 1% of the microsquare arrays.

Figure 5.11 shows the optical images obtained for the C30µ1d array after experimentation.

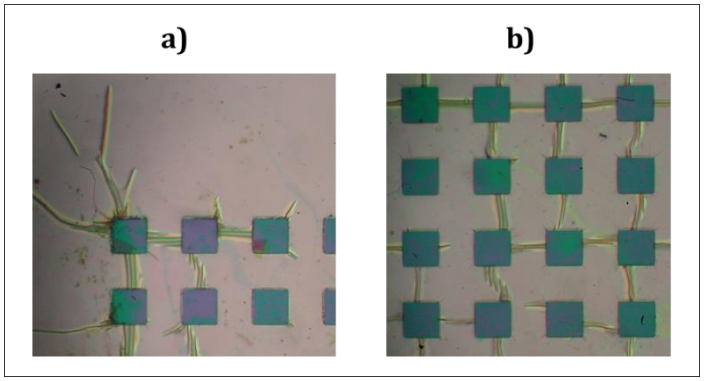

Figure 5.11: Optical image of the C30µ1d chip after experimentation, showing **a)** one corner of the electrode **b)** a part of a central portion of the electrode.

The entire array shows fracturing over the parylene surface between the electrode elements. If the underlying platinum is exposed, this enhanced active electrode area could have been contributing to the overall currents observed. In

contrast, the optical image of the microsquare array showed no such fracturing over the surface, as shown in Figure 5.12.

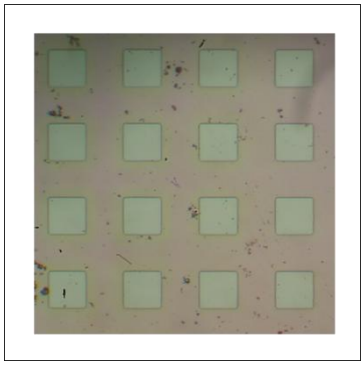

Figure 5.12: Optical image of a central part of the S30µ1d array after experimentation.

A similar response was observed for the C20µ4d array (Figure 5.13 a)), with fractures all across the array surface, in contrast with the S20µ4d chip, which again, does not show any fracturing, as shown in Figure 5.13 b).

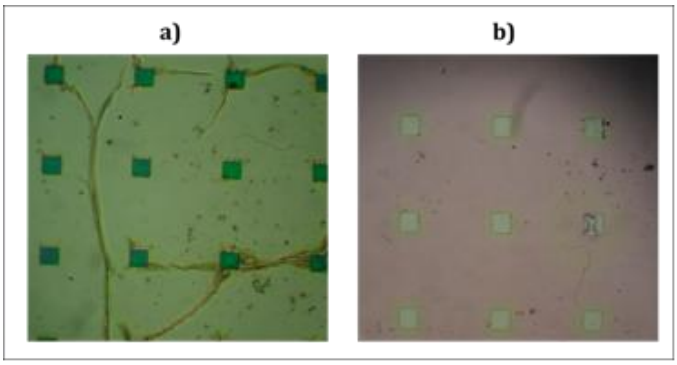

Figure 5.13: Showing **a)** the optical image of a central part of the C20µ4d array ((20 µm)^2 cavity, 4d spacing) after experimentation; and **b)** the optical image of a central part of the S20µ4d array after experimentation.

In fact all the CaviArE chips showed fracturing after experimentation. Studies of capacitance were carried out to see if the fracturing was exposing large areas of platinum.

5.3.1.2. Calculating Electrode Roughness and Capacitance.

Several experiments were undertaken to estimate the electrode roughness and the capacitance expected, per cm^2 for platinum. Silicon oxide was grown on the wafer and Platinum was deposited on to the titanium adhesion layer, as described in section 5.2.1. without depositing an insulating layer over the top.

The silicon wafer was then diced to give sample chips. The area of platinum exposed to solution was accurately calculated and the platinum samples were cleaned in 0.1 M KCl in the same manner as the CaviArE and microsquare arrays.

EIS responses were then recorded in KCl [0.1 M] for frequencies between 1000 Hz and 1 Hz at a dc potential of 0.25 V. Figure 5.14 shows a typical EIS response of a platinum sample in 0.1 M potassium chloride electrolyte.

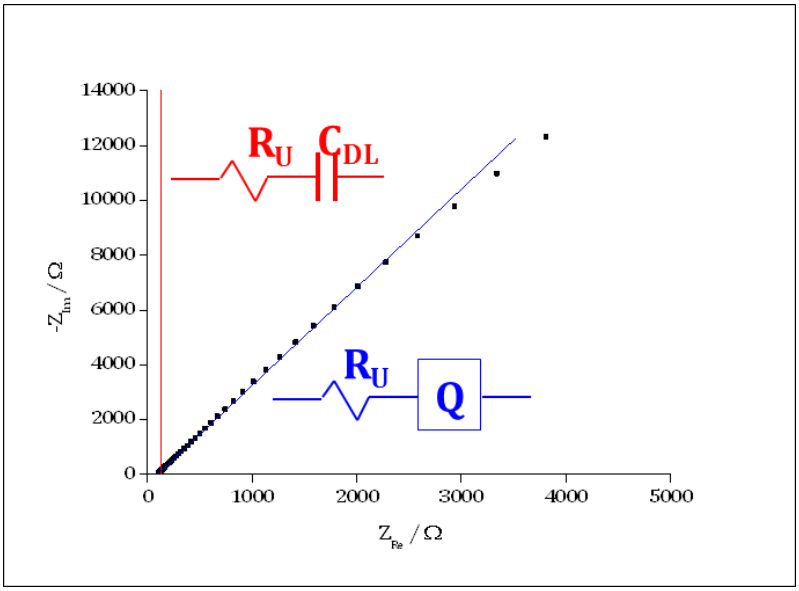

Figure 5.14: Nyquist plot obtained from a platinum sample with an active area of 0.56 cm^2 between 1000 Hz and 1 Hz and dc = 0.25 V in 0.1 M aqueous KCl. The red line shows the fit to an equivalent circuit with a resistor in series with a pure capacitor (-R-C_{DL}-) and the blue line show the fit to an equivalent circuit with a resistor in series with a constant phase element (-R-Q-). R_u = 108 ± 16 Ω, C_{DL} = 9.0 ±0.5 μF, Q_0 = (1.723 ± 0.007) x10^{-5} Ss^n and n = 0.836 ± 0.001.

Clearly a simple C_{DL} circuit is unable to fit the EIS data accurately requiring a CPE parameter in order to attain a good model fit. This implies that the electrode surface has increased dimensionality due to surface roughness. A phase angle of 75.2^0 (nx90^0) was determined. The average roughness factor, n for a range of experiments was 0.84 ± 0.04, giving a phase angle of 75.6^0. This value is similar to the phase angle calculated in section 3.5 for a platinum macrodisc electrode.

Even though the simple –R_U-C_{DL}- does not accurately fit the circuit, an estimate of the double layer capacitance can be obtained. A capacitance of 9.0 ±

0.5 µF for an active area of 0.56 cm^2, calculated from Figure 5.14 would give a capacitance of 16.1 µF cm^{-2}. In fact the average capacitance value calculated for several samples utilising this method was 16.0 ± 0.5 µF cm^{-2}. This is a reasonable value of capacitance for platinum and is in the same order of magnitude as the capacitance calculated using the CPE modified Randles' circuit for the platinum macrodisc electrode in section 3.5.

Since the above analysis provided a reasonable method to determine roughness factor and capacitance, similar experiments were carried out on numerous CaviArE devices. Figure 5.15 a) shows a typical EIS response in KCl [0.1 M] for frequencies between 1000 Hz and 1 Hz at a dc potential of 0.25 V. Figure 5.15 b) shows the corresponding C30µ3d CV response in ferricyanide [10 mM] at 5 mVs^{-1}.

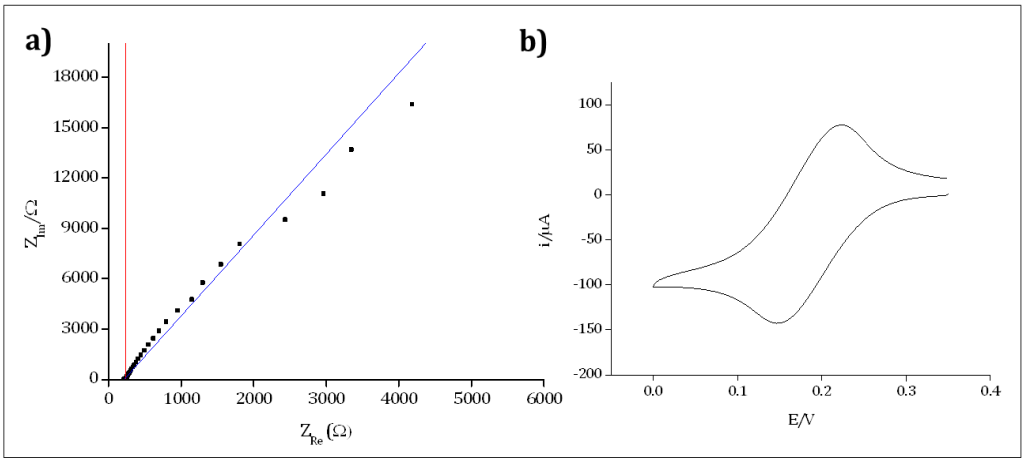

Figure 5.15: Showing **a)** the Nyquist plot of a C30µ3d array in KCl [0.1 M] between the frequencies of 1000 Hz and 1 Hz at E_{dc} = 0.25 V, with the red line showing the fit to the -R-C_{DL}- equivalent circuit and the blue line showing the fit to the -R-Q- equivalent circuit giving R_U = 216 ± 7 Ω, Q_0 = (3.8 ± 0.1) x10^{-5} Ss^n, roughness factor n = 0.872 ± 0.009 and a capacitance, C_{DL} of 31 ± 2 µF; and **b)** is the corresponding first scan CV in 10 mM ferricyanide between 0.35 V and 0.00 V and at a sweep rate of 5 mVs^{-1}.

The uncompensated resistance of 216 ± 7 Ω is in the same order of magnitude as the uncompensated resistance (108 ± 16 Ω) calculated for the 0.56 cm^2 sample chip in Figure 5.14. The resistance is only 2 times larger, which is surprising since the geometric area of the electrode is 1.0584x10^{-4} cm^2 and therefore it would be expected to be many times greater. The roughness factor,

determined in Figure 5.15 a) is similar to that given in Figure 5.14 and gives a phase angle of 78.5^0 A.

The C_{DL} value of 31 ± 2 μF is however very large for a system with a supposed geometric area of 1.0584×10^{-4} cm^2. This would give a capacitance of 425 mF cm^{-2}, which is clearly unrealistic and thus indicative that a much larger active area has been exposed to the solution.

Figure 5.16 shows the optical image for the C30μ3d array analysed above.

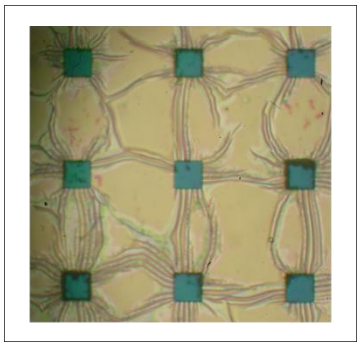

Figure 5.16: Optical image of a central part of the C30μ3d array ((30 μm)^2 cavity, 3d spacing) after experimentation.

Due to the problems of fracturing occurring in the parylene insulation during experimentation, alternative insulating layers were explored.

5.3.2. PECVD Nitride Insulation

Silicon nitride has been shown to have good electrochemical barrier properties for silicon-based microsensors[20,21]. In order to combat the fracturing observed during preliminary investigations, Dr Jonathon Terry, and Professor Anthony Walton (SMC) modified the fabrication process and instead of parylene, a silicon nitride insulation layer was deposited initially using plasma enhanced chemical vapour deposition (PECVD) method. This method of deposition was chosen since it produces films with low tensile stress, reducing possible buckling of the thin underlying platinum layer or cracking within the nitride passivation layer[22]. During the second photolithographic process, 2200 nm of positive photoresist was spun deposited rather than the usual 1500 nm, in order to

protect the surface from scratches during the etching process. Microsquare arrays were not fabricated for this study. The first observation noted was that there appeared to be a loss of resolution when utilizing this method.

Optically, the CaviArE arrays within supposed 10 µm and 20 µm square depressions were seen to be rounded after this process (Figure 5.17).

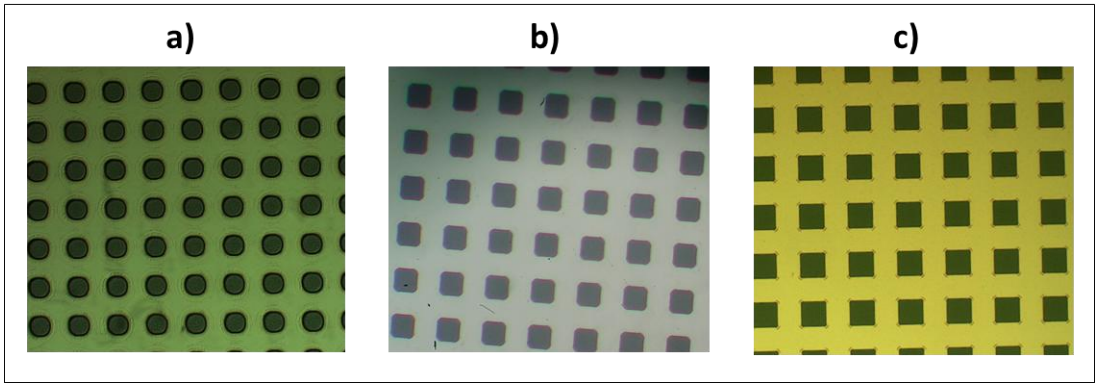

Figure 5.17: Optical images of **a)** a region of a C10µ1d array with PECVD nitride insulation, viewed with the Zeiss Axiotron microscope and captured with the Diagnostics Spot Insight QE digital camera; **b)** the optical image of a region of a C20µ1d array with PECVD nitride insulation viewed under the Olympus BH-2 microscope and captured with the Sony MVC-FD200 digital camera; **c)** the optical image of a region of a C30µ1d array with PECVD nitride insulation, viewed with the Zeiss Axiotron microscope and captured with the Diagnostics Spot Insight QE digital camera.

The arrays at 2d, 3d and 4d spacing show a similar pattern, with the (10 µm)^2 cavities being almost circular in appearance, the (20 µm)^2 cavities showing some rounding and the (30 um)^2 cavities showing a well-defined square. Patterning and etching through the thicker photoresist layer decreased the accuracy with which the smaller electrodes could be resolved. This prevented systematic analysis, as it was unknown what effect this rounding had on the electrode response.

All electrodes were cleaned in KCl [0.1 mM] prior to experimentation, then EIS measurements in 0.1 M KCl was performed in order to measure the capacitance and roughness of the system before CVs in ferricyanide [10 mM] were carried out. Figure 5.18 shows typical KCl EIS response and corresponding first scan ferricyanide CVs at 1 mVs^{-1}, 5 mVs^{-1} and 100 mVs^{-1}.

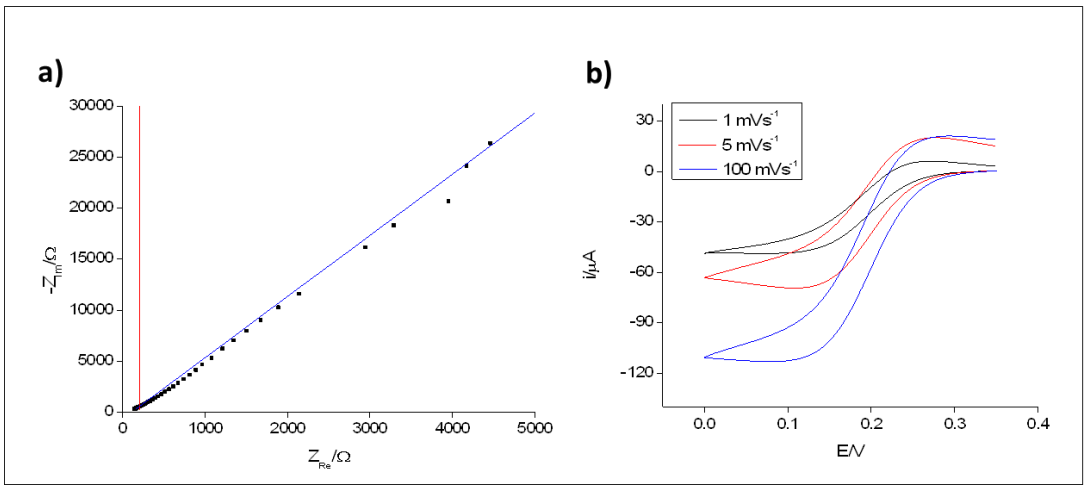

Figure 5.18: Showing **a)** the Nyquist plot of the C30µ2d array (PECVD insulated) in KCl [0.1 M] between the frequencies of 1000 Hz and 1 Hz at E_{dc} = +0.25 V, with the red line showing the fit to the -R-C_{DL}- equivalent circuit and the blue line showing the fit to the -R-Q- equivalent circuit; giving R_U = 113 ± 13 Ω, Q_0 = (1.4 ± 0.1) x10^{-6} Ss^n, roughness factor n = 0.895 ± 0.005 and a capacitance, C_{DL} of 0.88 ± 0.03 µF; and **b)** is the corresponding first scan CVs in 10 mM ferricyanide between 0.35 V and 0.00 V and at a sweep rate of 1 mVs^{-1}(black plot), 5 mVs^{-1} (red plot) and 100 mVs^{-1} (blue plot).

Again the uncompensated resistance of 113 ± 13 Ω, is very similar to the capacitance calculated for the sample chip (108 +16 Ω), which suggests that at least at high frequencies both substrates have a similar active area. The roughness factor, n of 0.895 ± 0.005 gives a phase angle of 80.6^0 which suggests a slightly reduced roughening of this particular substrate, in comparison with the sample. The Q_0 value however, is an order of magnitude smaller than recorded in either Figure 5.15 a) or in Figure 5.14. The estimated capacitance in Figure 5.18 a) of 0.88 ± 0.03 µF, for a supposed geometric area 1.8816x10^{-4} cm^2 implies a capacitance of 4.04 mF cm^{-2}. This is 2 orders of magnitude smaller than that calculated in Figure 5.15 a) for the parylene insulated arrays, however it is still several orders of magnitude larger than that calculated, for either a platinum macrodisc (section 3.5) or during the platinum sample chip studies. Over a range of experiments upon CaviArE substrates of different size and pitch, there was quite a range of capacitance values with an average value of 6 ± 2 mF cm^{-2}.

All arrays were viewed optically after experimentation and there was no sign of fracturing on the surface, suggesting that the nitride layer remained intact. Figure 5.19 shows the optical image of the C30µ2d array, whose electrochemical data is given in figure 5.18.

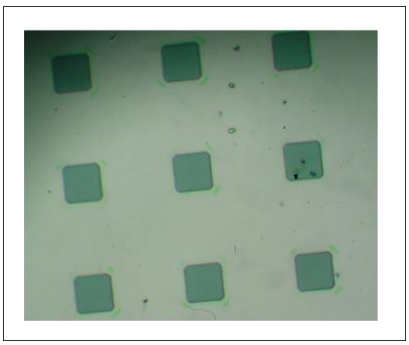

Figure 5.19: Optical image of a central part of the C30µ2d array ((30 µm)^2 cavity, 2d spacing) after experimentation.

As none of the electrode arrays were fractured, the large capacitance value is unlikely to be due to the capacitance from exposed metal from fracturing. One postulation is pinholes throughout the nitride layer causing a larger active electrode area. Schmitt *et al*[20] discuss how the formation of pinholes during the PECVD process is influenced by the choice of parameters. They state that for temperatures above 300^{o}C the pinhole density is less than 1 pinhole per cm^2 but for temperatures below 300^{o}C, the pinhole density can be very much higher. Since the PECVD experimental temperature was 300^{o}C (section 5.2.2), it is possible that pinholes may have contributed to this increased capacitance value.

Another postulate was that perhaps there was inadequate insulation of the platinum band around the entire edge of the silicon substrate, which had been insulated with nail-varnish in all prior experiments. In order to test these hypotheses, several substrates were fabricated as blank chips; that is, the entire fabrication process was carried out except for patterning of the actual array elements. This provided substrates with a layer of platinum entirely insulated by nitride except for the contact pad and the platinum band exposed during dicing of the chips.

Nail varnish had seemingly been used successfully by the Mount group to insulate the edges of previous research electrodes, however since the CaviArE architecture produces electrodes arrays with a very small geometric area, even small exposed areas may add substantially to the response observed. Initially nail varnish was painted around the edges of the un-patterned chips and

experiments undertaken to compare the responses to those of the CaviArE substrates.

Figure 5.20 shows a typical CV response of such an experiment during KCl cleaning and the corresponding response obtained in ferricyanide [10 mM]

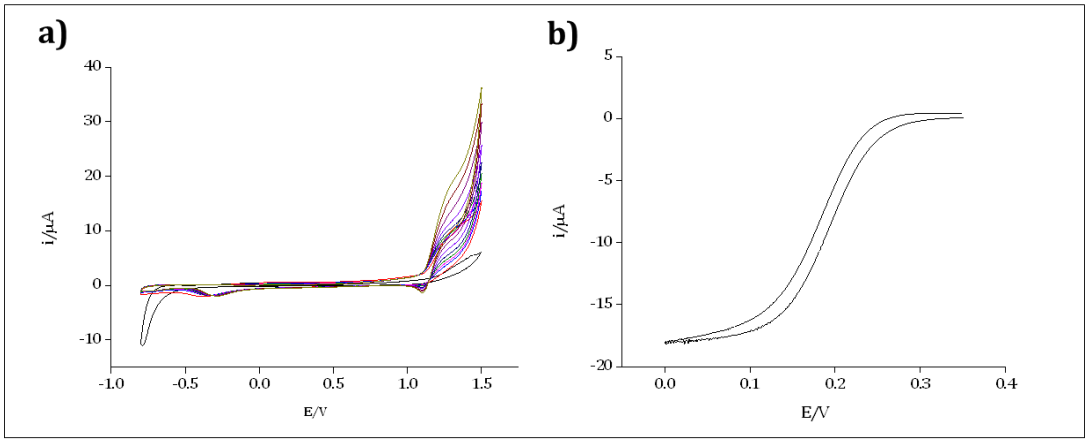

Figure 5.20: Showing **a)** a CV obtained in KCl [0.1 M] during 10 cleaning cycles between 1.6 V and -0.6 V at 100 mVs^{-1}, of an un-patterned nitride platinum chip insulated with nail varnish around the edges; and **b)** the corresponding first scan CV obtained in potassium ferricyanide [10 mM] between 0.35 v and 0.00 V at 5 mVs^{-1}.

It is observed that Figure 5.20 a) shows a typical cleaning profile for platinum and Figure 5.20 b) shows a sigmoidal ferricyanide reduction current. This supports the hypotheses that either there must be platinum exposure around the edges and/or through pin holes in the nitride surface.

Figure 5.21 shows a comparison of the response of a typical un-patterned substrate with that of C30µ2d given in Figure 5.18 at 5 mVs^{-1}.

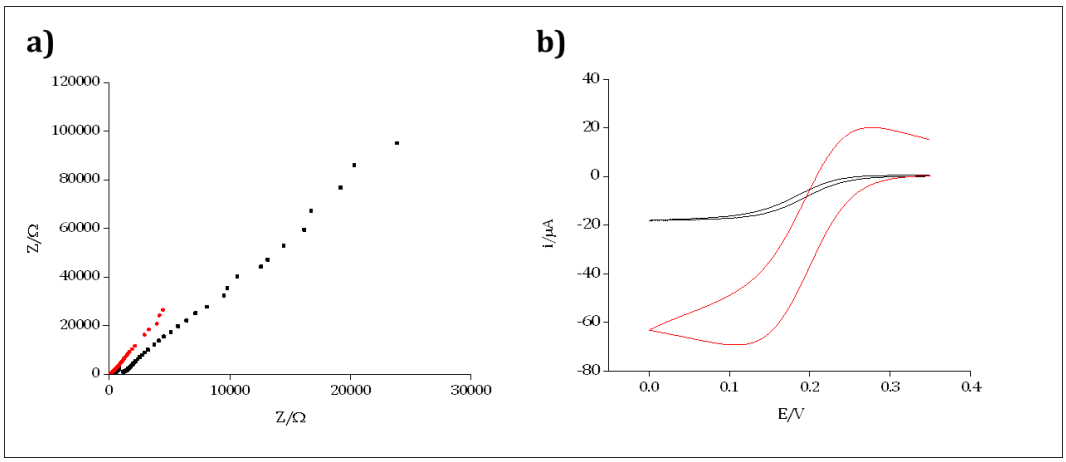

Figure 5.21: Typical plots of **a)** the Nyquist plots in 0.1 M KCl between 1000 Hz and 1 Hz at E_{dc} = +0.25 V, for C30μ2d from Figure 5.16 a) (red) and for an un-patterned Pt substrate insulated with nail varnish around the edges (black). For the latter R_U = 1.0 ± 0.1 kΩ, C_{DL} = 0.427 ± 0.02 μF, Y_0 = (7.6 ± 0.2) x10^{-7} S and n =0.854 ± 0.005; **b)** are the corresponding first scan CVs obtained in ferricyanide [10 mM] for C30μ2d (red) and the un-patterned Pt substrate (black) at 5 mVs^{-1}.

The total current of the un-patterned substrate is 27% of the current recorded for the C30μ2d array, suggesting that pinhole and/or edge platinum exposure may contribute significantly to the total current observed.

It was still unclear whether this current was caused by pin holes or insufficient insulation of the edges. Similar experiments were then carried out, using silicon rubber as edge insulation as this was expected to insulate the edges more effectively. Figure 5.22 shows a typical cleaning profile and ferricyanide reduction CV obtained from such an experiment.

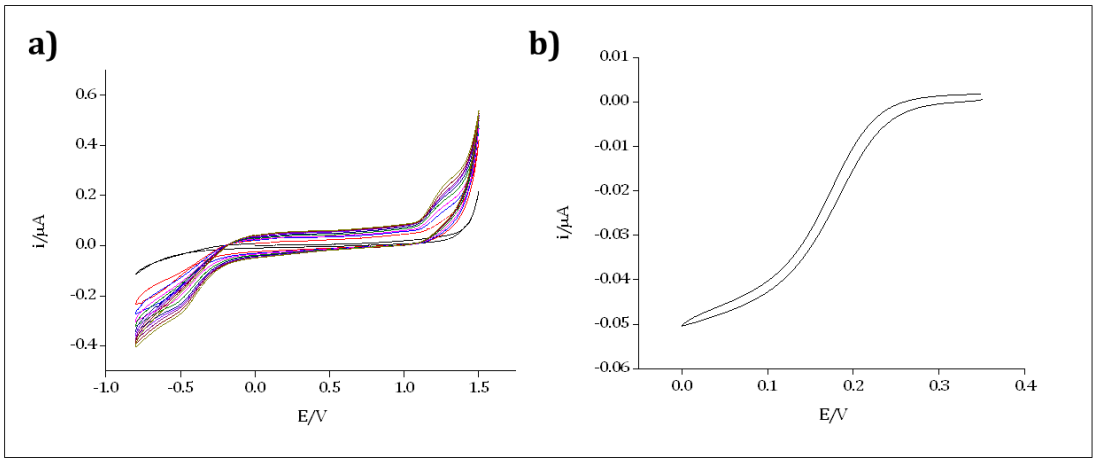

Figure 5.22: Showing **a)** a CV obtained in KCl [0.1 M] during 10 cleaning cycles between 1.6 V and -0.6 V at 100 mVs^{-1}, of an un-patterned nitride platinum substrate insulated with silicone rubber around the edges; and **b)** the subsequent first scan CV obtained in potassium ferricyanide [10 mM] between 0.35 v and 0.00 V at 5 mVs^{-1}.

It is clear that some electrochemistry on a platinum surface is still occurring and a sigmoidal reversible ferricyanide response is observed. However, Figure 5.23 shows the comparison of this silicon rubber-insulated substrate to that with nail varnish insulation.

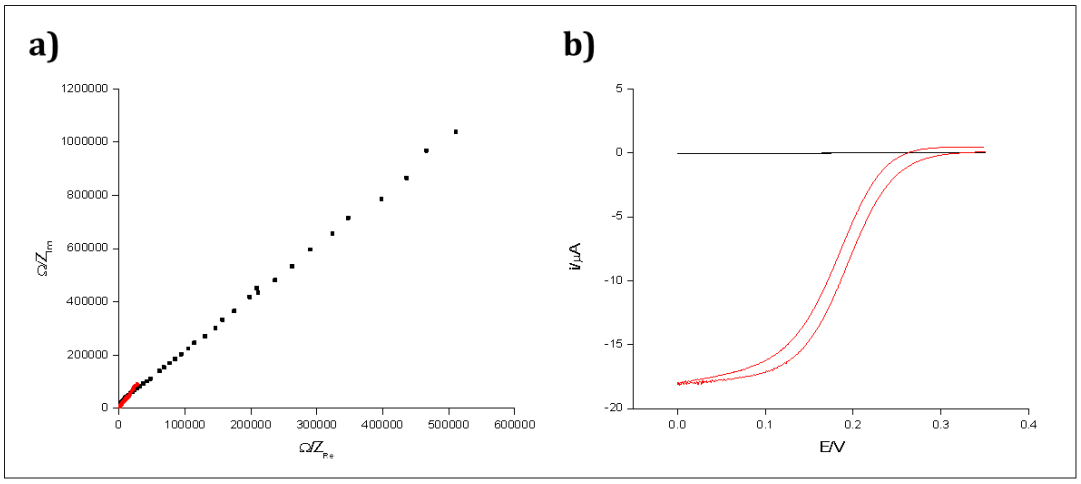

Figure 5.23: Typical plots of **a)** the Nyquist plots in 0.1 M KCl between 1000 Hz and 1 Hz at E_{dc} = +0.25 V, for an un-patterned Pt substrate insulated with nail varnish around the edges (red) and for an un-patterned Pt substrate insulated with silicon rubber around the edges (black). For the latter R_U = 6.9 ± 0.1 kΩ, C_{DL} = 36 ± 4 nF, Y_0 = (9.2 ± 0.3) x10^{-8} S and n =0.723 ±0.006; **b)** are the corresponding first scan CVs obtained in ferricyanide [10 mM] for an un-patterned Pt substrate insulated with nail varnish around the edges (red) and for an un-patterned Pt substrate insulated with silicon rubber around the edges (black).

Figure 5.23 shows that negligible current is passed for silicon rubber insulated edges in comparison to that observed for the un-patterned substrates with the edges insulated by nail varnish. The small current still observed may be due to some presence of pin holes in the nitride surface but it is not sufficient to significantly affect the currents observed for the CaviArE devices. The responses using nail varnish and silicon rubber actually varied quite significantly, suggesting that some human error was occurring during coating of the substrate edges. It was therefore decided that a new fabrication mask should be developed to avoid edge platinum entirely (see section 5.3.3).

5.3.3. LPCVD Nitride Insulation and Recessed Edges

The enhanced CaviArE fabrication process (Generation 3) utilised a photomask which produced substrates with recessed edges, thus preventing platinum exposure around the edge of the chip after dicing. The LPCVD method was also used to deposit nitride instead of PECVD, as this method produces a high

density, very uniform passivation layer without pin holes, with layers that have been established as being a good barrier to the diffusion of water[22].

Figure 5.24 shows a typical SEM of a cross section through one element of the array device and an optical image of the central region of one of the CaviArE arrays produced with this method.

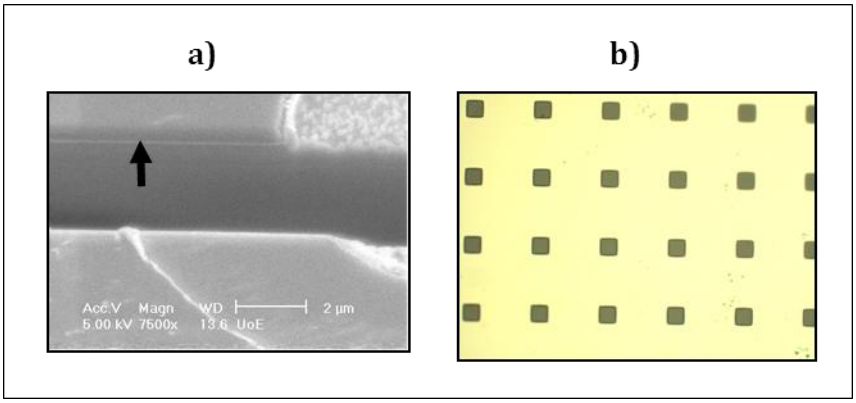

Figure 5.24: a) Shows an SEM image of a focused ion beam (FIB) cross section through a square depression in a fabricated structure following etching. The thin Pt nanoband (indicated by the arrow) can be seen running horizontally on the front face of the upper section, leading to the etched area in the top right of the picture. Electrochemical cleaning is employed to remove any etch deposits along the depression edge; **b)** shows an optical microscope image of the C30µ3d fabricated array viewed with the Zeiss Axiotron microscope and captured with a Diagnostics Instruments Spot Insight QE digital camera. The square edge dimension and separation is 30 and 90 µm respectively and the nanoband, of 50 nm thickness, is positioned in the centre of the depression edge. There are 1764 (42 x 42) squares, giving a total band area of 1.06×10^{-4} cm^2.

During these preliminary studies one array architecture was decided upon for characterisation. The C30µ3d architecture was chosen, since $(30\ \mu m)^2$ cavities could be reproducibly and repeatedly fabricated with high resolution (as shown in Figure 5.17 c)). Each resulting array comprised 30 µm square holes separated by 90 µm. The total array still occupies a 5 x 5 mm footprint and contains 1764 (42 x 42) electrodes within this area. Figure 5.25 shows cleaning of a typical C30µ3d array in 0.1 M KCl and corresponding first scan CV in 10 mM ferricyanide at 5 mVs^{-1}.

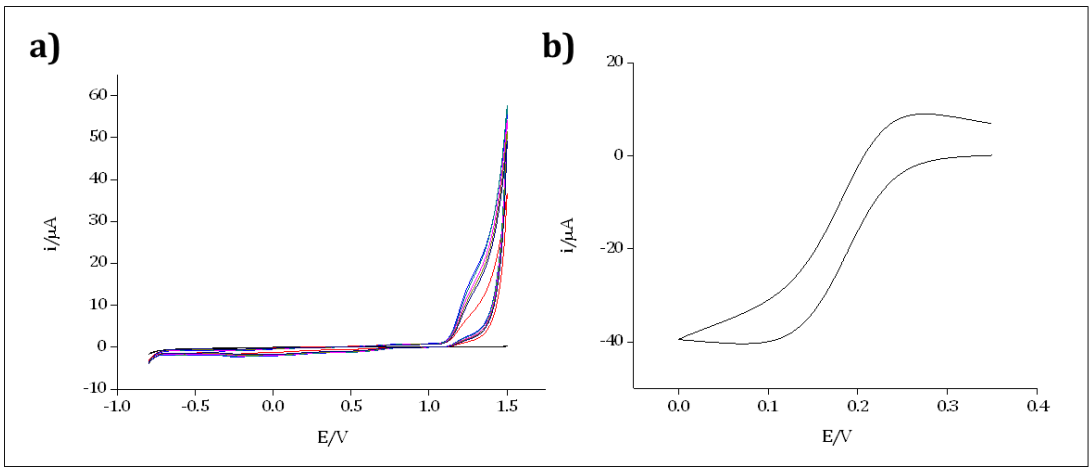

Figure 5.25: Showing **a)** the CV cleaning profile of a C30μ3d array for 30 scans in KCl [0.1 M] between +1.5 and -0.8 V at a sweep rate of 100 mVs^{-1} and a current cap of 10 μA; and **b)** the corresponding first scan CV in ferricyanide [10 mM] between 0.35 V and 0.00 V at 5 mVs^{-1}.

It is clear that Figure 5.25 a) shows a characteristic KCl platinum cleaning profile and the CV in Figure 5.25 b) is characteristic of ferricyanide reduction. However during many experiments, KCl was not sufficient at removing all of the impurities from the CaviArE arrays, often requiring an excessive number of scans and long cleaning periods. Reversible ferricyanide responses were difficult to achieve with this cleaning technique. Therefore cleaning in sulfuric acid was resumed, since, unlike parylene, silicon nitride should not have been affected by the harsher cleaning conditions in aqueous sulfuric acid. Figure 5.26 shows a typical cyclic voltammogram recorded during 30 cleaning scans of a C30μ3d electrode array in sulfuric acid [0.05 M].

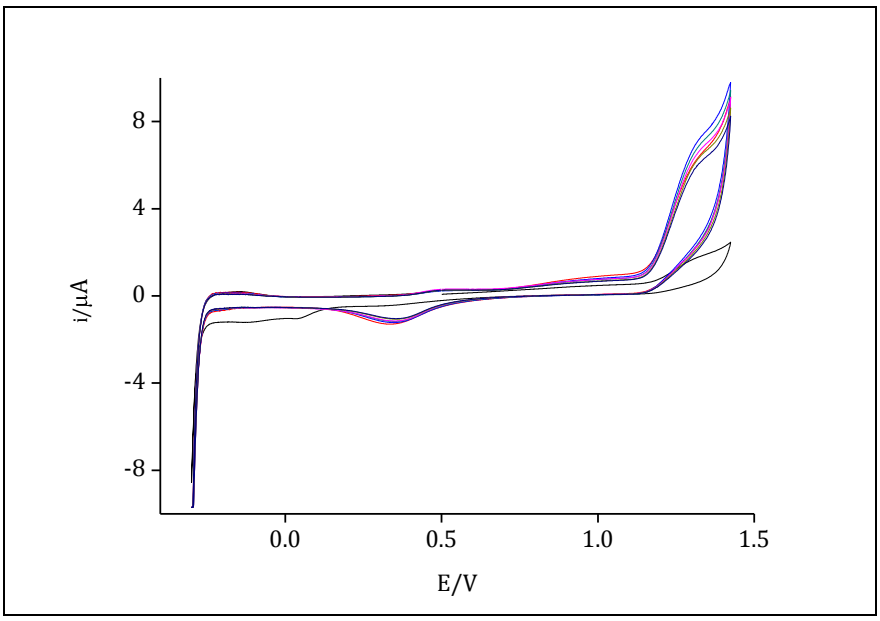

Figure 5.26: Typical CV showing successive cycles of the C30μ3d array electrode in degassed (with Argon) 0.05 M aqueous sulfuric acid at a potential sweep rate of v = 100 mV s^{-1}.

A characteristic oxygen adsorption and oxidation wave is observed above +0.8V on the oxidative scan, with the onset of further solvent based oxidation near +1.2 V. On the reductive scan, there is also a characteristic oxide stripping peak below +0.5V, along with the onset of a characteristically steep solvent reduction current near -0.3 V and its associated sharp hydrogen gas product re-oxidation peaks immediately on the reverse re-oxidative scan. These are characteristic of a clean platinum electrode, and the observed currents, which increase with cycle number then plateau as oxygen and hydrogen production leads to a progressively cleaner electrode surface, are characteristic of a Platinum multi-electrode array.

Figure 5.27 shows the corresponding CV in 10 mM ferricyanide after cleaning the substrate in sulfuric acid for 30 cycles. For comparison the response of the best KCl cleaned C30μ3d substrate, (Figure 5.23 b)) is also given.

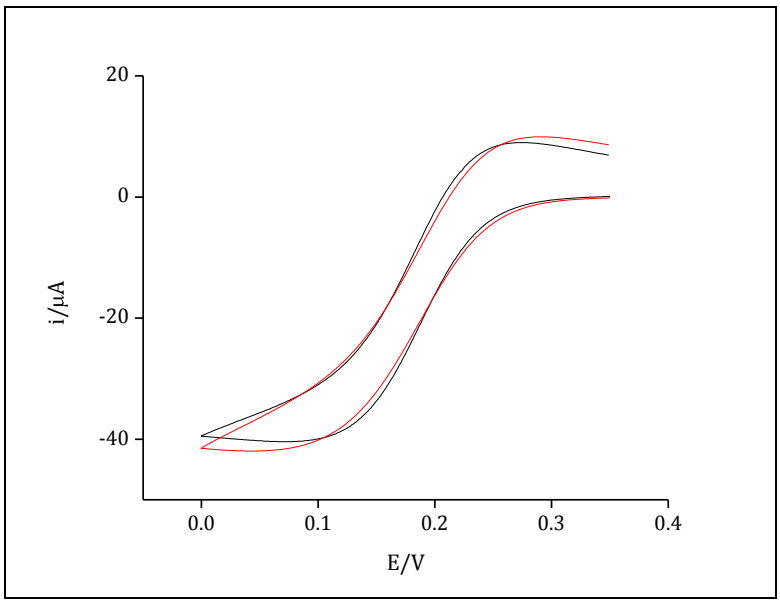

Figure 5.27: Ferricyanide (10 mM) reduction CV comparison at a sweep rate of 5 mVs^{-1} for a C30μ3d array electrode after cleaning in KCl (black plot) which has a maximum current of 40.41 μA and for a C30μ3d array cleaned in sulfuric acid (red plot) with a maxim current of 41.96 μA).

It can be seen in Figure 5.27 that cleaning in both sulfuric acid [0.05 M] and in KCl [0.1 M] produce very similar CVs in 10 mM ferricyanide, with only 3.7% difference in their responses. The remainder of the results shown are that of typical responses for C30μ3d substrates cleaned in sulfuric acid. Figure 5.28 shows a number of CV responses for different C30μ3d chips at different sweep rates, obtained after cleaning the substrates in sulfuric for between 30-60 cycles.

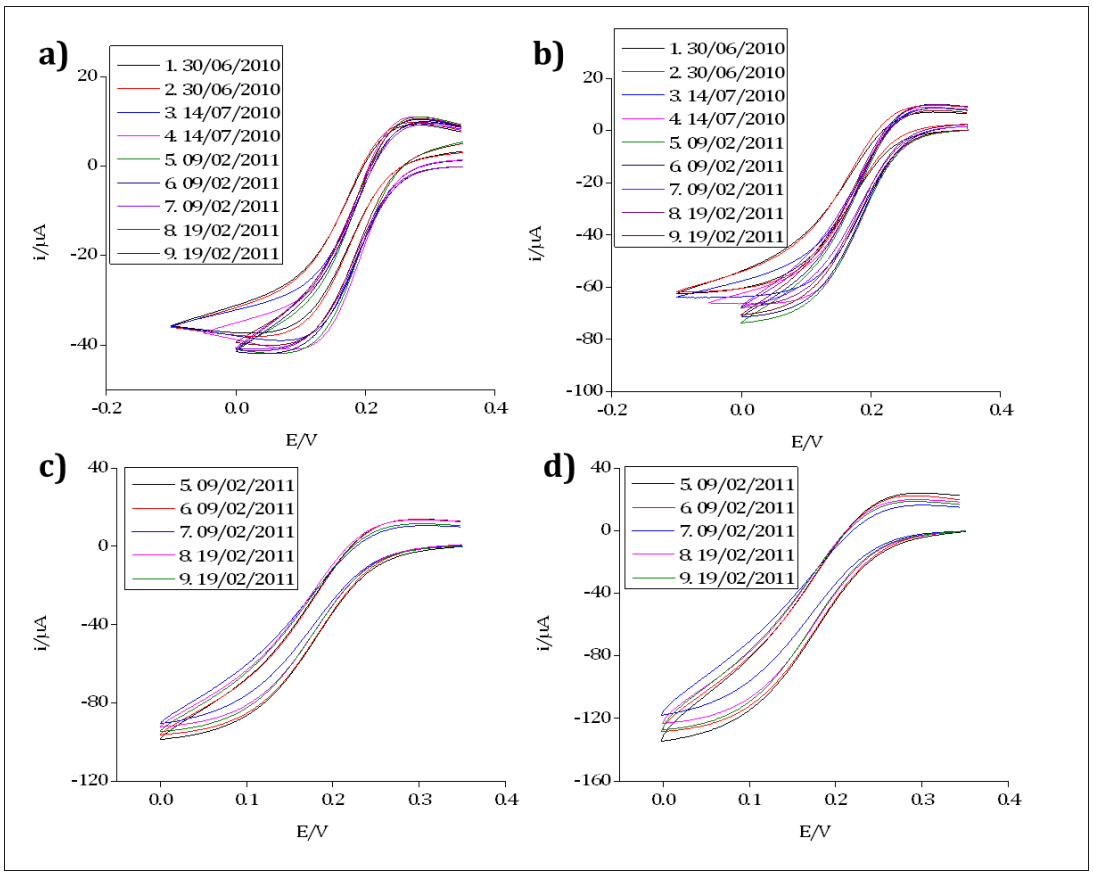

Figure 5.28: First sweep CV responses of several C30µ3d substrates in ferricyanide [10mM] at different sweep rates with: **a)** the responses at 5 mVs^{-1} with an average maximum current of 40 ± 2 µA; **b)** the responses at 500 mVs^{-1} with an average maximum current of 66 ± 5 µA; **c)** the responses at 5 Vs^{-1} with an average maximum current of 95 ± 3 µA; and **d)** the responses at 30 Vs^{-1} with an average maximum current of 126 ± 6 µA. It must be noted that early experiments were not run at very high sweep rates as the response was only just beginning to become understood. The potential window was also taken out to -0.05 or -0.1 V to observe the shape of the curve at more negative potentials. The electrodes are numbered in chronological order, i.e. Exp. 1, was carried out first.

When considering limiting currents, overall variation of around 12% in current response was found. This can be attributed to the difficulty in cleaning the arrays effectively, even in sulfuric acid. This will be discussed in greater in detail in section 6.3.2 when using EIS, which is much more sensitive to impurities on the electrode surface. It must be noted that even for CaviArE substrates 5-9 in figures 5.28 a) and b), which are representative, of the best cleaned electrode responses, there is a 4 % variation in their current values. The slopes of the CVs also gives some indication of the cleanliness of the electrode surface and figure 5.28 a) and b) clearly show that during earlier experiments the electrodes were not as clean as in later experiments, when the number of cleaning cycles was increased in an attempt to remove more

impurities from the surface. This reduced the overall variation in current response.

Now considering the 4% variation, temperature can also have an impact on the current response, since the diffusion coefficient is dependent on the temperature. The diffusion coefficient of ferricyanide, quoted in section 2.2 is given for a temperature of 298 K. However, due to the issues of convective stirring in water baths, the majority of the electrode arrays were analysed without temperature control. Therefore deviation in electrode current output could also be caused by small temperature changes of the solution in the lab. In fact the solution temperature was recorded before experimentation and the average temperature was 292 ± 2 K. Several experiments were performed in a water bath where the solutions were heated and maintained at 298 K in order to look at the deviation in current response. However in order to obtain representative data, the temperature control had to be turned off when gathering data, as the heating system caused substantial stirring within the solution. Therefore this method could not be used to gather data over longer time periods, as the solution began to cool over time. Figure 5.29 shows the CV responses for a C30µ3d electrode in such a temperature controlled experiment at 298 K, compared to the best cleaned C30µ3d (electrode number 6 from figure 5.28) response at lab temperature.

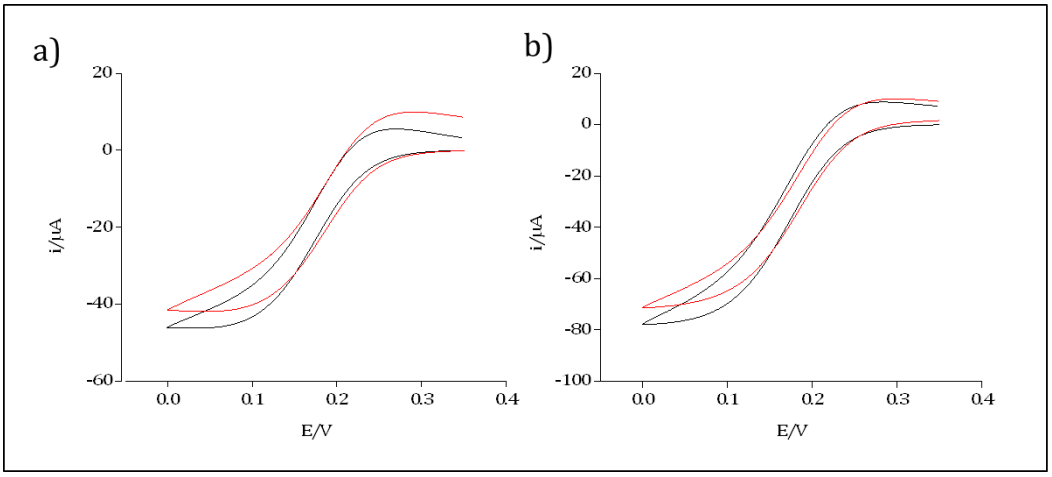

Figure 5.29: Comparison of two C30µ3d substrates in ferricyanide [10 mM] at 298 K (black plot) and 291 K (red plot): where **a)** shows the response at 5 mVs^{-1}. The maximum current at 298 K is -46.27 µA and the maximum current at 291 K is 41.96 µA; b**)** shows the response at 500 mVs^{-1}. The maximum current at 298 K is -78.03 µA and the maximum current at 291 K is 71.47 µA.

Figure 5.29 shows that there does appear to be an increase in current response with increase in temperature with a deviation of almost 9% from the electrode monitored at lab temperature. This shows that an increase in temperature can substantially increase the limiting current response. The natural variation in lab temperature did not exceed 294 K and therefore the 4% variation may be due to small temperature fluctuations in the lab.

Since there are 1764 electrode elements within the CaviArE substrates under investigation, it is encouraging to observe that the current response does not appear to be affected when one or two of the electrode elements are not fabricated effectively. Figure 5.30 shows an optical image of one of the C30µ3d electrode arrays and shows that one of the electrodes was found to be malformed.

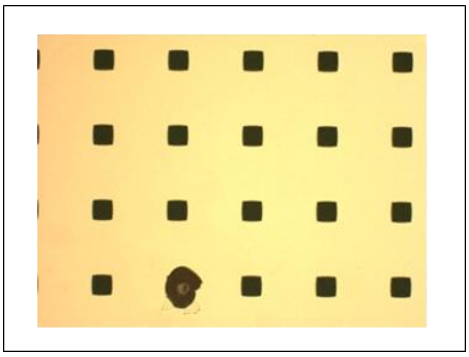

Figure 5.30: Optical image of portion of a C30µ3d electrode array with a malformed electrode in the field of view, under the Zeiss Axiotron microscope and captured with a Diagnostics Instruments Spot Insight QE digital camera.

Figure 5.31: shows the corresponding CV obtained for the electrode array shown in Figure 5.28 in ferricyanide [10 mM], compared to the response from a very clean, well fabricated C30µ3d electrode (electrode number 6 from figure 5.28).

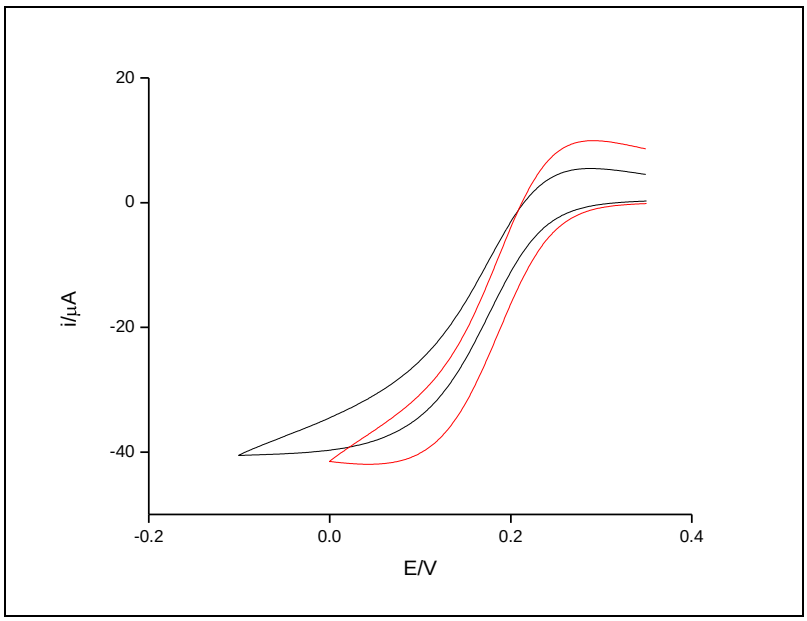

Figure 5.31: Ferricyanide [10 mM] reduction CV comparison at a sweep rate of 5 mVs^{-1} (black line) for a C30µ3d array with a malformed electrode with a maximum current of 40.53 µA and for (red line) a very clean, well fabricated C30µ3d array with a maxim current of 41.96 µA).

The difference in the electrode current responses recorded in Figure 5.31 is 3.4% (or 1.43 µA) which is well within the variation observed between other, well formed, electrode arrays.

Since the C30µ3d electrodes analysed during this research consistently produce very similar responses in ferricyanide, it provides confidence that these responses are indeed the true C30µ3d responses of electrochemical reduction of ferricyanide. A full analysis of the data will be presented in Chapter 6 and 7; however, before a thorough study could be undertaken, a number of practical measurement issues needed to be addressed.

As several electrode arrays were analysed at the same time, an interesting observation was made. The cyclic voltammetric response in ferricyanide became more sigmoidal, the closer the crocodile clip, holding the substrate was to the argon stream. Figure 5.32 shows the schematic diagram of the experiment lid, with numbered crocodile clip ports and two CVs recorded on different crocodile clips.

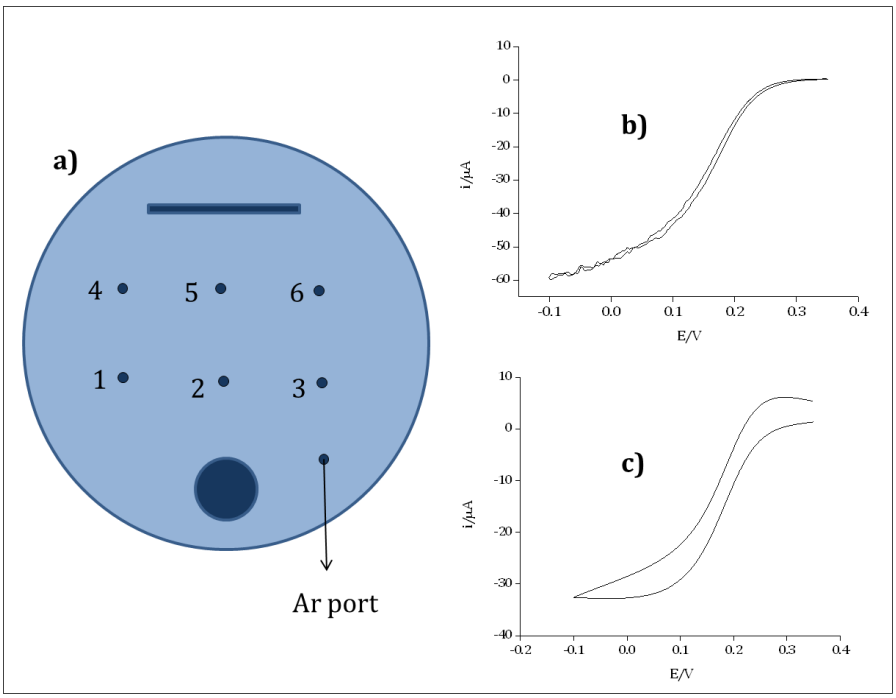

Figure 5.32: showing **a)** the schematic diagram of the experiment lid designed specifically for this project, the crocodile clip ports are numbered from 1-6 and the port for the argon stream is also labelled; **b)** a CV obtained in 10 mM ferricyanide for a C30µ3d array attached to port 3; and **c)** a CV obtained for a C30µ3d attached to port 5.

This suggests that even though the argon stream was flowing slowly to provide an argon blanket over the surface of the previously de-aerated solution, it also provided enough convective stirring to affect the CV response. Since this response was different on different crocodile clips and indeed on different days and since the argon flow speed could not be accurately controlled reproducibly, it was decided that an argon blanket would not be used. Studies were undertaken which showed that oxygen reduction occurred at more negative potentials than recorded during ferricyanide reduction and therefore it was not necessary to deoxygenate the solution prior to ferricyanide analysis. An argon blanket was still blown over the surface during acid cleaning as these CV responses are influenced by oxygen reduction.

Another problem encountered, was caused by the crocodile clips becoming rusted. Even though care was taken to prevent wicking of solution up the back of the silicon substrate, the crocodile clips were constantly exposed to the moist atmosphere in the headspace of the analysis vessel, hence rusting was

observed and the crocodile clips had to be changed regularly, to ensure good electrical contact with the arrays.

In order to overcome this problem, edge connectors (JST, 11FMN-BTK-A) were used to connect the CaviArE substrates. An insulated wire was partially stripped at both ends and soldered to all the protruding edge connection teeth, to ensure good electrical connection with the platinum contact pad. The edge connector was then sealed with epoxy resin (Araldite), as shown in Figure 5.33.

Figure 5.33: Photographic image (Sony, Cybershot DSC P200) of one of the C30µ3d substrates attached to an edge connector (JST, 11FMN-BTK-A) and sealed with epoxy resin (Araldite), with a wire soldered to the edge connector teeth protruding from the top.

The metal teeth were then also sealed with epoxy resin prior to experimentation to prevent exposure of the protruding teeth to solution. Using the connectors, multiple arrays could be analysed using the experiment lid designed, as the wires could be pushed through the six ports and connected to the Multiplex device via crocodile clips outside of the experimental vessel.

Even though the issue of passivation product build-up was seemingly overcome, by using ferricyanide only as the initial reactant (rather than an equimolar mixture of ferri/ferrocyanide), the voltmammetric response of an electrode array over time was undertaken to see if passivation product still builds up over long periods. One of the C30µ3d arrays was, after acid cleaning, placed in 10 mM ferricyanide and three CV scans were recorded periodically

every 30 minutes over a period of 15 hours at a sweep rate of 5 mVs^{-1} and 500 mVs^{-1}. Figure 5.34 shows selected CV responses from this study.

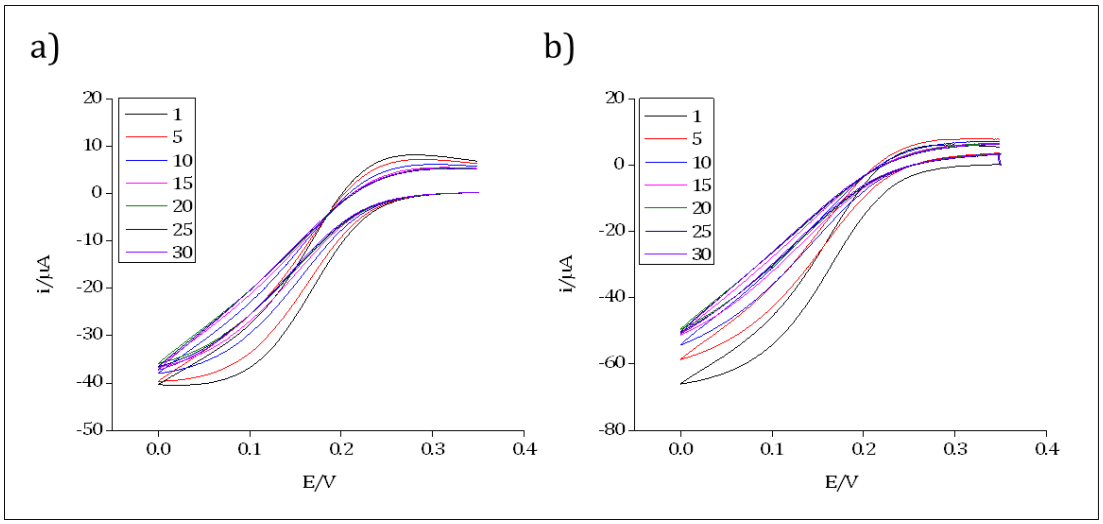

Figure 5.34: Showing first scan CVs obtained periodically over 15 hours in 10 mM ferricyanide of a C30μ3d at **a)** 5 mVs^{-1} and **b)** 500 mVs-1. After the first scan 1, the CVs after every 2.5 hours are shown.

Figure 5.34 clearly shows that the ferricyanide response does decay over time, suggesting that a passivation layer may build up on the electrode surface during repeated ferricyanide reduction and re-oxidation cycles. However this degradation of response does not occur over the time frames of ordinary experiments. EIS experiments at different dc potentials takes less than one hour for each electrode, and substantial degradation was only recorded after 2.5 hours. It is encouraging to note, that the electrode was not irreversibly inactivated. Upon cleaning in sulfuric acid, the passivation layer was fully removed and the electrode response was recovered.

Finally EIS studies were undertaken in ferricyanide and it was found that the frequency range used, for both the single microsquares and for the microsquare arrays was not sufficient for the study of the CaviArE devices. Figure 5.35 shows a typical EIS response for a C30μ3d array in ferricyanide [10 mM] between 1000 Hz and 0.1 Hz and rms amplitude of 0.001 V, and the corresponding response between $1x10^6$ Hz and 0.1 Hz and rms amplitude of 0.01 V.

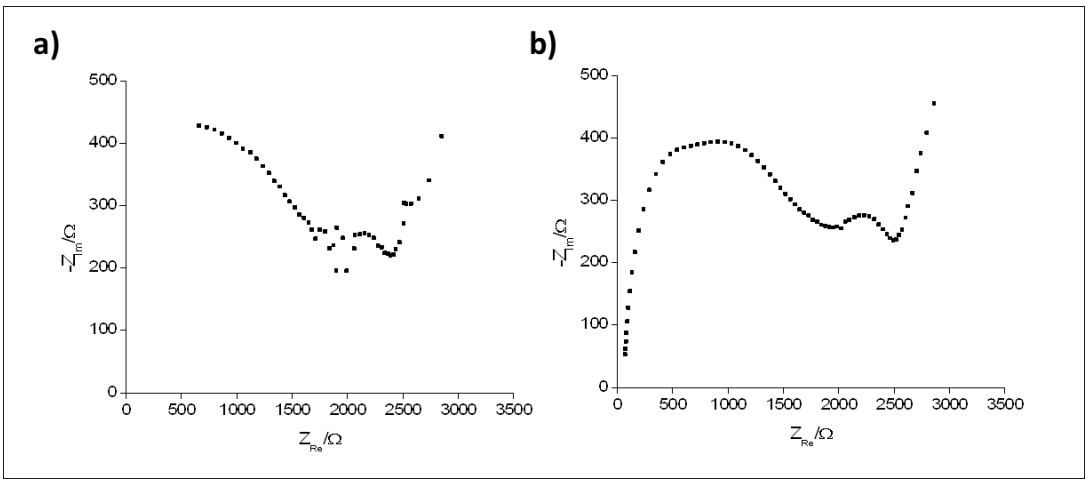

Figure 5.35: Showing **a)** a typical Nyquist plot obtained for a C30µ3d array in ferricyanide [10 mM] at dc potential of 0.190 V between frequencies of $1x10^3$ Hz and 0.01 Hz and ac amplitude 1 mV rms; and **b)** the Nyquist plot of the same substrate between $61x10^3$ Hz and 0.01 Hz and ac amplitude 10 mV rms.

It is clear that the frequency range shown in Figure 5.35 a) does not probe the entire CaviArE EIS response and therefore the frequency range had to be increased. There is also a lot of unwanted noise, preventing the response from being accurately analysed. As the degree of noise depends on the ac voltage rms amplitude, this was increased to 10 mV in subsequent experiments. This is still small enough to assure linearization of the ac response for equivalent circuit analysis.

5.4. Conclusions

The CaviArE design presented in this chapter was first patented in 1999[19] However, research and development of the materials and fabrication processes needed to be carried out, before a systematic study of the electrochemical responses could be undertaken; and indeed before the design could be presented as a viable industrial sensing device. The fabrication process of CaviArE, Generation 3, described in section 5.2.3 provides a robust and viable method for producing, reproducible nanoelectrode arrays of controlled dimensions. This method provides a well characterised procedure for making CaviArE (and square arrays), which are appropriately insulated, well defined and give reproducible, characteristic micro- and nano- electrochemical responses. A full analysis of the CaviArE devices will now be presented in Chapter's 6 and 7.

5.5. References

(1) Heinze, J. *Angewandte Chemie International Edition in English* **1993**, 1268.

(2) Forster, R. J. *Chemical Society Reviews* **1994**, *23*, 289

(3) Stulik, K., C. Amatore, K. Holub, V. Marecek and W. Kutner *Pure and Applied Chemistry* **2000**, *72*, 1483.

(4) Bard, A. J.; Faulkner, L. R. *Electrochemical Methods, Fundamentals and Aplications*; Second ed.; John Wiley and Sons, Inc.: Hoboken, 2001.

(5) Bond, A. M. *Analyst* **1994**, *119*, 1R.

(6) Tu, Y.; Lin, Y. H.; Ren, Z. F. *Nano Lett.* **2003**, *3*, 107.

(7) Heller, I.; Kong, J.; Heering, H. A.; Williams, K. A.; Lemay, S. G.; Dekker, C. *Nano Lett.* **2005**, *5*, 137.

(8) Wei, D. C.; Liu, Y. Q.; Cao, L. C.; Wang, Y.; Zhang, H. L.; Yu, G. *Nano Lett.* **2008**, *8*, 1625.

(9) Arrigan, D. W. M. *Analyst* **2004**, *129*, 1157.

(10) Compton, R. G.; Wildgoose, G. G.; Rees, N. V.; Streeter, I.; Baron, R. *Chemical Physics Letters* **2008**, *459*, 1.

(11) Murray, R. W. *Chemical Reviews* **2008**, *108*, 2688.

(12) Feeney, R.; Kounaves, S. P. *Electroanalysis* **2000**, *12*, 677.

(13) Fleischmann, M.; Pons, S. *Analytical Chemistry* **1987**, *59*, 1391A.

(14) Gerasopoulos, K.; Chen, X. L.; Culver, J.; Wang, C. S.; Ghodssi, R. *Chemical Communications*, *46*, 7349.

(15) Alonso-Lomillo, M. A. n.; RÃ¼diger, O.; Maroto-Valiente, A.; Velez, M.; RodrÃ-guez-Ramos, I.; MuÃ±oz, F. J.; FernÃ¡ndez, V. c. M.; De Lacey, A. L. *Nano Lett.* **2007**, *7*, 1603.

(16) Koenigsmann, C.; Zhou, W.-p.; Adzic, R. R.; Sutter, E.; Wong, S. S. *Nano Lett.*, *10*, 2806.

(17) Hu, R.; Cola, B. A.; Haram, N.; Barisci, J. N.; Lee, S.; Stoughton, S.; Wallace, G.; Too, C.; Thomas, M.; Gestos, A.; Cruz, M. E. d.; Ferraris, J. P.; Zakhidov, A. A.; Baughman, R. H. *Nano Lett.*, *10*, 838.

(18) Li, Q.; Penner, R. M. *Nano Lett.* **2005**, *5*, 1720.

(19) Freeman, N. J.; Mount, A. R. United Kingdom, 1999; Vol. WO/1999/060392.

(20) Schmitt, G.; Schultze, J. W.; Fassbender, F.; Buss, G.; Luth, H.; Schoning, M. J. *Electrochimica Acta* **1999**, *44*, 3865.

(21) Sherman, A. *Journal of The Electrochemical Society* **1990**, *137*, 1892.

(22) May, G. S.; Sze, S. M. *Fundamentals of Semiconductor fabrication*; Wiley International Esdition ed.; John Wiley ans Sons.: Hoboken, 2004.

6. Voltammetric Characterisation of nanoband Cavity Array Electrodes (CaviArE)

6.1. Introduction

Chapter 5 described the development of a fabrication method (section 5.2.3) that produces well defined microsquare arrays and nanoband arrays which are robust and provide reproducible responses and so they can be used for systematic study. Of greatest interest for this research is the nanoband Cavity array electrode (CaviArE) design. The nanoarray offers the advantages of large currents similar to that of a macroelectrode, with the increased sensitivity and characteristics of a nanoelectrode.

This chapter investigates the voltammetric response of the novel electrode array architecture developed in chapter 5 with the aim of demonstrating that the resulting response is reproducible, quantifiable and characteristic of a nanoband electrode of high effective area. For initial studies one geometry the, (30 μm)^2 hole, 90 μm spaced CaviArE design (C30μ3d) was chosen in order to carry out a systematic and thorough study. The voltammetric data of the corresponding microsquare array (S30μ3d) is also presented for direct comparison. Figure 6.1 shows the optical microscope images of a central section of the S30μ3d array compared with a C30μ3d array.

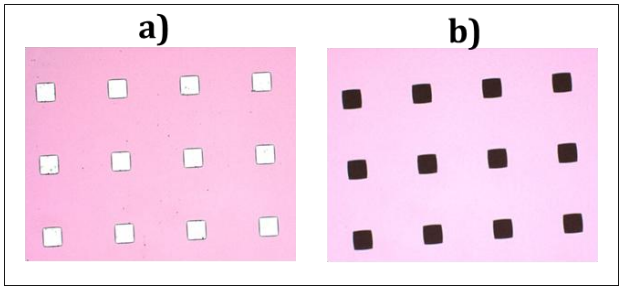

Figure 6.1: Optical images viewed under the Zeiss Axiotron microscope and captured with the Diagnostics Instruments Spot Insight QE digital camera showing **a)** the S30μ3d architecture ((30 μm)^2 electrodes, 3d spacing) and **b)** the C30μ3d architecture ((30 μm)^2 cavities, 3d spacing).

As with the single microsquare electrodes (Chapter 4), this chapter primarily focuses on the voltammetric responses of CaviArE (C30μ3d) arrays in

10 mM ferricyanide (section 6.3.1.), considering the cyclic voltammetric and current-time transient data analysing the responses. The CaviArE response in lower ferricyanide [1.0 mM] concentrations will also be presented as well as the response in ferrocene carboxylic acid [1.0 mM]. Finally, the response of CaviArE devices of different dimensions and pitches will be presented.

6.2. Specific Experimental

6.2.1. Electrolytes

6.2.1.1. Ferricyanide Solutions

All aqueous ferricyanide solutions [10 mM] were prepared as described in section 3.1.1. Ferricyanide [1 mM] was prepared in a 250 cm^3 volumetric flask by taking 25 cm^3 ferricyanide [10 mM] and making up to the mark with KCl [0.1 M] stock solution.

6.2.1.2. Ferrocene Carboxylic Acid Solution

Ferrocene carboxylic acid [1 mM] (Alfa Aesar, 98%) was added to aqueous KCl solution [0.1 M] and dissolution was aided by the addition of sodium hydroxide [3 M] (Sigma Aldrich, ACS reagent ≥ 98%); drop wise, to the solution and by sonification. The solution pH was measured as 11.65 prior to experimentation.

6.2.2. Ferrocene Carboxylic Acid Measurements

The electrode array was first electrochemically cleaned in degassed aqueous sulfuric acid [0.05 M] between +1.6 and -0.37 V for 50 cycles at 100 mV s^{-1} (see section 3.4.1.1) and then placed in the ferrocene carboxylic acid solution. Cyclic voltammograms were recorded at a range of sweep rates from 5 mV s^{-1} to 1 V s^{-1} vs. SCE and optimised as cycling between +0.05 V and +0.55 V or +0.60 V, since the E^{θ} value for this system is 0.275 V. Potential steps were recorded from +0.05 V to 0.5 V, +0.55 V and 0.275 V for ten seconds at a sample time of 0.05 s^{-1}. All other analysis was undertaken as described in section 3.4.

6.3. Results and Discussion

6.3.1. Voltammetric Response of the C30µ3d arrays in 10 mM potassium Ferricyanide

The electrode arrays were cleaned in sulfuric acid by successive cycling until the CV profile no longer changed. The electrodes were than analysed in 10 mM ferricyanide. Figure 6.2 shows the typical first sweep CVs obtained for the reduction of ferricyanide over a wide range of sweep rates (from 5 mVs^{-1} to 30 Vs^{-1}).

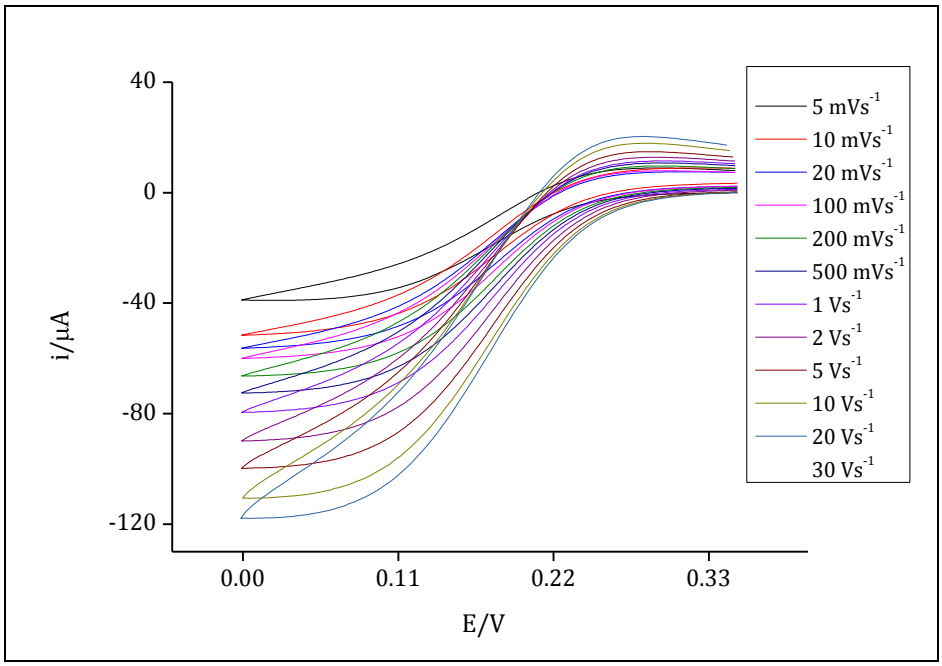

Figure 6.2: Typical first sweep CVs obtained for the reduction of 10 mM ferricyanide in 0.10 M KCl solution at the sweep rates shown. The onset sweep potential, E, was +0.35 V with the initial direction of scan to negative potentials.

It is clear that pseudo-steady-state voltammograms are obtained with near sigmoidal CV shapes. The current magnitudes are tens to hundreds of microamps, which indicate the response of all the 1764 square enclosed nanobands in the array. The currents are pseudo-steady-state as their magnitude is sensitive to sweep rate. It is clear from these data that E < +0.05 V corresponds to a mass-transport-limited current. Figure 6.3 shows a typical optical image of the C30µ3d arrays after experimentation.

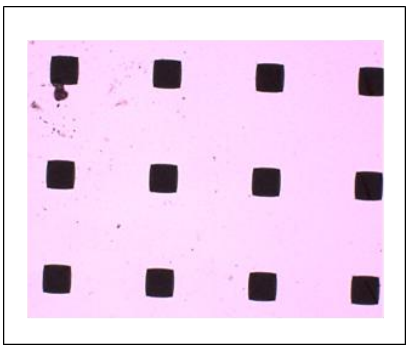

Figure 6.3: Optical image of a central section of a C30µ3d array after experimentation viewed under the Zeiss Axiotron microscope and captured with the Diagnostics Instruments Spot Insight QE digital camera. The crystals observed in the left hand upper corner are likely to be ferricyanide crystals, which have dried on the surface.

The figure confirms that the electrode surface was not damaged during experimentation, providing confidence that the pseudo-state responses are the true response of the CaviArE devices.

It has been established[1-3] that pseudo-steady-state conditions are observed for planar microband or cylindrical electrodes; this suggests that the CaviArE devices may behave similarly to planar nanobands. If this is the case, the question is: in what time range is planar nanoband behaviour observed? It has previously been shown[1] (section 2.4, table 2.1), that at a sufficiently long time, t, to ensure cylindrical diffusion is occurring, the mass transfer limiting current, i_L, for a band is given as[1]:

$$i_L = \frac{2\pi n F D c^{\infty} l}{\ln\left[\frac{4(Dt)}{r^2}\right]} \qquad \textbf{Eqn. 6.1}$$

where l is the length of the microband and r is related to the electrode width, w by $r = w/\pi$. However, a more generalized expression can be given as:

$$|i_L| = \frac{2\pi n F D c^{\infty} l}{\ln\left[\frac{K(Dt)}{w^2}\right]} \qquad \textbf{Eqn. 6.2}$$

where the value of the constant, K depends on the electrode geometry. For a planar microband this value is 4π and 64 at medium and long times,

respectively[4]. It is unclear, however, what the value of K would be for diffusion to these nanoband CaviArE devices, arranged vertically in each depression. Rearrangement of equation 6.2 and substitution for the microband area, A = lw, gives

$$|i_L|^{-1} = \left(\frac{2\pi nDAFc^{\infty}}{w}\right)^{-1} \left\{\ln\left(\frac{KD}{w^2}\right) + \ln t\right\} \qquad \textbf{Eqn. 6.3}$$

This indicates that a plot of $|i_L|^{-1}$ versus ln$t$ should be a straight line of gradient, $\boldsymbol{m = ((2\pi DAFc^{\infty})/w)^{-1}}$ and ln$t$ axis intercept of – ln(KD/w^2).

For any potential the general expression is:

$$|i|^{-1} = \left(\frac{2\pi nDAF(c^{\infty}-c^{0}}{w}\right)^{-1} \left\{\ln\left(\frac{KD}{w^2}\right) + \ln t\right\} \qquad \textbf{Eqn. 6.4}$$

where $|i|$ is the current obtained at this potential and where c^0 is the concentration of the redox species at the electrode at this potential. Figure 6.4 a) shows a typical current-time transient plot with a potential step of +0.35 to +0.05 V, a potential which should correspond to the diffusion limited current, i_L.

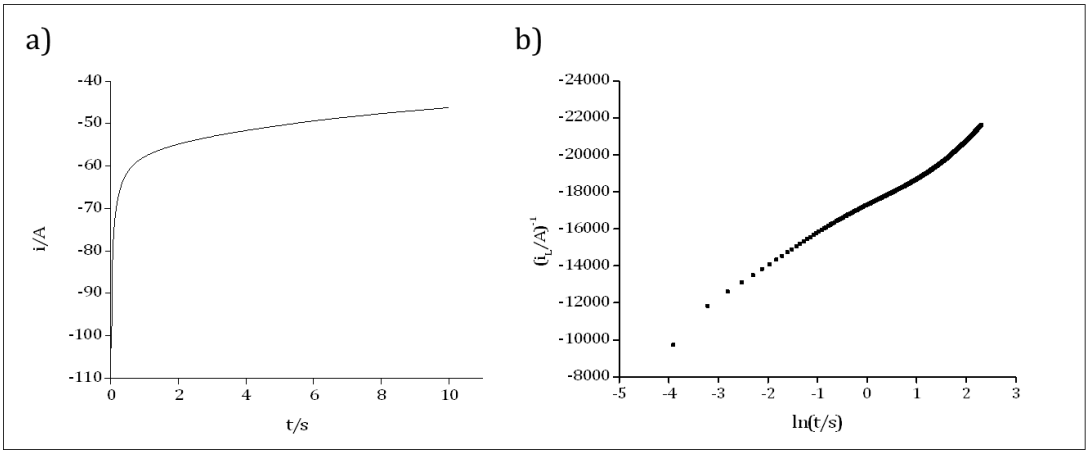

Figure 6.4: Showing **a)** the current-time transient graph obtained for a C30µ3d substrate in ferricyanide [10 mM] with a potential step from +0.35 V to +0.05 V, recorded for 10 seconds; and **b)** the corresponding $|i_L|$ vs. ln$t$ plot.

The resulting plot of $|i_L|^{-1}$ vs. ln$t$ is shown in Figure 6.4 b). It is clear that there are three distinct regions in Figure 6.4 b). The first is below ln$t$ ≈ -0.5, the

second is a straight line region between ln$t$ ≈ -0.5 to ln$t$ ≈ +1.3, whilst the third is above ln$t$ ≈ +1.3. Figure 6.5 shows the diffusional regimes speculated to be occurring between each distinct region of the $|i_L|^{-1}$ vs. ln$t$ plot.

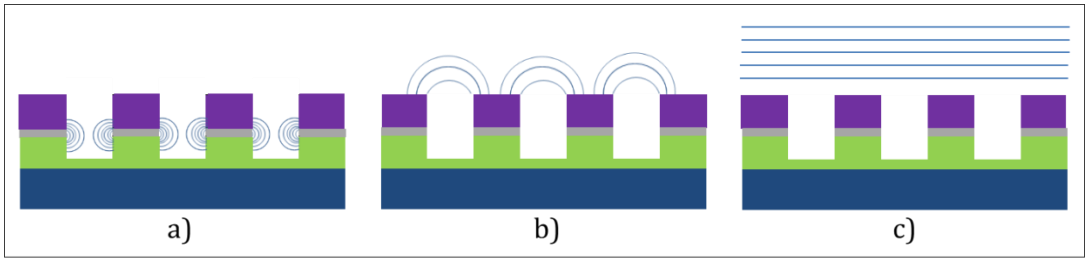

Figure 6.5: Schematic diagram to show the diffusional regimes attributed to the three distinct regions in Figure 6.4 b) where a) is radial diffusion within the microsquare cavity occuring between ln$t$ = -3 and ln$t$ = -0.5, b) is radial diffusion outside of the cavity occurring between ln$t$ = -0.5 and ln$t$ = +1.3 and c) is planar diffusion towards the entire array occuring above ln$t$ > +1.3.

It was speculated that the straight line response between ln$t$ = -3 and ln$t$ ≈ -0.5 is the response of radial diffusion within the isolated microsquare cavities (Fig. 6.5 a)). The straight line region between ln$t$ ≈ -0.5 to ln$t$ ≈ +1.3 was hypothesised to be due to the response of radial diffusion outside of the cavity (Fig. 6.5 b)) whilst the region above ln$t$ ≈+1.3 was postulated to be the response of the overlapping arrays (Fig. 6.5 c)).

The deviation from a straight line at ln$t$ = -4 was postulated to be either due to capacitive charging or perhaps the response of linear diffusion to the nanoband in a time region dominated by the Cotrellian current model (Eqn. 2.8). To look at this Cottrell hypothesis, the Cottrell equation (Eqn. 2.8) was used to calculate the expected Cottrell current contribution at ln$t$ = -4 (0.05 s). For a nanoband with a width of 5 x 10^{-6} cm and length of 0.012 cm, the Cottrell current at 0.05 s for ferricyanide reduction is calculated to be 6.06 x 10^{-11} A, which translates to a current of -1.07 x10^{-7} A for 1764 individual nanoband electrodes. This corresponds to a value of -9.35 X 10^{6} A^{-1}. In comparison, i^{-1} experimentally calculated at ln$t$ = -4 is -9.05 X10^{3} A^{-1}. This shows that that the Cottrell current is 1000 times smaller than the currents recorded experimentally at ln$t$ = -4 providing evidence that the deviation in response is not due to a Cottrell-dependent current response and therefore more likely caused by small charging currents at these fast times.

Turning back to Figure 6.4 b), there are two distinct regions where radial diffusion towards the individual electrodes is occurring, region a) (between ln*t* = -3 and ln*t* = -0.5) where radial diffusion within the cavity is expected to be occurring and region b) (between ln*t* = -0.5 and ln*t* = +1.3) where radial diffusion outside of the cavity has been established. It was unclear to which region, if any, nanoband theory might be applied. It is clear that in both regions the current is inversely proportional to ln*t* and therefore decreasing with time, so band-like behavior is likely to be occurring in both time domains.

For the graph given in Figure 6.4 b), linear regression lines were plotted for both regions between ln*t* = -3 and ln*t* = -0.5 and between ln*t* = -0.6 and ln*t* = +1.2. They both gave good straight lines and the fits are shown in Figure 6.6.

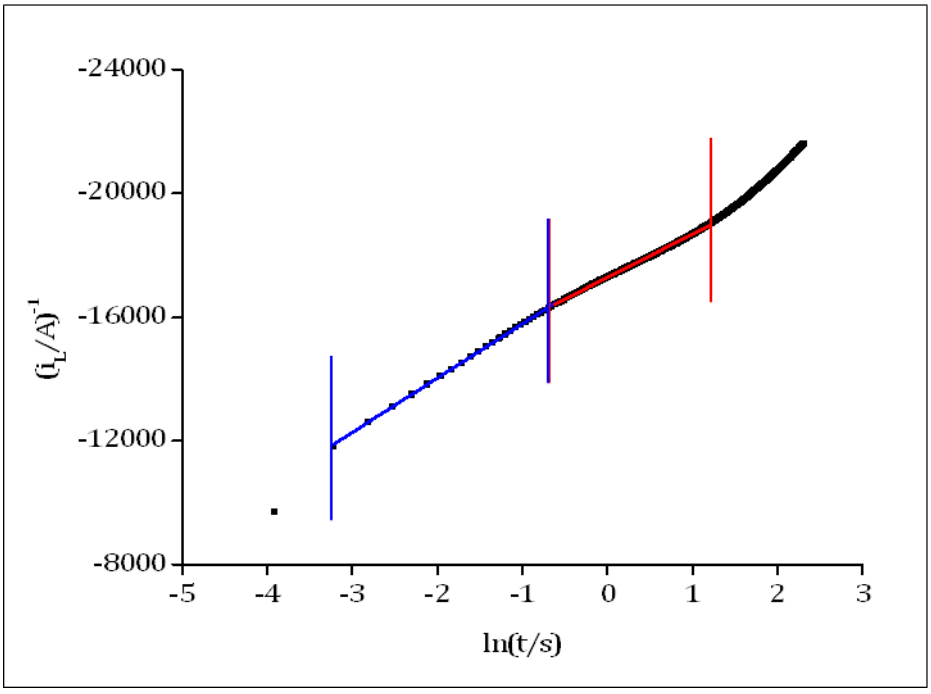

Figure 6.6: Plot of $|i_L|^{-1}$ vs. ln*t* for a typical C30µ3d array in ferricyanide [10 mM] between ln*t* = -1.0 to ln*t* = +2.8 with a linear best fits line plotted between ln*t* = -3.2 and ln*t* = -0.61 (blue line) and between ln*t* = -0.6 to lnt = +1.2 (red line). The blue linear regression has a slope, m = -1752 ± 6 A^{-1} and an intercept, c = -17530 ± 10 A^{-1} and correlation coefficient. r = 0.999. The red linear regression has a slope, m = -1409 ± 4 A^{-1} and an intercept, c = -17283 ± 3 A^{-1} and correlation coefficient, r = 0.999.

A good straight line is observed between ln*t* = -0.6 at and ln*t* = +1.2, in Figure 6.6 and for *w* = 50.0 nm, yields an experimental value of *K* = 0.76 ± 0.1 from

Equation 6.3, whereas the line between ln$t$ = -3.2 and ln$t$ = -0.6 yields an experimental value of K = 0.024 ± 0.01 for w = 50.0 nm. However, since K should be a constant proportional to $1/w^2$, the response at fast time scales may also indicate an apparent increase in electrode width within this time regime. This is consistent with the Warburg parameter measured during EIS analysis in section 7.3.2.3, suggesting that the diffusional regime established over this time period may not be simple radial diffusion from the electrode but a more complicated diffusional regime occurring over the entire width the cavity (Figure 7.23). Presently the exact diffusional regimes occurring within the cavity are unclear and further research, perhaps in conjunction with computer simulation, is required to better understand the electrode response at fast times. EIS is a more sensitive technique than current-time transient analysis to probe these questions and the diffusional regimes will be discussed in more detail in chapter 7.

Since the substrate also shows band behavior during the intermediate time regime (in this case between ln$t$ = -0.6 and ln$t$ = +1.2) and the radial diffusion profile outside of the cavity is better understood, it was decided that linear regression would be fitted over the intermediate time regimes for the remainder of the study. Good straight lines, within this similar region for all electrode arrays analysed was observed. However, although it appears, statistically, that the slope and intercept can be calculated accurately, with only a small error for individual experiments, the variation in response between different experiments is large. This suggests that the error is much greater than initially observed. Table 6.1 provides an example of some of the varying slopes and intercepts obtained from different $|i_L|^{-1}$ vs. ln$t$ plots over a range of 30µ3d experiments for a potential step from +0.35 V to +0.05 V. The corresponding K values calculated are also given.

Experiment	y-intercept (i/ A)$^{-1}$	Slope / (i/A)$^{-1}$	x-intercept (ln(t/s))	K
1	-17484 ± 9	-1512 ± 8	11.6	0.37
2	-22095 ± 2	-1460 ± 5	15.1	13.37
3	-18065 ± 3	-1381 ± 6	13.1	1.72
4	-16158 ± 3	-1307 ± 5	12.4	0.84
5	-16160 ± 3	-1367 ± 6	11.8	0.49
6	-22988 ± 2	-1460 ± 5	15.8	24.65
7	-17265 ± 3	-1345 ± 4	12.8	1.34
8	-17283 ± 3	-1409 ± 4	12.3	0.76
9	-16183 ± 3	-1302 ± 3	12.4	0.90
Average	**-18187**	**-1393**	**13.0**	**4.94**
Standard deviation	**2567**	**73**	**1.7**	**8.47**

Table 6.1: Table to show several slopes and y-intercept values, obtained from plots of $|i_L|^{-1}$ vs. ln$t$ over a range of C30µ3d experiments for a potential step from +0.35 V to +0.05 V. The corresponding K values calculated are given as are the average values and standard deviation of the data.

It is clear from the data in Table 6.1 that the error between experiments is large, specifically regarding extrapolation of the slope to the y-intercept. The average value calculated for K is 5 ± 8. In fact since K ∝ e^{-lnt}, a variation of 13 ± 2 in ln$t$ actually corresponds to a possible factor of 10 variation in K. The value of K must be positive but could realistically have a value of >0 - 10 - < 100. This method of determining K is therefore not effective. Parallel simulation studies may provide a better estimate for K during future research.

The diffusion layer from a nanoband, where ferricyanide has been depleted by the electrode reaction, will be expected to grow with a characteristic thickness, L of[5]:

$$L = (\pi D t)^{1/2} \qquad \textbf{Eqn. 6.5}$$

The thickness of the depletion layer at the upper and lower limits of the linear regression line, shown in Figure 6.13 was calculated. For ln$t$ = +1.2 (3.32 s) the depletion layer thickness is 85.3 µm. For the C30µ3d architecture, each microsquare cavity is separated by 90 µm and therefore diffusional overlap would be expected to occur as the depletion layer reaches a similar thickness (at near 3.69 s or ln$t$ = 1.30). The current will drop when diffusion layers from

neighbouring nanobands overlap and thus the departure observed in Figure 6.13 is therefore consistent with a reduction in current due to diffusional overlap from neighbouring depressions. The depletion layer thickness calculated from the upper limit of the visually selected linear regression line, further validates this.

The depletion layer thickness calculated from the lower limit of the linear regression line at ln*t* = -0.58 (0.55 s) is 34.7 µm. Since the microsquare cavities are 30 µm in length, planar diffusion outside of the hole would not be expected to be observed until the depletion layer reaches at least this thickness, which is consistent with the value obtained from the linear regression line. This behavior is therefore consistent with diffusion to a band of characteristic nano-dimension and demonstrates the applicability of equation 6.3. The fact that a straight line is observed below lnt ≈ -0.5, suggests that nanoband behaviour is also occurring within the cavity, though the exact diffusional regime is presently unknown.

Current-time transients were also obtained for these electrodes over a period of ten seconds at different potential steps. Figure 6.6 shows typical current-time transients and corresponding $|i|^{-1}$ vs. ln*t* plots recorded.

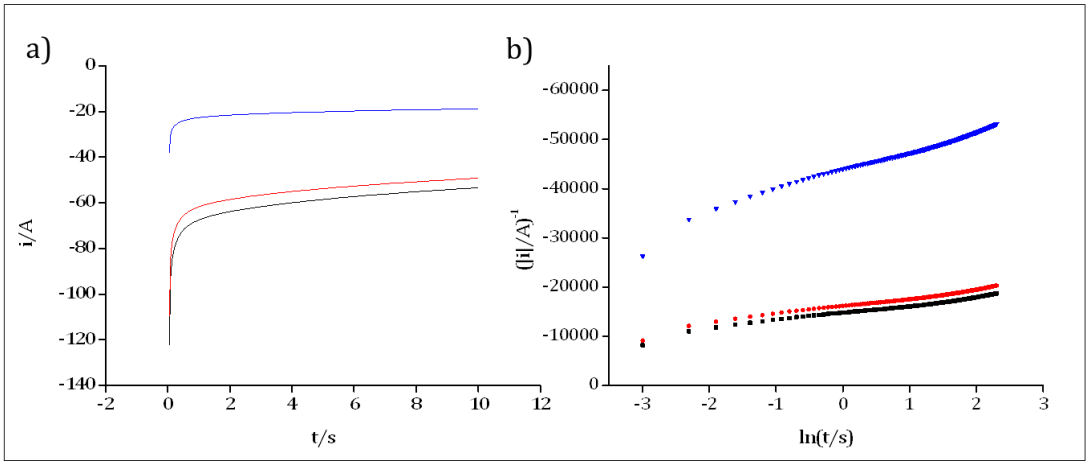

Figure 6.7: Plot of **a)** the current time transient plots, obtained for a C30µ3d substrate in ferricyanide [10 mM] for ten seconds for potential steps of +0.35 V to 0.00 V (black); +0.35 V to +0.05 V (red); and +0.35 V to +0.19 V (pink); and **b)** the corresponding $|i|^{-1}$ vs. lnt plots.

It is reassuring to see that the three diffusional regions observed in Figure 6.4 b) occur at the same times for all potential steps recorded. Linear regression lines

were therefore fitted to the graphs obtained for the different potential steps of numerous C30µ3d arrays, between the same regions as that for the potential step from +0.35 V to +0.05 V. The average values and standard deviation for each potential step is recorded in table 6.2 below. The values of *K* are also calculated.

Potential Step / V	**Average value of gradient / $(i/A)^{-1}$**	**Average y-intercept / $(i/A)^{-1}$**	**Average x-intercept (ln(t/s))**	***K***
+0.35 – 0.00	-1390 ± 122	-18799 ± 3002	13.5 ± 2	2.5 ±8
+0.35 – +0.05	-1393 ± 72	-18187 ± 2567	12.9 ± 2	1.5 ±8
+0.35 – +0.19	-3186 ± 372	-47646 ± 6978	15.0 ± 2	11.7 ± 8

Table 6.2: Table showing the average values obtained for of C30µ3d arrays, at a range of potential steps, in ferricyanide [10 mM]. The linear lines of best for individual electrode arrays all had correlation coefficients ≥ 0.99 and the errors for both the slope and the intercept were small. However variation between electrode arrays have a much larger error, the values of *K* calculated from the x-intercept data is also given.

The gradient of the slope does not change, within experimental error, for potential steps of +0.35 to 0.00 V and +0.35 to +0.05 V. This would be expected to be the case as both steps are in the region where limiting current is observed on the CVs. The standard potential, E^{θ} for ferricyanide, for the systems under investigation, is close to +0.19 V. If equation 6.4 applies, at E^{θ}, $c^0 = c^{\infty}/2$, therefore it would be expected that a slope of $|i|^{-1}$ vs. ln$t$ plot for a potential step of +0.35 V - +0.19 V would yield a gradient 2 times greater than that of the slope calculated at $|i_L|$. It is satisfying that the value of -3186 ± 372 A^{-1} is, within experimental error, double that recorded for a potential step of 0.35 V to 0.05 V. The value of *K* should be the same for any potential step but the value recorded in Table 6.2, for a potential step of +0.19 V is larger than the average value of *K* recorded in the limiting case. This further indicates that K cannot be determined accurately.

For CV studies, if an assumption is made that time, t, can be measured from the onset potential of the electron transfer reaction, E_{on}, then $t = |E_L - E_{on}|/v$, where E_L is the potential at which the mass transport limiting current is observed, and v is the sweep rate. This means that at any fixed E_L

$$|i_L|^{-1} = \left(\frac{2\pi DAFc^{\infty}}{w}\right)^{-1}\{B - \ln v\} \qquad \textbf{Eqn. 6.6}$$

where B is a combined constant $\ln\left(\frac{KD}{w^2}\right) + \ln[|E_L - E_{on}|]$. Thus, analogous to equation 6.4, at any value, E the expression is

$$|i_L|^{-1} = \left(\frac{2\pi DAFc^{\infty} - c^0}{w}\right)^{-1}\{B - \ln v\} \qquad \textbf{Eqn. 6.7}$$

For this study, E_{on} was taken to be 0.35 V, the potential at which ferricycanide is fully oxidised and a potential just before any reduction reaction begins to take place. E_L was taken to be 0.05 V. This is within the potential region where the current is mass-transport limited rather than potential dependent and within the region where pseudo-state currents are observed. The potentials (E_{on} and E_L) were selected to be the same as those used for the potential step from 0.35 V to 0.05 V, chosen for the current-time transient data. Figure 6.9 shows a typical plot of $|i_L|^{-1}$ versus ln$v$ for the forward scan of the data in Figure 6.2 at a potential of +0.05 V.

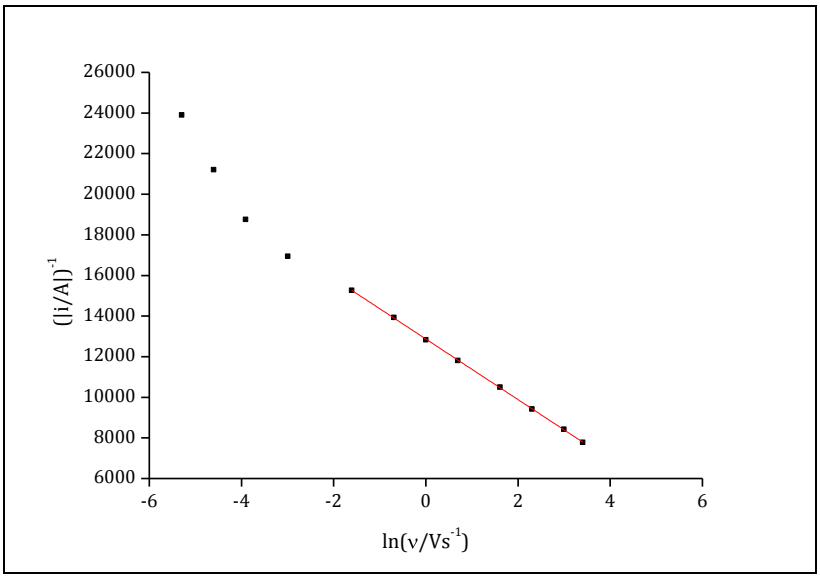

Figure 6.8: A plot of $|i|^{-1}$ vs. ln$v$ for a C30µ3d substrate in ferricyanide [10 mM] at different sweep rates and recorded at a potential of 0.05 V on the forward sweep. The least fit regression line shown is that for sweep rates above 50 mVs^{-1} and the slope recorded is -1450 ± 90 A^{-1} with correlation coefficient, r = 0.99994.

It is clear that an excellent fit to a straight line is observed except at the lowest sweep rates, which indicates this nanoband array fits well to established planar microband theory across around three orders of magnitude of sweep rates. It is not surprising that at the lowest sweep rates a value of i_L lower than predicted is obtained. As calculated, using equation 6.5, diffusional overlap will be expected from neighbouring depressions when t > 3.69 seconds, which for E_L = + 0.05 V is consistent with any sweep rate slower than 100 mVs^{-1}. Therefore, this departure can be attributed to significant overlap of the diffusion layers from nanobands in neighbouring depressions in the array at these slow sweep rate.

When w = 50.0 nm, using the gradient of -1450 ± 90 A^{-1} recorded in Figure 6.8, a value of A = (8.10 ± 0.06) x 10^{-5} cm^2 can be calculated. This compares to the geometric area of all the enclosed nanobands of 1.06x10^{-4} cm^2, or 80% of the response expected if all the nanoband area were planar. This is entirely consistent with completely active nanobands; as these nanobands are on the inner surface of the depression, some diffusional layer overlap from neighbouring parts of the band, particularly in the corners, is inevitable, which to some extent must reduce the effective area compared to entirely planar nanobands.

It is satisfying to note that the gradient of the linear regression in Figure 6.8 of -1450 ± 90 A^{-1} is also in good agreement, within experimental error, to the gradient (-1410 ± 70 A^{-1}) of the linear regression line determined over intermediate times (red line between ln$t$ = -0.6 and ln$t$ = +1.2) in Figure 6.6. This further validates that linear regression fitting of the i_L^{-1} vs ln$t$ graphs over the intermediate time regime does indeed model band behavior of the CaviArEs. This is in contrast to the larger gradient of -1752 ± 105 A^{-1} calculated over fast times.

Plots of $|i|^{-1}$ versus ln$v$ were also plotted for potentials of +0.19 V recorded at different sweep rates and a typical response is shown in figure 6.10 below.

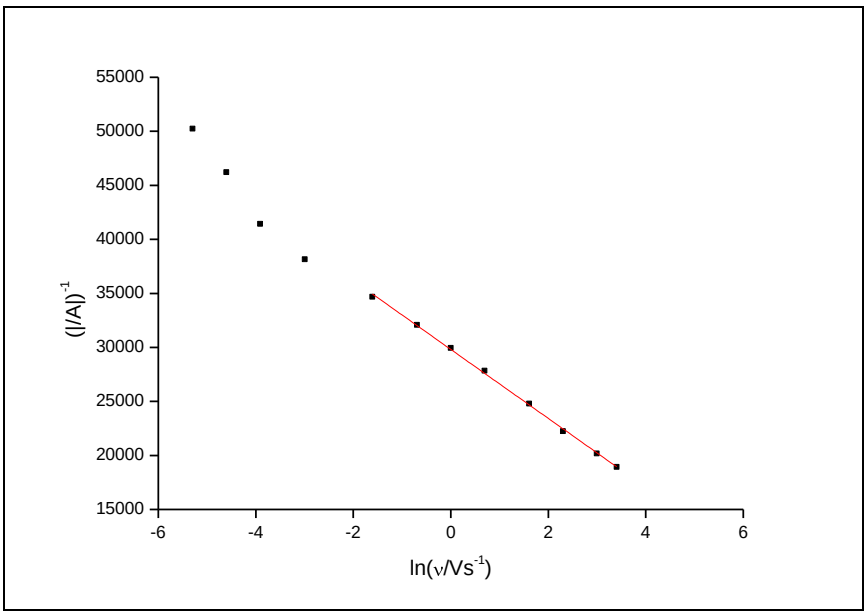

Figure 6.9: A plot of $|i|^{-1}$ vs. lnν for a C30µ3d substrate in ferricyanide [10 mM] at different sweep rates and recorded at a potential of 0.19 V on the forward sweep. The least fit regression line shown is that for sweep rates above 50 mVs^{-1} and the slope recorded is -3192 ± 508 A^{-1} with correlation coefficient, r = 0.99943.

Analogous to equation 6.5, equation 6.7 predicts that at E^{θ}, the gradient of the slope should be two times greater than the gradient expected at the limiting potential. As expected, the slope at 0.19 V (-3152 ± 508) is double, within experimental error to that recorded at 0.05 V. It is also the same, within experimental to that recorded in Figure 6.6 over intermediate times of the i^{-1} vs ln*t* slope.

It is noteworthy that a large and constant effective area is observed for these systems over several orders of magnitude of sweep rate, which greatly simplifies quantitative electroanalysis. This excellent response is observed, even at 30 V s^{-1}, which is one of the fastest sweep rates obtainable using commercially available potentiostats. This indicates that there is very low actual and parasitic capacitance associated with the architecture. This can be attributed to the low effective electrode area relative to the high mass transfer rate resulting in negligible double layer charging currents relative to the observed signal, even at the fastest sweep rates. Figure 6.11 shows representative CVs at low, medium and high sweep rates, with and without ferricyanide, which illustrates this point.

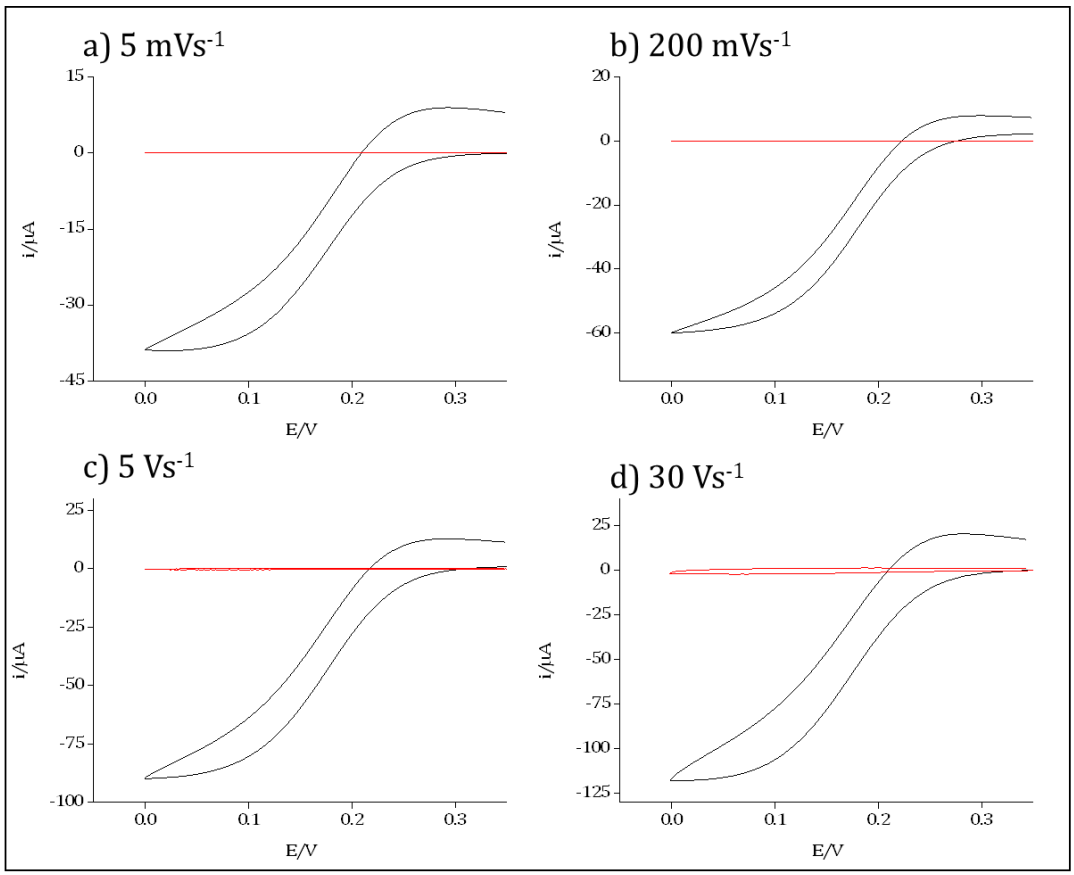

Figure 6.11: Typical first sweep CVs recorded at (a) v = 5 mV s^{-1} (b) v = 200 mV s^{-1} (c) v = 5 V s^{-1} (d) 30 V s^{-1} obtained in 0.10 M KCl aqueous electrolyte with (black) and without (red) 10 mM ferricyanide.

This is very different to the observed response from the equivalent (30 μm)^2 square electrode array (S30μ3d) shown in Figure 6.10.

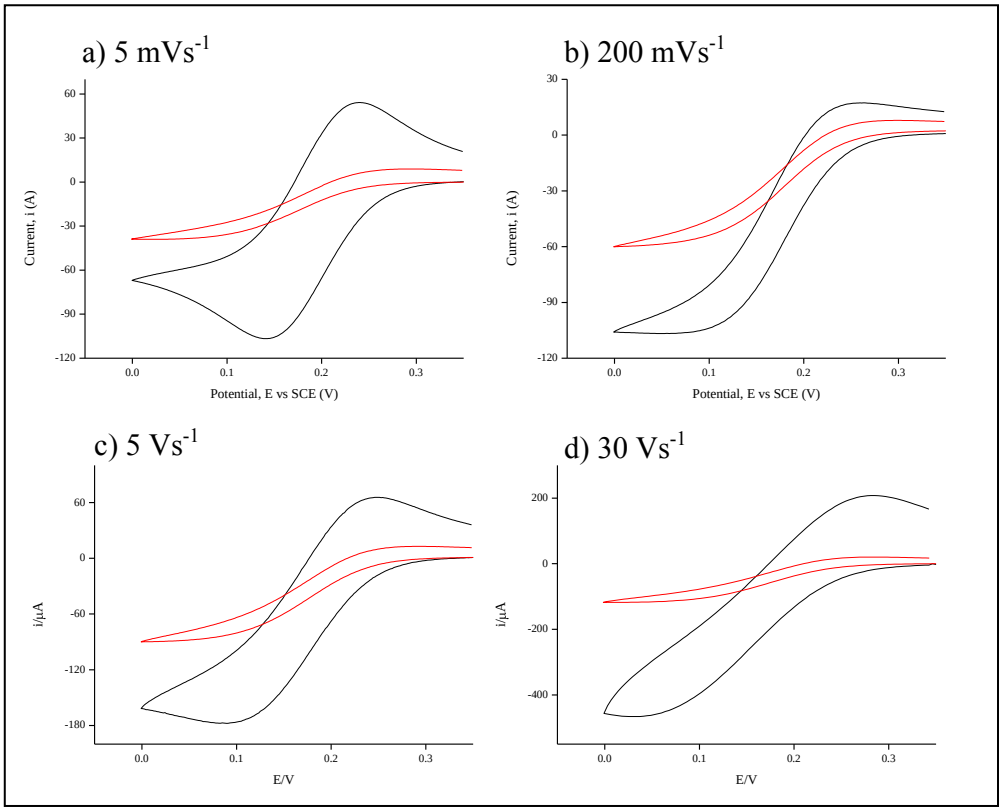

Figure 6.12: Typical first sweep CVs of a C30µ3d array (red) recorded at (a) ν = 5 mV s^{-1} (b) ν = 200 mV s^{-1} (c) ν = 5 V s^{-1} (d) 30 V s^{-1} in 0.1 M KCl aqueous electrolyte with 10 mM ferricyanide compared to the equivalent 1764 elements for the S30µ3d microsquare electrode array (black)

Figure 6.12 a) shows that at slow sweep rates the S30µ3d array shows peaked currents and enhanced ferrocyanide re-oxidation peaks are observed due to increased diffusional overlap between neighbouring electrodes. At the fastest sweep rates (Figures 6.10 c) and d)), large current differences are observed between forward and reverse scans. This is characteristic of a large contribution of non-Faradaic charging currents to the overall response. The superimposed response from the C30µ3d array demonstrates that up to one half of the current of the square array is observed compared to that of the S30µ3d array, despite the CaviArE device being only 0.67% of the microsquare electrode array area. This indicates the efficiency of CaviArE mass transfer and explains why low nanoband charging currents (which scale with area) are observed. The effects of the observed capacitance will be measured in more detail in Chapter 7.

From the CV data, it can be seen that the ferricyanide reduction reaction begins to occur at ~ 0.30 V. This means that the reduction reaction occurs in

0.008 s at a sweep rate of 30 Vs^{-1}. Inserting this time into Equation 6.5 yields a depletion thickness of the 4.2 µm at E_L = + 0.05 V during the time it takes for one forward sweep. This corresponds to depletion within the depression and is at a length scale where surface boundary effects and the depression edge should markedly reduce the effect of convective transport. Under these conditions, the response would be expected to be insensitive to solution convection. This is clearly shown in Figure 6.11, which compares CVs obtained at slow, medium and fast sweep rate with and without solution stirring.

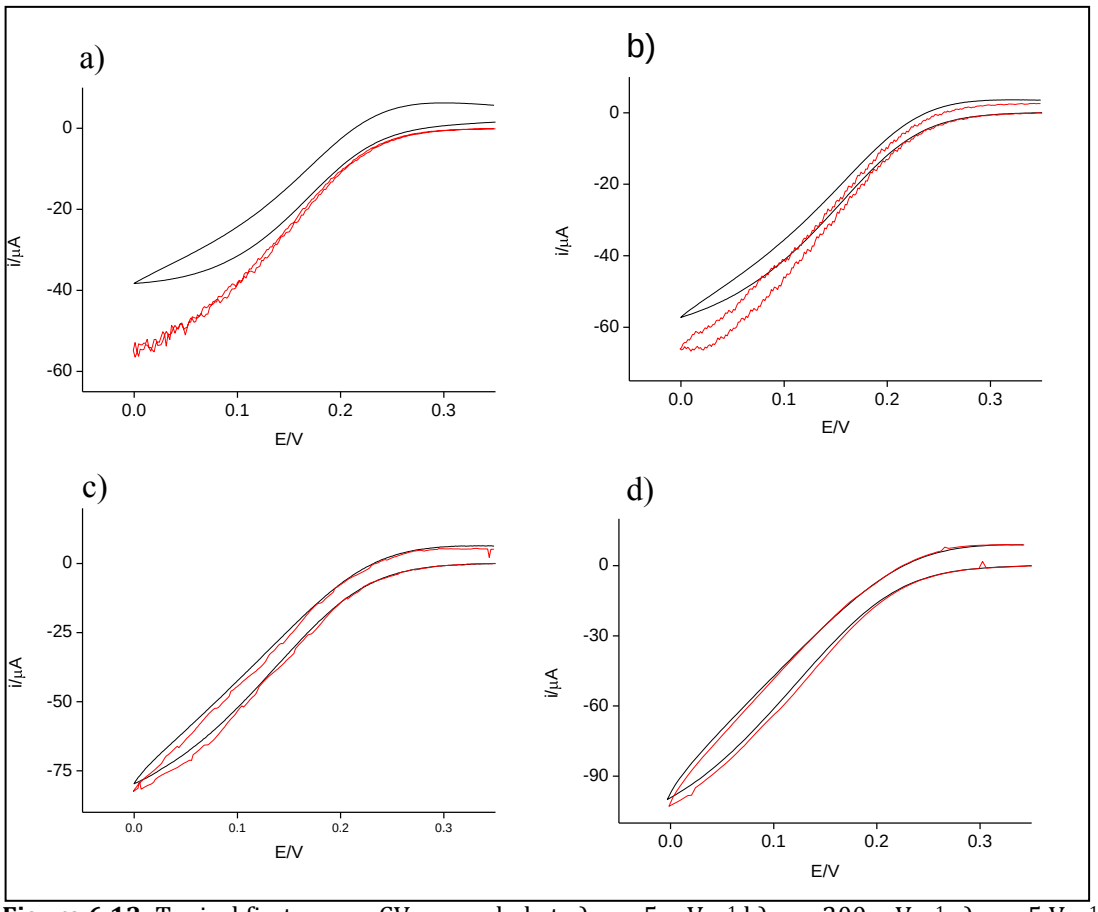

Figure 6.13: Typical first sweep CVs recorded at a) v = 5 mV s^{-1} b) v = 200 mV s^{-1} c) v = 5 V s^{-1} d) 30 V s^{-1} obtained in 0.10 M KCl aqueous electrolyte with 10 mM ferricyanide with (red) and without (black) stirring the solution by means of a stirrer bar.

Figure 6.11 clearly shows that after 5 mVs^{-1} the response of the stirred and unstirred solution is effectively the same. This shows that limiting currents are established very quickly and further verifies that the mass transport is extremely efficient for these devices.

6.3.2. Voltammetric Response of the C30µ3d arrays in 1 mM potassium Ferricyanide

The C30µ3d array was cleaned in sulfuric acid [0.05 M] prior to experimentation and gave a typical cleaning response as shown in figure 5.26. Figure 6.12 shows a typical CV response in ferricyanide [1 mM] at different sweep rates after extensive acid cleaning.

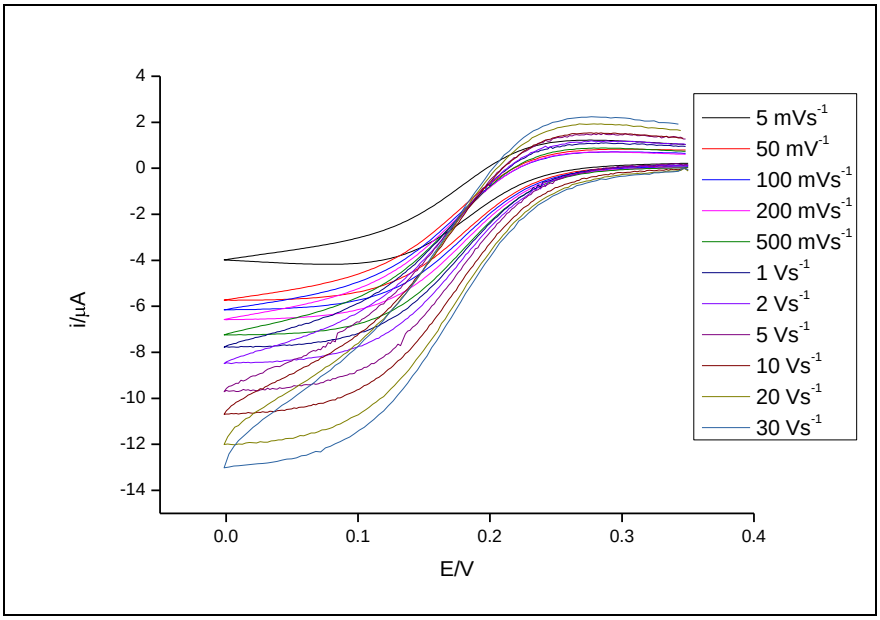

Figure 6.12: Typical first sweep CVs obtained for the reduction of 1 mM ferricyanide in 0.10 M KCl solution at the sweep rates shown. The onset sweep potential, E, was +0.35 V with the initial direction of scan to negative potentials.

The response looks almost identical to that shown in Figure 6.1 except, as expected the currents are smaller. The separation of the forwards and reverse sweep is slightly wider at very fast sweep rates which can be attributed to increased R_UC_{DL} charging effects (section 1.2.1) in these very low concentrations.

From Equation 6.6, a plot of $|i_L|^{-1}$ vs. ln$v$ should give a slope which is ten times larger than that obtained in 10 mM ferricyanide. Figure 6.13 shows such a plot.

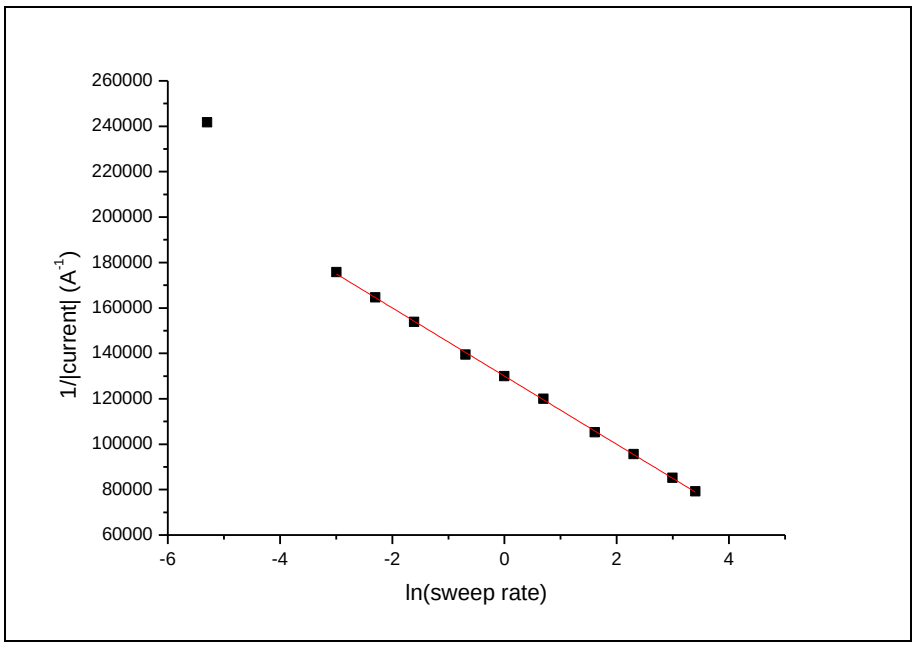

Figure 6.13 A plot of $|i|^{-1}$ vs. ln$v$ for a C30µ3d substrate in ferricyanide [1 mM] at different sweep rates and recorded at a potential of +0.05 V on the forward sweep. The least fit regression line shown is that for sweep rates above 50 mVs^{-1} and the slope , m is -15016 ± 179 A^{-1} with correlation coefficient, r = 0.9998.

It is satisfying that the ratio of this slope of -15000 ± 200 in 1 mM Ferricyanide to that of -1450 (± 90) for 10 mM ferricyanide (Figure 6.10) is 10.5 ± 0.9 which corresponds to this value of dilution within experimental error. If the C30µ3d response in 1 mM ferricyanide is comparable to that in 10 mM ferricyanide, a plot of i_L^{-1} vs. ln$t$ should also produce a graph, with a gradient that is 10 times greater than the response in 10 mM. Figure 6.14 shows a plot of i^{-1} vs. lnt for a potential step from 0.35 V to 0.05 V and the corresponding linear fit.

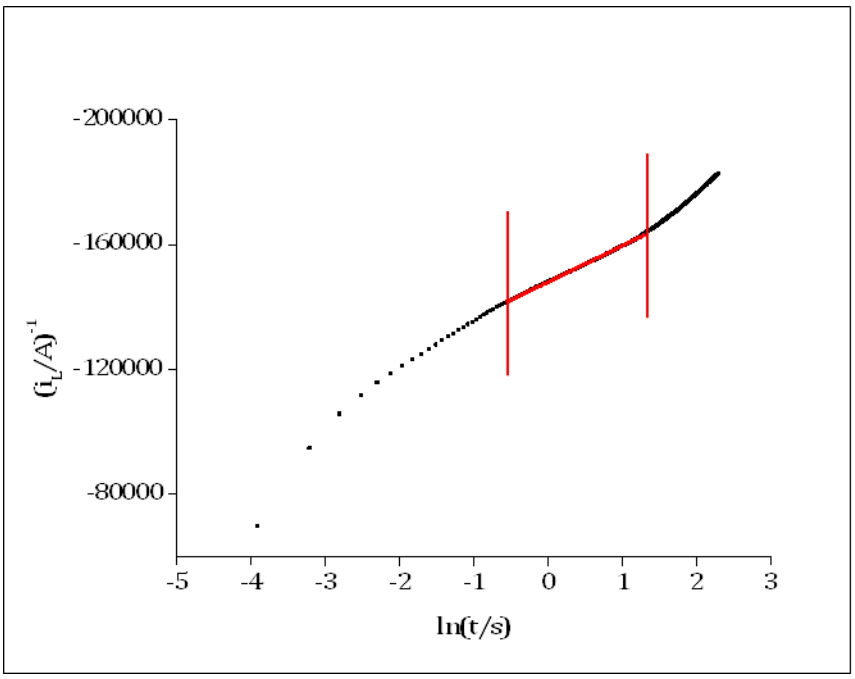

Figure 6.14: Graph to show a plot of $|i_L|^{-1}$ vs. ln$t$ for a typical C30µ3d array in ferricyanide [1 mM] between ln$t$ = -4.0 and ln$t$ = +2.8 with a linear best fit line plotted between ln$t$ = -0.6 to ln$t$ = +1.2. The slope of the graph is -11598 ± 127 A^{-1} and the intercept is -147936 ± 122 A^{-1} and the fit has a correlation coefficient of 0.9993.

The ratio of this slope, of -11598 ± 122 in 1 mM ferricyanide to the average slope of -1390 ± 70 in 10 mM ferricyanide is 8.3 ± 0.5, is approximately an order of magnitude greater, as would be expected. The value of *K* calculated from this data is 1.2, which again shows the difficulty in accurately predicting K using this method.

6.3.3. Voltammetric Response of the C30µ3d arrays in 1 mM Ferrocene Carboxylic Acid

Even though the response in 1 mM ferricyanide suggests that passivation caused by surface reactions is not influencing the CaviArE response, it was important to analyse the response in other redox agents, to be completely confident in the data. Ferrocene carboxylic acid was chosen since it can be dissolved in aqueous medium and undergoes a 1-elctron transfer reaction, similar to ferricyanide. However no possible surface reactions can occur using this redox couple.

Several experiments were carried out using ferrocene carboxylic acid at a similar concentration, 0.95 mM. A low concentration was used to ensure full

dissolution in water. KCl [0.1 M] background electrolyte was used thus NaOH [3 M] was added drop-wise to aid in the dissolution of the ferrocene carboxylic acid through the formation of the soluble carboxylate species

Figure 6.15 a) shows the CV responses of 0.95 mM aqueous ferrocene carboxylic acid at different sweep rates and Figure 6.15 b) shows the CV responses of 1 mM aqueous potassium ferricyanide at the same sweep rates.

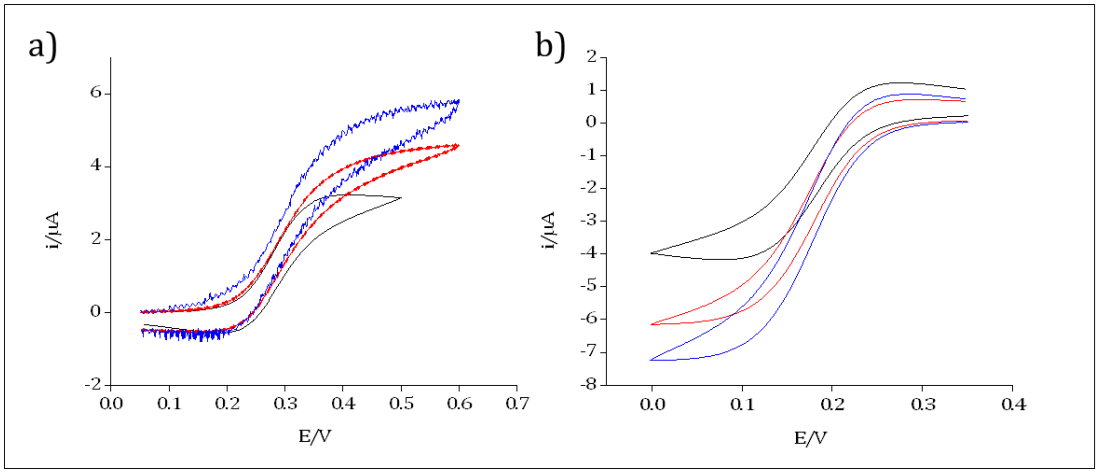

Figure 6.15: a) Typical CV responses for the oxidation of 0.95 mM ferrocene carboxylic acid between +0.05 V and +0.5/0.55 V vs. SCE at 5 mVs^{-1} (black), 100 mVs^{-s} (red) and 500 mVs^{-1}; and **b)** typical CV responses for the reduction of 1 mM potassium ferricyanide between +0.35 V and 0.00 V vs. SCE at the same sweep rates.

It is satisfying that the CV responses of ferrocene carboxylic acid, although oxidative rather than reductive as expected are a very similar shape to those recorded at the same sweep rates for 1 mM potassium ferricyanide which indicates similar electrochemical activity. The $E_{1/2}$ potential calculated from these CV responses of +0.275 V coincides well with the quoted literature standard potential value[67].

Figure 6.16 shows the current-time transient plot and corresponding plot of i^{-1} vs. ln$t$ for a potential step from 0.05 V to 0.5 V.

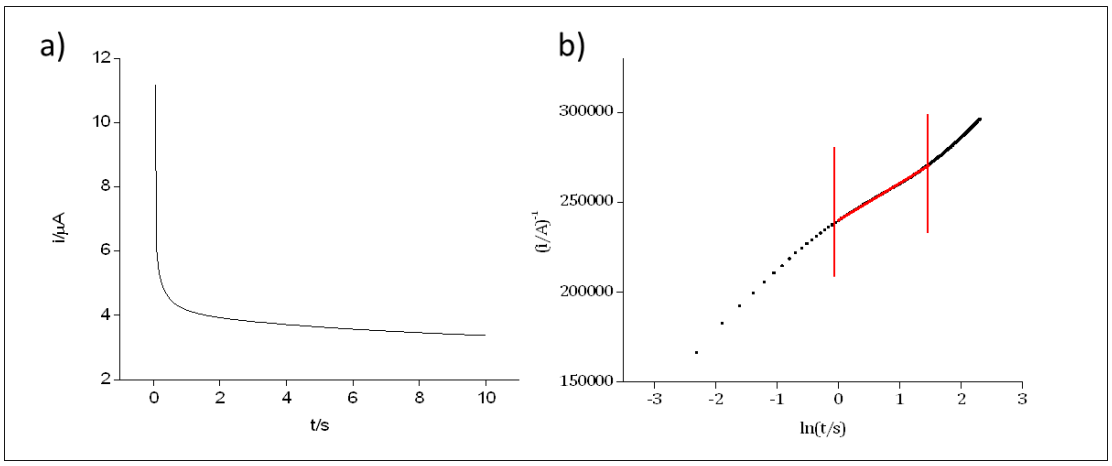

Figure 6.16: a) shows current-time transient graph for a potential step from 0.05 V to 0.50 V (vs. SCE); **b)** shows the corresponding i^{-1} vs. ln$t$ plot with a linear regression fit between ln$t$ = 0 and ln$t$ = 1.5, with a correlation coefficient of 0.9996, a slope of 20644 ± 73 A^{-1} and an intercept of 240035 ± 75 A^{-1}.

The limiting slope calculated from figure 6.60 b) in the region shown of |20644| ± 73 is approximately 1.3 times larger than the limiting slope calculated in 1 mM ferricyanide of |15086| ± 168. This is consistent with the difference in magnitudes of the CVs seen in Figure 6.15 and implies a diffusion coefficient of 1.3 times smaller ($5x10^{-6}cm^2s^{-1}$). As the reported literature value for the diffusion coefficient of ferrocene carboxylic acid ranges from $3.0x10^{-6}$ cm^2s^{-1} to $5.4x10^{-6}$ cm^2s^{-1} depending on the pH and electrolyte used[6-8], this behavior is entirely as expected.

The linear regression line was fitted visually between ln$t$ = 0 and ln$t$ = 1.5, using D =$5x10^{-6}$ which corresponds to a lower limit thickness of 39 μm and an upper limit of 84 μm. These values also correspond well to planar diffusion outside of the $(30\ \mu m)^2$ cavity prior to overlap of layers of neighbouring elements in the array, spaced 90 μm apart.

As from equation 6.3 and 6.4, the *ln*t axis intercept is $-ln(KD/w^2)$, and a value of K = 0.56 can be calculated from the ferrocene carboxylic acid data, using the diffusion coefficient of $5x10^{-6}$ cm^2s^{-1}. This is of a similar magnitude to those calculated in sections 6.3.1 and 6.3.2.

6.3.4. *Voltammetric Response of CaviArE devices of different size and pitch*

6.3.4.1. Analysis of the Effects of Cavity Spacing

In order to probe the effects of cavity spacing, due to time limitations, selected CaviArE architectures were studied which could be directly compared with the 30µ3d arrays characterized in sections 6.3.1 to 6.3.3. The analysis of 30 µm CaviArE systems with their different d-spacing, 30µ1d, 30µ2d and 30µ4d will be considered here. Figure 6.17 shows optical images of these different architectures.

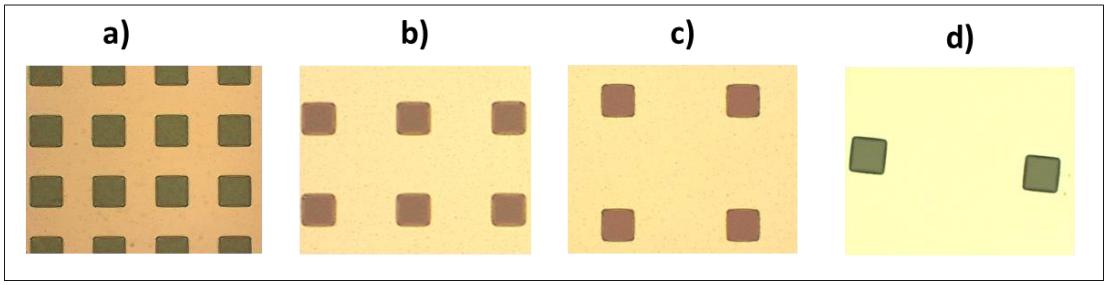

Figure 6.17: Optical images viewed under the Zeiss Axiotron microscope and captured with the Diagnostics Instruments Spot Insight QE digital camera showing **a)** the 30µ1d architecture with active electrode geometric area of 4.1334×10^{-4} cm^2; **b)** the 30µ2d architecture with active electrode geometric area of 1.8816×10^{-4} xcm^2; **c)** the 30µ3d architecture with active electrode geometric area of 1.0584×10^{-4} cm^2; and **d)** the 30µ4d architecture with active electrode geometric area of 6.936×10^{-5} cm^2.

All these images show well defined cavities and spacing. Figure 6.18 shows the typical CVs obtained for these architectures at different sweep rates.

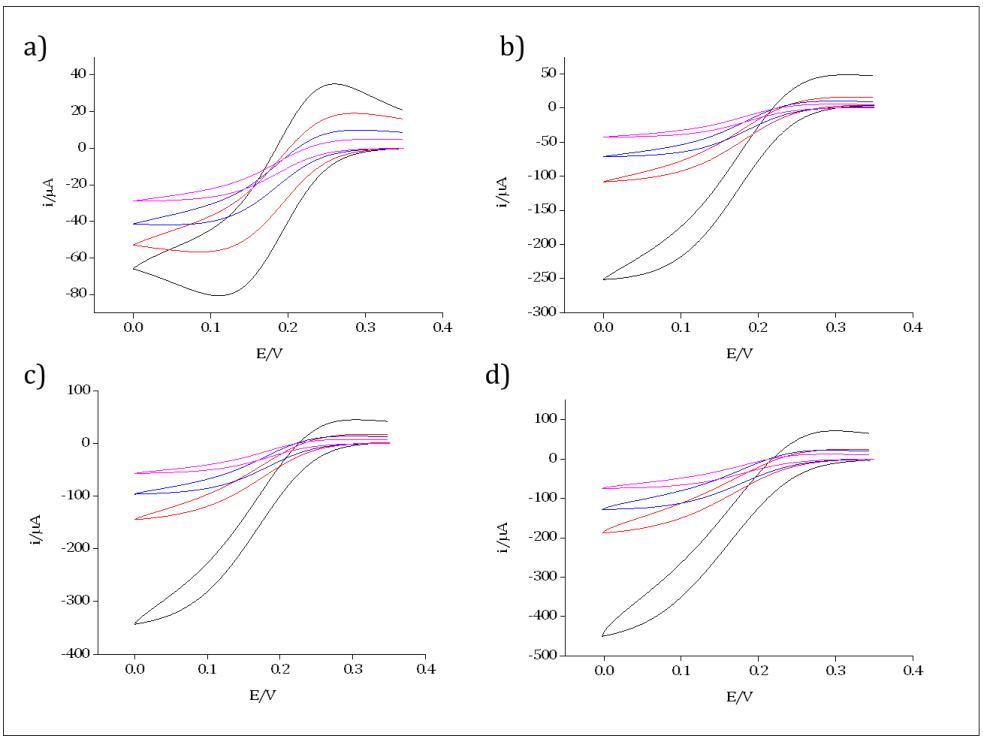

Figure 6.18: Showing the CV comparison in ferricyanide [10 mM] between 0.35 V and 0.00 V for 30μ1d (black), 30μ2d (red) , 30μ3d (blue) and 30μ4d (pink) at **a)** 5 mVs^{-1}, **b)** 500 mVs^{-1}, **c)** 5 Vs^{-1} and **d)** 30 Vs^{-1}.

As expected, the C3μ1d CaviArE response has the largest current output, since it has the largest active electrode geometric area. Figure 6.19 therefore shows the current response for these arrays, normalised for their active area, $\frac{i}{A_{active}}$ (given in A cm^{-2}).

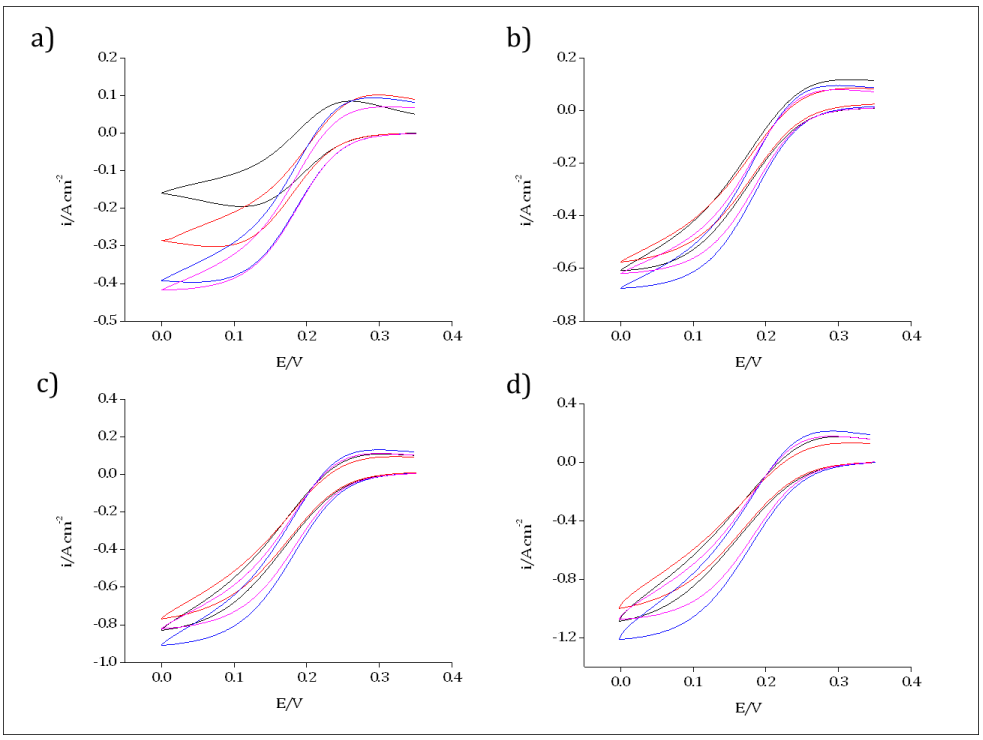

Figure 6.19: Showing the CV comparison in ferricyanide [10 mM] between 0.35 V and 0.00 V for 30µ1d (black), 30µ2d (red) , 30µ3d (blue) and 30µ4d (pink) normalized for active electrode area $\left(\frac{i}{A_{active}}\right)$ at **a)** 5 mVs^{-1}, **b)** 500 mVs^{-1}, **c)** 5 Vs^{-1} and **d)** 30 Vs^{-1}.

It is satisfying to observe that at high sweep rates, the CVs have very similar current densities, indicative that these are the responses of the individual, isolated electrodes. The small variation in current may due to cleanliness of the electrode surface and/or small fluctuations in lab temperature. From the CV data, it appears that the C30µ3d array is the most clean and the C30µ2d array is the least clean (see section 7.3.4.1 for EIS confirmation of this observation).

At low frequencies, the current responses do not overlay, this is indicative that significant diffusional overlap is occurring at 5 mVs^{-1}. Consistent with expectation, the CVs confirm that the greatest overlap occurs with the C30µ1d array, yielding the lowest currents. Figure 6.20 shows the corresponding plots of $|i_L|^{-1}$ vs. lnν, for the four different architectures at all sweep rates and a potential of 0.05 V

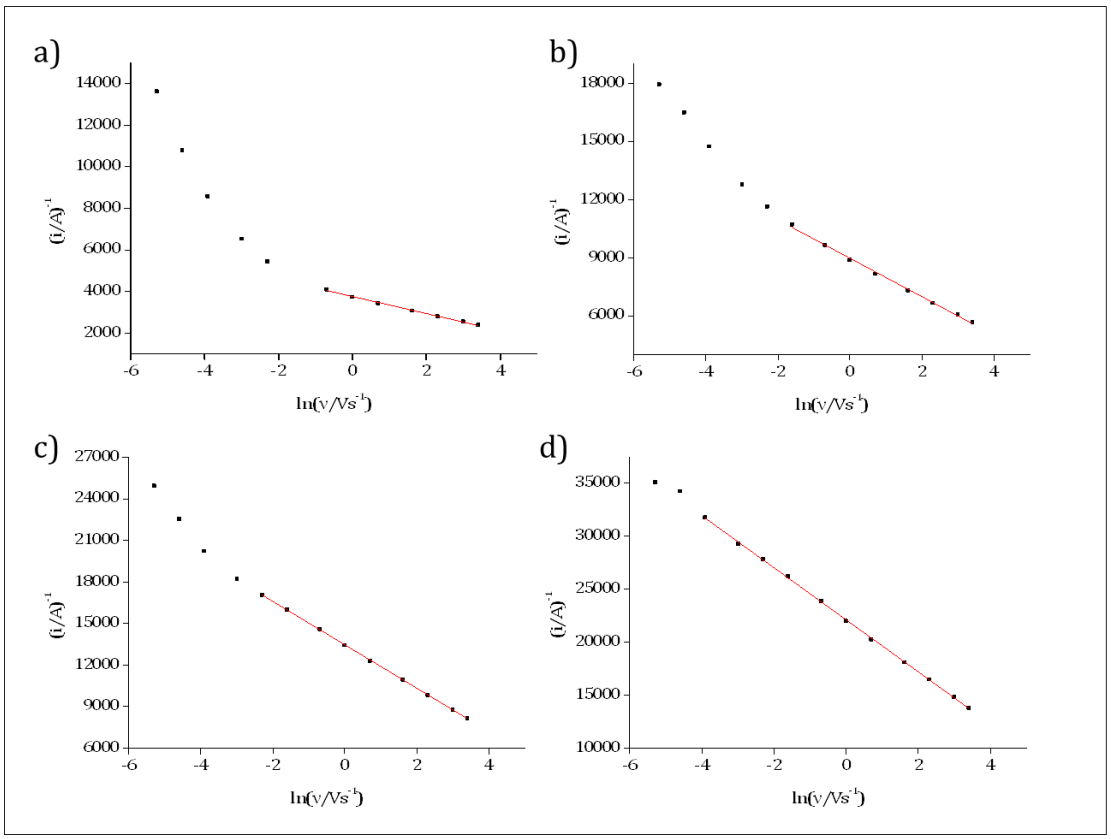

Figure 6.20: Typical plots of $|i_L|^{-1}$ vs. lnν showing **a)** the C30µ1d array with a fit from 500 mVs^{-1} to 30 Vs^{-1}, giving m = -410 ± 96 A^{-1} r = 0.997; **b)** the C30µ2d array with a fit from 200 mVs^{-1} to 30 Vs^{-1}, m = -1020 ± 21 A^{-1} and r = 0.995; **c)** the C30µ3d array with a fit from 100 mVs^{-1} to 30 Vs^{-1}, giving m = -1460 ± 96 A^{-1} and r = 0.999. **d)** the C30µ4d array with a fit from 20 mVs^{-1} to 30 Vs^{-1}, giving m = -2450 ± 76 A^{-1} and r = 0.999.

As expected, the figure above shows that as the microsquare cavities get further apart, the diffusional overlap of neighbouring diffusional fields occurs at slower and slower sweep rates (as seen by the departure of the data from the regression line). Current time transients for these arrays were also obtained, carrying out a potential step from +0.35 V to 0.05 V at t = 0 seconds, (Figure 6.21).

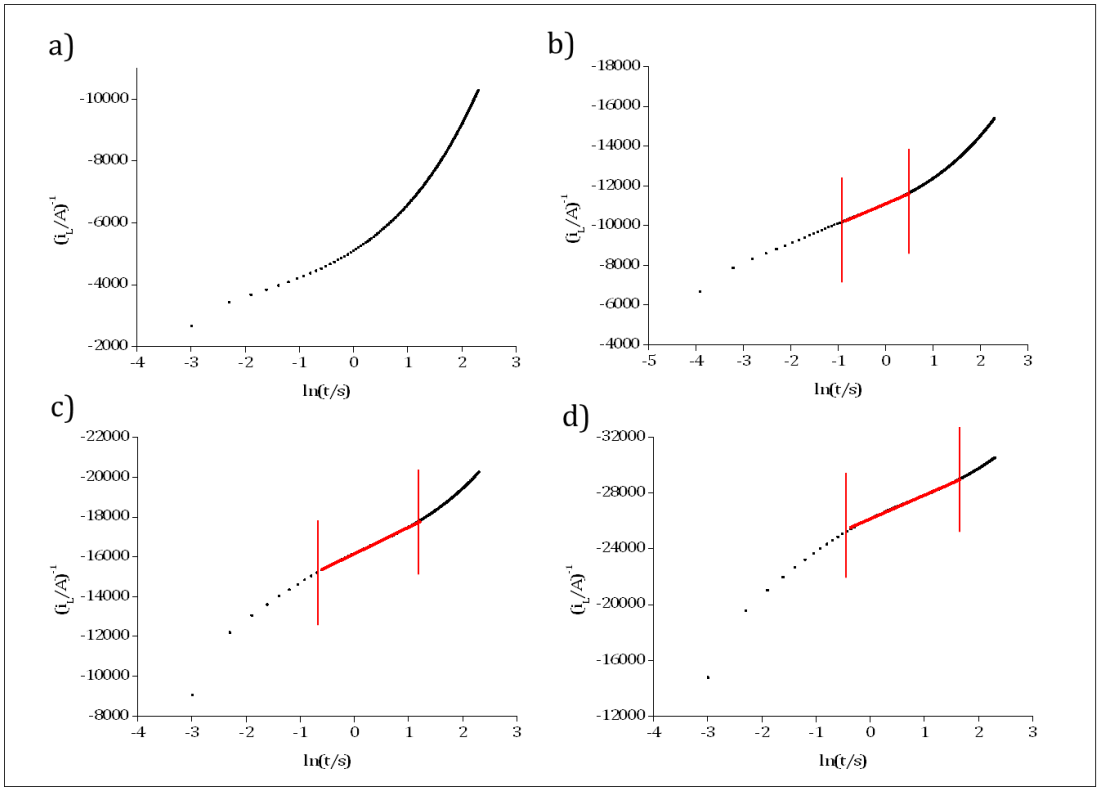

Figure 6.21: Typical plots of $|i_L|^{-1}$ vs. lnt for potential steps from +0.35 V to +0.05 V at t = 0 seconds, for a period of 10 seconds in 10 mM ferricyanide. **a)** Is the response of the C30µ1d array, which does not have a distinctive linear region associated with isolated band diffusion outside of the cavity. **b)** Is the response of a C30µ2d array with a linear fit between ln$t$ = -0.91 (L = 30 µm) to ln$t$ = +0.49 (L = 60 µm), giving m = -1023 ± 16 A^{-1}, c = -1110± 213 A^{-1} and r = 0.9995. **c)** Is the response of a C30µ3d array with a linear fit between ln$t$ = -0.62 (L = 34 µm) to ln$t$ = +1.23 (L = 87 µm), giving m = -1460 ± 70 A^{-1}, c = -17300 ± 715 A^{-1} and r = 0.9993. **d)** Is the response of a C30µ4d array between ln$t$ = -0.36 (L = 39 µm) to ln$t$ = +1.87 (L = 119 µm), giving m = -1790 ± 93 A^{-1}, c = -26100 ± 220 A^{-1} and r = 0.9983.

Figure 6.21 shows that for the C30µ3d arrays, the upper and lower limits of the linear regression line approximately correspond to the electrode spacing and to the size of the microsquare cavity, respectively; that is a lower limit of 30 µm, and an upper limit of 60 µm, 90 µm and 120 µm for graphs b), c) and d) respectively. C30µm1d, does not have a distinctive linear region associated with isolated band diffusion outside of the cavity, and seems to be dominated by diffusion within the cavity and the response from the overlapping array elements. Indeed, since the size of the cavity and the spacing are comparable, the diffusional field would be expected to overlap very rapidly and this is consistent with the i^{-1} vs. lnv response for C30µ1d in Figure 6.20 a). This confirms that the linear region analysed is that of isolated band diffusion outside of the cavity and the lower limit of the regression line corresponds to

the initial establishment of this band diffusion outside of the cavity and the upper limit is where the diffusional fields begin to overlap.

Table 6.3 shows the average gradients and associated error over several experiments, calculated for the different CaviArE architectures for both the $|i_L|^{-1}$ vs. ln*t* plots and the $|i_L|^{-1}$ vs. ln*v* plots. The table also gives the normalised slope, calculated with respect to the active electrode area and for the square cavity for area for each of the architectures.

CaviArE Architecture	**Average Slope for $\|i_L\|^{-1}$ vs. ln*t* /A^{-1}**	**Average Slope for $\|i_L\|^{-1}$ vs. ln*v* / A^{-1}**	**slope per active electrode area for $\|i_L\|^{-1}$ vs. ln*t* / A^{-1} cm^{-2}**	**slope per active Electrode area for $\|i_L\|^{-1}$ vs. ln*v* A^{-1} cm^{-2}**	**Slope per Cavity area for $\|i_L\|^{-1}$ vs. ln*t* / A^{-1} cm^{-2}**	**Slope per Cavity area for $\|i_L\|^{-1}$ vs. ln*v* / A^{-1} cm^{-2}**
C30µ1d	n/a	-479 ± 96	n/a	-0.20 ± 0.02	n/a	-29.70
C30µ2d	-1012 ±16	-1005 ± 21	-0.19 ±0.04	-0.19 ± 0.02	-28.56	-28.37
C30µ3d	-1393 ±73	-1458 ±96	-0.15 ± 0.04	-0.15 ± 0.02	-22.12	-23.15
C30µ4d	-1670 ±93	-2550 ±76	-0.12 ±0.04	-0.16 ± 0.02	-17.37	-23.41
		Average	**-0.15 ± 0.04**	**-0.17 ±0.02**	**-23 ± 6**	**-26 ± 3**

Table 6.3: Table to compare the gradients obtained for the different (30 µm)^2 CaviArE architectures for graphs of $|i_L|^{-1}$ vs. lnt and for graphs of $|i_L|$ vs. *lnv.*

Equations 6.3 and 6.6 show that, analytically, the gradients of each of the CaviArE architectures should be the same for both types of plot. This cannot be calculated for C30µ1d data, and this is not true for the C30µ4d array, which shows a large variation in the average gradients in Table 6.3. The normalised slope (accounting for both the differences in active electrode area and cavity square area) should be the same at the limiting potential for all 30µ CaviArE devices, provided that the electrodes behave independently of one another.

Figure 6.19 does show some variation in current response due to electrode cleanliness and/or fluctuations in lab temperature and therefore some variation in the slope was expected. Table 6.3 shows that the slopes are all the same within experimental error, when accounting for active electrode area or

cavity area. The variation in slope observed is similar to the variation of the currents in Figure 6.19.

Table 6.4 shows the average slope obtained from plots of $|i_L|^{-1}$ vs. ln$t$ and the corresponding extrapolated y-intercept for each of the architectures in Figure 6.20. The values of K from these data are also given in the table.

CaviArE Architecture	Average Slope / A^{-1}	Average y-intercept / A^{-1}	Calculated value of K from Eqn. 6.2
C30µ1d	n/a	n/a	n/a
C30µ2d	-1012 ±16	-10911 ± 213	0.18
C30µ3d	-1393 ±73	-17031 ± 715	0.71
C30µ4d	-1670 ±93	-27190 ± 220	33.63

Table 6.4: Table to show the average slope and y-intercept obtained from graphs of $|i_L|^{-1}$ vs. ln$t$ for the different (30 µm)^2 CaviArE architectures of different spacing. The corresponding values of K are also given.

The values of K calculated are again within a similar range as calculated in sections 6.3.1 to 6.3.3.

6.3.4.2. Analysis of the Effect of Cavity Size

In order to probe the effects of cavity size, analysis of the 3d spaced CaviArE substrates with different cavity sizes was also carried out. Figure 6.22 show optical images of the C10µ3d, C20µ3d, C50µ3d and C100µ3d architectures.

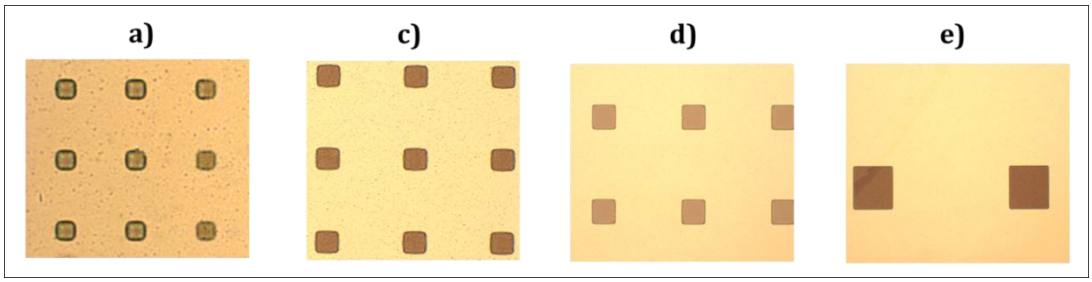

Figure 6.22: Optical images viewed under the Zeiss Axiotron microscope and captured with the Diagnostics Instruments Spot Insight QE digital camera showing **a) C**10µ3d architecture with active electrode geometric area of 3.125x10^{-4} cm^2; **b)** C20µ3d architecture with active electrode geometric area of 1.5876x10^{-4} cm^2; **c)** C50µ3d architecture with active geometric area of geometric area of 6.25x10^{-5} cm^2; and **d)** C100µ3d architecture with active geometric area of 3.38x10^{-5} cm^2.

It is gratifying to observe that by using a thinner layer of photoresist during LPCVD patterning, compared with the PECVD patterning (section 5.2.3), the (10 µm)^2 and (20 µm)^2 architectures are much better resolved. Figure 6.23 shows

typical CVs obtained for these architectures at different sweep rates, including their comparison with the C30µ3d architecture.

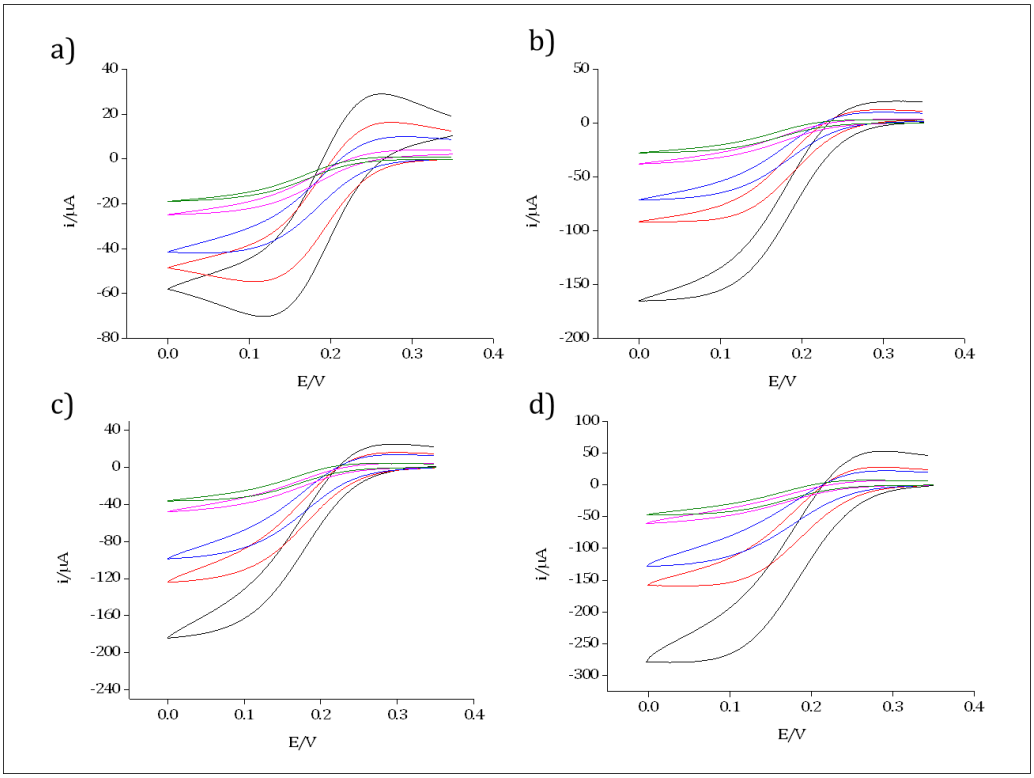

Figure 6.23: Showing the CV comparison in ferricyanide [10 mM] between 0.35 V and 0.00 V for C10µ3d (black), C20µ3d (red) , C30µ3d (blue), C50µ3d (pink) and C100µ3d (green) at **a)** 5 mVs^{-1}, **b)** 500 mVs^{-1}, **c)** 5 Vs^{-1} and **d)** 30 Vs^{-1}.

As expected, the C10µ3d CaviArE response has the largest current output, since it has the largest active electrode geometric area. Figure 6.24 therefore shows the current response for these arrays, normalized for their active area, $\frac{i}{A_{active}}$ (given in A cm^{-2}).

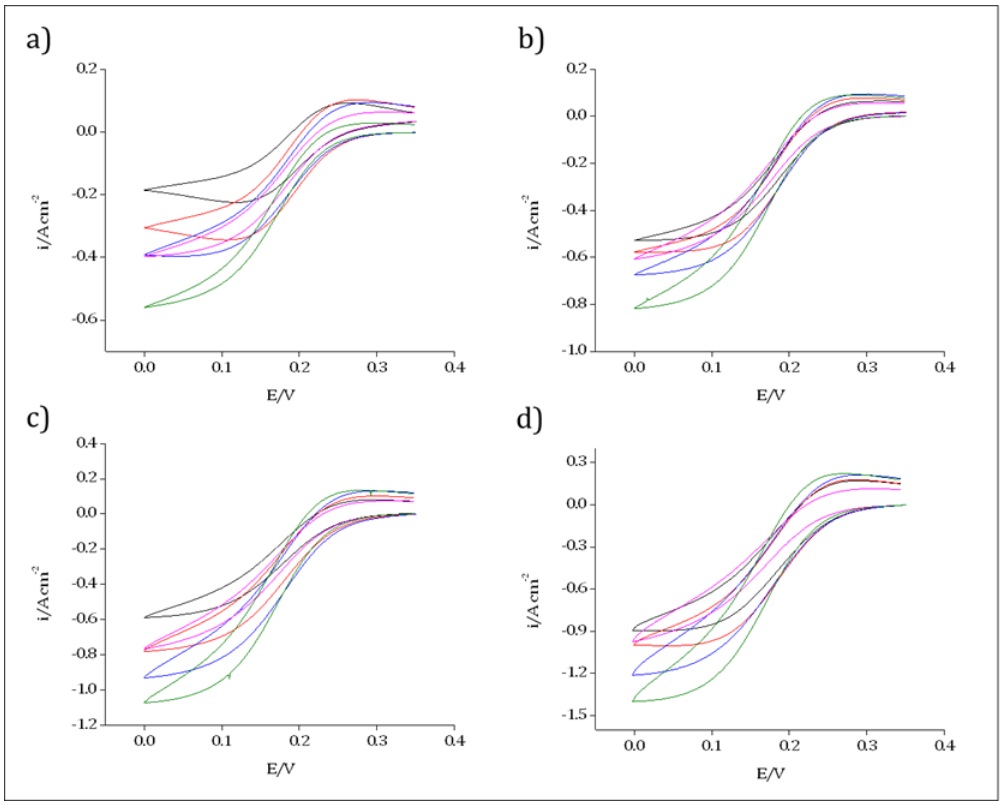

Figure 6.24: Showing the CV comparison in ferricyanide [10 mM] between 0.35 V and 0.00 V for C10µ3d (black), C20µ3d (red) , C30µ3d (blue), C50µ3d (pink) and C100µ3d (green) normalized for active electrode area $\left(\frac{i}{A_{active}}\right)$ at **a)** 5 mVs^{-1}, **b)** 500 mVs^{-1}, **c)** 5 Vs^{-1} and **d)** 30 Vs^{-1}.

In this case it is clear that the CV responses do not overlay, and, generally the current density increase with increasing cavity size. The exception to this is C50µ3d, but this electrode array was not cleaned as well as the other electrodes and this is suspected to be the reason in deviation from the general trend. Due to time limitations only two electrode arrays of each different cavity size were analysed fully and therefore it would be advantageous to repeat much of these experiments in order to obtain a more comprehensive study.

Figure 6.25 shows the corresponding plots of $|i_L|^{-1}$ vs. *lnv*, for the four different architectures (excluding C30µ3d) at all sweep rates and a potential of 0.05 V

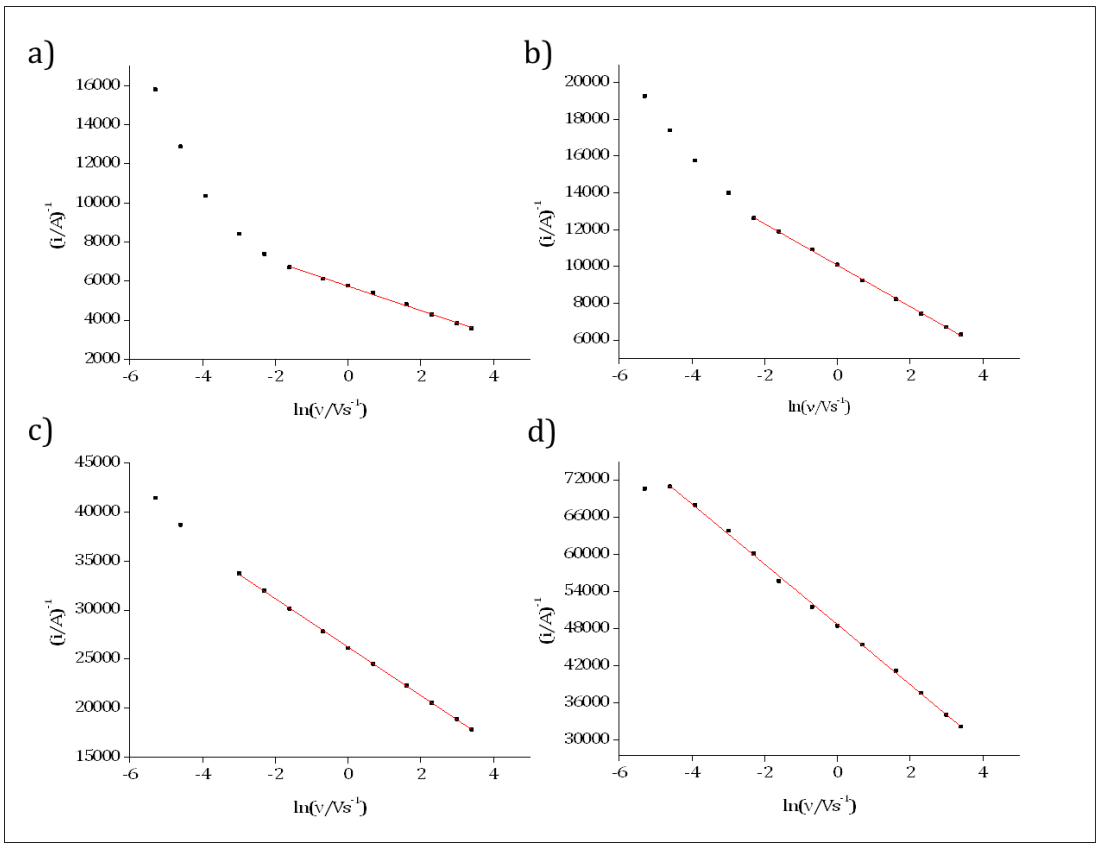

Figure 6.25: Plots of $|i_L|^{-1}$ vs. ln$v$ of **a)** the C10µ3d array with a fit from 200 mVs^{-1} to 30 Vs^{-1}, giving m = -620 ±27 and r = 0.9995; **b)** the C20µ3d array with a fit from 100 mVs^{-1} to 30 Vs^{-1}, giving m = -1130 ± 11 r = 0.9997; **c)** the C50µ3d array with a fit from 50 mVs^{-1} to 30 Vs^{-1}, giving m = -2470 ± 38 and r = 0.9999 and **d)** the C100µ3d array with a fit from 10 mVs^{-1} to 30 Vs^{-1}, giving m = -4900 ± 470 r = 0.9995.

Again as expected, the figure above shows that the smaller the microsquare cavity and hence cavity separation, the earlier the diffusion layers overlap, as depicted by the deviation in current response from the straight line. Current time transients for the different sized arrays were also obtained for a potential step from +0.35 V to +0.05 V in order to compare the gradients of the $|i_L|^{-1}$ vs. lnt plots with those of the plots of $|i_L|^{-1}$ vs. ln$v$ above. Figure 6.26 shows these graphs obtained for a time period of ten seconds.

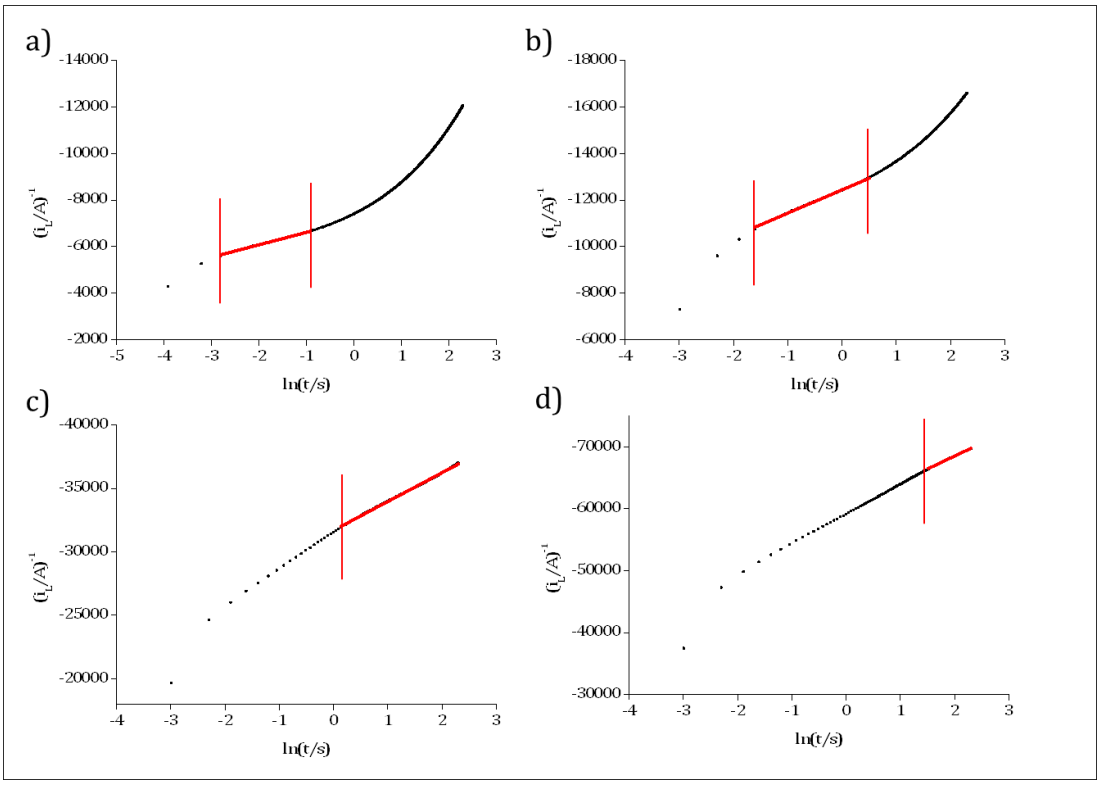

Figure 6.26: Plots of $|i_L|^{-1}$ vs. ln$t$ according to Equation 6.6 for **a)** the C10µ3d array, with a linear fit between ln$t$ = -2.813 (L = 11 µm) to ln$t$ = -0.916 (L = 30 µm), giving m = -530 ± 56 A^{-1}, c = -7140 ± 550 A^{-1} r = 0.9989; **b)** the C20µ3d array with a linear fit between ln$t$ = -1.609 (L = 21 µm) to ln$t$ = +0.501 (60 µm), giving m = -12430 ± 23 A^{-1}, c = -12000 ± 1094 A^{-1} r = 0.9990; **c)** the C50µ3d array with a linear fit between ln$t$ = +0.140 (L = 50 µm) to ln$t$ = +2.303 (L = 148 µm), giving m = -2270 ± 54 A^{-1}, c = -32000 ± 3100 and r = 0.9998; and **d)** the C30µ4d array between ln$t$ = +1.515 (L = 99 µm) to ln$t$ = +2.303 (L = 148 µm) , giving m = -4200 ± 290 A^{-1}, c = -60000 ± 1900 A^{-1} and r = 0.9996.

It is clear from Figure 6.26 that establishment of band diffusion outside of the cavity occurs at longer and longer times as the cavity size (and hence separation) increases. The figure also shows that, the diffusion layer thickness, L (Eqn. 6.5) calculated from the lower ln$t$ limit of the regression line, is remarkably similar to the size of the corresponding electrode cavity, of 10 µm, 20 µm, 50 µm and 100 µm for graphs a), b), c) and d) respectively. This confirms that establishment of band diffusion outside of the individual isolated cavities is dependent on the cavity size, which suggests that the diffusion layer develops within and fills the entire cavity, before growing out of the hole. It is also clear from the diffusion layer thickness calculated at the upper limit of the regression line, that diffusional overlap also corresponds to the cavity spacing (as expected from work in sections 6.3.1 to 6.3.4). The diffusion layer thickness calculated in Figures a) and b) and c) correlate well with the cavity separation length. However it is clear from Figure 6.26 d) that over a period of 10 seconds, the

C100µ3d diffusional fields have not yet begun to overlap. Equation 6.5 can also be used to determine the approximate time, when diffusional overlap might be expected, and for a separation of 300 µm, the time of overlap might be expected to occur over time frames of approximately 40 seconds (ln = 3.71). Therefore in order to observe the overlapping response of C100µ3d arrays, the potential step experiment would need to be recorded for much longer time periods. Since data was collected for only ten seconds, only a small portion of the linear region for the C100µ3d response could be fitted.

Table 6.5 shows the average gradients and associated error over several experiments, calculated for the different CaviArE architectures for both the $|i_L|^{-1}$ vs. ln$t$ plots and the $|i_L|^{-1}$ vs. lnν plots. The table also gives the normalised slope, calculated with respect to the active electrode area and for square-cavity area for each of the architectures.

CaviArE Architecture	**Average Slope for $\|i_L\|^{-1}$ vs. ln$t$ /A^{-1}**	**Average Slope for $\|i_L\|^{-1}$ vs. lnν / A^{-1}**	**Slope per active electrode area for $\|i_L\|^{-1}$ vs. ln$t$ / A^{-1} cm^{-2}**	**Slope per active electrode area for $\|i_L\|^{-1}$ vs. lnν / A^{-1} cm^{-2}**	**Slope per Cavity area for $\|i_L\|^{-1}$ vs. ln$t$ / A^{-1} cm^{-2}**	**Slope per Cavity area for $\|i_L\|^{-1}$ vs. lnν / A^{-1} cm^{-2}**
C10µ3d	-596 ± 58	-641 ± 27	-0.19 ± 0.02	-0.20 ± 0.02	-9.31	-10.02
C20µ3d	-998 ± 23	-1133 ± 10	-0.16 ± 0.02	-0.18 ±0.02	-15.84	-17.99
C30µ3d	-1397 ± 73	-1458 ± 96	-0.15 ± 0.02	-0.15 ± 0.02	-22.12	-23.15
C50µ3d	-2225 ± 55	-2444 ± 38	-0.14 ± 0.02	-0.15 ± 0.02	-34.77	-38.19
C100µ3d	-4407 ± 291	-4401 ± 468	-0.15 ± 0.02	-0.15 ± 0.02	-74.48	-74.39
		Average	**-0.16 ± 0.02**	**-0.17 ±0.02**		

Table 6.5: Table to compare the gradients obtained for the 3d spaced CaviArE architectures of different sized microsquare cavity, for graphs of $|i_L|^{-1}$ vs. ln$t$ and for graphs of $|i_L|$ vs. lnν.

It is clear that the average slope calculated using both Equations 6.3 ($|i_L|^{-1}$ vs. ln$t$) and 6.6 ($|i_L|^{-1}$ vs. lnν) are very similar for each individual architecture, and that the normalized slope with respect to active electrode area are the same

within experimental error for all architectures. However the normalised slopes with respect to cavity square area appear to increase with increasing cavity size.

Table 6.6 shows the average slope obtained from plots of $|i_L|^{-1}$ vs. lnt and corresponding y-intercept for each of the architectures in Figure 6.23. The values of K from these data are also given in the table.

CaviArE Architecture	Average Slope	Average intercept / A^{-1}	Calculated value of K
C10µ3d	-596 (±58)	-7700 ± 550	1.46 ± 8
C20µ3d	-998 (±23)	-13100 ± 1094	1.74 ± 8
C30µ3d	-1397 (±73)	-17031 ± 715	0.71 ± 8
C50µ3d	-2225 (±55)	-34390 ± 3104	12.35 ± 8
C100µ3d	-4407 (±291)	-61040 ± 1910	3.51 ± 8

Table 6.6: Table to show the average slope and y-intercept obtained from graphs of $|i_L|^{-1}$ vs. lnt for the 3d spaced CaviArE architectures of different sized microsquare cavity. The corresponding values of *K* are also given.

Although an accurate value of *K* has still not been derived, the values are again within the same region as calculated for all previous sections. This work has shown that all data is consistent with nanoband behavior during intermediate times, where diffusion out of the cavity is established.

6.4. Conclusions

It has been demonstrated in this chapter that the novel nanoarray architecture, developed in Chapter 5, is robust and provides quantifiable electrochemical responses. As outlined in the introduction, one of the challenges in nanoelectrode research is the difficulty in fabricating such small electrode architectures with controlled dimensions and pitch. The patented design method developed in chapter 5, provides a reproducible fabrication process which utlises standard microlithographic techniques to produce well defined nanoarrays with controllable dimensions and as far as the author is aware, such designs have not previously been presented in the literature. Since the length, spacing and even the width of these electrode arrays can be easily controlled utilising common microfabrication processes, these CaviArE, and indeed other designs, which may make use of similar fabrication processes, have real opportunities for enabling systematic characterisation of nanoelectrode responses.

It is interesting that the cyclic voltammetric and chronoamperometric data seem to fit to microband theory in both fast and intermediate time domains. That is, they have a $1/\ln t$ dependency, rather than a time-independent current response. This suggests that, at least within these regions, the CaviArE substrates behave very similarly to nanoband arrays of high effective area and therefore established microband theory can be used to analyse the responses. The response at fast times, however, for all electrode architectures has a steeper gradient and due to the relationships, $m = ((2\pi DAFc^{\infty})/w)^{-1}$ and x-axis intercept = $-\ln(KD/w^2)$, this either indicates that within this time regime smaller values of K are observed or that there is an apparent increase in electrode width. In Chapter 7 the time regimes and diffusional processes are probed in more detail using EIS analysis and it will be shown that similar apparent increases in electrode width are also observed over similar time scales due to the diffusional fields established. Further experimental research, in combination with transient computer simulations is required in order to better understand the electrode responses over fast time domains.

Due to the CaviArE architecture and possible interaction of diffusional fields in the corners, the total active electrode area is lower than the geometric area. Table 6.7 shows what percentage of the geometric area is effective during these studies (calculated using the slopes of the i_L vs. $\ln v$ plots and inserting into Eqn. 6.6).

CaviArE Architecture	Electrode geometric area / cm^2	Effective Electrode area (from i_L vs. ln$v$) / cm^2	Percentage effective area / cm^2
C30µ1d	4.1334×10^{-4}	2.47×10^{-4}	59.75
C30µ2d	1.886×10^{-4}	1.18×10^{-4}	62.71
C30µ3d	1.0584×10^{-4}	8.10×10^{-5}	76.71
C30µ4d	6.936×10^{-5}	4.63×10^{-5}	66.75
C10µ3d	3.125×10^{-4}	1.84×10^{-4}	58.88
C20µ3d	1.5876×10^{-4}	1.04×10^{-4}	65.51
C50µ3d	6.25×10^{-5}	4.83×10^{-5}	77.28
C100µ4d	3.3×10^{-5}	2.68×10^{-5}	81.21

Figure 6.7: Table 6.7 showing the geometric electrode area and the effective active area, (calculated using equation 6.6 and the average slopes obtained from plots of i_L vs. ln$v$), for each of the electrode architectures studied in this work.

In general, the percentage effective area appears to increase with increasing cavity size, as might be expected if the contribution of corner depletion has a lesser effect on larger cavities. The trend for arrays of different spacing is less conclusive and should be expected to be the same in regions where the electrode elements behave independently of one another. On average, over a range of experiments and architectures, the percentage effect area is approximately 69 ± 9%. Nevertheless, the associated current densities are still extremely high, due to effective mass transport. In fact the arrays give approximately half of the current output compared to an equivalent microsquare array even though CaviArE's have less than 1 % of the square electrode area and indeed with a marked reduction of the capacitive effects associated with the microsquare array. This allows excellent pseudo-steady state responses to be recorded even at 30 Vs^{-1}. An attempt to determine the constant K in Equation 6.2 for these CaviArE devices during intermediate time scales, concluded that K could not be measured accurately. This is not surprising since the calculation of K is an exponential of an extrapolation. However it can be determined that K is in the range >0 - 10 - <100, which is consistent with a nanoband.

The CaviArE analysis in 1 mM potassium ferricyanide produces very similar responses as those recorded in 10 mM potassium ferricyanide, with current densities being an order of magnitude smaller, as expected. The data

obtained from the chronamperometric data also scales with ferricyanide concentration, as expected.

Experiments were also performed in 1mM ferrocene carboxylic acid to test whether similar behavior was observed using other redox couples. This is satisfying, and verifies that the data obtained for both redox couples is representative of the true CaviArE response within these time domains.

Finally the analyses of several different CaviArE architectures, in comparison with C30µ3d arrays, in general, do follow predicted patterns expected for the response of nanoband arrays. There are some discrepancies between the slopes obtained for graphs of $|i_L|^{-1}$ vs. *lnv* compared with graphs of $i_L|^{-1}$ vs. ln*t*, and it would be interesting to analyse the CV responses over a wider data set and indeed across different architectures in order to obtain a more comprehensive understanding of the CaviArE response. Transient simulation models and experiments on single CaviArE elements, may also provide a better understanding of the entire response over all time domains.

Voltammetric and chronamperometric experiments have shown good fits to microband theory, at least within specific time regions, however cyclic voltammetry only provides information about the CaviArE responses at pseudo-steady state and the chronoamperometric data, at present can only be confidently fitted over a very small time region. Electrochemical Impedance Spectroscopy will be employed in Chapter 7, in order to study, the CaviArE response over all frequencies studied.

6.5. References

(1) Heinze, J. *Angewandte Chemie International Edition in English* **1993**, 1268.

(2) Amatore, C. In *I. Rubenstein (Ed) Physical Electrochemistry: Principles Methods and Applications*; Marcel Decker: New York, 1995, p 131.

(3) Berduque, A.; Lanyon, Y. H.; Beni, V.; Herzog, G.; Watson, Y. E.; Rodgers, K.; Stam, F.; Alderman, J.; Arrigan, D. W. M. *Talanta* **2007**, *71*, 1022.

(4) Caston, S. L.; McCarley, R. L. *Journal of Electroanalytical Chemistry* **2002**, *529*, 10.

(5) Stulik, K., C. Amatore, K. Holub, V. Marecek and W. Kutner *Pure and Applied Chemistry* **2000**, *72*, 1483.

(6) Millan, K. M.; Mikkelsen, S. R. *Analytical Chemistry* **1993**, *65*, 2317.

(7) Cass, A. E. G.; Davis, G.; Francis, G. D.; Hill, H. A. O.; Aston, W. J.; Higgins, I. J.; Plotkin, E. V.; Scott, L. D. L.; Turner, A. P. F. *Analytical Chemistry* **1984**, *56*, 667.

(8) Matsue, T.; Evans, D. H.; Osa, T.; Kobayashi, N. *Journal of the American Chemical Society* **1985**, *107*, 3411.

7. EIS Characterisation of the Nanoband Cavity Array Electrodes (CaviArE)

7.1. Introduction

Voltammetry and chronoamperometry experimentation (Chapter 6) has established that the CaviArE response is consistent with nanoband theory at medium times. This chapter concerns fundamental analysis of CaviArE devices using EIS. As in chapter 6, initially the response of the C30µ3d architectures will be studied in detail. The EIS response will be studied over a range of frequencies (times) and as there is no equivalent circuit for the CaviArE, equivalent circuit(s) will be developed to model the response. Full EIS analysis of the corresponding microsquare array (S30µ3d) is also presented in order to better understand and compare the CaviArE response. Additionally, the effect of redox concentration in the EIS response of the C30µ3d array is presented, along with the EIS responses of different CaviArE architectures.

7.2. Specific Experimental

All solutions and experimental details were as described in chapter 3 and 1 mM ferricyanide solution was prepared as in section 6.2.1.1.

7.3. Results and Discussion

7.3.1. EIS Fitting and Analysis of the S30µ3d Array

For comparison with the CaviArE system, the response of the S30µ3d array is now presented. Single microsquares (S50µ) have been fully analysed in chapter 4, and the response associated with individual microsquares in this array is well understood. Analysing the EIS response of S30µ3d arrays is now used to aid in the understanding of the CaviArE system.

The typical response and analysis of the S30µ3d microsquare array is shown in Figure 7.1.

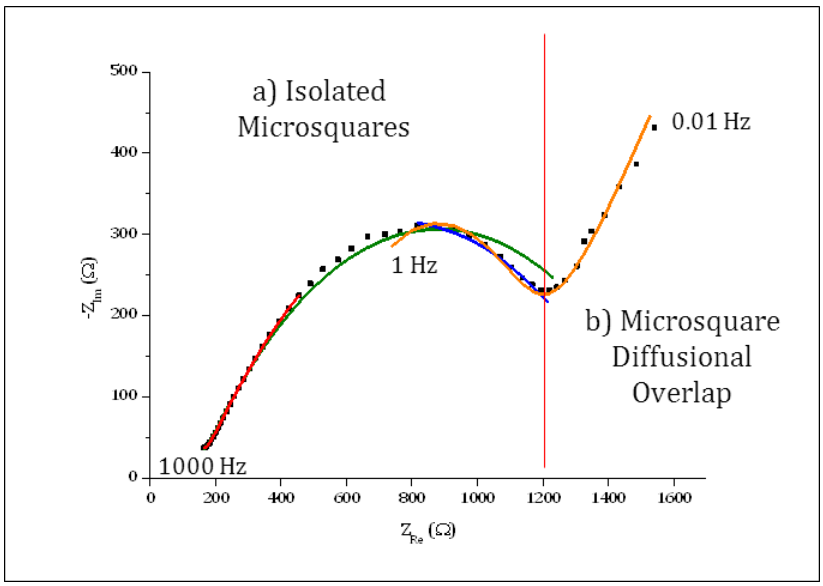

Figure 7.1: Typical Nyquist plot obtained for the S30µ3d substrate at *E*dc = 0.19 V in ferricyanide [10 mM] between f = 1x10^3 Hz and 0.01 Hz, where the high frequency region (region a)) corresponds with diffusion from the isolated microsquares and the low frequency region (region b)) corresponds with microsquare diffusional overlap.

The green plot represents the modified Randles' equivalent circuit fit (Figure 2.13) to frequencies from 1x10^3 Hz to 0.105 Hz, assigned in section 4.3.5, attempting to model the whole isolated microsquare response; the red plot represents the modified Randles' equivalent circuit fitted to frequencies from 1x10^3 Hz to 5.690 Hz, which enables R_U, C_{DL}, R_{CT} and Z_W to be calculated for the individual microsquare response; the blue plot represents the modified Randles' equivalent circuit fitted to frequencies from 1.099 Hz to 0.105 Hz, enabling values of R_{NL} to be determined; and the orange plot represents an equivalent circuit fit using a resistor and Warburg parameter in parallel to fit frequencies from 0.687 Hz to 0.01 Hz in order to calculate Z_W associated with microsquare diffusional overlap.

Region a) can be attributed to the response of the individual, isolated microsquare electrodes in the array and the data fits to the same modified Randles' equivalent circuit (Figure 2.13) as the single microsquare electrodes in Chapter 4 (Figure 4.27 in section 4.3.5). Just like the single microsquares these data cannot be fitted accurately (black line) to the entire frequency range in this region. As in chapter 4, this can be attributed to differences in the development of the diffusion layer for microsquare and microdisc electrodes with time. Instead, as with chapter 4, the equivalent circuit can be accurately fitted to the

high (red line) and low (blue line) frequencies in this region, separately in order to obtain accurate values for R_U, C_{DL}, R_{NL} and Z_W (Y_0). This response is therefore again characteristic of isolated microsquare electrodes.

The values of R_U and C_{DL} obtained by fitting to frequencies between $1x10^3$ Hz and 5.690 Hz give average uncompensated resistances for the S30µ3d substrate of 71 ± 13 Ω. The average double layer capacitance for the S30µ3d substrates is 0.257 ± 0.064 µF. The total area of the S30µ3d electrode array is $1.5625x10^{-2}$ cm^2, so the average capacitance of the S30µ3d substrates is 16.4 µF cm^{-2}, which, is a reasonable value for platinum and comparable to that calculated for the capacitance of 16.0 µF cm^{-2} in chapter 5 (section 5.3.1.2).

It is satisfying to observe that the charge transfer resistance is again extremely small, as with single microsquare electrodes (chapter 4) which is indicative of a clean platinum surface. Also similar to the single microsquare response, the Warburg impedance, at each dc potential can be obtained by fitting the modified Randles' circuit to frequencies between $1x10^3$ Hz and 5.690 Hz. Figure 7.2 shows these data plotted as a function of E_{dc} and the blue line is the fit to the thermodynamic model given in equation 2.44.

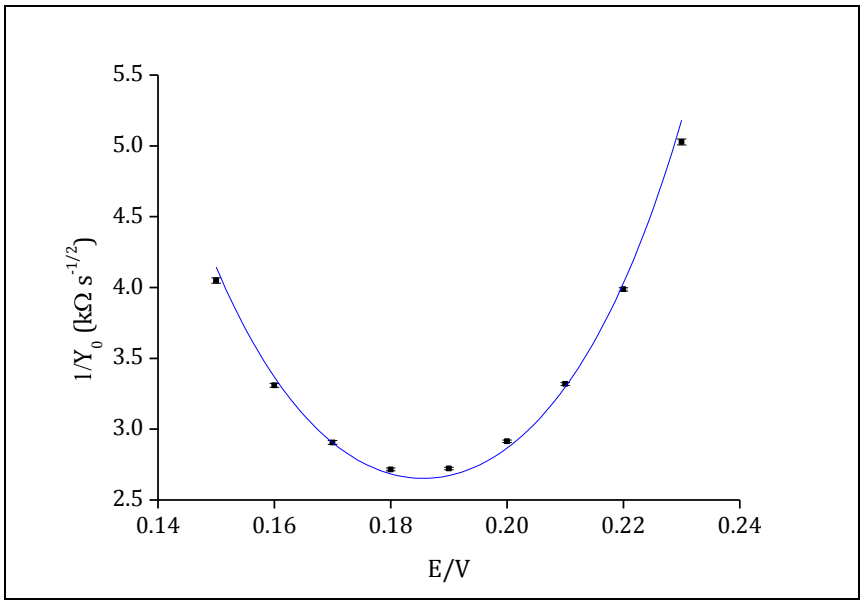

Figure 7.2: Plot of $1/Y_0$ vs. E_{dc} found by fitting the EIS data using the modified Randle's circuit to frequencies of $1x10^3$ Hz to 5.690 Hz. The blue line is the fit to the thermodynamic expression (eqn. 2.44) and gives a correlation coefficient of 0.995 and $1/Y_0^{min}$ value of 2.65 (± 0.02) kΩ $s^{-1/2}$ and $E_{1/2}$ value of 0.186 (± $3.86x10^{-4}$) V.

It is encouraging to observe that the thermodynamic expression fits extremely well to the Warburg ($1/Y_0$) data. In Chapter 4, equation 4.6 was used to further validate the value of $1/Y_0^{min}$ obtained via this model. For an area of 1.5625×10^{-2} cm^2 the Warburg coefficient, σ is 1.85 kΩ $s^{-1/2}$, which translates to a $1/Y_0^{min}$ value of 2.62 kΩ $s^{-1/2}$ in a bulk concentration of 10 mM. This is the same within experimental error, as the $1/Y_0^{min}$ value of 2.65 (±0.02) kΩ $s^{-1/2}$ obtained in Figure 7.2 which therefore indicates that the Warburg diffusion observed at high frequencies is that linear diffusion of ferri/ferrocyanide to/from isolated microsquares.

The Non-linear resistance, at different dc potentials can be obtained by fitting the modified Randles' Circuit to frequencies between 1.099 Hz and 0.105 Hz, fixing the values of R_U, C_{DL} and R_{CT} to those found at high frequencies. The curve obtained is given in Figure 7.3. The blue line again representing the thermodynamic fit which is given by equation 2.42.

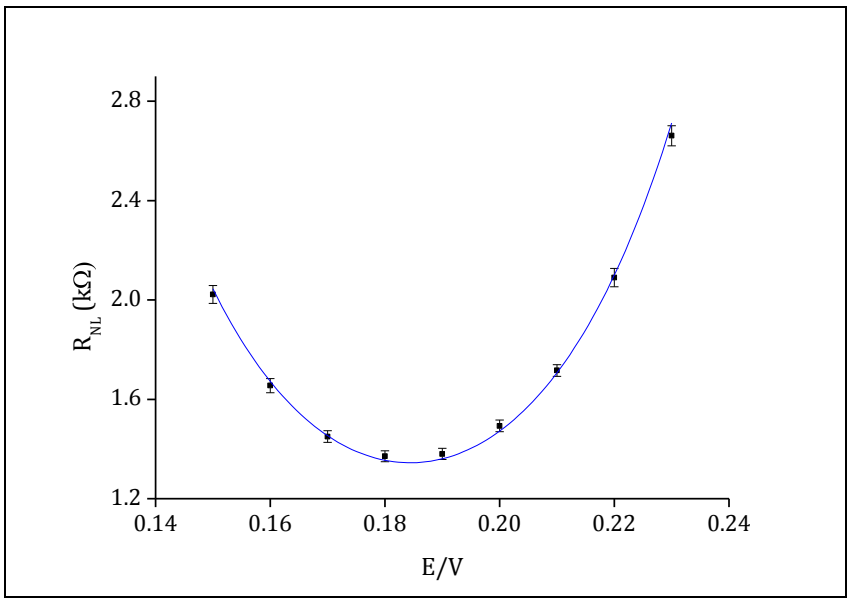

Figure 7.3: Plot of R_{NL} vs. E_{dc} found by fitting the EIS data using the modified Randle's circuit to frequencies of 1.099 Hz to 0.105 Hz. The blue line is the fit to the thermodynamic expression (eqn. 2.42) and gives a correlation coefficient of 0.998; R_{NL}^{min} value of 1.345 (± 6.144×10^{-3}) kΩ and $E_{1/2}$ value of 0.184 (± 2.63×10^{-4}) V.

Again the thermodynamic expression fits extremely accurately to the data obtained, providing confidence in the modified Randles' circuit fit at these frequencies.

Region b) (of Fig. 7.1) shows the response of the electrode array as the individual electrodes overlap. This can again be modelled as a Warburg impedance, Z_W (Y_0) which is consistent with linear diffusion across the entire array area, as the diffusion layers from each array element have completely overlapped (Figure 1.5 d). Figure 7.4 shows the equivalent circuit used to model the Warburg impedance in region 7.1 b).

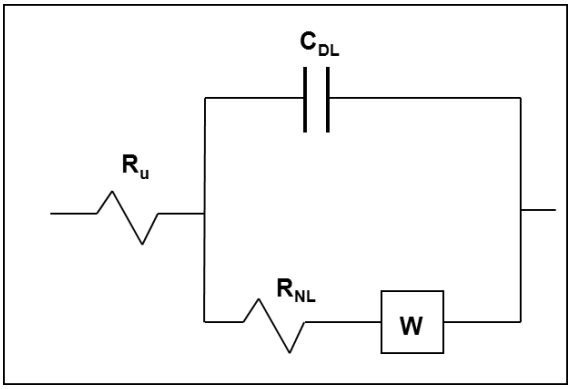

Figure 7.4: Schematic representation of the equivalent Circuit used to model the frequencies from 0.687 Hz to 0.01 Hz, which models a part of the microsquare non-linear resistance and the Warburg impedance associated with the overlapping microsquares in the array.

It should be noted that this equivalent circuit is not likely to be physically realistic, but provides a sound way of obtaining an accurate value of the Warburg impedance of the overlapping arrays. This unreality is demonstrated by the fact the average R_U value of 699 ± 141 Ω, and the average C_{DL} value of 0.3 ± 0.07 mF are physically unrealistic. However is useful for analysing the Warburg impedance.

Figure 7.5 shows a plot of $1/Y_0$ against E, obtained from the Warburg impedance at different dc potentials using the equivalent circuit shown in Figure 7.4.

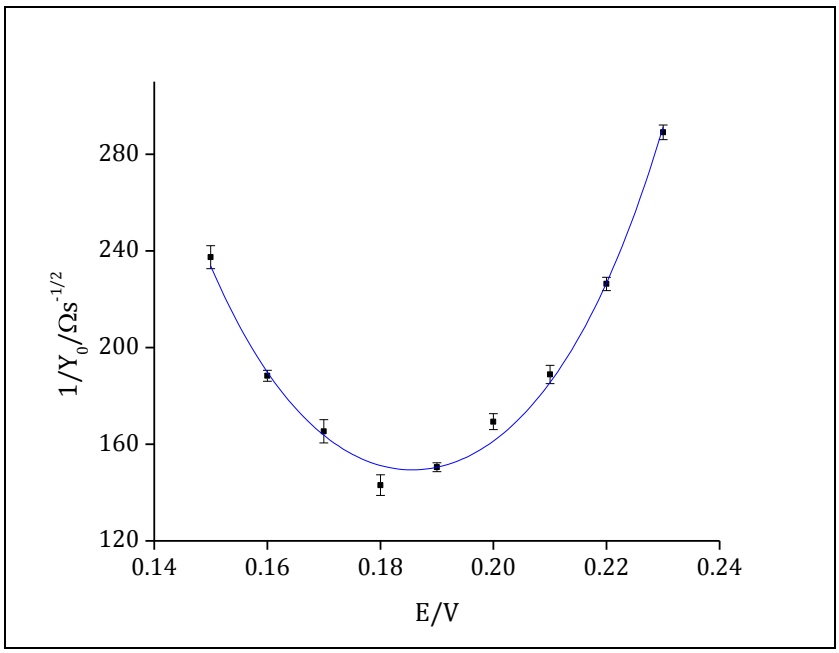

Figure 7.5: Plot of $1/Y_0$ vs. E_{dc} found by fitting the EIS data using the equivalent circuit shown in Figure 6.29 to frequencies of 0.687 Hz to 0.01 Hz. The blue line is the fit to the thermodynamic expression (eqn. 2.44) and gives a correlation coefficient of 0.996; a $1/Y_0^{min}$ value of 149 ± 20 Ω $s^{-1/2}$ and $E_{1/2}$ value of 0.186 ± 0.001 V.

The value of Y_0 in this region should be characteristic of planar diffusion across the entire microelectrode array (5x5 mm) and can be calculated mathematically again using equation 4.6. In this case therefore, for an area of 0.254 cm^2 the Warburg coefficient, σ^{min} is calculated to be 114 $\Omega s^{-1/2}$ which translates to a value of $1/Y_0^{min}$ of 161 $\Omega s^{-1/2}$. The value of 149 ± 20 $\Omega s^{-1/2}$ calculated in Figure 7.5 is within experimental error of that calculated mathematically.

7.3.2. EIS Fitting and analysis of the (30 µm)², 90µm spaced CaviArE (C30µ3d) architecture

7.3.2.1. Preliminary Observations

Figure 7.6 shows a typical EIS response obtained for the C30µ3d substrates in ferricyanide [10 mM] over a frequency range of 61x10^3 Hz and 0.01 Hz at different dc potentials.

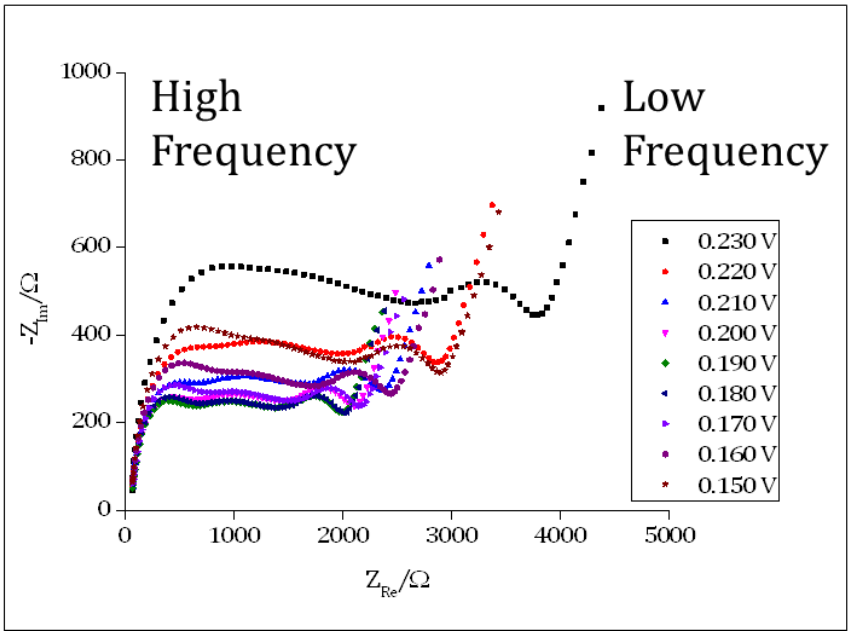

Figure 7.6: Typical Nyquist plot obtained for C30µ3d substrate in ferricyanide [10 mM] as the dc potential was systematically changed from +0.230 V to +0.150 V. For these and all subsequent EIS data, the frequency range recorded is between 61×10^3 Hz and 0.01 Hz, with rms amplitude of 10 mV.

The impedance of the reaction should be smallest at E^θ and increase as the potential moves away from E^θ in both the oxidizing and reducing directions. In almost all cases the Nyquist plot with the smallest impedance, was obtained at +0.190 V during batch macro collection. For consistency, Nyquist plots at Edc = +0.190 V will be presented for the remainder of the chapter.

In order to check this response to ensure that the Nyquist plot obtained was the electrochemical response of potassium ferricyanide, and that capacitive charging was not contributing to the CaviArE response observed, several control experiments were undertaken. The batch macro EIS experiment was run for several CaviArE substrates in KCl [0.1 M] only for a range of Edc. Figure 7.7 shows a typical EIS response in KCl compared to that in Ferricyanide.

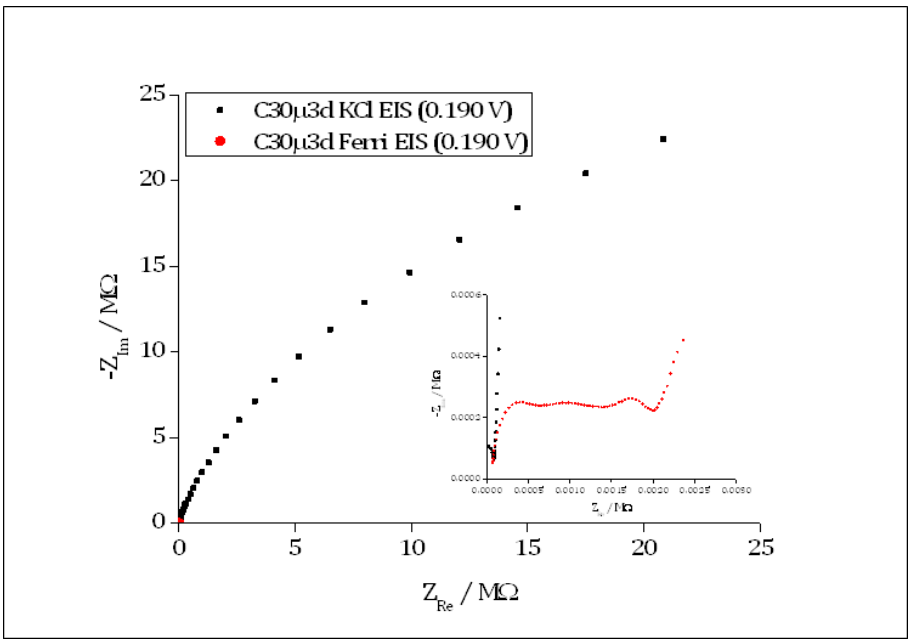

Figure 7.7: Nyquist plot showing the response of C30µ3d array in KCl [0.1 M] (black squares) and the corresponding Nyquist plot with added ferricyanide [10 mM] at 0.190 V, with inset to show the high frequency intercept.

It is clear that the resistance of the KCl electrochemical experiment is several orders of magnitude greater than the response in ferricyanide. This provided confidence that there is negligible contribution of capacitive charging at the lower frequencies. However, the high frequency behaviour is similar in each case which suggests that capacitive charging might dominate the response at high frequency.

Figure 7.8 shows a typical EIS response obtained for a C30µ3d substrate at dc = 0.190 V.

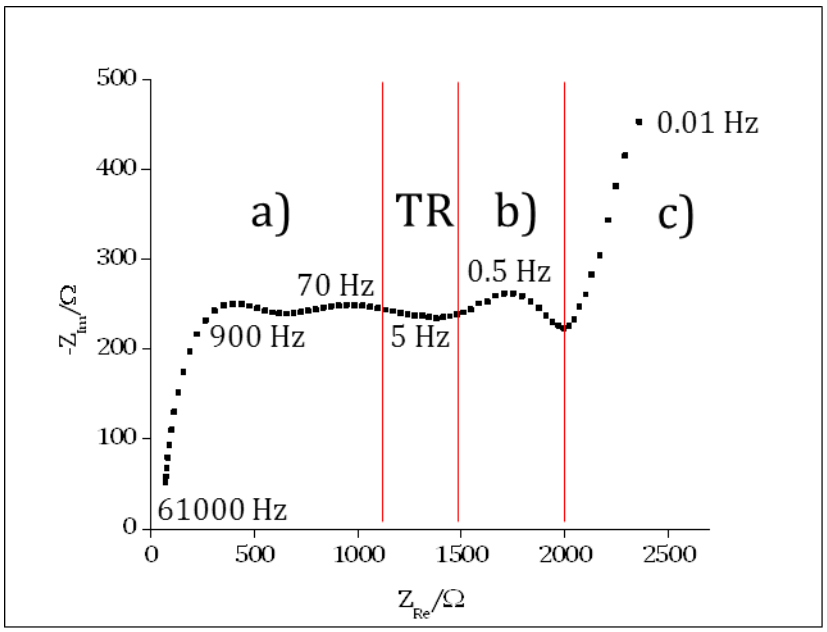

Figure 7.8: Typical Nyquist plot obtained for C30µ3d at Edc = 0.19 V in ferricyanide [10 mM]. Region **a)** at high frequencies is attributed to the diffusional regime within the individual cavities; region **b)** at medium/low frequencies is attributed to diffusion outside of the individual, isolated cavities and region **c)** at the lowest frequencies is attributed to diffusional microsquare overlap. The region termed TR in figure 7.8 is the transition region.

There are four distinct and notable regions of the Nyquist plot. Region a) is seen at the highest frequencies and is distinctive of a CaviArE electrode, given that the frequency is related to the diffusion layer thickness, through equation Eqn. 6.5. This region can be associated to diffusion within the individual microsquare cavities and thus the response of the enclosed nanoband (Figure 7.9 a)). The transition region, TR at medium frequencies, can thus be assumed to be the response as the depletion zone begins to fill the entire cavity and grow out of the hole. Region b) at medium/low frequencies can be attributed to radial diffusion from the isolated cavities (Figure 7.9 b)). Finally, region c), at the lowest frequencies can be attributed to planar diffusion towards the entire array (Figure 7.9 c)). Asside from the Transistion region, which is not observed in the current-time transient plots, the same diffusional regimes as in chapter 6 (Figure 6.5), can be used to describe the diffusion processes occurring over time in regions a), b) and c) of the Nyquist plot.

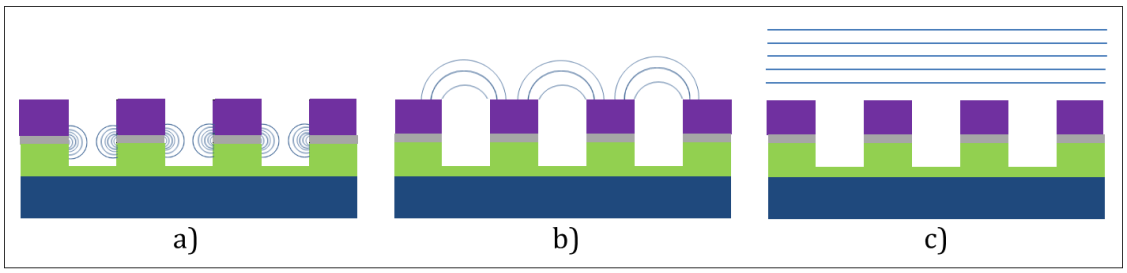

Figure 7.9: Schematic diagram to show the diffusional regimes attribute to regions a), b) and c) in Figure 7.8, where a) is radial diffusion within the microsquare cavity, b) is radial diffusion outside of the cavity and c) is planar diffusion towards the entire array.

To justify the assignment of these regions, several observations were made. It is clear that there is quite a variation between the EIS responses of the C30µ3d substrates, as shown in Figure 7.10. This variation primarily occurs at frequencies, in region a) and is thought to be caused by variation in the cleanliness of the electrode surface and hence variation of the charge-transfer resistance.

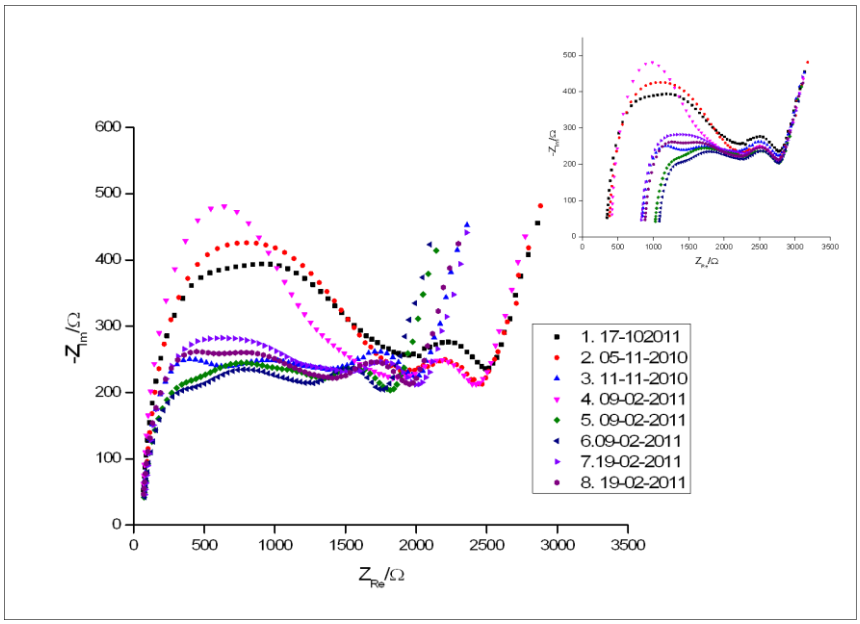

Figure 7.10: Typical Nyquist plot showing 8 different responses of C30µ3d substrates in ferricyanide [10 mM] at E_{dc} = 0.190 V between frequencies of 61x10^3 Hz and 0.01 Hz and ac amplitude of 10 mV rms. Inset shows the plot where the data has been shifted along Z_{Re} axis to align all the Warburg parameters associated with diffusion to the entire array (regions b) and c)).

The aligned plot (inset, figure 7.10) shows that there is very little variation in response in regions b) and c) the low frequency response, providing confidence that this is the planar diffusional response for the entire C30µ3d array in

ferricyanide. Figure 7.11 also shows the C30µ3d substrate given in Figure 7.8, superimposed on the corresponding response for the (S30µ3d) platinum array.

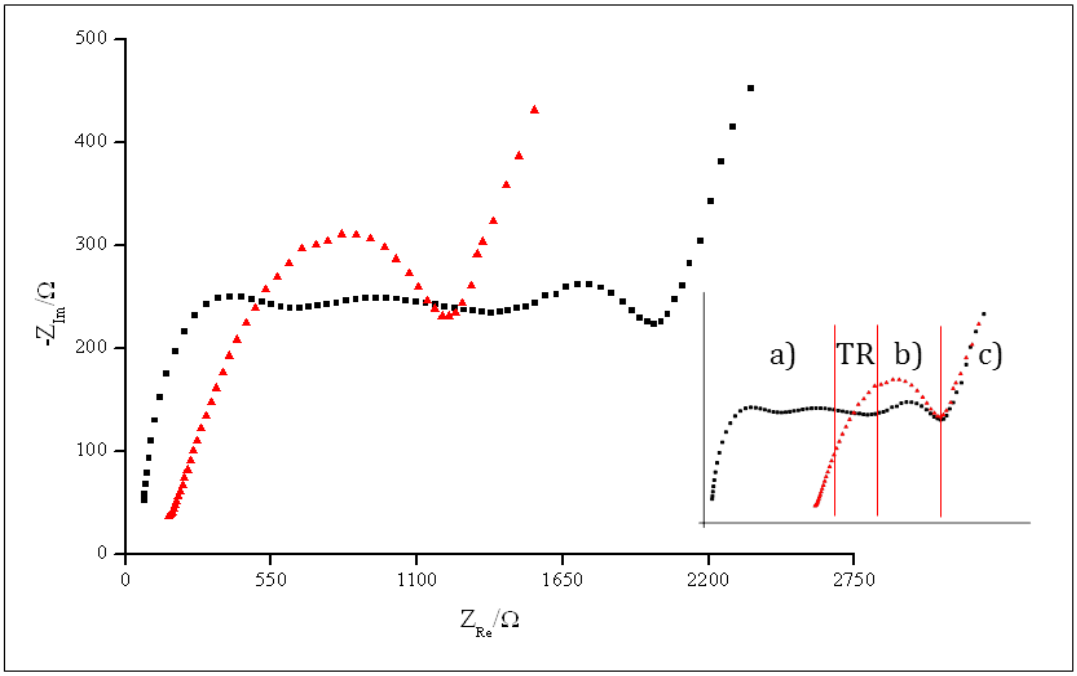

Figure 7.11: Typical Nyquist plots of a C30µ3d array (black squares) and an S30µ3d array (red triangles) at a dc potential of 0.19 V in ferricyanide [10 mM]. The C30µ3d response was recorded between $61x10^3$ Hz and 0.01 Hz and ac 10 mV rms; the S30µ3d response was recorded between $1x10^3$ Hz and 0.01 Hz and ac 1 mV rms. The inset shows the plot where the S30µ3d response has been shifted along the x-axis in order to overlay the Warburg resistance associated with overlap of both the microsquare and nanoband electrodes.

The inset clearly shows that the diffusional response in regions b) and c) is similar for both the S30µ3d array and the C30µ3d array. Although in the case of the S30µ3d response in region b) seems slightly larger than the equivalent planar diffusional response of the C30µ3d array. This difference is within 2 standard deviations of the natural variation observed between different C30µ3d arrays given in Figure 7.8. Thus the CaviArE response seems be the same as the S30µ3d array in regions b) and c), which is good evidence that this region results from the diffusional response from the microsquare element in both cases (and in regards to CaviArE, indicative of diffusion outside of square cavity).

7.3.2.2. Low Frequency Fitting and Analysis of the C303d Substrates

Previous data suggest that the diffusional regimes in regions b) and c), the low frequency range of the C30µ3d EIS response (Figure 7.8), develop in a similar

manner to the low frequency response of the S30µ3d array (Figure 7.1). The same method therefore, was used to exhibit physical parameters for these regions (section 4.3.1). The modified Randles' equivalent circuit (Figure 2.13) used for S30µ3d in section 4.3.1 was again used to determine the non-linear resistance, associated with radial diffusion from the isolated microsquare cavities (region b)). The equivalent circuit shown in Figure 7.4 was also again used to determine the Warburg impedance associated with planar diffusion to the entire array in region c).

Figure 7.12 shows a typical Nyquist plot of a C30µ3d array at E_{dc} = 0.190 V Equivalent circuit fits to the low frequency data (regions b) and c)) are shown.

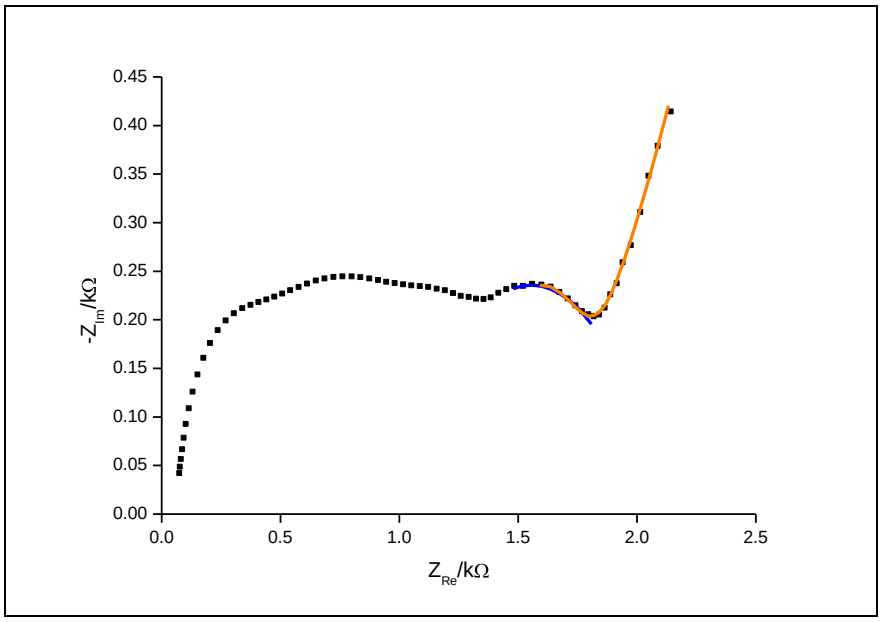

Figure 7.12: Typical Nyquist plot obtained for a C30µ3d substrate in ferricyanide between 61x10^3 Hz and 0.1 Hz at a dc potential E_{dc} = 0.19 V. The blue line shows the fit using the modified Randles' circuit between frequencies of 1.06 Hz to 0.13 Hz. The orange line shows the fit using the equivalent circuit given in Figure 7.4 between frequencies of 0.53 Hz to 0.01 Hz.

In order to obtain an estimate of the non-linear resistance, R_{NL}^{b} associated with radial diffusion from the cavity (blue line, region b)); the modified Randles' equivalent circuit was used and fitted over a similar frequency range as the S30µ3d array (Figure 7.5).

Figure 7.13 shows a typical plot of R_{NL}^{b} versus E_{dc}.

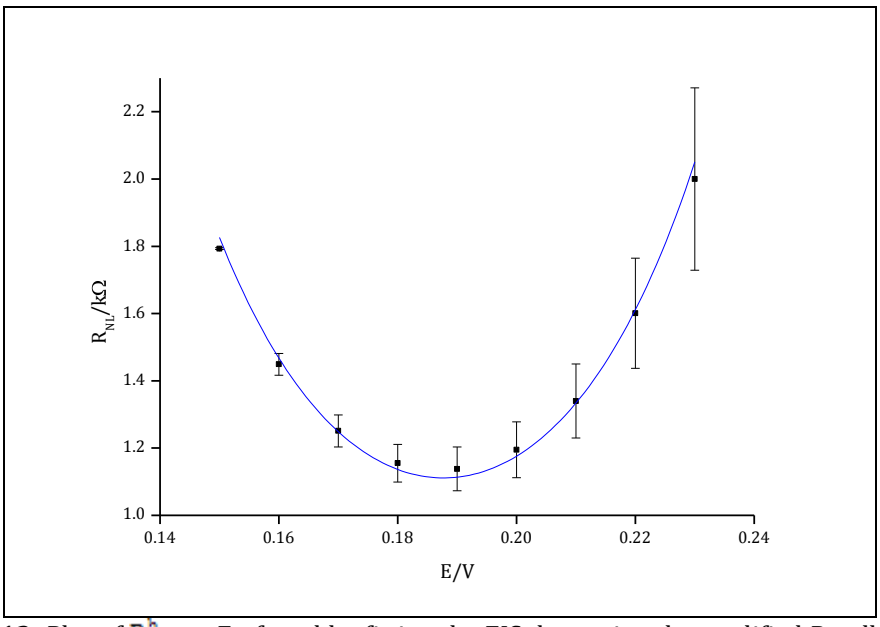

Figure 7.13: Plot of R_{NL}^{b} vs. E_{dc} found by fitting the EIS data using the modified Randle's circuit to frequencies of 1.06 Hz to 0.13 Hz. The blue line is the fit to the thermodynamic expression (eqn. 2.42) with a correlation coefficient of 0.994; $R_{NL}^{b,min}$ value of 1.1 ± 0.1 kΩ and $E_{1/2}$ value of 0.188 ± 0.005 V.[i]

The average value of $R_{NL}^{b,min}$ for the C30μ3d substrates is 1.2 ± 0.1 kΩ, which is the same, within experimental error, as the value of R_{NL} for S30μ3d of 1.345 ± 0.006 kΩ. This is consistent with comparable diffusional transport in region b).

The transition region, TR is observed between frequencies of approximately 40 Hz and 4 Hz. There would be expected to be differences in the EIS response between CaviArE and square arrays in this region and at present no equivalent circuit has been derivived to model this response. However the modified Randles' circuit does seem to fit very well over frequencies between 1.06 Hz and 0.13 Hz for region b) and this fit enables values of the Warburg impedance, Y_0^b to be obtained. Figure 7.14 shows a typical plot of the resulting $1/Y_0^b$ verses E_{dc}.

[i] The error shown in Figure 7.12 is the standard deviation between all R_{NL} C30μ3d values calculated during this research, the error for each individual experiment is very small, similar to that of the S30μ3d data but the variation between experiments is slightly larger. All errors given for the C30μ3d plots are the standard deviation over a number of experiments.

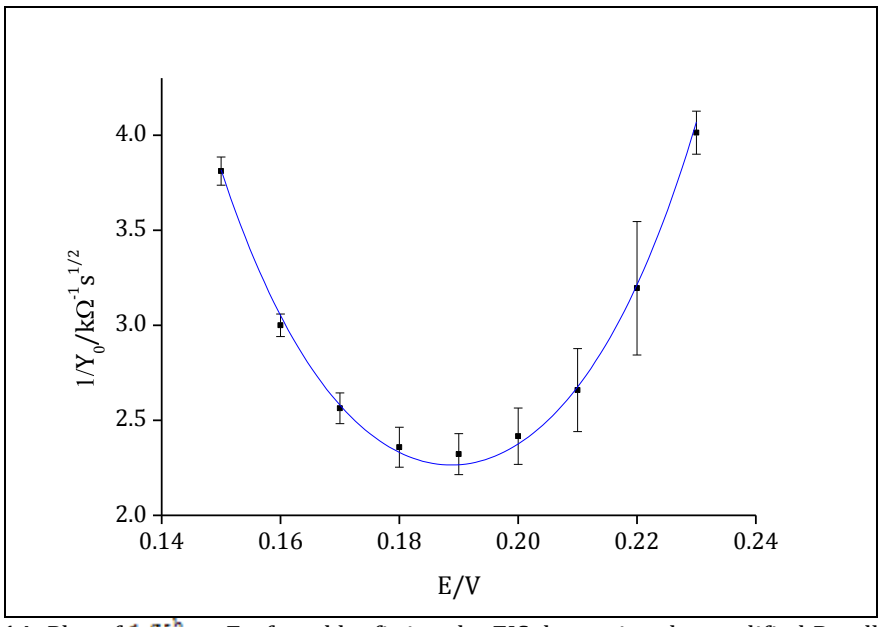

Figure 7.14: Plot of $1/Y_0^b$ vs. E_{dc} found by fitting the EIS data using the modified Randles' circuit to frequencies between 1.06 Hz and 0.13 Hz. The blue line is the fit to the thermodynamic expression (eqn. 2.44) with a correlation coefficient, r = 0.997; $1/Y_0^{b,min}$ = 2.3 ± 0.2 kΩ $s^{-1/2}$ and $E_{1/2}$ = 0.189 ± 0.002 V.

It is satisfying that the average value for $1/Y_0^{b,min}$ is 2.4 ± 0.2 kΩ$s^{-1/2}$ for the CaviArE nanobands is the same, within experimental error, as that calculated for S30µ3d of 2.65 ± 0.02 kΩ $s^{-1/2}$. This response is therefore characteristic of planar diffusion from individual squares and CaviArE square cavities.

As for S30µ3d, the Warburg impedance Y_0^c, associated with complete planar diffusion over the entire array (region c)), shown by the orange curve in Figure 7.12, was also fitted using the equivalent circuit given in Figure 7.4. Figure 7.15 shows the graph of the $1/Y_0^c$ values obtained from this fitting, against E_{dc}.

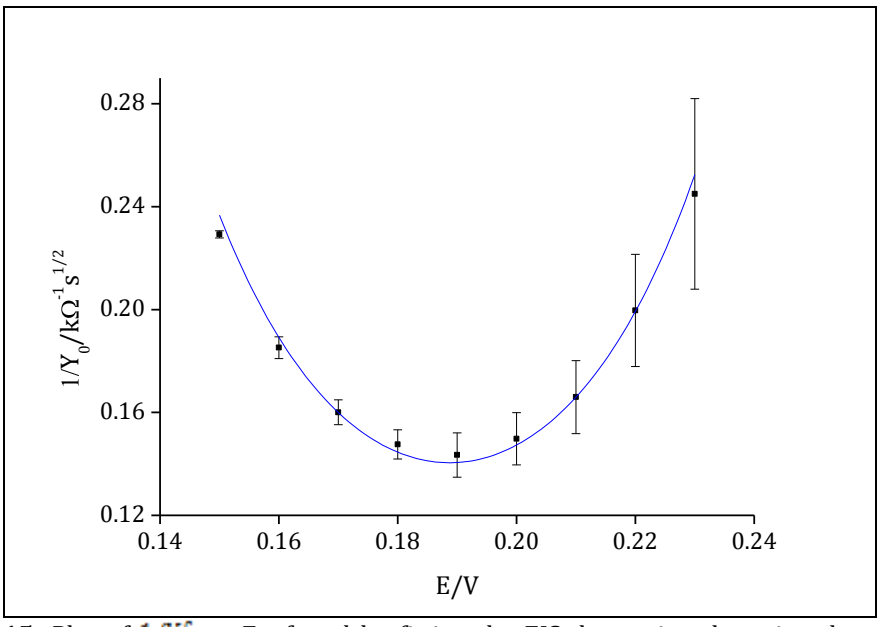

Figure 7.15: Plot of $1/Y_0^c$ vs. E_{dc} found by fitting the EIS data using the using the equivalent circuit in Figure 6.29 to frequencies of 0.53 Hz to 0.01 Hz (region c)). The blue line is the fit to the thermodynamic expression (eqn. 2.44) and gives r = 0.992; $1/Y_0^{c,\,min}$ = 140 ± 6 $\Omega s^{-1/2}$ and $E_{1/2}$ = 0.189 ± 0.001 V.

The average $1/Y_0^{c,\,min}$ value calculated over a range of frequencies is 147 ±6 $\Omega s^{-1/2}$ and is the same, within experimental error, as the $1/Y_0^{min}$ value of 149 ± 0.02 Ω $s^{-1/2}$ calculated for the S30µ3d substrate. There should be a quantifiable relationship between the Warburg parameter, Y_0^b associated with planar diffusion from the CaviArE cavity in region b) (Figure 7.13), and this Warburg parameter Y_0^c calculated at the lowest frequencies in region c) (Figure 7.16) associated with linear diffusion across the entire array. For these (30 µm), 3d spaced cavities (where d is equal to the edge dimension of the square cavity), the area of the entire array is 16 times that of the cavities, (Figure 7.16), so Y_0^c should be 16 times that of the Warburg impedance associated with the individual cavities.

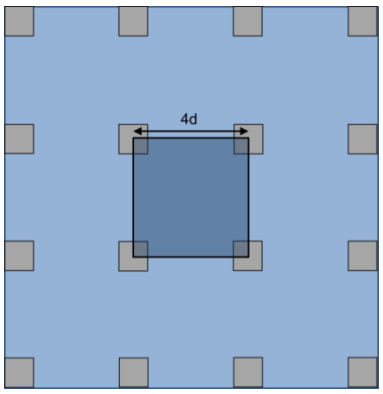

Figure 7.16: Schematic diagram of the difference between the areas of the cavities and that of the entire electrode array. For cavities 3d spaced, this relationship is $4d^2$, or 16.

Table 7.1 shows typical values of Y_0^b and Y_0^c calculated for C30µ3d, from data fits between frequencies of 1.06 Hz and 0.13 Hz and between frequencies of 0.53 Hz and 0.01 Hz respectively, at different E_{dc}.

Warburg Comparison			
E / V	**Y_0^b, 1.06 Hz to 0.13 Hz (region b)) / $\Omega^{-1}s^{1/2}$**	**Y_0^c, 1.06 Hz to 0.13 Hz (region c)) / $\Omega^{-1}s^{1/2}$**	**Difference**
0.15	2.62×10^{-4}	4.36×10^{-3}	16.62
0.16	3.33×10^{-4}	5.40×10^{-3}	16.20
0.17	3.90×10^{-4}	6.25×10^{-3}	16.01
0.18	4.24×10^{-4}	6.77×10^{-3}	15.98
0.19	4.31×10^{-4}	6.97×10^{-3}	16.19
0.2	4.14×10^{-4}	6.68×10^{-3}	16.13
0.21	3.76×10^{-4}	6.02×10^{-3}	16.02
0.22	3.13×10^{-4}	5.01×10^{-3}	16.00
0.23	2.49×10^{-4}	4.08×10^{-3}	16.38

Table 7.1: Table to show the relationship between Y_0^b and Y_0^c at different E_{dc} calculated for C30µ3d, from data fits between frequencies of 1.06 Hz and 0.13 Hz (region b))) and between frequencies of 0.53 Hz and 0.01 Hz (region c)) respectively. The average difference is 16.17 ± 0.21.

It can be seen from the data in Table 7.1, that the ratio between Y_0^b and Y_0^c is 16.2 ± 2. In fact the average ratio over a range of experiments is 16.0 ± 0.3 at all potentials. This confirms that the Warburg elements in regions b) and c) describe planar diffusion to cavities and across the whole array respectively.

7.3.2.3. High Frequency Fitting and Analysis of the C30μ3d Substrates

An equivalent circuit needed to be established to fit these novel electrodes at high frequency (region a)). There are very few papers available which model the EIS of nanobands, but Alden and Compton[1] have deduced expressions to describe the real, Z_{Re} and imaginary, Z_{Im} components of the EIS response for microband electrodes of length, *l* and width, *w* under two dimensional diffusion control. Since the cyclic voltammetric and potential step data suggest that the CaviArE substrates fit to microband theory (Chapter 6), these expressions were considered for their applicability.

In this treatment an ac potential, E, of frequency, ω (radians s^{-1}) is applied to the electrode:

$$E(t) = E_{dc} + \Delta E cos(\omega t) \qquad \textbf{Eqn. 7.1}$$

Where as usual for EIS, the amplitude of the perturbation is assumed sufficiently small that $\Delta E \ll \frac{RT}{F}$.

The measured impedance for any electrode system is:

$$Z(\omega) = Z_{Re} - jZ_{Im} \qquad \textbf{Eqn. 2.21}$$

Alden and Compton calculate Z_{Re} and Z_{Im} by assuming that frequencies, f ($\omega/2\pi$) are greater than $D/2w$, giving:

$$Z_{Re} = \frac{X + Y\sqrt{\frac{\omega}{2}}}{\left(X + Y\sqrt{\frac{\omega}{2}}\right)^2 + \left(Y\frac{\sqrt{\omega}}{2}\right)^2} \qquad \textbf{Eqn. 7.2}$$

and

$$Z_{Im} = \frac{Y\sqrt{\frac{\omega}{2}}}{\left(X+Y\sqrt{\frac{\omega}{2}}\right)^2+\left(Y\frac{\sqrt{\omega}}{2}\right)^2}$$ **Eqn. 7.3**

X is defined as,

$$X = \frac{\alpha'}{M}$$ **Eqn. 7.4**

where $\alpha' = n\mathbf{F}c^{\infty}Dl$ and *l*, in this instance is the length of the electrode

Y is defined as,

$$Y = \frac{\alpha'\gamma'\pi^{1/2}}{M}$$ **Eqn. 7.5**

where $\gamma' = w/\pi^{1/2}D^{1/2}$ and in which *w* is the width of the electrode and

$$M = 4\left(\frac{\mathbf{R}T}{n\mathbf{F}}\right)\cosh^2\left(\frac{\theta}{2}\right)$$ **Eqn. 7.6**

where

$$\theta = \left(\frac{nF}{RT}\right)[E_{dc} - \mathrm{E}^{\theta}]$$ **Eqn. 7.7**

when $E_{dc} = E^{\theta}$, $\cosh^2(\theta/2) = 1$ and thus $M = 4\mathbf{R}T/n\mathbf{F}$.

Using these parameters, the response for the diffusion of ferricyanide [10 mM] towards a linear, planar nanoband of *w* = 50 nm of equivalent length, *l* (0.012 cm) to the nanoband electrode in a $(30\ \mu m)^2$ cavity, can be calculated for the frequency range studied experimentally in this work (Figure 7.17).

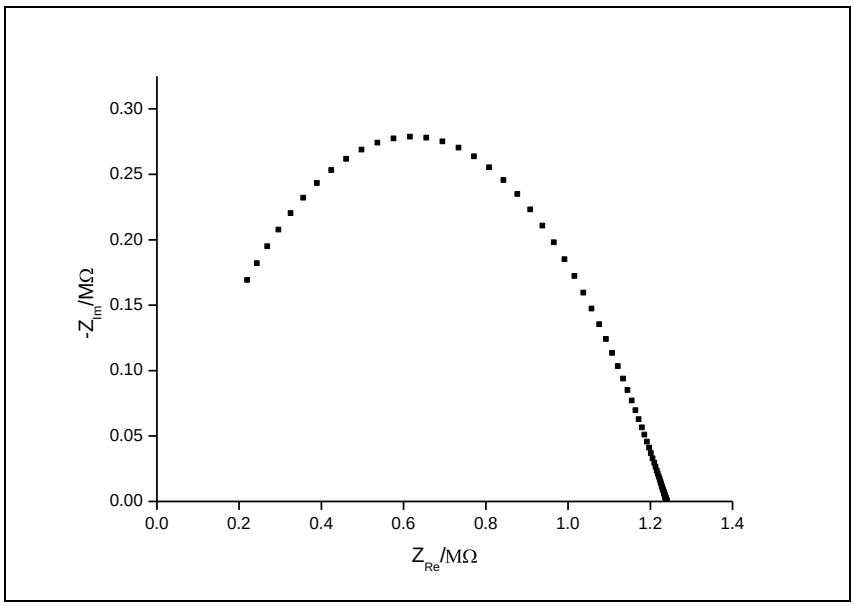

Figure 7.17: Nyquist plot calculated from Equations 6.7 and 6.8 over a frequency range between $1x10^{-6}$ Hz and 0.01 Hz, for one nanoband electrode of 50 nm width and 0.012 cm length, using the diffusion coefficient of ferricyanide and T = 298 K.

The plot shows an apparently near semi-circular response. It can be shown mathematically that this response is equivalent to a Warburg element and resistor in parallel, the equivalent circuit in Figure 7.18.

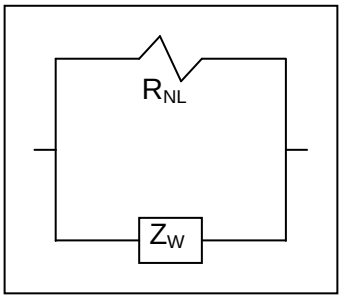

Figure 7.18: Equivalent circuit, representing the EIS response of a single nanoband electrode

The total admittance of this circuit is a combination of the admittance associated with the Warburg impedance and the admittance of the non-linear resistance.

$$\frac{1}{Z} = \frac{1}{Z_W} + \frac{1}{Z_{R_{NL}}} \qquad \textbf{Eqn. 7.8}$$

where:

$$Z_W = \frac{\sigma}{\omega^{1/2}} - \frac{j\sigma}{\omega^{1/2}} \qquad \textbf{Eqn. 7.9}$$

and

$$Z_{R_{NL}} = R_{NL} \qquad \textbf{Eqn. 7.10}$$

Thus

$$\frac{1}{Z} = \frac{1}{\left(\frac{\sigma}{\omega^{1/2}} - \frac{j\sigma}{\omega^{1/2}}\right)} + \frac{1}{R_{NL}} \qquad \textbf{Eqn. 7.11}$$

For simplicity, let

$$\frac{\sigma}{\omega^{1/2}} = A \qquad \textbf{Eqn. 7.12}$$

Thus Eqn. 7.11 equates to

$$\frac{1}{Z} = \frac{1}{A - jA} + (R_{NL})^{-1} \qquad \textbf{Eqn. 7.13}$$

Rearrangement and collection of terms leads to

$$\frac{1}{Z} = \frac{1}{2A}(1 + j) + (R_{NL})^{-1} \qquad \textbf{Eqn. 7.14}$$

Therefore to calculate total impedance, Z:

$$Z = \left(\frac{1}{2A}(1 + j) + (R_{NL})^{-1}\right) \qquad \textbf{Eqn. 7.15}$$

This can be rearranged to give

$$Z = \frac{\left(\frac{1}{2A}+\frac{1}{R_{NL}}-\frac{j}{2A}\right)}{\left(\frac{1}{2A}+\frac{1}{R_{NL}}\right)^2+\frac{1}{4A^2}}$$ **Eqn. 7.16**

Substituting for A gives:

$$Z = \frac{\left(\frac{\omega^{1/2}}{2\sigma}+\frac{1}{R_{NL}}-\frac{j\omega^{1/2}}{2\sigma}\right)}{\left(\left(\frac{\omega^{1/2}}{2\sigma}+\frac{1}{R_{NL}}\right)^2+\frac{\omega}{4\sigma^2}\right)}$$ **Eqn. 7.17**

Therefore

$$Z_{Re} = \frac{\left(\frac{\omega^{1/2}}{2\sigma}+\frac{1}{R_{NL}}\right)}{\left(\frac{\omega^{1/2}}{2\sigma}+\frac{1}{R_{NL}}\right)^2+\frac{\omega}{4\sigma^2}}$$ **Eqn. 7.18**

and

$$Z_{Re} = \frac{\left(\frac{\omega^{1/2}}{2\sigma}\right)}{\left(\frac{\omega^{1/2}}{2\sigma}+\frac{1}{R_{NL}}\right)^2+\frac{\omega}{4\sigma^2}}$$ **Eqn. 7.19**

The above equations hence take the exact form of equations 7.2 and 7.3 showing that

$$X = \frac{1}{R_{NL}}$$ **Eqn. 7.20**

and

$$Y = \frac{1}{\sqrt{2}\sigma}$$ **Eqn. 7.21**

This therefore suggests microband diffusional transport can be modelled with the equivalent circuit element given in Figure 7.17. This may also explain why the modified Randles' circuit can be used in region b) where microband diffusion outside of the cavity had been observed for C30µ3d (Chapter 6).

The high frequency region of the C30µ3d EIS data (region a)) in Figure 7.8 provides information about the uncompensated resistance, R_U, capacitance, C_{DL} and charge transfer resistance R_{CT} as well as the Warburg impedance Z_W and non-linear resistance, R_{NL} associated with diffusion towards the nanoband within the cavity. The modified Randles' circuit therefore should also be able to model this entire region with reasonable accuracy.

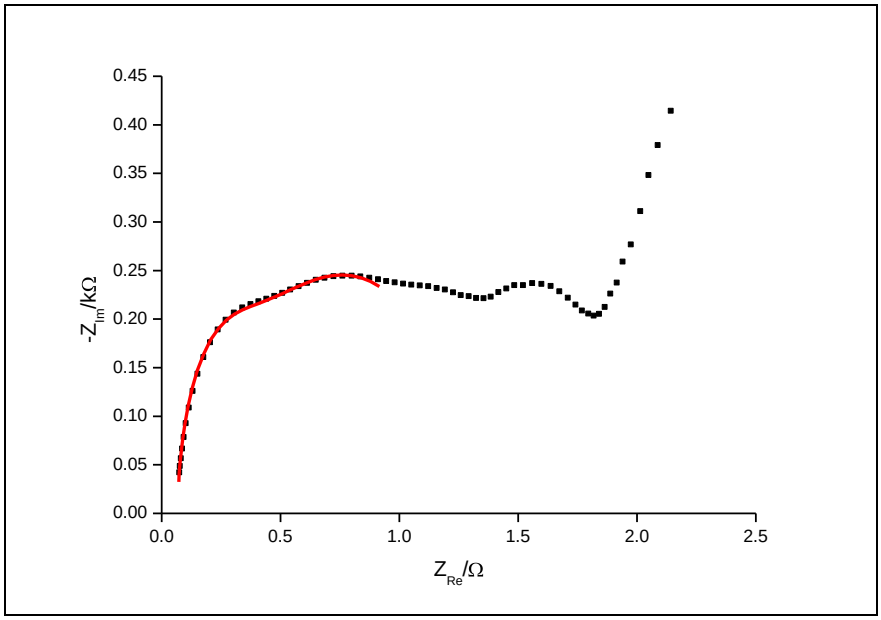

Figure 7.19: Typical Nyquist plot obtained for C30µ3d in 10 mM ferricyanide between 61x10^3 Hz and 0.01 Hz, at E_{dc} = 0.19 V. The red line shows the model fit using the modified Randle's circuit to frequencies between 61x10^3 Hz and 55.83 Hz.

The modified Randles' circuit does indeed appear to fit well to the high frequency data (Figure 7.19) and indeed similar fits were observed for all E_{dc}. Figure 7.20 shows a graph of the non-linear resistances, R^a_{NL} obtained using this circuit, versus E_{dc}.

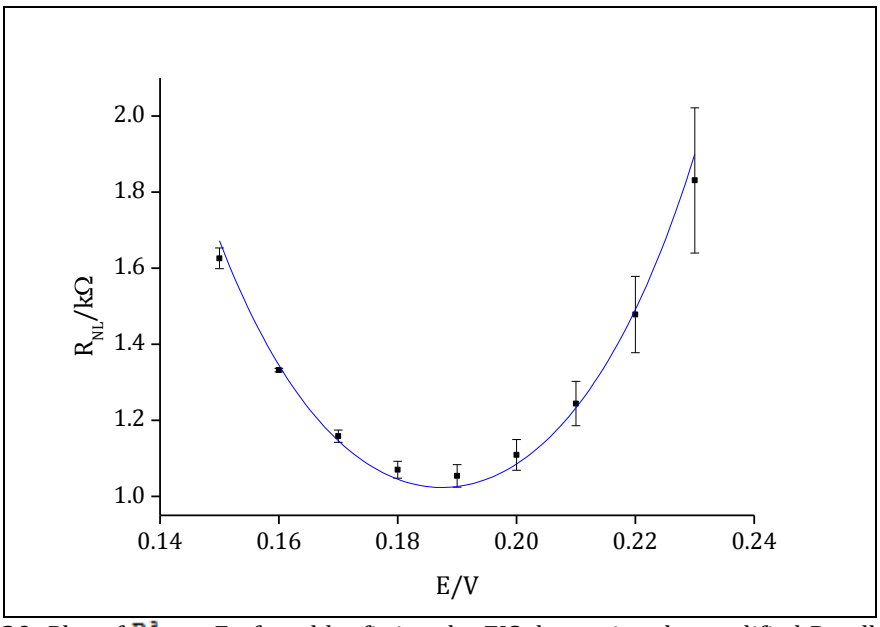

Figure 7.20: Plot of R_{NL}^{a} vs. E_{dc} found by fitting the EIS data using the modified Randles' circuit between frequencies of 61x10^3 Hz and 55.83 Hz. The blue line is the fit to the thermodynamic expression (eqn. 2.42) with a correlation coefficient, r = 0.991; $R_{NL}^{a,min}$ = 1.02 ± 0.04 kΩ and $E_{1/2}$ = 0.187 ± 0.001 V.

The average non-linear resistance, $R_{NL}^{a,min}$ at E^{θ}, recorded for the C30µ3d substrates over a range of experiments is 1065 ± 42 Ω., which would correspond to a value of 1.88 MΩ, for one single cavity nanoband electrode.

Equation 7.20, determined from the relationship between Compton's expressions and the model equivalent circuit used to fit the EIS experimental data, can be used to compare the theoretical value of *X* for a planar nanoband, to that of the CaviArE architecture for the same band width and total length.

Using equations 7.4 and 7.6, the theoretical value of *X* for a 50 nm wide electrode of 0.012 cm length is 8.06x10^{-7} Ω^{-1} compared with 5.32x10^{-7} Ω^{-1} (Eqn. 7.20) calculated from the average experimental value of $R_{NL}^{a,min}$, which is 65% of the value estimated via Compton's expressions. This difference is the same, within experimental error to the percentage effective error calculated in Chapter 6 (Table 6.7), and indeed therefore, the $1/R_{NL}$ would be expected to be smaller due to interaction and overlap of diffusional fields between the corners and neighbouring sides of the cavity. Additional to this is the fact that, in reality, bands do not have a steady-state current. Since band electrodes do not have a time-independent limiting current, the value of R_{NL} (and thus *X*), in reality will

also vary with time (frequency). Therefore it must be noted that even though the modified Randles' circuit seems to fit the high frequency data (region a)) with accuracy, and this fit is justified by Compton's theoretical derivations, the model must be only an approximation. The fact that the experimental and theoretical values correspond as well as they do provides confidence that the CaviArE substrates do indeed behave as nanobands, all be it with a reduced effective area than if the bands were planar.

Turning now to the values of charge-transfer resistance, R_{CT}, as shown in Figure 7.10, there is a large variation in responses between EIS data collected for different C30µ3d arrays. This is consistent with large differences in R_{CT} and hence cleanliness of the electrode surface. Since the C30µ3d electrodes are much smaller than the electrodes in the microsquare arrays, the charge transfer resistance is large, and at least comparable to the non-linear resistance (R^{a}_{NL}). This makes these electrodes more sensitive to variations in surface charge-transfer rates, making them very sensitive to even small amounts of impurities on the electrode surface. As discussed in section 1.3, one of the main reasons for developing nanoelectrodes is for their ability to measure fast charge-transfer kinetics. It was therefore hoped that the kinetics of redox couples with fast kinetics, for example ferri/ferrocyanide could be determined using this architecture (due to increased ratio between R_{CT}:R_{NL}.

Figure 7.21 a) shows Nyquist plots obtained for two C30µ3d arrays, one where the large charge transfer resistance observed, can be attributed to impurities on the electrode surface and the other where a much smaller charge transfer resistance is seen, indicative of a much cleaner electrode. The modified Randles' circuit is fitted to frequencies of 61×10^3 Hz to 27.74 Hz and 55.83 Hz respectively. Figure 7.21 b) shows the R_{CT} vs. E_{dc} curve for the dirtier electrode, which gives higher R_{CT} values and is most accurately modelled by the kinetic expression (Eqn. 2.39). Figure 7.21 c) shows the R_{CT} vs. E_{dc} curve for the cleaner electrode, which is modelled most accurately by the thermodynamic expression (Eqn. 2.41).

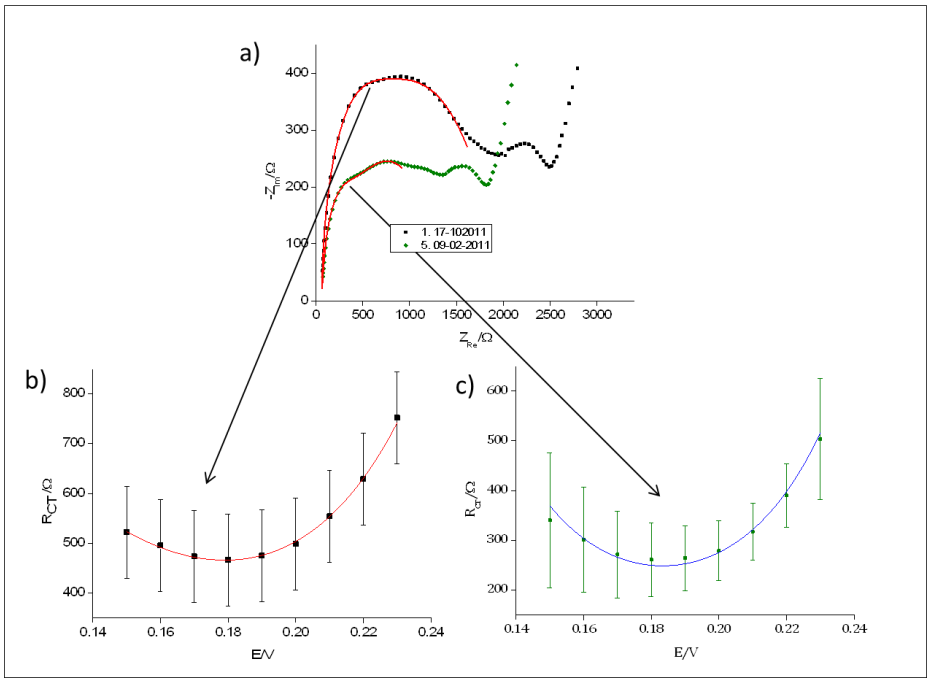

Figure 7.21: a) Nyquist plots showing the response of two C30µ3d substrates in ferricyanide [10 mM] at E_{dc} = 0.190 V, with high frequency fits to the modified Randles' circuit. Electrode array No. 1 (black squares, Fig. 7.10) shows a fit between 61x10^3 Hz and 27.74 Hz and is typical of a plot with a large R_{CT} at high frequencies corresponding hindered (dirtier electrode). Electrode array No. 5 (green diamonds, Fig. 7.10) shows a fit between 61x10^3 Hz and 55.83 Hz and has a much smaller R_{CT} value corresponding to charge transfer under thermodynamic control at a cleaner electrode surface. **b)** Shows a plot of R_{CT} vs. E_{dc} for electrode array No. 1 and the red line corresponds to a fit to the kinetic model (Eqn. 2.39) with a correlation coefficient, r = 0.998, $R_{CT,K}^{min}$ = 499 ± 92 Ω and $E_{1/2}$ = 0.199 (± 0.005) V. **c)** Shows a plot R_{CT} vs. E_{dc} for electrode No. 5 and the blue line corresponds to a fit to the thermodynamic model (Eqn. 2.41) with a correlation coefficient, r = 0.994, $R_{CT,e}^{min}$ = 248 ± 67 Ω and $E_{1/2}$ = 0.183 ± 0.003 V.

The kinetically hindered charge transfer resistance in Figure 7.21 b) is much larger than the thermodynamically limited charge transfer resistance shown in Figure 7.21 c) which provides evidence that this kinetic limitation is caused by a dirty electrode surface rather than the observation of fast ferricyanide reduction kinetics expected at a clean platinum surface. For the fast thermodynamic response, even though a kinetic response was not observed, the charge transfer resistance can still be used to infer the lower limit of the standard rate constant for the ferri/ferrocyanide redox reaction in these systems, by using the equation:

$$R_{CT}^{min} = \frac{RT}{AF^2 c}\left(\frac{2}{k^{\theta}}\right) \qquad \textbf{Eqn. 7.22}$$

For an electrode (area total 1.0584×10^{-4} cm^2), the rate constant, k^{Θ} for ferricyanide has a lower limit of 1.99 cm s^{-1} from the minimum charge transfer resistance ($R_{CT,e}^{min}$) in Figure 7.21 c). This is fast in comparison with a lower limit of 0.99 cm s^{-1} calculated from the $R_{CT,K}^{min}$ response in Figure 7.21 b) and much greater than the lower limit value of 0.05 cm s^{-1} calculated from the charge transfer resistance of the single (50 μm)^2 microsquare in chapter 4 (Figure 4.20).

In recent years research into the magnitude of the standard rate constant and apparent transfer coefficient of ferri/ferrocyanide has been carried out by a number of research groups. Krulik *et al*[2] discuss how the rate constant of ferricyanide is affected by choice and concentration of supporting electrolyte. Using a platinum rotating disc electrode, they quote experimental values of between 0.047 and 0.2 cm s^{-1}. Winkler[3] determined the kinetics of ferricyanide at a 0.2 mm and 12.5 μm platinum electrode using square wave voltammetry at different frequencies and quotes values of the standard rate constant between 0.135 and 0.25 cm s^{-1}. Feeney and Kounaves[4] quote values of 0.35 to 0.43 cm s^{-1} from various Iridium microelectrodes. Zhang *et al*[5] conducted a thorough study of ferricyanide kinetics at different sized Pt-Ir nanoelectrodes of different radii and quote values from 0.12 to 17.28 cm s^{-1} as the radius of the electrode decreases. Chen and Aoki[6], however, describe how overestimation of rate constants can be calculated at very small nanoelectrodes due to the comparable size of the mean free path length, λ with the diffusion layer thickness and thus, a breakdown of electro-neutrality (section 1.3.1). Zhang describes how this can be accounted for in their research and states that the values of rate constant predicted in the paper are reasonable estimates. It must be noted, however, that for a radius of 55.2 nm[5] (similar to the width of the C30μ3d band), the measured rate constant was 0.2 cm s^{-1}. In fact the lower limit value of k^{θ} obtained for the C30μ3d substrate was very much higher than all values found in the literature for similar sized electrodes in 0.1 M KCl. Since the width of the electrode is 50 nm and the electrode response seems to correlate well with microband theory, it is not believed that deviation in electro-neutrality is the cause of this fast rate constant. It must also be noted that if the true kinetic

response could be observed by cleaning the electrode further, the actual value of k^{θ} may be even larger. This suggests that the C30µ3d architecture may be a very efficient at determining fast electrode kinetics.

Values of the Warburg impedance, $1/Y_0^a$, at high frequencies can also be determined using the modified Randles' circuit. However, if the charge transfer resistance is large, it is quite difficult to fit this parameter accurately. Figure 7.22 shows a typical graph of $1/Y_0^a$ versus E_{dc} for a C30µ3d array when the charge transfer is under thermodynamic control, calculated using the modified Randles' circuit between frequencies of 61x10^3 Hz and 55.83 Hz.

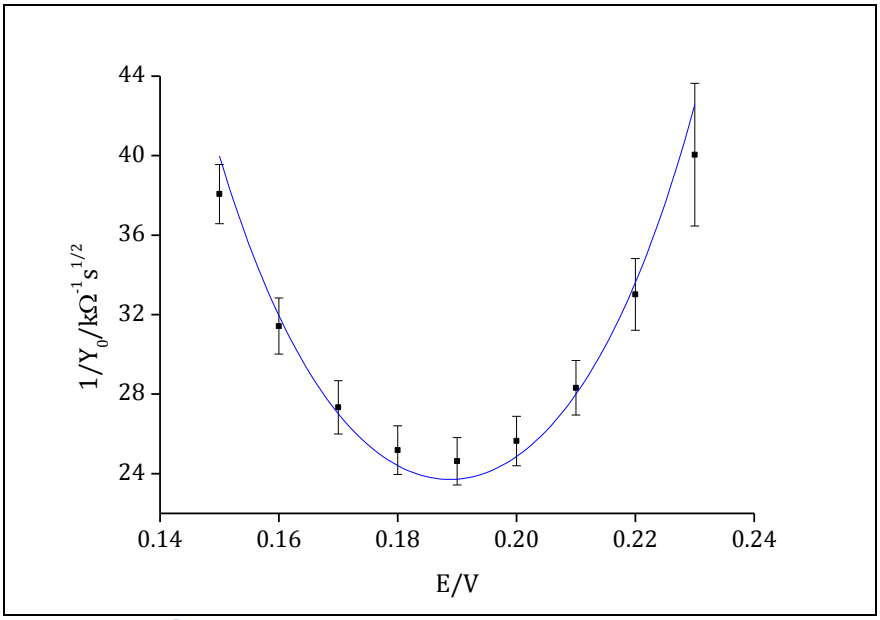

Figure 7.22: Plot of $1/Y_0^a$ vs. E_{dc} found by fitting the EIS data using the modified Randles' circuit to frequencies of 61x10^3 Hz to 55.83 Hz. The blue line is the fit to the thermodynamic expression (eqn. 2.44) with a correlation coefficient, r = 0.973; $1/Y_0^{a,min}$ = 24 ± 1 kΩ s$^{-1/2}$ and $E_{1/2}$ = 0.189 ± 0.001 V.

The average value of $1/Y_0^{a,min}$ calculated for the C30µ3d arrays is 22.3 ± 1 kΩ s$^{-1/2}$. As discussed in section 2.6.2, the Warburg coefficient, σ can be calculated from $1/Y_0$ by multiplying the value by $1/\sqrt{2}$. For one C30µ3d electrode this translates to a σ value of 28.560x10^6 Ω s$^{-1/2}$. When inserting this value into Compton's Equation 7.22, a *Y* value of 2.476x10^{-8} Ω^{-1}s$^{1/2}$ is obtained. This is an order of magnitude (13 times) smaller, than the value of *Y* (3.334x10^{-7} Ω^{-1}s$^{1/2}$) calculated using Equation 7.6. This suggests that planar diffusion occurs over an area that is 13 times larger than the nanobands.

The Warburg parameter region on most of the C30µ3d plots occurs between approximately 1460 Hz and 225 Hz. This corresponds to a diffusional regime occurring between 0.7 ms and 4.4 ms. By utilising equation 6.5 the depletion thickness *L* at these times would be 1.2 µm and 3.1 µm respectively. Since the Cavity is only 1.05 µm deep, it suggests that the Warburg impedance observed may not actually be the linear diffusion associated with the 50 nm band, but rather linear diffusion in the cavity. The schematic diagram in Figure 7.23 shows the postulated diffusional regime that might be established during experimentation between these time scales.

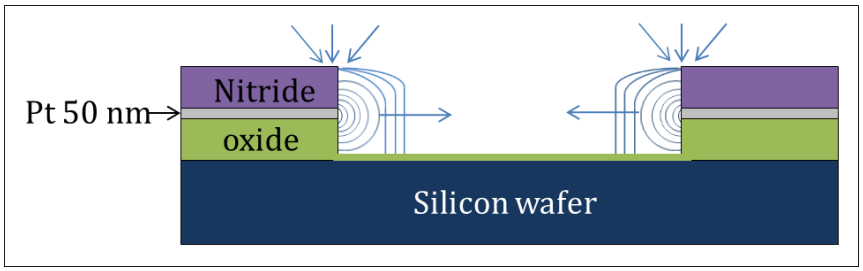

Figure 7.23: schematic representation of a postulated explanation as to why the Warburg element, Y_0^a at high frequencies is an order magnitude larger than expected. The silicon wafer 'floor' of the cavity prevents the development of non-linear diffusion in this direction, causing a seemingly linear diffusion field developing across the length of the cavity at these high frequencies (diagram not to scale).

This hypothesis, assumes that due to extremely efficient mass transport to the cavity edges, the Warburg impedance associated with the band electrode only, develops extremely quickly (within microseconds). As the radial growth from the electrode reaches micrometre dimensions, it may begin to grow asymmetrically due to the insulating floor of the cavity. This would cause the diffusion fields to appear to grow linearly, for some time before pseudo-steady-state diffusion was reached. During EIS collection, this linear growth may develop like a Warburg component 'seeing' a much larger electrode.

The average total value of capacitance, C_{DL}, calculated for the C30µ3d arrays is 66 ± 11 nF which, as expected is smaller than the capacitance calculated for the S30µ3d array of 257 (± 64) nF. However the average capacitance per cm^2 is almost 40 times larger, with a value of 622 µF cm^{-2} compared with just 16.4 µF for the S30µ3d array. It should be noted however that this capacitance is still many times smaller than the capacitance recorded in

section 5.3.1 and 5.3.2 during development of these arrays and therefore the increased capacitance observed is not postulated to be caused by any fracturing of the surface, pin holes or other unaccounted platinum exposure. Some of the increased capacitance may be due to increased roughening of the electrode surface by the extensive cleaning of electrode in sulphuric acid forming Platinum oxide and oxygen insertion and expansion. In a paper by Evans and Mount *et al* [7] a roughness factor of up to 12.3 was recorded from acid cleaning of platinum microelectrodes. It is not unrealistic therefore to postulate that the intensive cleaning conditions inflicted upon these very small nanobands, may induce even greater roughening effects. It also cannot be discounted that there may either be some leakage around the band electrode, to give a larger area, or even some contribution of the charging of the entire platinum plate at higher frequencies. Never the less, the total capacitance is still much smaller than the square arrays. As shown in Chapter 6, the CV responses are unaffected by capacitive charging, even at very fast sweep rates and the CV responses and EIS responses at lower frequencies generally seem to correlate well with EIS theory.

The average uncompensated resistance for the S30µ3d substrates is 71 ±13 Ω, which is the same; within experimental to error as the average uncompensated resistance recorded for the C30µ3d substrates of 69 ± 7 Ω. If this uncompensated resistance recorded, were due only to the active electrode area, the uncompensated resistance of the microsquare arrays would be much smaller since the array has a far greater active platinum area, when compared with the CaviArE substrates. The postulated reason for the similarity in R_U values is that the resistance observed is that of the entire platinum film coating the silicon substrate. These areas (even when allowing for the small variation in depth of substrate immersion), will be similar for both the microsquare arrays and the CaviArE architecture. A suggested equivalent circuit for this observation is shown in Figure 7.24

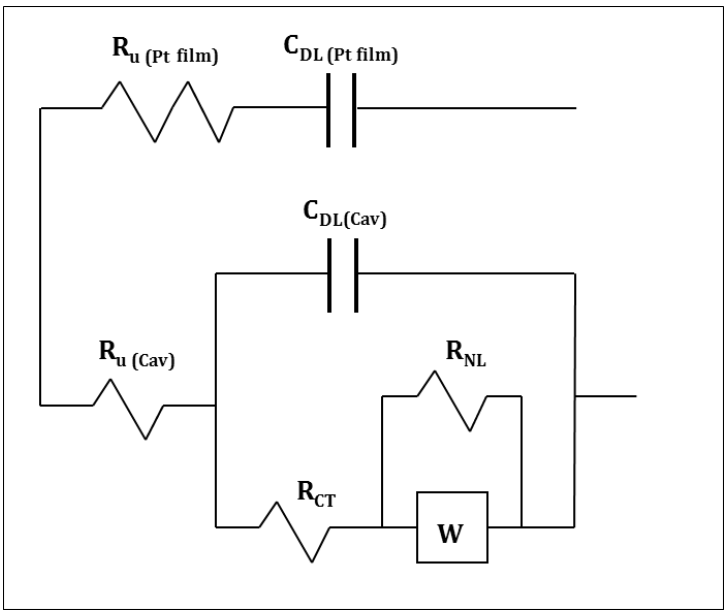

Figure 7.24: Schematic representation of the postulated equivalent circuit required to model the high frequency C30µ3d EIS data.

Figure 7.24 shows the postulated equivalent circuit modelling the response at C30µ3d electrodes at high frequency, with the R_U, C_{DL} response of the entire platinum film in series with the R_U response of the active C30µ3d array area. At very high frequencies, the uncompensated resistance associated with the large area platinum layer, the platinum film is lower than that associated with the C30µ3d nanobands due to the massively larger area and therefore dominates the response. The platinum film capacitance however, will be very small due to the very thick insulating layer of low dielectric SiN. The dielectric constant of silicon nitride is 7[8] therefore the capacitance associated with charging over the entire plate is approximately 13 nF cm^{-2} which means that the double layer charging time will be fast, blocking the upper current path at all but the highest frequencies. This will lead to exclusive CaviArE response as the frequency decreases, which explains why the simpler modified Randles' circuit fit is able to model the CaviArE response at all but the highest frequencies.

Having considered the EIS response of regions a), b) and c), the transition region, TR is the only region which has not been fitted and analysed during this study. Since the diffusional regime in this region is not yet fully understood it is difficult to apply a model to the data. However it is likely that given the calculated diffusion layer thickness of between 7.4 µm and 23 µm in

this frequency range, the transition region corresponds to the transformation from diffusion within the cavities (region a)) to diffusion outside the cavities (region b)).

7.3.1. EIS Response of the C30µ3d Arrays in 1 mM Potassium Ferricyanide

Figure 7.25 shows a typical Nyquist plot obtained for a C30µ3d substrate in 1 mM ferricyanide, in comparison with a plot obtained for a C30µ3d substrate in10 mM ferricyanide over the same frequency range.

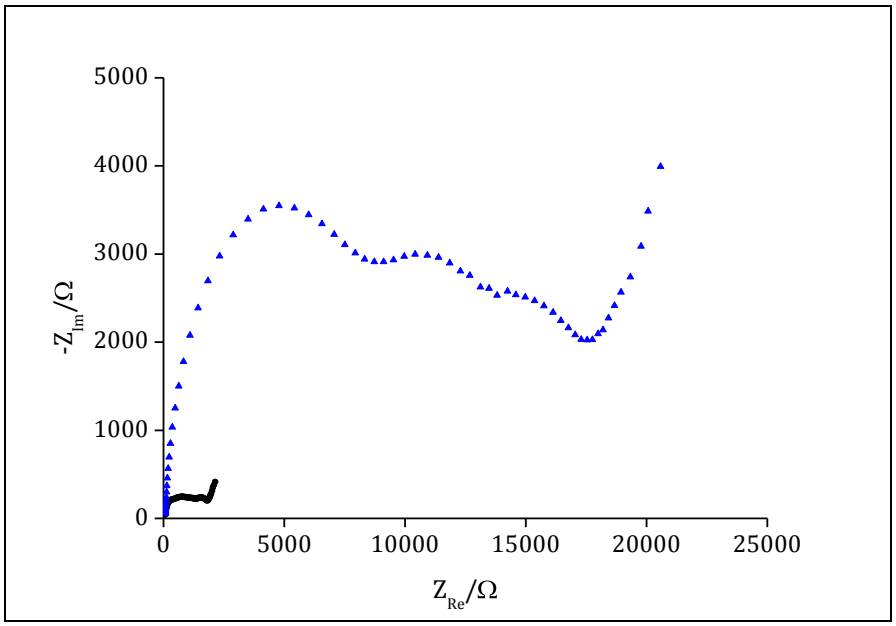

Figure 7.25: Typical Nyquist plots of a C30µ3d array in ferricyanide [10 mM] (black circles) compared to that of a C30µ3d array in ferricyanide [1 mM] (blue triangles) at a dc potential of 0.19 V. Both responses were recorded between 61x10^3 Hz and 0.01 Hz.

It is clear that the EIS response in 1 mM ferricyanide is approximately an order of magnitude greater than the EIS response in 10 mM. The Nyquist plot was analysed using the same equivalent circuits as those applied in section 7.3.2 in order to compare the two responses and confirm the applicability of the developed EIS analysis.

Figure 7.26 shows the Nyquist plot for a C30µ3d array in 1 mM ferricyanide, which has again been split into the four distinct regions. It also shows the corresponding equivalent circuit, fits at high and low frequencies.

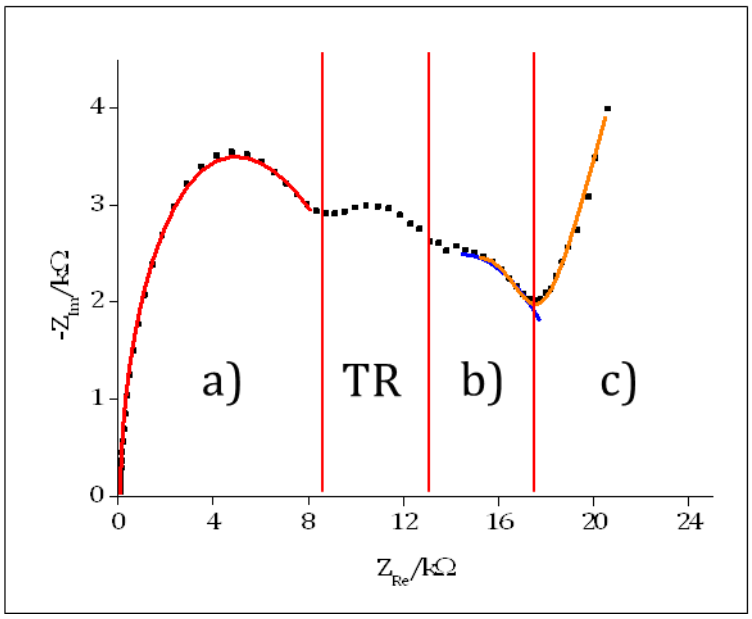

Figure 7.26: Nyquist plot obtained for a C30µ3d substrate at a dc potential of 0.19 V in ferricyanide [1 mM] where region **a)** at high frequencies is attributed to the diffusional regime within the individual cavities, region **b)** at medium/low frequencies is attributed to planar diffusion from the individual, isolated cavities and region **c)** at the lowest frequencies, attributed to planar diffusion to the entire array area. The region termed **TR** is the transition region, that is, the region in which the depletion zone begins to fill the entire cavity, and also has begun to grow out of the hole.

It is satisfying that the average capacitance, C_{DL}, calculated for this experiment of 76 ± 2 nF is the same, within experimental error, to the average capacitance of 66 ± 11 nF calculated for a range of C30µ3d arrays in ferricyanide [10 mM]. It is also reassuring that the average uncompensated resistance, R_U of 86 ± 4 Ω is also similar to the value of 69 ± 7 Ω for a C30µ3d substrate in 10 mM ferricyanide.

Figure 7.27 shows a plot of the variation in charge transfer resistance, R_{CT} with E_{dc} for this C30µ3d substrate in 1 mM ferricyanide, with both the kinetic and thermodynamic models fitted to the data.

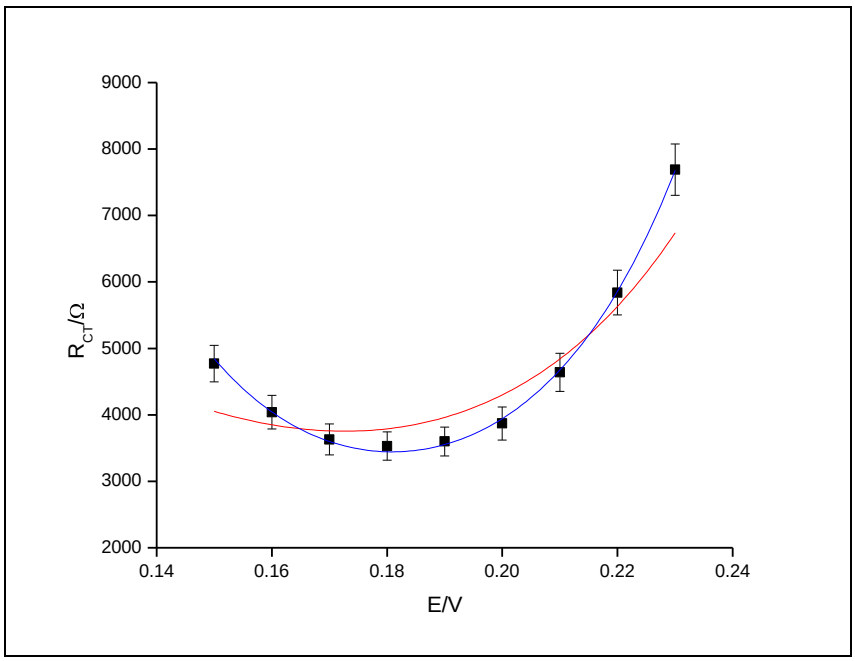

Figure 7.27: Plot of R_{CT} vs. E_{dc} found by fitting the EIS data using the modified Randles' circuit to frequencies of 61×10^3 Hz to 35.11 Hz. The red line is the fit to the kinetic expression (eqn. 2.39) with a correlation coefficient, r = 0.888; R_{CT}^{min} = 4 ± 2 kΩ; $E_{1/2}$ = +0.19 ± 0.09 V and α_{Ox} = +0.33 ± 0.72. The blue line is the fit to the thermodynamic expression (eqn. 2.41) with a correlation coefficient, r = 0.998; R_{CT}^{min} = 3.44 ± 0.02 kΩ and $E_{1/2}$ = 0.181 ± 0.001 V.

The R_{CT} curve in Figure 7.27 clearly fits best to the thermodynamic expression. The value of charge transfer resistance of 3.44 ± 0.02 kΩ is 14 times greater than the value of charge transfer resistance of 248 ± 22 Ω calculated from the data in Figure 7.21 c) (also fitted to the thermodynamic model). The value of resistance in 1 mM ferricyanide should be approximately 10 times the value for a C30µ3d array in 10 mM ferricyanide, suggesting that the electrode is perhaps not quite as clean as that in Figure 7.21 c). The minimum standard rate constant calculated for this system is therefore 0.96 cms^{-1}.

Figure 7.28 shows the plot of non-linear resistance, $R_{NL}^{a,min}$ vs. E_{dc} calculated for the C30µ3d substrate in 1 mM ferricyanide.

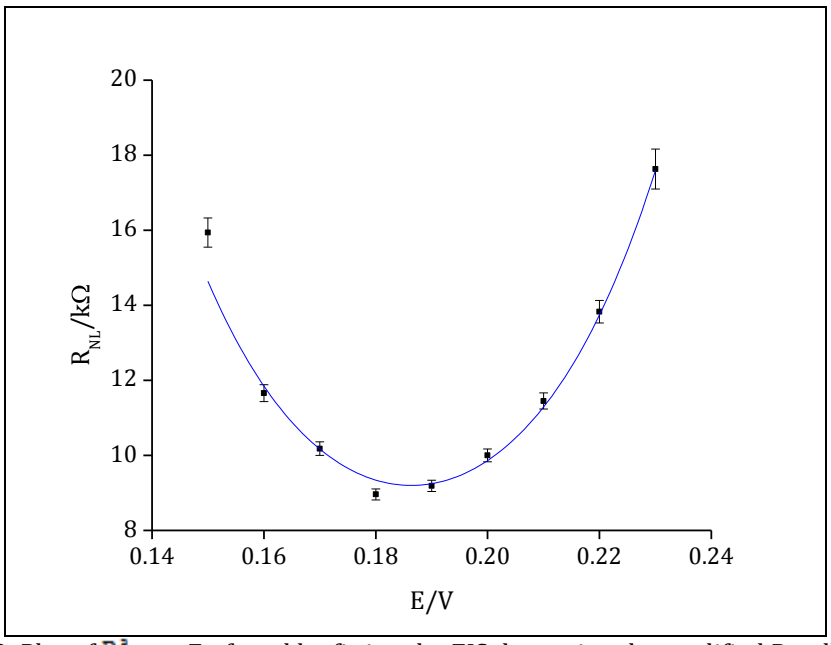

Figure 7.28: Plot of R_{NL}^{a} vs. E_{dc} found by fitting the EIS data using the modified Randle's circuit t between frequencies of 61x10^3 Hz to 35.11 Hz. The blue line is the fit to the thermodynamic expression (eqn. 2.42) with a correlation coefficient of, r = 0.998; $R_{NL}^{a,min}$ = 9 ± 1 kΩ and $E_{1/2}$ = 0.186 ± 0.001 V.

The value of $R_{NL}^{a,min}$ of 9 ± 1 kΩ is 9 (±2) times greater than the value of $R_{NL}^{a,min}$ of 1.0 ± 0.2 kΩ which is an order of magnitude greater resistance within experimental error.

Figure 7.29 shows a graph of $1/Y_0^a$ with E_{dc}.

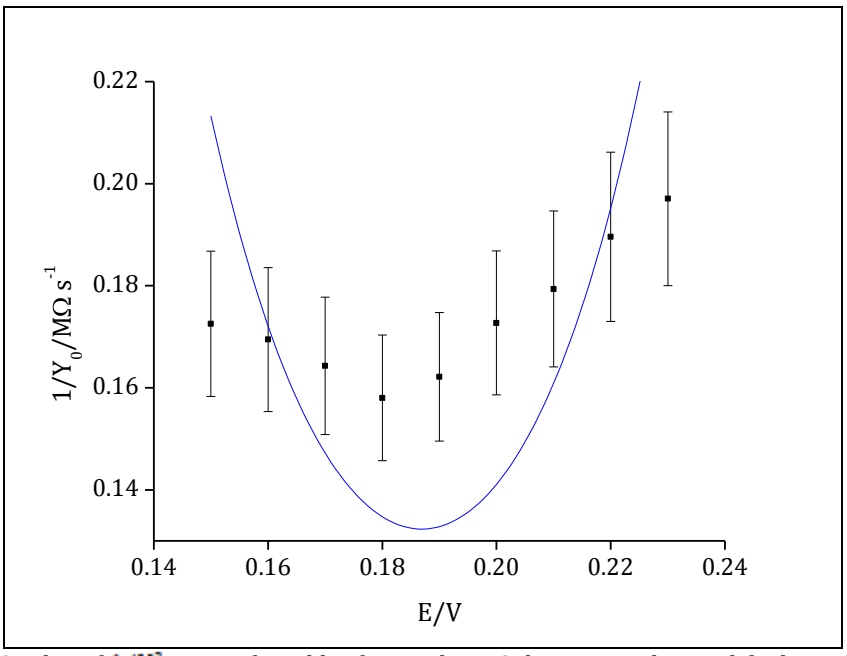

Figure 7.29: Plot of $1/Y_0^a$ vs. E_{dc} found by fitting the EIS data using the modified Randle's circuit to frequencies of $61x10^3$ Hz to 35.11 Hz. The blue line is the fit to the thermodynamic expression (eqn. 2.44) with a correlation coefficient, r = -2.433; $1/Y_0^{a,\,min}$ of 0.13 ± 0.08 MΩ $s^{-1/2}$ and $E_{1/2}$ = 0.187 (± 0.003) V.

In contrast to the data in 10 mM ferricyanide, the Warburg impedance data calculated at high frequencies have large errors. This may be caused by the fact that there is not as distinctive a separation between the charge transfer resistance circuit element and the Warburg and that the charge transfer resistance is slightly larger, making the Warburg harder to fit.

Figure 7.30 shows a graph of non-linear resistance, R_{NL}^b recorded for frequencies between 0.84 Hz and 0.10 Hz and calculated from a fit to the modified Randle's circuit.

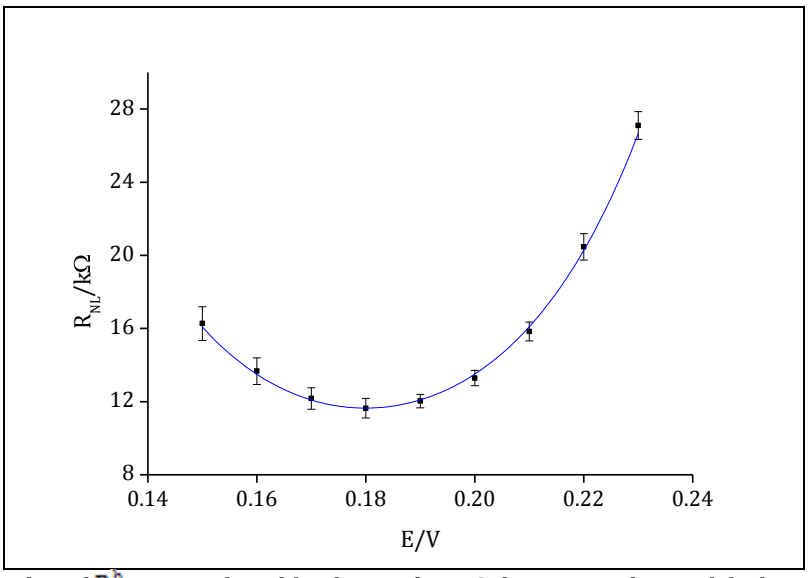

Figure 7.30: Plot of R_{NL}^{b} vs. E_{dc} found by fitting the EIS data using the modified Randle's circuit to frequencies of 0.84 Hz to 0.10 Hz. The blue line is the fit to the thermodynamic expression (eqn. 2.41) with a correlation coefficient, r = 0.999; $R_{NL}^{b,min}$ = 11.26 ± 0.07 kΩ and $E_{1/2}$ of 0.179 ± 0.001 V.

The value of $R_{NL}^{b,min}$ calculated for the C30µ3d substrate in 1 mM potassium ferricyanide of 11.26 ± 0.07 kΩ is 10.5 (± 1.6) times greater than the value of 1.1 ± 0.1 kΩ calculated from Figure 6.32 for a C30µ3d substrate in 10 mM potassium ferricyanide, which is the same within experimental errorl as the increase in resistance expected for a solution which in 10 times lower in concentration.

Figure 7.31 shows the plot of $1/Y_0^b$ with E_{dc} recorded for frequencies between 0.84 Hz and 0.10 Hz and calculated by a fit to the modified Randles' circuit.

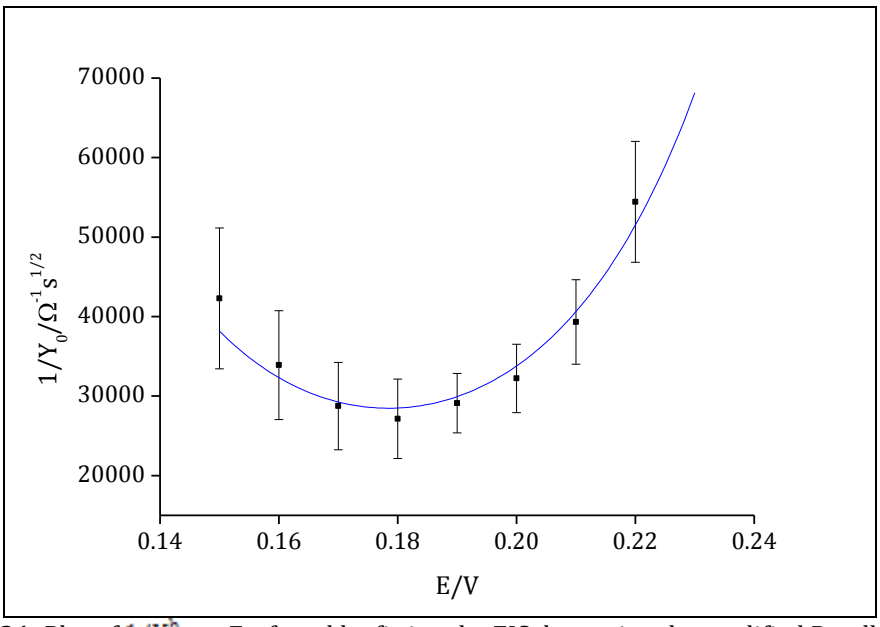

Figure 7.31: Plot of $1/Y_0^b$ vs. E_{dc} found by fitting the EIS data using the modified Randle's circuit between frequencies of 0.84 Hz and 0.10 Hz. The blue line is the fit to the thermodynamic expression (eqn. 2.44) with a correlation coefficient, r = 0.986; $1/Y_0^{b,\,min}$ of 28.5± 0.7 kΩ $s^{-1/2}$ and $E_{1/2}$ = 0.178 ± 0.001 V.

Since the Warburg parameter appears to be masked by the transition region, TR, for this data, it is not surprising that the errors are relatively large. A value of 28.5 ± 0.7 kΩ $s^{-1/2}$ is 11.9 (±1.4) times larger than the value of 2.4 ± 0.2 kΩ$s^{-1/2}$ obtained from Figure 7.14 for a C30µ3d substrate in 10 mM ferricyanide.

Figure 7.32 is a graph of $1/Y_0^c$ versus E_{dc} associated with linear diffusion across the whole array with fitting between frequencies 0.42 Hz and 0.01 Hz.

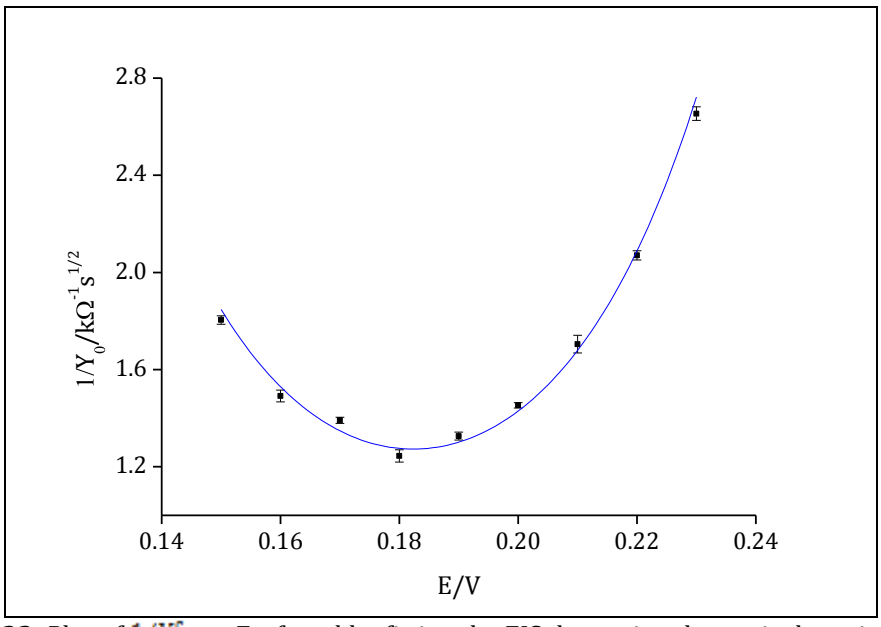

Figure 7.32: Plot of $1/Y_0^c$ vs. E_{dc} found by fitting the EIS data using the equivalent circuit given in Figure 7.4 to fit frequencies between 0.42 Hz and 0.01 Hz. The blue line is the fit to the thermodynamic expression (eqn. 2.44) with a correlation coefficient, r = 0.993; $1/Y_0^{b,\,min}$ = 1.27 ± 0.01 kΩ $s^{-1/2}$ and $E_{1/2}$ = 0.182 ± 0.001 V.

The Warburg coefficient of 1.27 ± 0.01 kΩ $s^{-1/2}$ is 9.0 (± 0.5) times greater than the value of 140 (± 6.) Ω $s^{-1/2}$ obtained for array overlap in 10 mM ferricyanide. Overall, as expected, resistances for the C30µ3d array in 1 mM potassium ferricyanide are an order of magnitude greater than the responses obtained in 10 mM potassium ferricyanide, which provides confidence that the EIS response observed for C30µ3d substrates in ferricyanide is independent of redox concentration.

7.3.2. EIS Response of CaviArE devices of different Size and Pitch

7.3.2.1. EIS Analysis of the Effects of Cavity Spacing,

Having established methods of EIS analysis for C30µ3d, Figure 7.33 shows the Nyquist plots of C30µ1d, C30µ2d, C30µ3d and C30µ4d arrays at E_{dc} = +0.19 V, the inset again shows the plots normalised for CaviArE electrode geometric area and shifted along the Z_{Re} axis to align the low frequency data.

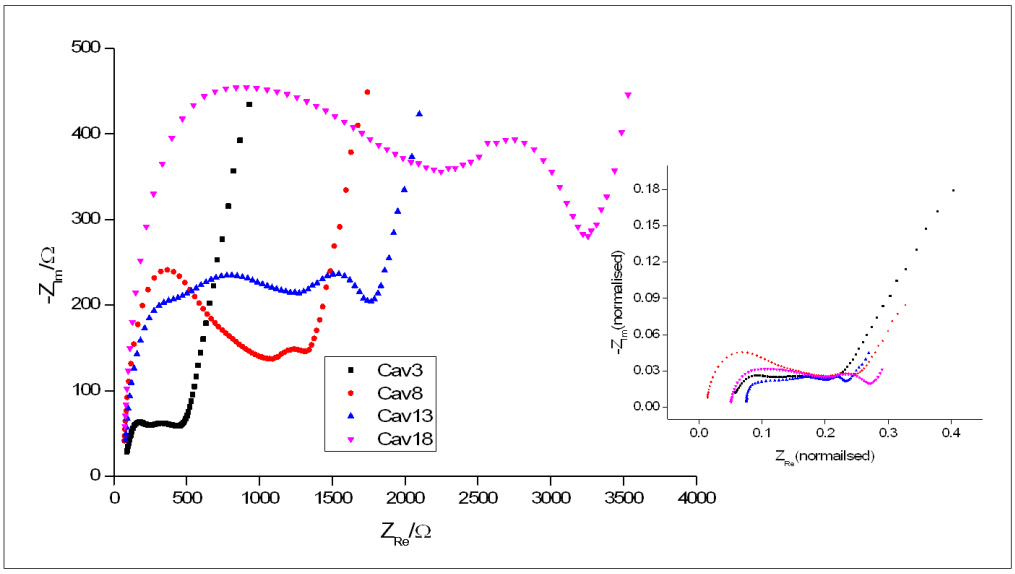

Figure 7.33: Typical Nyquist plots obtained for C30µ1d, C30µ2d, C30µ3d and C30µ4d at a dc potential of 0.19 V in ferricyanide [10 mM], recorded between 61×10^3 Hz and 0.01 Hz and ac 10 mV rms. The inset shows the plot where the array responses have been normalized for active area and shifted to overlay the low frequency semicircles.

It is satisfying to observe that the impedance of the arrays at high and low frequency increases with electrode spacing, as expected due to a decrease in active electrode area. However, at the very lowest frequencies, the Warburg Impedance (Y_0^S), due to the response of planar diffusion to the entire array, for all CaviArE architectures, has a similar value. The inset shows that when normalising for electrode area, the C30µ2d has the largest charge transfer per unit area, suggesting this electrode array is the least clean. As can also be seen by the inset of Figure 7.32, the electrode elements overlap at different frequencies and as expected the 1d architecture elements overlap at the highest frequencies (most quickly) and the 4d architecture elements overlap at the lowest frequencies (after the longest time scales). It was difficult to align the plots accurately but, it is clear from Figure 7.3s, that the frequency range over which the overlapping Warburg response is observed, decreases with electrode spacing.

Figure 7.34, shows the Nyquist plots of the four architectures showing the equivalent circuit fits at high and low frequency. Since all the nanobands were contained within $(30\ \mu m)^2$ cavities, the frequency range over which the high frequency data (region a)) fitted was the same for all electrodes. The

frequency range for the low frequency data (regions b) and c)), differed since the diffusion layers from neighbouring electrode elements overlapped at different times.

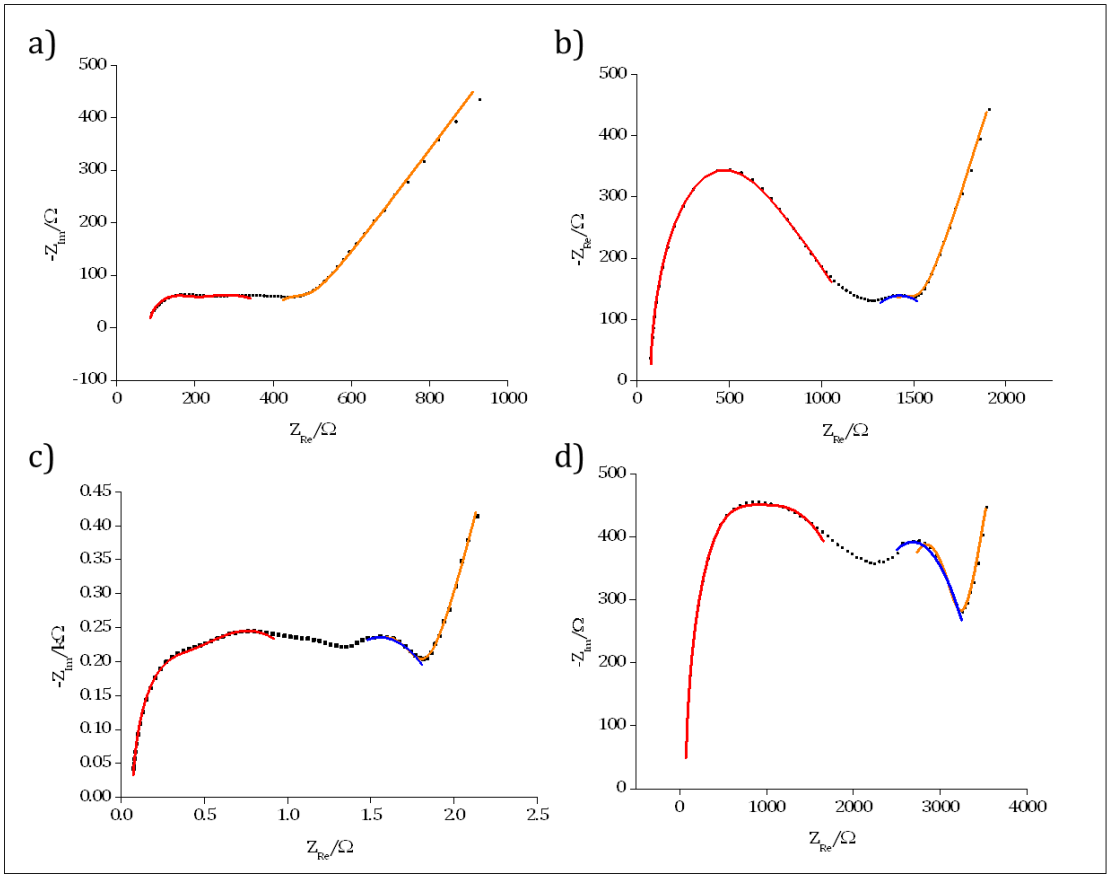

Figure 7.34: Nyquist plots and equivalent circuit fitting of **a)** the C30µ1d array, with the red line showing the modified Randles' circuit fit between 61x10^3 Hz and 55.83 Hz and the orange line showing the equivalent circuit fit given in Figure 7.4 between 1.33 Hz and 0.01 Hz; **b)** the C30µ2d array, with the red line showing the modified Randles' circuit fit between 61x10^3 Hz and 55.83 Hz, the blue line showing the modified Randles' circuit fit between 2.13 Hz and 0.26 Hz and the orange line showing the equivalent circuit fit given in Figure 7.4 between 0.84 Hz and 0.01 Hz; **c)** the C30µ3d array, with the red line showing the modified Randles' circuit fit between 61x10^3 Hz and 55.83 Hz, the blue line showing the modified Randles' circuit fit between 1.06 Hz and 0.13 Hz and the orange line showing the equivalent circuit fit given in Figure 7.4 between 0.53 Hz and 0.01 Hz; and **d)** the C30µ4d array, with the red line showing the modified Randles' circuit fit between 61x10^3 Hz and 55.83 Hz the blue line showing the modified Randles' circuit fit between 0.83 Hz and 0.51 Hz and the orange line showing the equivalent circuit fit as in Figure 7.4 between 0.26 Hz and 0.01 Hz.

The equivalent circuit models seem able to fit the different CaviArE architectures with reasonable accuracy. In line with the voltammetric response (section 6.3.4.1), the EIS data obtained from the C30µ1d architecture (Figure 7.34 a), shows that the array elements overlap very quickly, almost as soon as the depletion zones grow out of the individual cavities. Because of this the modified Randles' circuit model at low frequencies (blue line on other graphs)

was unable to be fitted to the data. The equivalent circuit parameters, R_{CT}, R_{NL} and $1/Y_0$, obtained by fitting at high and low frequencies to the EIS data at different E_{dc} produced parabolic curves, similar to those observed in sections 7.3.1 to 7.3.3 which could be modelled by the kinetic and thermodynamic expressions derived in section 2.6.3. Table 7.2 presents an overview of the average circuit parameters obtained, from fitting the modified Randles' circuit to the C30µ1d, C30µ2d, C30µ3d and C30µ1d responses at high frequencies (region a)), red line in Figure 7.34).

High frequency (region a)) fit to the modified Randle's Circuit				
CaviArE architecture	**C30µ1d**	**C30µ2d**	**C30µ3d**	**C30µ4d**
Geometric Area / cm²	4.1334x10^{-4}	1.8816x10^{-4}	1.0584x10^{-4}	6.936x10^{-5}
Average R_U / Ω	81 (± 4)	74 (± 4)	70 (± 6)	71 (± 5)
Average C_{DL} / nF	188 (± 4)	95.0 (± 5.4)	66.9 (± 1.1)	53.9 (± 2.1)
C_{DL} per cm² / mFcm^{-2}	0.45 (± 0.01)	0.50 (± 0.02)	0.63 (± 0.02)	0.78 (± 0.03)
Average R_{CT}^{min} / Ω	98 (± 12) (kinetic)	540 (± 55) (kinetic)	248 (± 67) (thermodynamic)	578 (± 86) (thermodynamic)
Rate constant, k^0, Lower Limit / cms^{-1}	1.3 (± 0.2)	0.52 (± 0.05)	2.0 (± 0.5)	1.3 (± 0.2)
Average $R_{NL}^{a,min}$ / kΩ	0.27 (±45)	646 (± 64)	1065 (± 42)	1912 (± 248)
Average $1/Y_0^{a,min}$ / kΩs$^{-1/2}$	6.9 (±1.9)	22.2 (± 1.5)	22.9 (± 1.1)	38.5 (± 7.5)
Expected $1/Y_0^{a,min}$ (Eqn. 4.6) / kΩs$^{-1/2}$	98.9	218	386	588

Table 7.2: Table to present the data obtained from fitting the modified Randles' circuit to the C30µ1d, C30µ2d, and C30µ3d and C30µ1d responses at high frequencies. The table also quotes the geometric, active area for each architecture, for reference. The table quotes the average uncompensated resistance and average capacitance for each system under investigation, along with the capacitance per cubic centimetre. The charge transfer resistance, R_{CT} can be modelled either by kinetics (Eqn. 2.39) or thermodynamics (Eqn. 2.41), the model used as well as the R_{CT}^{min} value is given in the table. The rate constant associated with this charge transfer resistance is also stated. Values of R_{NL} and $1/Y_0^a$ vs. E_{dc} fit thermodynamic expressions, Eqn. 2.42 and 2.44 respectively and $R_{NL}^{a,min}$ and $1/Y_0^{a,min}$ values obtained from the fits are given in the table. The $1/Y_0^{a,min}$ value expected for each architecture according to the geometric area of the electrode array was calculated using Eqn. 4.6 and these values are given for comparison with the experimental values observed.

The values of uncompensated resistance are similar for all architectures. Given the difference in active electrode area this adds further support that this response is likely to be the electrolyte resistance arising from charging and discharging of the entire platinum plate. The average capacitances unit area is also very similar; suggesting that the capacitance observed for the C30µ3d arrays in section 7.3.2 is representative of the capacitance of these CaviArE devices. These capacitances are on average 30-40 times greater than the capacitance per cubic cm recorded for the microsquare arrays. As discussed in section 7.3.2, this may be due to increased roughening of the electrode, surface, or a small amount of leakage around the band. Since the expected C_{DL} value for charging associated with Silicon nitride is only 13 nF cm^{-2}, this is extremely small in comparison to the overall capacitance observed and therefore contribute negligibly to the response. This could be tested by varying the thickness of silicon nitride and monitoring effect on overall capacitance value. The thickness of the platinum band could also be changed to observe if the capacitance values scale with electrode width. This would indicate if the capacitance observed is a fundamental response of the CaviArE electrode. Ensuring good fabrication and etching and would reduce possible leakage effects.

The C30µ3d, response gives the fastest recorded rate constant, derived from the value of R_{CT}^{min}, suggesting this electrode array was the most clean. This is reiterated in the inset of Figure 7.32. C30µ2d gives the lowest rate constant value and a kinetic response again suggesting that the electrode surface is least clean.

The Warburg parameter $1/Y_0^{a\,min}$ recorded for all CaviArE devices, experimentally is typically and consistently an order of magnitude smaller than the $1/Y_0^{a\,min}$ value expected from the array geometric area. This is further evidence that the Warburg impedance observed may be due to planar diffusion across the entire shallow cavity depth (Figure 7.23), rather than the planar diffusion to the electrode only.

Table 7.3 presents an overview of the average circuit parameters obtained, from fitting the modified Randles' circuit to the C30µ1d, C30µ2d, C30µ3d and C30µ1d responses at low frequencies (blue and orange lines in Figure 7.33).

Low frequency (regions b) and c)) fit to the modified Randle's Circuit, modelling a microsquare response and to the equivalent circuit given in Figure 7.4 modelling diffusional overlap.				
CaviArE architecture	**C30µ1d**	**C30µ2d**	**C30µ3d**	**C30µ4d**
Geometric Area / cm²	4.1334×10^{-4}	1.8816×10^{-4}	1.0584×10^{-4}	6.936×10^{-5}
Average Isolated $R_{NL}^{b,min}$ / kΩ	n/a	0.63 (±0.07)	1.35 (±0.61)	1.82 (±0.22)
Average Isolated $1/Y_0^{b,min}$ / kΩs$^{-1/2}$	n/a	1.33 (±0.2)	2.42 (0.23)	3.83 (±0.45)
Average overlap $1/Y_0^{c,min}$ / Ωs$^{-1/2}$	154 (±7)	141 (±17)	147 (±6)	139 (±2)
Experimental $1/Y_0^{min}$ ratio	n/a	9 (± 1.8)	16.0 (± 1.6)	27.3 (± 3.1)
Expected $1/Y_0^{min}$ ratio	4	9	16	25

Table 7.3: Data obtained from fitting the modified Randles' circuit (region b)) and the circuit given in Figure 7.4 (region c)) to the C30µ1d, C30µ2d, C30µ3d and C30µ1d array responses at low frequencies. The table also quotes the electrode geometric active area, for each architecture, for reference. The table quotes the average Warburg parameter, $1/Y_0^{b,min}$ associated with planar diffusion to each isolated cavity after the depletion zone has filled the cavity and also quotes the average non-linear resistance $R_{NL}^{b,min}$ associated with radial diffusion from each isolated Cavity (region b)). The diffusional regime at this frequency range is expected to develop in a similar manner to a microsquare array of the same architecture. The Warburg parameter $1/Y_0^{c,min}$ associated with planar diffusion to the entire array (region c)), is recorded and the ratio between to the two Warburg parameters is given. Since the diffusional fields, of the C30µ1d device, overlap almost as soon as the depletion zone grows out of the cavity, some of the data could not be recorded for this chip.

As shown schematically in Figure 7.16 and in Table 7.1, there is a relationship between the Warburg impedance recorded for planar diffusion to the entire electrode array Y_0^c, and for that of the planar diffusion to each isolated cavity Y_0^b. For C30µ3d arrays, the $1/Y_0$ ratio recorded should be 16. In general, for microsquare elements of different separations, this ratio should be $(x+1)^2$, where x is the element spacing. Thus for a 30µ1d array, the ratio would be 4. Unfortunately this ratio cannot be extracted from the data as there is an insufficient frequency range to fit the region b) Warburg element. The expected ratio for a 30µ2d array is 9 and indeed the ratio of 9 (± 2) recorded is in line

with expectation. The expected ratio for a 30µ4d array is 25, the value of 27 (± 3) was recorded experimentally, and is the same, within experimental error. It is also reassuring to note that the values of $R_{NL}^{b,min}$ are the same, within experimental error, to those recorded for $R_{NL}^{a\,min}$ at high frequency for all CaviArE separations. This further validates that hemispherical and therefore time-insensitive responses are established extremely quickly for these arrays. In general, the $(30\mu m)^2$ CaviArE devices with different separations, behave in a similar manner to the extensively studied C30µ3d arrays and in the manner expected theoretically for EIS equivalent circuit analysis.

7.3.4.2. EIS Analysis of the Effects of Cavity Size

Figure 7.35 shows the Nyquist plots of C10µ3d, C20µ3d, C30µ3d and C50µ3d and C1003d at a dc potential of 0.19 V, the inset shows the plots normalised for CaviArE area and shifted along the Z_{Re} axis to align the low frequency data.

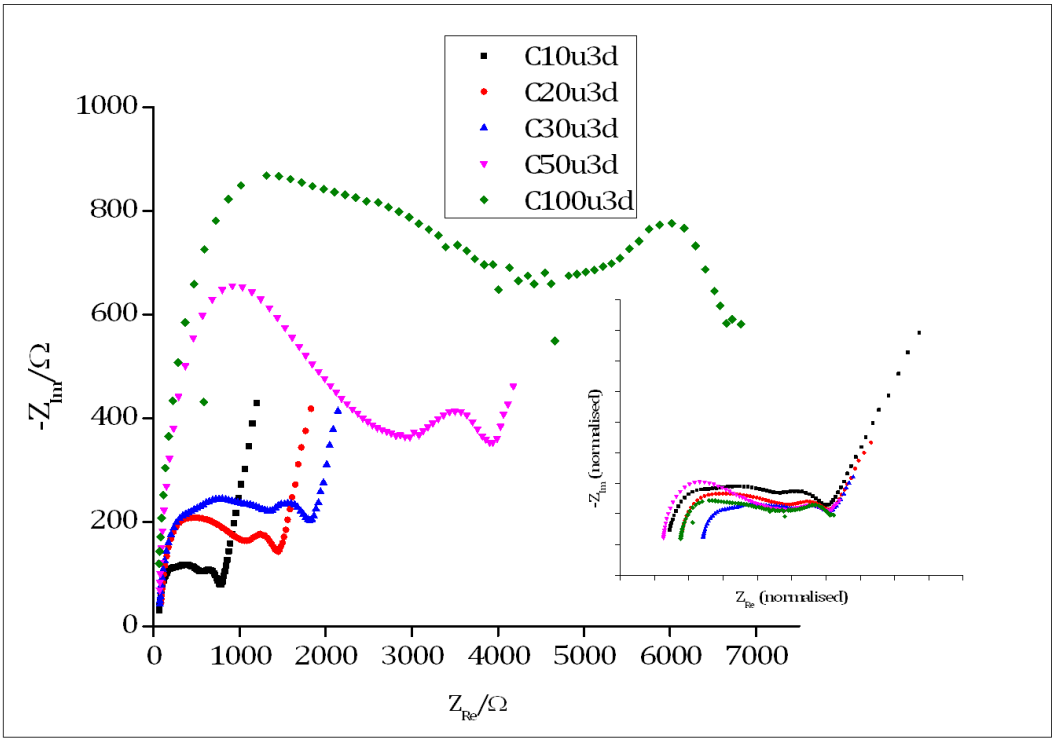

Figure 7.35: Typical Nyquist plots obtained for C10µ3d, C20µ3d, C30µ3d, C50µ3d and C100µ3d at a dc potential of 0.19 V in ferricyanide [10 mM], recorded between $61x10^3$ Hz and 0.01 Hz and ac 10 mV rms. The inset shows the plot where the array responses have been normalized for active area and shifted to overlay the low frequency Warburg parameter.

It is satisfying to observe that in general the impedance of the arrays at high and low frequency increases with electrode size, as expected due to a decrease in

active electrode area with size. As in Figure 7.32, the Warburg Impedance at the very lowest frequencies, have a similar value for all CaviArE architectures. This is because the total electrode footprint area (5 x 5 mm) remains the same for all architectures. The inset shows when normalising for electrode geometric area, that the C50µ3d array seems to have the highest charge transfer per unit area, suggesting this electrode array is the least clean, and the C30µ3d array still seems to be the cleanest. As can also be seen by the inset of Figure 7.35, the onset of low frequency Warburg behaviour occurs at different frequencies and as expected the C10µ3d architecture elements overlap at the highest frequencies (most quickly) and the C100µ3d architecture elements hardly overlap at all over the frequency range studied. A frequency of 0.01 Hz corresponds to a time of 100 seconds. In section 6.3.4.2, the C100µ3d arrays were calculated to begin to overlap at approximately 41 seconds. Therefore some overlap should be observed on the EIS plot. The two very lowest frequencies do seem to show deviation from the isolated non-linear response.

Figure 7.36 shows the Nyquist plots of C10µ3d, C20µ3d, C50µ3d and C100µ3d with the corresponding equivalent circuit fits at high and low frequency.

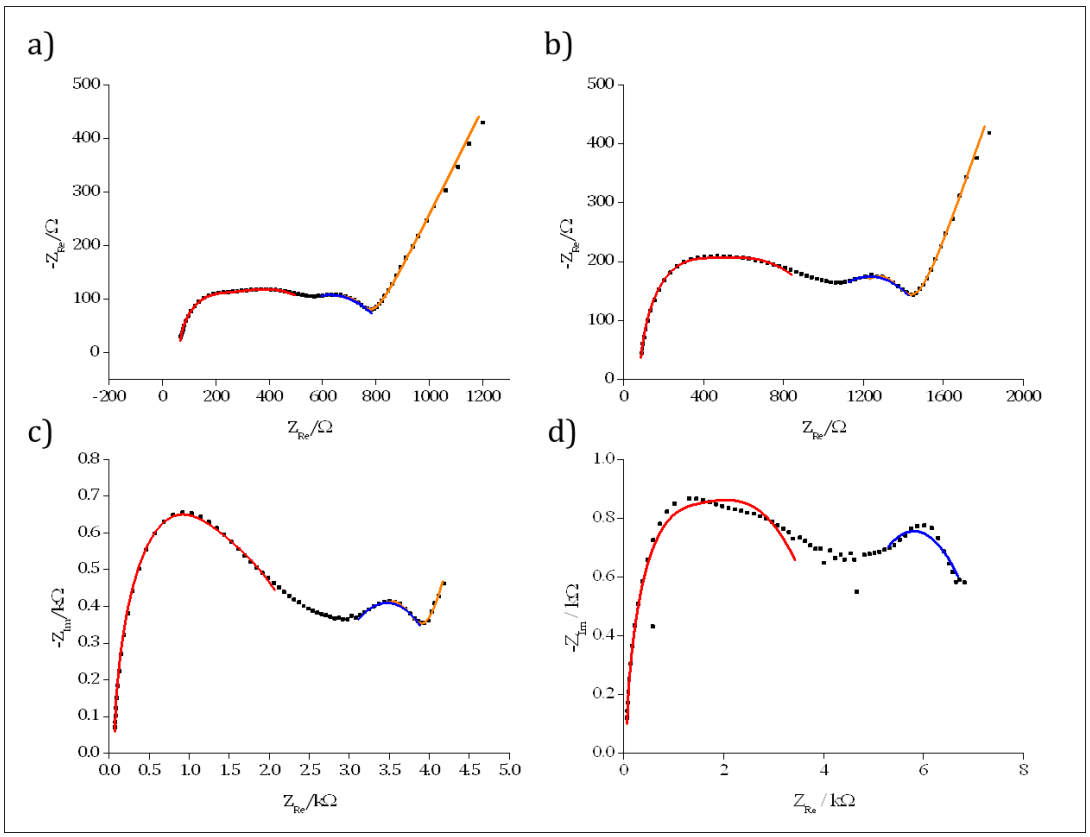

Figure 7.35: Nyquist plots and equivalent circuit fitting of **a)** the C10µ3d array, with the red line showing the modified Randles' circuit fit between 61x10^3 Hz and 70.5 Hz, the blue line showing the modified Randles' circuit fit between 13.8 Hz and 0.84 Hz and the orange line showing the equivalent circuit fit given in Figure 7.4 between 5.42 Hz and 0.01 Hz; **b)** the C20µ3d array, with the red line showing the modified Randles' circuit fit between 61x10^3 Hz and 70.5 Hz, the blue line showing the modified Randles' circuit fit between 4.30 Hz and 0.33 Hz and the orange line showing the equivalent circuit fit given in Figure 7.4 between 1.69 Hz and 0.01 Hz; **c)** the C50µ3d array, with the red line showing the modified Randles' circuit fit between 61x10^3 Hz and 70.5 Hz, the blue line showing the modified Randles' circuit fit between 0.84 Hz and 0.05 Hz and the orange line showing the equivalent circuit fit given in Figure 7.4 between 0.21 Hz and 0.01 Hz; and **d)** the C1000µ3d array, with the red line showing the modified Randles' circuit fit between 61x10^3 Hz and 22.0 Hz and the blue line showing the modified Randles' circuit fit between 0.26 Hz and 0.16 Hz.

The equivalent circuit models seem able to fit all CaviArE architectures with reasonable accuracy except the C100µ3d array. The EIS response of the C100µ3d array showing in Figure 7.36 d) has more noise than the other arrays, which could have led to less accurate fitting of the data. The (100 µm)^2 cavity is also quite large and arguably at a size where macroelectrode rather than microelectrode responses may begin to be observed and where fitting with the modified Randles' circuit may break down. This may also explain the inaccurate fitting of the EIS data. The Warburg impedance associated with planar diffusion to the entire array could not be obtained for C100µ3d as there were not enough data points in this region.

The equivalent circuit parameters, R_{CT}, R_{NL} and $1/Y_0$, obtained by fitting to the high and low frequency EIS data at different E_{dc}, produced parabolic curves, similar to those observed in sections 7.3.1 to 7.3.3 which could be fitted to the kinetic and thermodynamic expressions derived in section 2.6.3. Table 7.4 presents an overview of the average circuit parameters obtained, from fitting the modified Randles' circuit to the C10µ3d, C20µ3d, C30µ3d, C50µ3d and C100µ3d responses at high frequencies (region a)), red line in Figure 7.33).

High frequency fit to the modified Randle's Circuit					
CaviArE architecture	**C10µ3d**	**C20µ3d**	**C30µ3d**	**C50µ3d**	**C100µ3d**
Geometric Area / cm²	3.125x10^{-4}	1.5876x10^{-4}	1.0584x10^{-4}	6.25x10^{-5}	3.3x10^{-5}
Average R_U / Ω	73 (±7)	84 (±2)	70 (±6)	66 (±4)	70 (±8)
Average C_{DL} / nF	146 (±4)	75.5 (±4.1)	66.9 (±1.1)	44.8 (±5.1)	34.4 (±1.2)
C_{DL} per cm² / mFcm^{-2}	0.47	0.48	0.63	0.72	1.04
Average R_{CT}^{min} / Ω	142 (±70) (kinetic)	273 (±47) (kinetic)	248 (±67) (thermodynamic)	828 (±25) (kinetic)	1153 (±51) (thermodynamic)
Rate constant, k^0, Lower Limit / cms^{-1}	1.2 (± 0.6)	1.2 (± 0.2)	2.0 (± 0.5)	1.01 (± 0.03)	1.38 (± 0.06)
Average $R_{NL}^{a,min}$ / Ω	472 (±43)	790 ± (49)	1065 (±42)	1817 (±22)	3155 (±162)
Average $1/Y_0^{a,min}$ / kΩs$^{-1/2}$	14.0 (±0.4)	25.0 (±1.1)	22.9 (±1.1)	56.1 (±2.7)	61.5 (±3.8)
Expected $1/Y_0^{a,min}$ (Eqn. 4.6) / kΩs$^{-1/2}$	131	257	386	653	1237

Table 7.4: The data obtained from fitting the modified Randles' circuit to the C10µ3d, C20µ3d, C30µ3d, C50µ3d and 100µ3d responses at high frequencies. For reference, the table also quotes the geometric, electrode area for each architecture. The table quotes the average uncompensated resistance and average capacitance for each system under investigation, along with the capacitance per unit area. The charge transfer resistance, R_{CT} fit, kinetic (Eqn. 2.39) or thermodynamic (Eqn. 2.41) is given, as well as the R_{CT}^{min} value. The rate constant calculated from this charge transfer resistance is also stated. The $1/Y_0$ ^{min} value expected for each architecture according to the geometric area of the electrode array was calculated using Eqn. 4.6 and these values are given for comparison with the experimental values observed.

As for the data in Table 7.2 (section 7.3.4.1), the values of uncompensated resistance, are similar for all architectures, and indicative of the uncompensated

resistance of the entire platinum plate. The small variation in these is likely due to the variation in the amount of chip submersed in the solution. The average capacitance per unit area is also very similar, although the value does increase slightly as the electrode size increases. The capacitance for this dataset is on average approximately 40 times greater than the capacitance per unit area recorded for the microsquare arrays and huge in comparison to the expected 13 nF cm^{-2} capacitance associated with charging of silicon nitride. This difference observed still may be due to increased roughening of the electrode surface, or a small amount of leakage around the band.

The C30µ3d response still gives the fastest recorded rate constant, derived from the value of R_{CT}^{min}, suggesting this electrode array was the most clean. C50µ3d gives the lowest rate constant value, which again is reflected in the relatively large normalised charge transfer semicircle in inset Figure 7.35.

The Warburg parameter $1/Y_0^{a,min}$ recorded for all these CaviArE devices, experimentally is again an order of magnitude smaller than the $1/Y_0^{a,min}$ value expected from the arrays' geometric area. This again is evidence that the Warburg impedance observed may be due to the linear diffusion across the entire shallow cavity, rather than the linear diffusion from the electrode surface only. It is interesting that the 100µ3d array with the largest cavity size has a value around 20 times lower than the expected value of $1/Y_0^{a,min}$ consistent with diffusion across the entire micrometre cavity. The smaller values for smaller cavities may reflect increasing corner effects in these cavities.

Table 7.5 presents an overview of the average circuit parameters obtained, from fitting the modified Randles' circuit to the C10µ3d, C20µ3d, C30µ3d, C50µ3d and C100µ3d responses at low frequencies (blue and orange lines in Figure 7.35).

Low frequency fit to the modified Randle's Circuit, modelling a microsquare response and to the equivalent circuit given in Figure 7.4 modelling diffusional overlap.					
CaviArE architecture	**C10µ3d**	**C20µ3d**	**C30µ3d**	**C50µ3d**	**C100µ3d**
Geometric Area / cm²	3.125×10^{-4}	1.5876×10^{-4}	1.0584×10^{-4}	6.25×10^{-5}	3.3×10^{-5}
Average Isolated $R_{NL}^{b,min}$ / kΩ	0.50 (±0.13)	0.82 (±0.04)	1.35 (±0.61)	1.92 (±0.22)	3.45 (±0.42)
Average Isolated $1/Y_0^{b,min}$ / kΩs$^{-1/2}$	4.22 (±0.72)	2.71 (±0.14)	2.42 (0.23)	2.35 (±0.45)	2.72 (±0.17)
Average overlap $1/Y_0^{c,min}$ / Ωs$^{-1/2}$	145 (±28)	144 (±4)	147 (±6)	145 (±3)	n/a
Average $1/Y_0^{min}$ ratio	25.0 (± 6.4)	19.0 (± 1.1)	16.0 (± 1.6)	16.3 (± 3.1)	n/a
Expected $1/Y_0^{min}$ ratio	16	16	16	16	16

Table 7.5: Table to present the data obtained from fitting the modified Randles' circuit and the circuit given in Figure 7.4 to the C10µ3d, C20µ3d, C30µ3d, C50µ3d and C100µ3d responses at low frequencies. For reference, the table also quotes the geometric, active area for each architecture. The table quotes the average Warburg parameter, $1/Y_0^{b,min}$ associated with planar diffusion to each isolated cavity after the depletion zone has filled the cavity and also quotes the average non-linear resistance $R_{NL}^{b,min}$ associated with radial diffusion from each isolated Cavity (region b))). The diffusional regime at this frequency range is speculated to develop in a similar manner to a microsquare array of the same architecture. The Warburg parameter $1/Y_0^{c,min}$ associated with planar diffusion to the entire array (region c)), is recorded and the ratio between to the two Warburg parameters is given. Since the diffusional fields, of the C30µ1d device, overlap almost as soon as the depletion zone grows out of the cavity, some of the data could not be recorded for this chip.

Since all, the electrode arrays in this section are 3d spaced a ratio of 16 between the $1/Y_0^{b,min}$ and $1/Y_0^{c,min}$ should be observed for all architectures. Although there is some variation in the value all ratios are essential within two standard deviations and similar within experimental error to the expected value. Again, the values of $R_{NL}^{b,min}$ are the same, within experimental error, to those recorded for $R_{NL}^{a\,min}$ at high frequency for all CaviArE dimensions indicating that hemispherical and therefore time-insensitive responses are established extremely quickly for all CaviArE architectures studied.

7.4. Conclusions

This chapter has provided a thorough study of the electrochemical impedance response of the novel nanoband cavity array electrodes developed in chapter 5.

This work complements the voltammetric studies carried out in chapter 6 and further enhances the understanding of the array response.

To the author's knowledge, EIS analysis of such array architectures has not previously been carried out. Indeed, no in depth experimental EIS studies or fitting with equivalent circuits for any nanoelectrode array system has previously been reported. Particular frequency ranges of the Nyquist plots were established and fitted with reasonable accuracy, using equivalent circuit fits. These were justified using Compton's theoretical planar microband EIS response and comparison with the microsquare response. The analysis has shown that the CaviArE devices fit well to microband theory in some frequency and time domains. However a complete model of the EIS response across all frequencies has not yet been established.

At high frequencies (region a)), the Nyquist plot is suspected to provide information regarding charge transfer rates and diffusional regimes within the isolated shallow microsquare cavities, from fits using a modified Randles' circuit. This circuit is shown to arise from Compton's analytical expressions[1] developed to model the EIS responses of planar microbands. It should be noted, however, that these expressions developed by Compton and Alden, do not take into account the fact that nanoband limiting currents change with time. Therefore this equivalent circuit is known only to be an approximation of the response. Nevertheless, the circuit fits well to all but the largest microsquare cavity architectures.

The uncompensated resistance, R_U determined using this circuit, is much lower than expected and similar for all CaviArE architectures and ferricyanide concentrations, which suggests that the uncompensated resistance recorded, is actually that coupled to the entire platinum film beneath the nitride insulation layer and not just that of the exposed nanobands within each cavity. The fact that the R_U recorded for the microsquare arrays is also the same, within experimental error, further supports this argument, leading to the development

of a modified equivalent circuit, which aids in explaining the response observed at these high frequencies (Figure 7.24).

The double layer capacitance, C_{DL}, is much smaller than for the corresponding microsquare array, (although larger per unit electrode area than expected for such systems). This ensures the CaviArE response is less affected than the equivalent microsquare array, by this capacitance. This further validates the voltammetric response in Figure 6.10 (section 6.3.1), which shows that the voltammetric response of an equivalent microsquare array is affected by a relatively large contribution from non-Faradaic double layer charging currents, whereas the CaviArE response is not. Even at low ferricyanide concentrations, the capacitive contribution to overall response is small.

Since the CaviArE dimensions are extremely small, it was expected that the charge transfer resistance would be enhanced in size compared to the non-linear resistance and therefore the charge transfer semicircle was expected to be more prominent than for the other architectures studied in this work. The variable and clearly observable semi-circular response at high frequencies was therefore postulated to be that of the electron charge transfer in parallel with capacitive charging. However, it should also be noted that the initial slopes (of this semi-circle) at very high frequencies also have a gradient of 1 and the non-linear circuit element is similar in shape to a semicircle. Therefore it cannot be ruled out on shape alone that these responses may not in fact be high frequency Warburg responses resulting from linear diffusion towards the individual nanoband electrodes. However, discrimination is possible, as unlike all other parameters modelled, which fit only to the thermodynamic model, the charge transfer responses at high frequencies fit to a kinetic expression when large and to a thermodynamic model as the substrates are cleaned further and the semicircle gets smaller. The experimental data obtained is therefore consistent with that of electron charge transfer at the electrode/electrolyte interface in parallel with capacitive charging since charge transfer is the only process which may be kinetically hindered in these experiments.

If, presuming that charge transfer is detectable, the fastest lower limit rate constant determined for these arrays was 1.99 cms^{-1} for 10 mM ferri/ferrocyanide. However, most rate constants recorded were slower than this and the variable high frequency responses show that it is challenging to clean the CaviArE electrodes fully and reproducibly. Future work might entail, studying different cleaning protocols in order to obtain very clean and reproducible electrode responses, with which very fast kinetic data may be obtained. However the standard rate constants recorded with these substrates are still amongst the highest values for ferri/ferrocyanide.

Over a range of experiments and architectures, the Warburg parameter (Y_0^a) calculated for the CaviArE devices is also an order of magnitude lower than would be expected, when calculated using the arrays' geometric area. A postulated reason for this, is that the Warburg impedance observed at high frequencies, is actually that of linear diffusion across entire cavity, rather than the actual linear diffusion away from the nanoband surface (which would only occur at extremely fast times). The postulated diffusional regime is represented schematically in Figure 7.22.

The non-linear resistance, $R_{NL}^{a,min}$ recorded at high frequencies, is in the same order of magnitude as that expected when utilising Compton's expressions for a single planar nanoband. The small difference can be accounted for by the fact that as the CaviArE nanobands are positioned around the edges of a Microsquare, some diffusional overlap and depleted mass transport may be expected in the corners. Since the non-linear resistance is also likely to change slightly with frequency, due to establishment of only pseudo-steady-state and time-dependent responses associated with nanobands, the theoretically derived R_{NL} values can only be an approximation, and therefore some deviation in response is expected.

At low frequencies, three diffusional regimes appear to be established. The first is associated with linear diffusional transport from/to each isolated square hole and can be modelled as a Warburg impedance parameter. The

second is the near hemispherical radial diffusional regime, established at longer times around each isolated cavity and modelled as a non-linear resistance. These low frequency data can be modelled using the same equivalent circuit as for a microsquare. It is reassuring to observe that the measured non-linear resistance, $R_{NL}^{b,min}$ at low frequency is the same, within experimental error, to $R_{NL}^{a,min}$ recorded at high frequencies for all array architectures studied. Finally the third diffusional regime is associated with overlap of these diffusion layers from neighbouring cavities and linear diffusion towards the entire array footprint. This can also be modelled as a Warburg impedance parameter. At low frequencies, the CaviArE devices have been established as behaving similarly to microsquare arrays.

Overall, the EIS data and their analyses have shown the applicability of these devices as electroanalytical devices and have provided quantitative knowledge of the charge transfer and diffusional processes occurring over most time scales. At present the transition region, TR (speculated to be the response of the CaviArE devices, as the depletion zone begins to fill the entire shallow cavity and grow out of the hole), has not been modelled with an equivalent circuit. Therefore more work needs to be carried out, perhaps in parallel with computer simulation in order to try and obtain a viable and physically realistic equivalent circuit able to fit the entire frequency range. These preliminary studies have shown that, nanoband arrays of controlled dimensions and predictable, characteristic nanoband response with micro- or even macroelectrode currents can be achieved through well-established microfabrication processes and that the CaviArE devices show real potential as enhanced electrochemical devices.

7.5. References

(1) Alden, J. A.; Compton, R. G. *Electoalanysis* **1996**, *8*, 30.

(2) Krulic, D.; Fatouros, N.; Khoshtariya, D., E. *Journal de Chimie Physique et de physico-Chimie Biologique* **1998**, *95*, 497.

(3) Winkler, K. *Journal of Electroanalytical Chemistry* **1995**, *388*, 151.

(4) Feeney, R.; Kounaves, S. P. *Electroanalysis* **2000**, *12*, 677.

(5) Zhang, Y.; Zhou, J.; Lin, L.; Lin, Z. *Electroanalysis* **2008**, *20*, 1490.

(6) Chen, J.; Aoki, K. *Electrochemistry Communications* **2002**, *4*, 24.

(7) Evans, S. A. G.; Terry, J. G.; Plank, N. O. V.; Walton, A. J.; Keane, L. M.; Campbell, C. J.; Ghazal, P.; Beattie, J. S.; Su, T.-J.; Crain, J.; Mount, A. R. *Electrochemistry Communications* **2005**, *7*, 125.

(8) Piccirillo, A.; Gobbi, A. L. *Journal of The Electrochemical Society* **1990**, *137*, 3910.

8. Conclusions and Further work

8.1. Introduction

In this thesis, the fabrication and systematic study of two main electrode systems has been presented – single platinum microsquare electrodes and nanoband cavity array electrodes (CaviArE). An overview of this work is presented below, and potential areas for future research are discussed.

8.2. Single platinum microsquare electrode

Chapter 4 presented the fabrication and analysis of single (50 μm)^2 platinum electrodes (S50μ). The results are contrasted to the well-established response of microdisc electrodes of equivalent diameter and show that enhanced limiting currents are observed for these microsquare systems, when compared to theoretical limiting currents suggested in the literature[1,2]. Through a combination of experiment and computer simulation, an empirical limiting current expression was produced which is thought to be able to more accurately calculate limiting currents of microsquares at all microsquare dimensions.

Since the postulated limiting current expression found in the literature (Eqn. 4.5) underestimates the limiting currents of these microsquare electrodes, it is clear that microsquare electrodes have increased mass transport limiting currents than discs of equal area. This may be because of the effects of enhanced diffusion at microsquare corners (Figure 8.1).

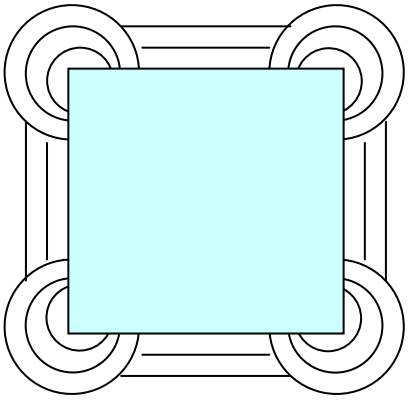

Figure 8.1: Schematic image showing postulated enhanced corner diffusion

If this theory is correct, it was postulated that as the square dimension decreased, this corner diffusion would have a greater influence on the overall current response and therefore the mass transport would be further enhanced, as the microsquare electrodes got smaller. However the steady-state FEM simulations shown in chapter 4 (section 4.3.6) showed a linear relationship for the microsquare limiting currents with edge dimension, indicating that as with microdiscs, the current densities at steady-state scale with size (Figure 4.31). This enabled a scaling factor to be used to derive an empirical limiting current expression (Eqn. 4.7).

The FEM simulations in chapter 4 also showed that the greatest mass transfer occurs at the outer edges of both the microsquare and microdisc electrode systems (shown by the increased mesh density observed in Figure 4.23). At least pictorially it was not clear if the microsquare electrodes also had further enhanced mass transport in the corners. This observation led to the suggestion that as with nanobands a theoretical expression depending on differences in edge lengths may yield a better estimate of the limiting current. The expression which matches microdisc and microsquare edge lenths is:

$$i_L = 4nF\mathbf{D}c\frac{2l}{\pi} \qquad \textbf{Eqn. 8.1}$$

However the limiting current value calculated using this expression for S50u is 85.7 nA, which is over 9% larger than both the average experimental value and the value obtained via simulation. As with CaviArE electrodes (Chapters 6 and 7), this may be due to the effects of hindered diffusion in the corners of the squares reducing edge response. These observations show that further investigation is required to try and better understand microsquare responses and confirm simulation prediction.

There are a number of future experiments which would be useful to carry out in order to confirm fundamental microsquare response. The most

easily achievable is to fabricate a range of different sized (e.g. (5 μm)^2, 10 μm)^2 (20 μm)^2 (30 μm)^2 and (100 μm)^2) single platinum microsquares using the same fabrication processes as described in section 4.2.1. A number of similar redox experiments to those carried out for the (50 μm)^2 electrodes could be undertaken. The limiting currents observed could then be compared to those obtained from the steady-state FEM simulations, to confirm that similar responses are observed experimentally and provide further data in order to enable full understanding of a microsquare response.

Single microsquare electrodes have been shown to have similar modified Tafel characteristics to microdiscs (Figure 4.22). The modified Randles circuit developed for microdisc analysis also fits well at low frequencies to the microsquare EIS data (Figure 4.26). This suggests that, at least at stead-steady, the diffusional regime is essentially hemispherical and similar to that of microdiscs. The steady-state FEM diffusional fields in Figure 4.24 also show very similar concentration profiles for both the microsquare and microdisc simulation which further validates this theory. However, in contrast to a microdisc response, the modified Randles circuit does not fit the microsquare EIS data over all frequencies (times). As discussed in section 4.3.5, the inability to fit EIS data over the entire frequency range, at any E_{dc} value, is indicative that the development of the microsquare diffusional fields, especially at medium time scales, is different to that of a microdisc. In order to better understand the diffusional processes occurring, it would be very beneficial to perform Transient FEM simulations, modelling the concentration profile development with time. FEM numerical computer models have also been utilised to model electrochemical impedance of microdisc electrodes[3,4]. It would be beneficial to use similar simulation techniques to model the Faradaic impedance of microsquare electrodes, in order to better understand the EIS response observed.

8.3. Nanoband Cavity Array Electrode (CaviArE) research

The voltammetric studies in chapter 6 and the EIS studies in chapter 7 have provided an in depth analysis of the novel CaviArE devices. To the author's

knowledge the work presented in this thesis provides the first in depth study of such architectures. The research has provided confidence that the microfabrication and electrochemical response of these devices are reproducible over a wide range of architectures and experiments and, the electrode arrays themselves, although difficult to clean are robust and reusable. Furthermore the reproducible standard microfabrication process outlined in Chapter 5 provides an excellent method of fabricating nano-scale electrode arrays with highly controllable dimensions. This has been a one of the greatest challenges during previous nanoelectrode research and is important as it provides a means of systematically studying nanoelectrode responses.

The voltammetric and chronamperometric studies, (Chapter 6) show that the response of these electrodes fit to nanoband theory, at least over intermediate times and although a complete model for the current-time transient (i_L^{-1} vs. ln$t$) response, has not been established, the diffusional regimes over different times has been identified. Linear regression lines can be fitted over intermediate times, with the lower limit corresponding to establishment of band diffusion outside of the cavity and the upper limit corresponding to establishment of electrode diffusional overlap and planar diffusion to the entire electrode array. When studying the i_L^{-1} vs. ln$t$ slopes over a range of CaviArE devices, these lower and upper limits have been shown to correspond very well to the size and spacing respectively, of the electrode array being studied. The lower and upper limits observed for the CaviArE response in 1 mM ferricyanide and in ferrocene carboxylic acid show this same relationship to the size and spacing of the CaviArE devices. A value of K in Equation 6.2 was calculated over a range of experiments, but since $K \propto e^{-\ln t}$ and requires extrapolation of the linear regression line, large errors accumulate and an accurate value of K was not determined. The value lies within the range >0 - 10 - < 100 and for data recorded during this research, most values were found to be in the lower limit of this range. Further research needs to be carried out in order to determine a better method of extracting K. Transient simulation models seem the obvious next step, in order to try to simulate the current response with time.

Plots of i_L^{-1} vs. ln$v$ obtained from the cyclic voltammetric data at 0.05 V and 0.19 V yield gradients of similar magnitude to the corresponding i_L^{-1} vs. ln$t$ for the different CaviArE architectures. Indeed the normalised slopes, when accounting for actual electrode area, yield similar values for both types of plot, regardless of size or separation of the CaviArE devices. Contrasting to this are the normalised slopes recorded, with respect to cavity square area, which increase as the cavity size increases. Analysis of a greater range of CaviArE devices is required before conclusive trends can be established.

The voltammetric data also shows that the CaviArE devices behave as nanobands with large effective area and that their responses, unlike microsquare arrays of similar architecture, are insensitive to real or parasitic capacitive charging, making these devices desirable for sensing applications. The slopes of the i_L^{-1} vs. ln$v$ plots can be used to determine this effective electrode area and shows that, on average, over a range of CaviArE devices, approximately 70% of the electrode geometric area is active during experimentation. This is postulated to be due to interaction of diffusional fields in the corners of the electrode device. This effective area in fact appears to increase as the dimensions of the square cavity increase, which may indicate that interaction of diffusional fields in corners remains constant irrespective of electrode size and therefore has a smaller impact on the overall response as the electrode edge dimension increases.

It is satisfying to observe that the diffusional regimes (and times) identified from the current-time transient data, closely follows those identified in the equivalent EIS response. Equivalent circuit models were fitted to all frequency regions except for the transition region, TR at medium frequencies. This region is speculated to be the region where the diffusional regime begins to transform from band diffusion within the cavity to band diffusion outside of the cavity - that is the region where the depletion zone begins to fill the hole completely. There is no obvious transition region present on the i_L^{-1} vs. ln$t$ plots for comparison and at present it is not known how this diffusional regime develops and therefore it could not be modelled with an equivalent circuit. This

is certainly an area which should be addressed in future research of these CaviArE devices.

Looking at the high frequency EIS responses (region a)), all data (except for the very large C100µ3d CaviArE architecture), fit well to a modified Randles' circuit established for a nanoband response (justified in chapter 7.3.2). However, since the uncompensated resistance is similar for all CaviArE architectures and indeed for the equivalent microsquare arrays, it suggests that the entire platinum plate may charge at very high frequencies. The EIS data also shows that the capacitance for these devices is an order of magnitude higher than would be expected for their geometric area, but that this capacitance only affects the electrode response at very high frequencies and therefore does not impact on the voltammetric responses. Since the underlying platinum plate may charge at the highest frequencies, the response can be more realistically represented by the equivalent circuit given in Figure 7.24.

The Warburg impedance at high frequencies and for all architectures is at least an order of magnitude smaller than expected. The speculated reason for this is given schematically in Figure 7.23 and is believed to be due to observation of linear diffusion across the entire depth of the 1050 nm cavity. The precise diffusional regime over these frequencies is not fully understood however. It is also interesting to note that the C100µ3d array with the largest cavity size has around 20 times the expected value of $1/Y_0^{a,\,min}$. This is consistent with diffusion across the entire micrometre cavity. The smaller values for smaller cavities may reflect increasing corner effects in these cavities. Transient FEM modelling may be a useful method of monitoring the concentration profiles over these fast time scales.

At high frequencies the CaviArE devices have however, been shown to have extremely variable charge transfer EIS responses. This is indicative of varying surface contamination and shows how difficult it is to reproducibly clean the electrodes using standard electrochemical cleaning methods. Research into alternative cleaning techniques may be of value during future

research of the CaviArE substrates. It is however, promising to observe very fast lower limit standard rate constant values in ferricyanide of up to 2 cm s^{-1} for the cleanest array; which is one of the fastest rates observed for ferricyanide on electrodes of this size.

The non-linear resistance, R_{NL}^{a} observed at fast time scales, in region a), is 66% of the magnitude expected for a single linear nanoband electrode of equivalent area[5]. This is a similar percentage to the effect active area and therefore the small difference in R_{NL} may be due to interaction and overlap of diffusional fields in the corners of the CaviArE electrodes. As noted in Chapter 7, since the non-linear resistance is also likely to change slightly with frequency, due to the time dependent responses associated with nanobands, the theoretically derived R_{NL} values can only be an approximation, and therefore some deviation in response is expected. It is satisfying to observe that values of R_{NL}^{b} are the same within experimental error to the values recorded for R_{NL}^{a} for all CaviArE separations which indicates that hemispherical, and hence time-insensitive responses, are established extremely quickly for these arrays. This provides evidence that pseudo-steady state responses are therefore established extremely quickly for these array architectures.

The low frequency CaviArE EIS data (regions b) and c)) has been shown to develop in a similar manner to a microsquare array response of similar square length and spacing. The equivalent circuits used to fit microsquare arrays in this frequency region also showed good fits to the CaviArE substrates. The impedance parameters obtained for CaviArE also had similar values to those of the corresponding microsquare array.

The ratio between the Warburg impedance associated with diffusion to the entire array ($1/Y_0^c$) and with that of planar diffusion, out of the CaviArE cavity ($1/Y_0^b$), is expected to have a well-defined value, calculated by $(1+x)^2$. In all cases the CaviArE devices followed this expected trend within experimental error.

Overall, this study has demonstrated that these devices may be suitable for sensing applications and even for electroanalysis of fast kinetics. Although more effective cleaning techniques may be of use, it is promising that very fast standard rate constants have been observed for the cleanest arrays (up to 2 cm s^{-1} for ferri/ferrocyanide). Since it would be reasonably easy to change the type of metal used, or functionalise the active electrode surface, there are many varied potential applications for these electrode arrays and they would be especially suited for sensitive biosensing and/or environmental analysis. For example gold could be electroplated and used for very sensitive detection of glucose oxidase[6] or acetylcholine could be detected using Nickel[7]. In recent years, due to the detrimental environmental impacts of heavy metal contamination, electrochemical monitoring of heavy metal concentrations has been of increasing interest[8]. These CaviArE devices may provide a robust, quantitative and reusable method for real-time monitoring of different heavy metals, such as Pb^{2+}, Cu^{2+} and Cd^{2+}. The concentration of dissolved oxygen is also a vital parameter in many industrial systems as well as in physiological and natural environments[9]. The Platinum CaviArE devices could potentially also be used as dissolved oxygen sensors.

Presently the 30µ3d architecture is being developed into a commercial device by the partner company Nanoflex Ltd. Figure 8.2 shows photographs of the device developed for industrial trials along with an image of one of the CaviArE chips used for analysis during much of this work.

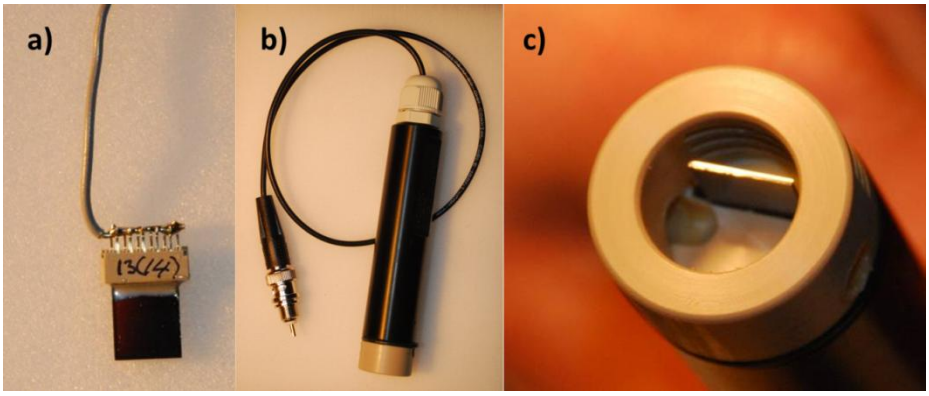

Figure 8.2: Photographic images of a prototype CaviArE device **a)** one of the CaviArE devices with edge connector. **b)** The CaviArE device showing the PEEK header (6.2 c) and Delrin body. The protruding insulated wire terminates with a BNC jack plug; **c)** the CaviArE substrate, which sits within the PEEK header for protection.

Figure 8.3 shows typical responses for these devices in comparison with a very clean C30µ3d substrate.

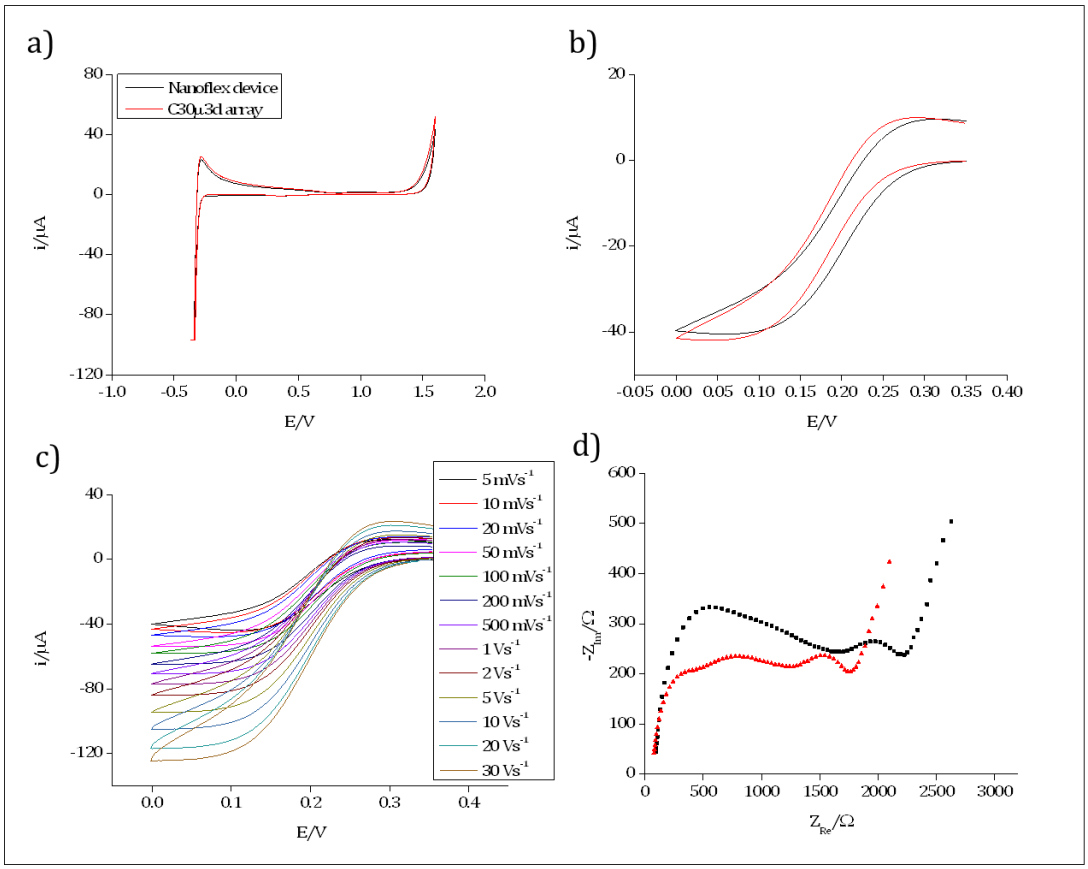

Figure 8.3: a) typical Cyclic voltammograms (CV) of the final cleaning scan, after cycles in 0.05 M aqueous sulfuric acid of a Nanoflex device (black) and a C30µ3d array (red) at sweep rate, v = 100 mV s^{-1}; **b)** typical first scan CVs in 10 mM potassium ferricyanide of a Nanoflex device (black) and a C30µ3d array (red); **c)** typical first scan CVs of a Nanoflex device obtained in 10 mM ferricyanide at different sweep rates; **d)** comparison of a typical Nanoflex EIS response in 10 mM potassium ferricyanide at E_{dc} = + 0.19 V (red) with a clean C30µ3d electrode response.

The data in Figure 8.3 shows that these devices behave in the same manner as the C30µ3d array and are suitable for commercial development, as they provide a more robust product, with the electrode array being protected within the sample header and all wires and contacts sealed inside the main body. The devices also have an easily accessible BNC jack plug for electrical connection.

Although these devices have attractive characteristics, there are a number of questions, especially regarding the EIS response of these CaviArE devices, which remain unclear. Firstly the Warburg impedance at high frequencies and for all architectures is at least an order of magnitude smaller than expected from the band dimensions. The suggested reason for this (Figure

7.22) is linear diffusion across the entire depth of the 1050 nm cavity. The i^{-1} vs ln*t* slopes over similar time scales appears to predict increased electrode width than the response at intermediate times, which compliments the EIS data. Also it is presently unclear why higher than expected capacitance values are recorded at high frequencies. Altering the thickness of the silicon nitride, or the platinum electrode width or even performing experiments on single square nanoband elements may provide insight into the EIS responses observed. Performing transient and steady-state FEM modelling may also provide useful information about the diffusional regimes which may aid in understanding the origins of these responses.

COMSOL steady-state, adaptive mesh simulations were successfully utilised in Chapter 4 to model the concentration gradients from a planar microdisc and microsquare electrode. Similar simulations were in fact also attempted for the CaviArE devices. Figure 8.4 shows the COMSOL 3D model developed for these FEM simulations.

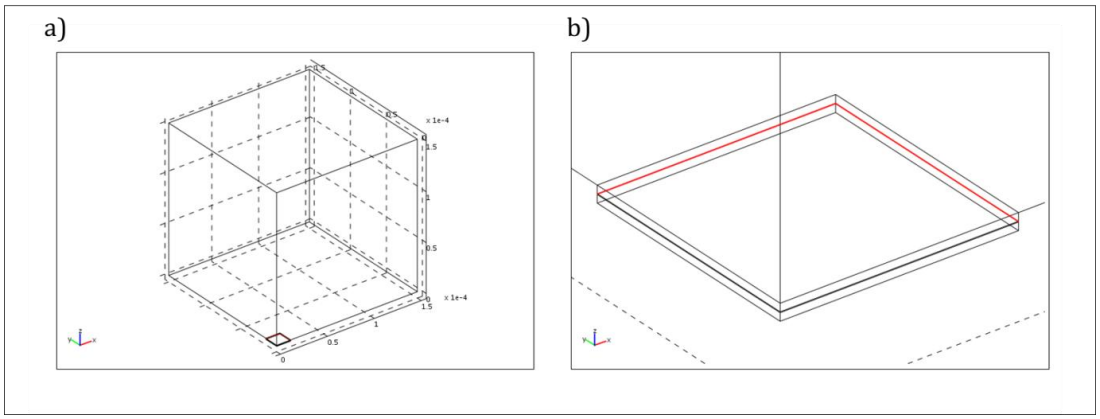

Figure 8.4: a) the COMSOL 3D model, with its $(150\ \mu m)^3$ simulation cube and 1050 nm depth cavity in one corner centred at y =0, x = 0 and z = 0. This shallow cube is 15 µm in width and models one quarter of a $(30\ \mu m)^2$ cavity **b)** close-up of the cavity, which comprises a 50 nm band, activated as an electrode on two sides (shown in pink) and sandwiched between two 500 nm thick insulating layers. As with the single microsquare arrays, the two front faces in this diagram are set as symmetry faces.

Figure 8.5 shows the resulting concentration profiles produced after steady-state FEM simulation.

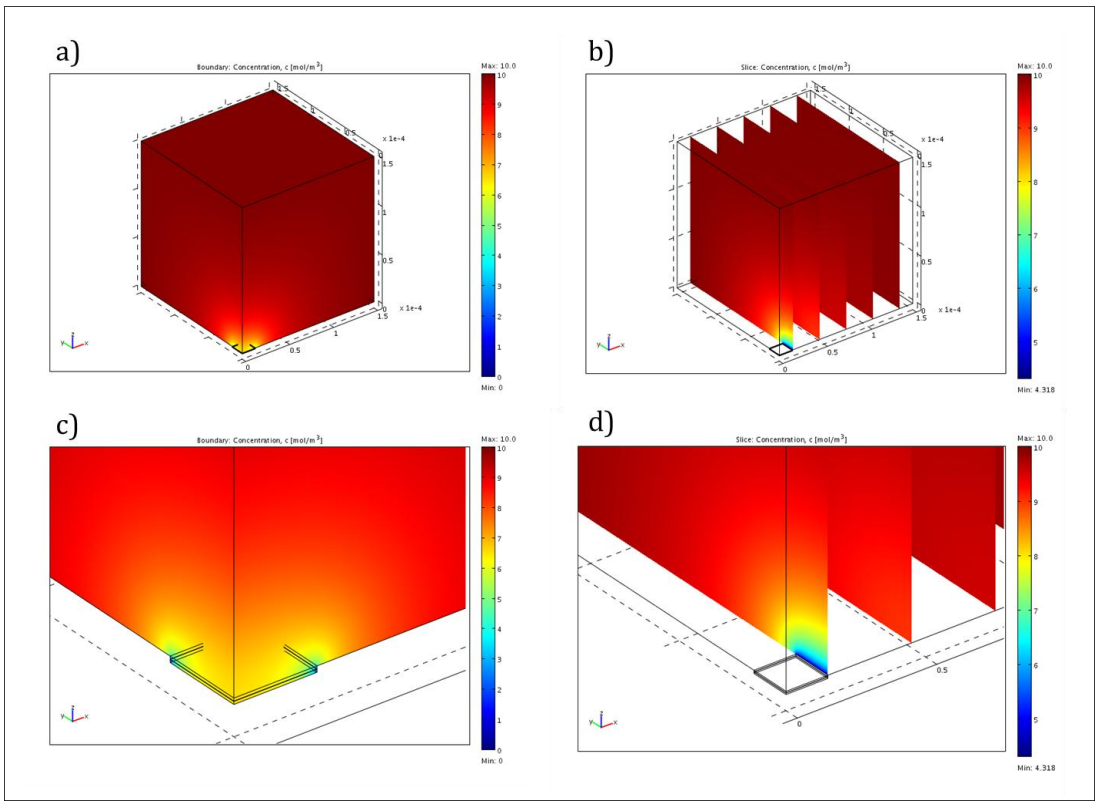

Figure 8.5: a) the concentration profiles obtained from FEM simulation of ferricyanide [10 mM] diffusional transport to the activated (30 μm)^2 50 nm CaviArE electrode, and **b)** corresponding slices from the profile. The images **c)** and **d)** are close-ups of the electrode cavity, showing the full and sliced concentration profiles respectively.

Figure 8.5 shows that as expected the concentration gradients change most rapidly around the nanoband electrode and the depletion layer is relatively thin. This steady-state simulation suggests that diffusion near the electrode is not hemispherical, but cylindrical, although further from the cavity the concentration gradients become more hemispherical and begin to resemble similar profiles to those observed for both the microdisc and microsquare electrodes. Figure 8.6 shows a graph of the current calculated with increasing mesh density (with progressive COMSOL FEM refinement).

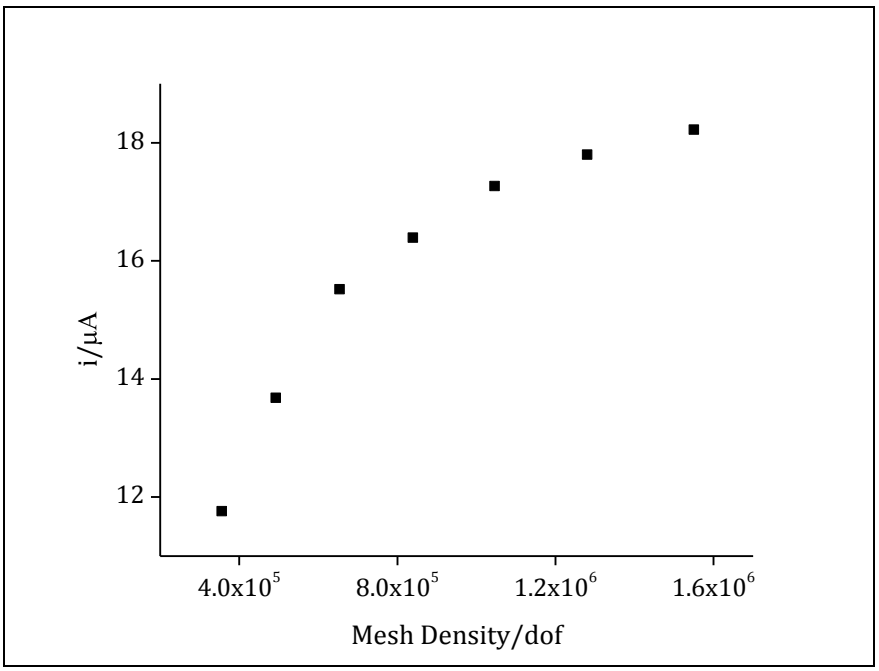

Figure 8.6: COMSOL simulated limiting currents for the $(30\ \mu m)^2$ C30u single CaviArE substrate as the mesh densities increases during refinement.

Several meshing problems were encountered when attempting to use the same adaptive mesh method as for the single microsquare simulations (Chapter 4). In fact, when using the default 'normal' meshing method, the program ran out of processing memory during the first iterations. The adaptive mesh therefore had to be run in a 'coarse' meshing mode, in order for the simulation to run to completion. The final current value attained for this simulation is 18.2 (± 0.5) nA, which would translate to a total current of 32 μA for the 1764 isolated electrodes in the 30μ3d architecture. This value is over 8 μA lower than the current found experimentally at 5 mVs^{-1} for the C30μ3d arrays (Chapter 6). At this slow sweep rate the diffusion fields from these electrodes are known to overlap, therefore the current would be expected to be lower than that of the isolated electrode response. This indicates that the simulation current is far lower than that obtained experimentally. Indeed even when using a coarse adaptive mesh refinement, the simulation still fell down after several iterations and the current in Figure 8.6 does not yet appear to be asymptotically approaching its steady state value. Although steady-state simulations are perhaps not the most appropriate models for the CaviArE devices, as it is likely that true steady-states will never be reached due to the time-dependent

response of nanobands, COMSOL meshing images (Figure 8.7) also revealed further issues with the adaptive FEM simulation method used.

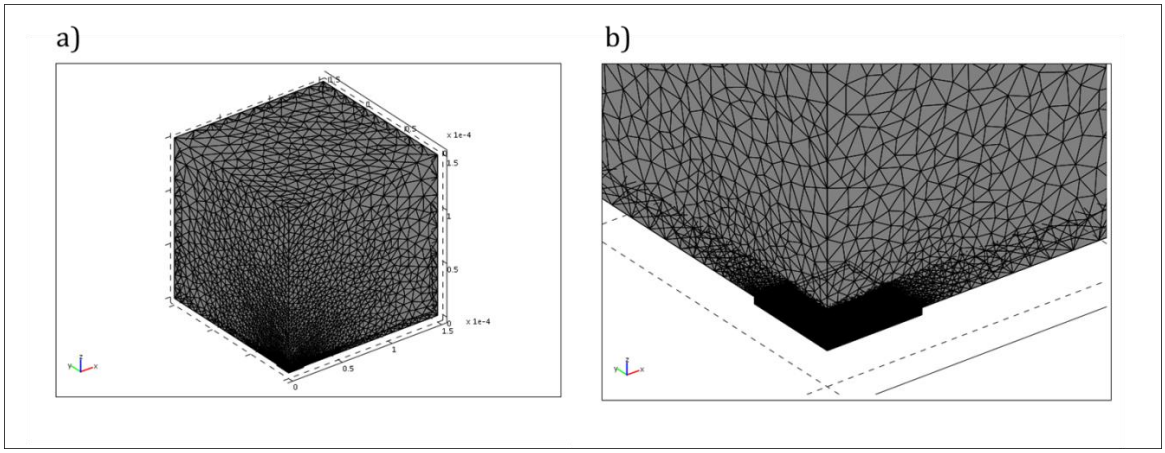

Figure 8.7a) The meshes produced by the COMSOL 3D FEM model; **b)** a close-up of the mesh close to the (30 μm)^2 cavity.

The first point to note, from Figure 8.7 a) is that the mesh is extremely dense, even after selecting the course meshing mode. It is obvious that differential calculation of such dense meshing will take a lot of processing memory and thus it is not surprising that the simulation fell down quickly. Since the concentration profile rapidly grows to bulk concentration, the mesh density in the outer regions of the model, does not need to be nearly as dense, since the concentration does not change a lot in this region. Secondly, as shown in Figure 8.7 b) it is odd that the mesh also appears densest around the insulation/symmetry face and less dense around most of the active electrode area. Cutress *et al*[10,11] in their work have outlined some of the accuracy issues they encountered when using COMSOL and suggest that such FEM modelling should be used with caution when modelling complex electrochemical systems. They state that by increasing mesh points, which generally increases simulation accuracy, errors in meshing can occur if the meshing is not controlled. This is consistent with the errors observed in these simulations. As the COMSOL software allows the modeller to manually select mesh densities and parameters, provided that the modeller has some understanding of the diffusional processes occurring during experimentation, there is scope to manually create very dense meshes in the regions where concentration gradients will be expected to change most rapidly and very course mesh densities in regions where concentration is

hardly changing. For example, by observation of the concentration profiles produced during these simulations (Figure 8.6), it is clear that the mesh does not need to be as dense as it is over the majority of the simulation space and that manually selecting the mesh to focus the densities in areas of high diffusional flux could hugely reduce the memory required and indeed the running time of each simulation, as well as improve simulation accuracy. These observations suggest that FEM modelling of CaviArE electrodes requires further development, and should proceed only with care and with steady-state and time-dependent experimental validation of accurate meshing and simulation.

Since these CaviArE devices have already shown robust, reproducible, well defined and quantitative electrochemical responses, through further experiment and modelling, a comprehensive understanding of these CaviArE devices should be possible. The devices have also already shown great potential for the electroanalysis of fast kinetics and once these electrode systems are further understood, there will certainly be many more potential applications for such devices. It has been a pleasure to have the opportunity to work on this research project and it is the hope of the author that the research is progressed and the full potential of the CaviArE devices understood.

8.4. References

(1) Morita, M., M.L. Longmire, R.W. Murray *Anallytical Chemistry* **1988**, *60*, 2770.

(2) Berduque, A.; Lanyon, Y. H.; Beni, V.; Herzog, G.; Watson, Y. E.; Rodgers, K.; Stam, F.; Alderman, J.; Arrigan, D. W. M. *Talanta* **2007**, *71*, 1022.

(3) Michel, R.; Montella, C.; Verdier, C.; Diard, J. P. *Electrochimica Acta*, *55*, 6263.

(4) Ferrigno, R.; Girault, H. H. *Journal of Electroanalytical Chemistry* **2000**, *492*, 1.

(5) Alden, J. A.; Compton, R. G. *Electoalanysis* **1996**, *8*, 30.

(6) Barton, A. C.; Collyer, S. D.; Davis, F.; Gornall, D. D.; Law, K. A.; Lawrence, E. C. D.; Mills, D. W.; Myler, S.; Pritchard, J. A.; Thompson, M.; Higson, S. P. J. *Biosensors and Bioelectronics* **2004**, *20*, 328.

(7) Sattarahmady, N.; Heli, H.; Moosavi-Movahedi, A. A. *Biosensors and Bioelectronics* **2010**, *25*, 2329.

(8) Feeney, R.; Kounaves, S. P. *Electroanalysis* **2000**, *12*, 677.

(9) Sosna, M., Guy Denault, Robin W. Pascal, Ralf D. Prien and Matt Mowlem *Sensors and Actuators B* **2007**, *123*, 344.

(10) Cutress, I. J.; Dickinson, E. J. F.; Compton, R. G. *Journal of Electroanalytical Chemistry* **2010**, *638*, 76.

(11) Cutress, I. J.; Compton, R. G. *Journal of Electroanalytical Chemistry* **2010** *645*, 159.

9. Acknowledgments

I wish to thank my primary Supervisor, Andrew Mount for all the time and dedication he has given to my project. I specifically wish to acknowledge the work he has done in helping me develop many of the mathematical modelling expressions used throughout this thesis. Mathematics has never been one of my strong points and I would never have been able to derive much of the mathematical theory without Andrew. Never the less, I have enjoyed the challenge of learning and understanding the mathematical concepts presented in this work and I appreciate the time Andrew took, helping me to fully grasp the theory. I would also like to thank Andrew for all the teaching he has given me in this subject area and for all the discussions we have had regarding necessary background research, especially in the theory of ac impedance and that of transmission lines.

I would like to thank Jonathon Terry, from the SMC for fabricating all the electrodes for me. Without him I would not have had a project to work on. Jonathon also deserves huge thanks for teaching me about the different electrode fabrication processes, accompanying me in the clean room when I first arrived and for his initial help using the optical microscope. He is always willing to help in any way he can and I appreciate the time he has given to my project.

I would like to thank Anthony Walton, my second supervisor and Director of the SMC, for all his expertise and input during my tenure as a PhD student. I appreciate the time spent in discussions with me relating to this research and am grateful of all the useful suggestions and ideas he has contributed. I also wish to thank him for calm and wise words he offered to me in the run up to the completion of this thesis. I know he will continue to be heavily involved in the next step of research regarding the CaviArE devices.

I also wish to offer thanks to Neville Freeman, who patented the original CaviArE design with my Supervisor. I understand he has aided in obtaining funding for my project, and has worked tirelessly, trying to promote the design

to industrial companies. He has also conducted his own studies on the electrodes and designed the Nanoflex industrial devices. He has always supported the work I have done, offering his help and advice when I needed it.

My former work colleague, John Henry was also a great support for me during the first year of my PhD and he is certainly worth acknowledging. He taught me how to use the Autolab software during my first few months and was constantly willing to help and provide advice on any inquiries I may have had regarding my research or with electrochemistry in general. He is one of the best electrochemists I have ever met, and I am very proud to have worked alongside him.

I would in fact like to thank the entire Mount group for the friendships, camaraderie and well needed lunch breaks during my time as a PhD student. Specific acknowledgement of Charlotte Brady is necessary as she has been working with the group since I started my PhD and we have worked and collaborated on paralleling projects for much of our time as PhD students. We have gone through all the highs and lows together, and she has listened to me natter on more than most people would be able to put up with. I wish her all the best as she comes to the end of her PhD.

I would like to thank my sister, Laura Woodvine, really just for being my sister and probably one of my best friends. I am really glad I have had the chance to spend some time with her over the past couple of months, whilst writing my thesis. I am so proud of all that she has achieved and the person she has grown to be. That in itself has encouraged me to work all the harder.

I would like to give special thanks to my Mum, Ailsa Woodvine and my Dad, Keith Woodvine, for whom this thesis is dedicated. They have supported and believed in me all of my life and I would not be who I am today without their love and guidance and their willingness to accept and support all the decisions I have ever made. I have been working on this thesis from home for the last two and half months and I certainly do not think I would have been able to finish it if

I wasn't at home. Being surrounded by the love and warmth of my family with their words of encouragement, good food and cups of coffee, has definitely helped me get over the hurdle. They also provided an environment, where I could completely immerse myself in my work, so I was able to write with very few distractions. I am thankful to them for this and more than I could ever put into words.

Finally I would like to thank my partner, Michael Snyder whom I met at the very beginning of my PhD adventure. He was there at the beginning and he is waiting for me at the end; and the in between, well I can honestly say, hold some of the best memories of my short life. I have been blessed to have led an extremely full life and have been presented with many amazing opportunities. I have always worked hard and grasped hold of everything life had to throw at me. However, if it's possible, I feel that my life got even fuller when Michael walked into it one wine and cheese evening, during the second week of my PhD. He has supported and loved me through all of the highs and the lows; and always with a smile and words of encouragement. It has been through him that I have seen the true meaning of hard work and it is because of him that I am determined never to lose sight of my dreams.

A. Appendices

A.1. Derivation of Thermodynamic Fitting Models

A1.1. Derivation of $R_{CT,e}$

The applied dc potential is related to the standard potential by[1]:

$$E_{dc} = E^{\ominus} + \frac{RT}{F}\ln\frac{\bar{b}}{\bar{a}} \qquad \textbf{Eqn. A1.1}$$

where $\bar{a}$ is the mean concentration of the oxidised species at the electrode surface and $\bar{b}$ is the mean concentration of the reduced species at the electrode surface, therefore

$$\frac{\bar{a}}{\bar{b}} = \exp\left(\frac{(E_{dc}-E^{\ominus})}{RT}F\right) \qquad \textbf{Eqn. A1.2}$$

Since $\bar{a} + \bar{b} = c$, where c is the total concentration of ferri/ferrocyanide then

$$\frac{\bar{a}}{c-\bar{a}} = \exp\left(\frac{(E_{dc}-E^{\ominus})}{RT}F\right) \qquad \textbf{Eqn. A1.3}$$

and

$$\bar{a}\left(\exp\left(\frac{(E_{dc}-E^{\ominus})}{RT}F\right)\right) = c\left(\exp\left(\frac{(E_{dc}+E^{\ominus})}{RT}F\right)\right) \qquad \textbf{Eqn. A1.4}$$

Let $N = \frac{(E_{dc}-E^{\ominus})}{RT}F$ thus,

$$\frac{\bar{a}}{c} = \left(\frac{\exp(N)}{1+\exp(N)}\right) \qquad \textbf{Eqn. A1.5}$$

Consequently

$$\frac{\bar{b}}{c} = \left(\frac{\exp(-N)}{1+\exp(-N)}\right) \qquad \textbf{Eqn. A1.6}$$

$R_{CT,e}$ is given by equation 2.40, thus

$$R_{CT,e} = \frac{RTl}{AD_e F^2 c}\left[\left(\frac{1+\exp(N)}{\exp(N)}\right)\left(\frac{1+\exp(-N)}{\exp(-N)}\right)\right] \qquad \textbf{Eqn. A1.7}$$

or

$$R_{CT,e} = \frac{RTl}{AD_e F^2 c}[2 + \exp(N) + \exp(-N)] \qquad \textbf{Eqn. A1.8}$$

When $E_{dc} = E^{\theta}$, N = 0 and $R_{CT,e} = R_{CT,e}^{min}$ Then

$$R_{CT,e}^{min} = \frac{4RTL}{ADF^2 c} \qquad \textbf{Eqn. A1.9}$$

By substituting equation A1.9 into equation A1.8, an expression for $R_{CT,e}$ can be derived

$$R_{CT,e} = \frac{R_{CT,e}^{min}}{4}[2 + \exp(N) + \exp(-N)] = R_{CT,e}^{min}\left(\cosh^2\left(\frac{N}{2}\right)\right) \qquad \textbf{Eqn. A1.10}$$

A1.2. Derivation of σ

For a one electron transfer process the Warburg coefficient, σ is given by[1]:

$$\sigma = \frac{RT}{F^2 A\sqrt{2}}\left(\frac{1}{D_O^{1/2} a^{\infty}} + \frac{1}{D_R^{1/2} b^{\infty}}\right) \qquad \textbf{Eqn. A1.11}$$

where D_O and D_R are the diffusion coefficients of the oxidised and reduced species respectively, a^{∞} and b^{∞} are the bulk concentrations of the oxidised and reduced species respectively and all other terms have their usual meaning[1].

For redox couples, the diffusion coefficients are normally very similar. Which means that $D_O \approx D_R = D$ and the equation can be simplified to

$$\sigma = \frac{RT}{F^2 A\sqrt{2}}\left(\frac{1}{a^{\infty}} + \frac{1}{b^{\infty}}\right) \qquad \textbf{Eqn. A1.12}$$

If the same logic is applied as for interpretation of charge transfer data at the electrode surface, it can be found that

$$\sigma = \frac{RT}{F^2 A\sqrt{2}c}\left(\frac{c^2}{\bar{a}\bar{b}}\right) \qquad \textbf{Eqn. A1.13}$$

where $\bar{a}$ and $\bar{b}$ are the mean concentrations of the oxidised and reduced species at the electrode surface respectively and c is the total concentration of the redox couple thoughout, including in the bulk. As with $R_{CT,e}$

$$\sigma = \frac{RT}{ADF^2\sqrt{2}c}[2 + \exp(N) + \exp(-N)] \qquad \textbf{Eqn. A1.14}$$

When $E_{dc} = E^{\theta}$, N = 0 and $\sigma = \sigma^{min}$

$$\sigma^{min} = \frac{4RT}{ADF^2\sqrt{2}c} \qquad \textbf{Eqn. A1.15}$$

Therefore

$$\sigma = \frac{\sigma^{min}}{4}[2 + \exp(N) + \exp(-N)] = \sigma^{min}cosh^2\left(\frac{N}{2}\right) \qquad \textbf{Eqn. A1.16}$$

A2. Impedance Batch Macro Input Parameters

A2.1. Platinum Macrodisc Electrode

Experiment no.	dc Potential / V	Begin frequency / Hz	End frequency / Hz	No. frequencies	Amplitude (rms) / V
1	0.150	1000	1	50	0.001
2	0.155	1000	1	50	0.001
3	0.160	1000	1	50	0.001
4	0.165	1000	1	50	0.001
5	0.170	1000	1	50	0.001
6	0.175	1000	1	50	0.001
7	0.180	1000	1	50	0.001
8	0.185	1000	1	50	0.001
9	0.190	1000	1	50	0.001
10	0.195	1000	1	50	0.001
11	0.200	1000	1	50	0.001
12	0.205	1000	1	50	0.001
13	0.210	1000	1	50	0.001
14	0.215	1000	1	50	0.001
15	0.220	1000	1	50	0.001
16	0.225	1000	1	50	0.001
17	0.230	1000	1	50	0.001

Figure A2.1: Table of E_{dc}, the frequency range and (rms) amplitude selected for impedance measurements for EIS studies of platinum macrodisc electrodes.

A2.2. Single S50μ Pt Squares and Pt Microsquare Arrays

Experiment no.	dc Potential / V	Begin frequency / Hz	End frequency / Hz	No. frequencies	Amplitude (rms) / V
1	0.150	1000	0.01	50	0.001
2	0.155	1000	0.01	50	0.001
3	0.160	1000	0.01	50	0.001
4	0.165	1000	0.01	50	0.001
5	0.170	1000	0.01	50	0.001
6	0.175	1000	0.01	50	0.001
7	0.180	1000	0.01	50	0.001
8	0.185	1000	0.01	50	0.001
9	0.190	1000	0.01	50	0.001
10	0.195	1000	0.01	50	0.001
11	0.200	1000	0.01	50	0.001
12	0.205	1000	0.01	50	0.001
13	0.210	1000	0.01	50	0.001
14	0.215	1000	0.01	50	0.001
15	0.220	1000	0.01	50	0.001
16	0.225	1000	0.01	50	0.001
17	0.230	1000	0.01	50	0.001

Figure A2.2: Table of E_{dc}, the frequency range and (rms) amplitude selected for impedance measurements for EIS studies of single platinum microsquare electrodes and platinum microsquare arrays.

A2.3. CaviArE

Experiment no.	dc Potential / V	Begin frequency / Hz	End frequency / Hz	No. frequencies	Amplitude (rms) / V
1	0.230	$61x10^3$	0.01	68	0.01
2	0.220	$61x10^3$	0.01	68	0.01
3	0.210	$61x10^3$	0.01	68	0.01
4	0.200	$61x10^3$	0.01	68	0.01
5	0.190	$61x10^3$	0.01	68	0.01
6	0.180	$61x10^3$	0.01	68	0.01
7	0.170	$61x10^3$	0.01	68	0.01
8	0.160	$61x10^3$	0.01	68	0.01
9	0.150	$61x10^3$	0.01	68	0.01

Figure A2.2: Table of E_{dc}, the frequency range and (rms) amplitude selected for impedance measurements for EIS studies of CaviArE.

A3. Calculation of the limiting current, i_L, from the value of R_{NL} from EIS Measurements

Considering the modified Tafel equation (section 2.5)

$$\ln\left(\frac{i_L}{i} - 1\right) = \frac{n\mathbf{F}\left(E - E_{1/2}\right)}{\mathbf{R}T} \qquad \textbf{Eqn. A3.1}$$

where i is the current at different potentials, E, i_L is the limiting current, $E_{1/2}$ is the half wave potential, n is the number of electrons transferred in the reaction, **F** is Faraday's constant, **R** is the universal gas constant and T is temperature. For a reduction reaction (with negative i_L) it should be noted that i_L decreases as E increases.

When $\Delta E = E_1 - E_2$ is applied the Tafel equation can be written as a set of simultaneous equations:

$$\ln\left(\frac{i_L}{i_1} - 1\right) = \frac{n\mathbf{F}\left(E_1 - E_{1/2}\right)}{\mathbf{R}T} \qquad \textbf{Eqn. A3.2}$$

and

$$\ln\left(\frac{i_L}{i_2} - 1\right) = \frac{n\mathbf{F}\left(E_2 - E_{1/2}\right)}{\mathbf{R}T} \qquad \textbf{Eqn. A3.3}$$

These can be re-arranged as:

$$\left(\frac{i_L}{i_1} - 1\right) = e\left(\frac{n\mathrm{F}\left(E_1 - E_{1/2}\right)}{\mathrm{R}T}\right) \qquad \textbf{Eqn. A3.4}$$

and

$$\left(\frac{i_L}{i_2} - 1\right) = e\left(\frac{n\mathrm{F}\left(E_2 - E_{1/2}\right)}{\mathrm{R}T}\right) \qquad \textbf{Eqn. A3.5}$$

For simplicity, let $P = E_2 - E_{1/2}$ and $\Delta E = E_1 - E_2$, thus

$$\left(\frac{i_L}{i_1} - 1\right) = e\left(\frac{n\mathrm{F}(P + \Delta E)}{\mathrm{R}T}\right) \qquad \textbf{Eqn. A3.6}$$

and

$$\left(\frac{i_L}{i_2} - 1\right) = e\left(\frac{n\mathrm{F}(P)}{\mathrm{R}T}\right) \qquad \textbf{Eqn. A3.7}$$

Subtracting A3.7 from A3.6 gives

$$\left(\frac{i_L}{i_1} - 1\right) - \left(\frac{i_L}{i_2} - 1\right) = e\left(\left(\frac{n\mathrm{F}(P + \Delta E)}{\mathrm{R}T}\right) - \left(\frac{n\mathrm{F}(P)}{\mathrm{R}T}\right)\right) \qquad \textbf{Eqn. A3.8}$$

which re-arranged gives

$$\left(\frac{i_L}{i_1} - 1\right) - \left(\frac{i_L}{i_2} - 1\right) = e\left(\frac{n\mathrm{F}(P)}{\mathrm{R}T}\right) \cdot e\left(\frac{n\mathrm{F}\Delta E}{\mathrm{R}T} - 1\right) \qquad \textbf{Eqn. A3.9}$$

Now as ΔE is small, $e^x \approx 1 + x$, and hence:

$$\left(\frac{i_L}{i_1} - 1\right) - \left(\frac{i_L}{i_2} - 1\right) = e\left(\frac{n\mathrm{F}(P)}{\mathrm{R}T}\right) \cdot \left(\frac{n\mathrm{F}\Delta E}{\mathrm{R}T}\right) \qquad \textbf{Eqn. A3.10}$$

The left hand side of this equation is $\frac{(i_L i_2 - i_2 i_1) - (i_L i_1 - i_2 i_1)}{i_2 i_1}$ which cancels to give:

$$\left(\frac{i_L(i_2 - i_1)}{i_2 i_1}\right) = e\left(\frac{n\mathrm{F}(P)}{\mathrm{R}T}\right) \cdot \left(\frac{n\mathrm{F}\Delta E}{\mathrm{R}T}\right) \qquad \textbf{Eqn. A3.11}$$

Let $i_2 - i_1 = -\Delta i$ (with the minus sign allowing for reduction) therefore

$$\left(-\frac{i_L(\Delta i)}{i_2 i_1}\right) = e\left(\frac{n\mathrm{F}(P)}{\mathrm{R}T}\right) \cdot \left(\frac{n\mathrm{F}\Delta E}{\mathrm{R}T}\right) \qquad \textbf{Eqn. A3.12}$$

Since $\frac{\Delta E}{\Delta i} = Z$, the impedance, then

$$Z = -\frac{\mathrm{R}T i_L}{n\mathrm{F} i_2 i_1} e\left(-\frac{n\mathrm{F}P}{\mathrm{R}T}\right) \qquad \textbf{Eqn. A3.13}$$

When

$$i = i_L\left(\frac{1}{e\left(\frac{E - E_{1/2} n\mathrm{F}}{\mathrm{R}T}\right) + 1}\right) \qquad \textbf{Eqn. A3.14}$$

and

$$i_2 i_1 = {i_L}^2 \left(\frac{1}{e\left(\frac{Pn\mathrm{F}}{\mathrm{R}T}\right) + 1}\right)\left(\frac{1}{e\left(\frac{(P + \Delta E) n\mathrm{F}}{\mathrm{R}T}\right)}\right) \approx {i_L}^2 \left(\frac{1}{e\left(\frac{Pn\mathrm{F}}{\mathrm{R}T}\right) + 1}\right)^2 \qquad \textbf{Eqn. A3.15}$$

This makes

$$Z = -\frac{\mathrm{R}T}{n\mathrm{F}i_L} e\left(-\frac{n\mathrm{F}P}{\mathrm{R}T}\right)\left(e\left(\frac{n\mathrm{F}P}{\mathrm{R}T+1}\right)\right)^2 \qquad \textbf{Eqn. A3.16}$$

It should be noted that the negative value before $\frac{\mathrm{R}T}{n\mathrm{F}i_L}$ is to make the value positive as i_L is negative. Thus re-arrangement gives

$$Z = -\frac{\mathrm{R}T}{n\mathrm{F}i_L}\left(e\left(\frac{n\mathrm{F}P}{\mathrm{R}T+1}\right)\right)\left(1+e\left(-\frac{n\mathrm{F}P}{\mathrm{R}T}\right)\right) \qquad \textbf{Eqn. A3.17}$$

Considering the impedance associated with the non-linear resistance, $Z_{R_{NL}}$, the expression is

$$Z_{R_{NL}} = -\frac{\mathrm{R}T}{n\mathrm{F}i_L}\left(2+e\left(\frac{n\mathrm{F}P}{\mathrm{R}T}\right)\right)+\left(e\left(-\frac{n\mathrm{F}P}{\mathrm{R}T}\right)\right) \qquad \textbf{Eqn. A3.18}$$

In general for an oxidation or reduction reaction the expression is

$$Z_{R_{NL}} = \frac{\mathrm{R}T}{n\mathrm{F}|i_L|}\left(2+e\left(\frac{n\mathrm{F}P}{\mathrm{R}T}\right)\right)+\left(e\left(-\frac{n\mathrm{F}P}{\mathrm{R}T}\right)\right) \qquad \textbf{Eqn. A3.19}$$

This expression will produces a bowl centred on $P = 0$ (essentially $E_{dc} = E_{1/2}$)

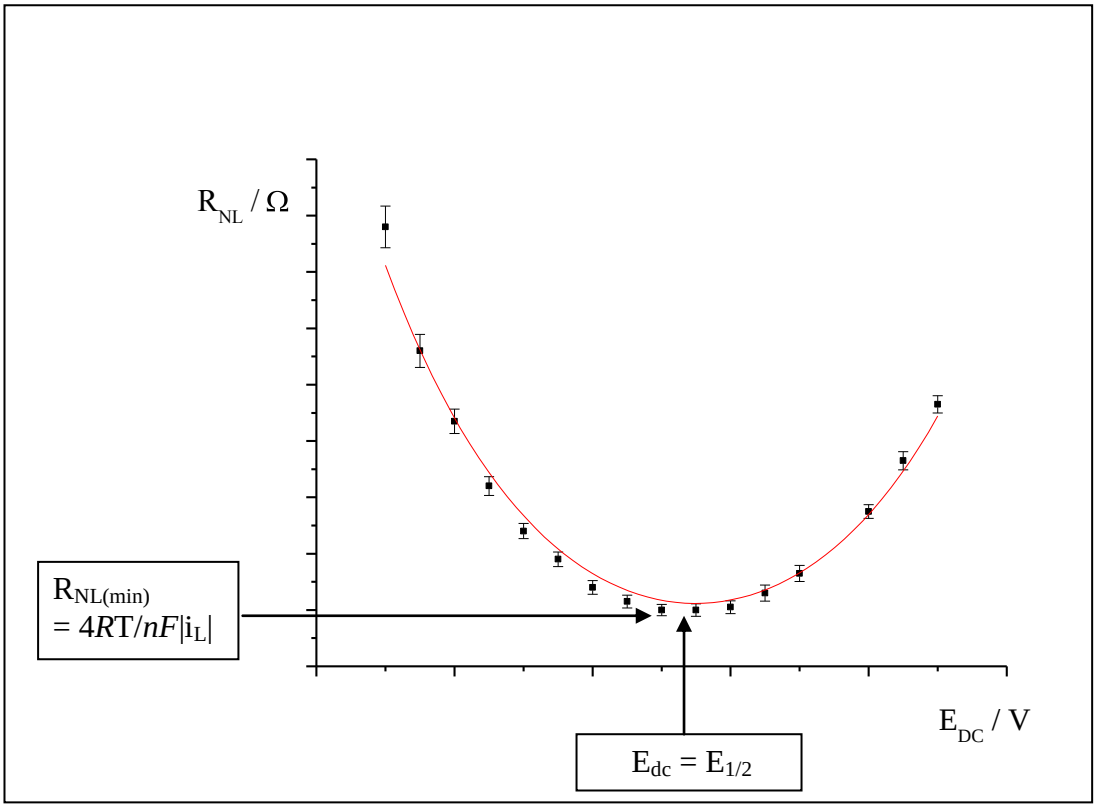

Figure A3.1: Plot of R_{NL} vs E, for a typical microelectrode, to show that the above derivation essentially becomes a parabolic curve, where the value of R_{NL}^{min} at $E_{1/2}$ can be used to calculate the limiting current, i_L.

This shows then that the limiting current can be calculated by the minimum non-linear resistance using the equation:

$$i_{L=} = \frac{4\mathbf{R}T}{n\mathbf{F}R_{NL}} \qquad \textbf{Eqn. A3.20}$$

A.4 Reference

(1) Bard, A. J.; Faulkner, L. R. *Electrochemical Methods, Fundamentals and Aplications*; Second ed.; John Wiley and Sons, Inc.: Hoboken, 2001.

A.5. Published paper

PAPER www.rsc.org/analyst | Analyst

The development and characterisation of square microfabricated electrode systems

Helena L. Woodvine,[a] Jonathan G. Terry,[b] Anthony J. Walton[b] and Andrew R. Mount*[a]

Received 27th November 2009, Accepted 26th January 2010
First published as an Advance Article on the web 16th February 2010
DOI: 10.1039/b924342a

This paper outlines the systematic production and characterisation of biocompatible square microfabricated electrode systems for electroanalysis. In contrast to previous results, a combination of simulation, theoretical analysis and measurement has established that there is an enhanced current density for a microsquare electrode under mass transport limiting current conditions when compared to a microdisc of equivalent size. This is not simply due to a difference in the effective areas of the electrodes as the difference is frequency (diffusion layer thickness) dependent; it can instead be attributed to the effects of enhanced diffusion at the corners of the microsquares on the growing diffusion layer.

Introduction

Microelectrodes, with at least one dimension on the micron length scale, have well-established analytical advantages over macroelectrodes.[1–3] Their enhanced hemispherical diffusion mass transport leads to the rapid establishment of steady state currents without external convection. They also have reduced iR drop, increased Faradaic current densities and therefore higher signal-to-noise ratios that vastly increase their detection sensitivity. They are therefore systems of considerable interest when developing electroanalytical methods. However, to achieve reproducible enhancement, there is a need to employ fabrication techniques and develop processes that give microelectrodes of specific size and shape, with optimised response. Photolithographic techniques (long established in semiconductor microfabrication) have made possible the fabrication of microelectrodes with controlled dimensions.[4,5] Recently, Berduque *et al.*[6] have used this approach to fabricate and characterise microsquare and microdisc electrodes. Their conclusion is consistent with a previous approximation[7] that a microsquare electrode has an equivalent mass transport limited current to a microdisc when its side length is equal to the disc's diameter. This is in contrast to Morita *et al.*,[5] who suggest an equivalent response from microdisc and microsquare electrodes of the same area. The resolution of whether a microsquare response can be readily related to that of a microdisc is important because microdisc electrodes have been well characterised, and their time dependent and steady-state responses solved analytically,[2,8,9] whereas microsquare electrodes are easier to fabricate accurately on the micron scale with standard pixellated photomasks. Through a combination of simulation and experiment, we address this issue and show that microsquare electrodes give a systematically higher limiting current density and different electrochemical impedance responses as a function of frequency to microdiscs of either relative dimension. This establishes the need for further fundamental microsquare characterisation. In addition, the fabrication of microsquare electrodes has been achieved using biocompatible materials, which should enable their use in biosensing and biodetection applications.[10]

[a]*School of Chemistry, The University of Edinburgh, Joseph Black Building, King's Buildings, West Mains Road, Edinburgh, EH9 3JJ, UK. E-mail: A.Mount@ed.ac.uk; Fax: +44 (0)131 6506453; Tel: +44 (0)131 6504747*
[b]*Institute for Integrated Systems, School of Engineering, The University of Edinburgh, Scottish Microelectronics Centre, King's Buildings, West Mains Road, Edinburgh, EH9 3JF, UK*

Experimental

Electrode fabrication

Square platinum electrodes of edge dimension 50 μm were fabricated on 3-inch ⟨100⟩ n-type silicon wafers (IDB Technologies) on which surface silicon dioxide insulation (500 nm) was grown using wet oxidation (1100 °C for 35 minutes in an O_2/H_2 atmosphere). Patterned electrodes were then fabricated using a lift-off process (Fig. 1).

A 450 nm layer of lift-off resist (LOR-5B, Microchem, Chestech) was spin deposited onto the wafer and baked for five minutes at 190 °C, to fix the undercut rate (Fig. 1a). This was followed by spin deposition of a 1 μm layer of positive photoresist (Megaposit SPR350, Microchem, Chestech), which was pre-baked for 60 seconds at 90 °C (Fig. 1b). Following flood exposure of the resist through the metallisation mask plate (Fig. 1c), the resist was developed (Microposit MF319 Developer, Microchem, Chestech) to give the required microelectrode pattern, complete with an undercut, to facilitate the lift-off process (Fig. 1d). The electrode film consisted of a 200 nm layer of sputter deposited platinum on a 5 nm sputter deposited chrome adhesion layer (Fig. 1e). The undercut ensures a discontinuous metal film, which enabled successful lift-off of the excess material during stripping using a resist remover (Microposit Remover 1165, Microchem, Chestech) (Fig. 1f). For biocompatible insulation of all but the electrode areas for solution study and contact pads for external connection, a 1 μm layer of Parylene was deposited. Parylene C dimer (741–767 mg) (FW 277.19, SCS Coatings Cas: 28804-46-8) was vaporised under vacuum and pyrolised in a room temperature deposition chamber to deposit the monomer gas as a transparent,

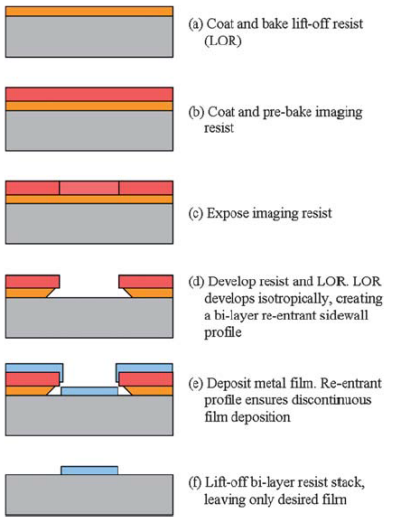

Fig. 1 Schematic diagram of the platinum array patterning process.

insulating polymer film. Patterning of the Parylene using standard photolithography, followed by reactive ion etching in oxygen plasma, was used to open up the defined electrode and contact pad areas. Fig. 2 shows a schematic of these 8 microsquare electrode devices, along with a photograph of an individual Pt microsquare produced by this technique. It should be noted that the deposited Pt microsquare was of 60 μm edge dimension, whilst the exposed hole in the Parylene area had a 50 μm edge dimension. The thickness of the recess defined by the Parylene layer is 2% of the edge dimension; it has been established for microdiscs that the response of these electrodes can be considered as essentially equivalent to planar electrodes, thereby simplifying simulation.[11]

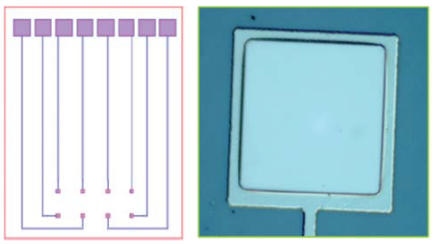

Fig. 2 Schematic diagram of the layout of an 8 platinum electrode chip (29 × 21.5 mm) with connection pads (top) wires and electrodes (bottom), alongside a photograph of a typical electrode produced by the described process.

Electrochemistry

Electrochemical studies were carried out in a Faraday cage using a PC controlled Autolab PGSTAT30 potentiostat with frequency response analyser module (Windsor Scientific). PC analysis used Autolab General Purpose Electrochemical software (GPES, version 4.9) and Frequency Response Analysis software (FRA, version 4.9) for voltammetry and electrochemical impedance spectroscopy (EIS) respectively. The microsquare was employed as working electrode, with a saturated calomel reference electrode (SCE) and platinum gauze counter electrode. All aqueous solutions were prepared with deionised water (Millipore MilliQ). Electrochemical experiments were performed using background electrolyte solutions of aqueous potassium chloride (Fisher Scientific, lab reagent grade, >99% purity, 0.1 M), with redox experiments using potassium ferricyanide, $K_3[Fe(CN)_6]$ (Fisons, SLR reagent grade, >99% purity, 10 mM) in background electrolyte. All solutions were thoroughly degassed using pure shield argon (BOC) for at least 20 minutes prior to experimentation and a blanket of argon was blown over the surface of the solutions during collection of data to preclude oxygen contamination.

Optical images

Microelectrodes were visually inspected using a Reichert Jung Polyvar-MET optical microscope (Leica). Images were captured using a DFC-300 camera and rendered using IM50 Image Manager Software (Leica).

Finite element method (FEM) simulation of ferricyanide reduction

Three dimensional FEM steady-state electrochemical diffusion simulations of ferricyanide reduction were carried out using COMSOL Multiphysics version 3.2b for Linux (COMSOL, Inc., Burlington, MA), run remotely from a Dell Pentium 4 PC using the Xfce 4 Desktop Environment interface (Xfce 4.4.2, Oliver Fourden©). One quarter of the 50 μm edge dimension square electrode and of the microdisc electrode were simulated in the space domain, utilising the symmetry associated with square and disc (Fig. 3).

These simulations assumed transport solely by diffusion, consistent with stagnant solution measurements; in 3-D, the transport equation for ferricyanide diffusion in the cube is:

$$\nabla(-D\nabla c) = 0 \quad (1)$$

where c is the concentration (set throughout to an initial value of 10 mM) and D is the isotropic diffusion coefficient, set as 6.98×10^{-10} m^2 s^{-1} for ferricyanide in 0.1 M KCl electrolyte.[12] Previous experiments and 2D simulations on microdisc array electrodes have established negligible interaction between neighbouring array elements at steady-state when electrodes are separated by more than 24 times the disc radius.[11,13] This suggests the steady-state diffusion layer for each microdisc extends to the order of 12 times the radius. In fact, as the diffusion layer actually increases with time, even when there are steady-state currents,[14,15] this establishes that a steady-state current is first found when the diffusion layer has reached this distance, and accurate

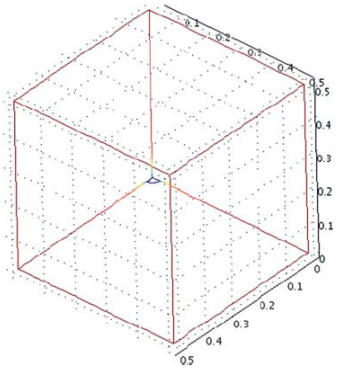

Fig. 3 The three dimensional model produced to simulate diffusion towards the activated electrode surface of a microdisc or a microsquare. The large 3D cube represents the simulation space and the small feature in the back corner of the bottom face (the origin of the x,y-plane) represents a quarter of the active microsquare or microdisc electrode. Dimensions shown are in millimetres.

steady-state calculations can be performed using a simulation space of this dimension and above. To avoid boundary effects due to concentration depletion at the edges of the space domain, a cube of 500 μm edge dimension (20 times the electrode radius) was used for simulation, with the electrode microdisc located as a quarter circle in the x,y-plane at $z = 0$ and the disc centre at $x = 0$, $y = 0$. Microsquare electrode simulation was carried out using a cube of the same dimension, with the quarter square of electrode of edge length 25 μm again located in the x,y-plane at $z = 0$, with full square centre at $x = 0$, $y = 0$ (Fig. 3). Conservation of symmetrical boundary conditions was applied to the $x = 0$ and $y = 0$ planes, with the ferricyanide concentration set to 0 on the electrode surface (to ensure the calculation of the mass transport limiting current) and the ferricyanide flux set to zero across the rest of the $z = 0$ plane, consistent with a Parylene insulated surface. At all other cube boundaries the concentration of ferricyanide was fixed at the bulk value of 10 mM. COMSOL readily enables the integrated flux across the electrode area, J, to be evaluated from the double integral of the local concentration gradients across the electrode surface:[16]

$$J = D\int_0^{l/2}\int_0^{l/2}\left.\frac{\mathrm{d}c}{\mathrm{d}z}\right|_{z=0}\mathrm{d}y\mathrm{d}x \qquad (2)$$

where l is the length of the square edge or disc diameter for microsquare or microdisc as appropriate. This can readily be converted to the limiting current at the electrode through:

$$i_\mathrm{L} = 4nFJ \qquad (3)$$

where n, the number of electrons transferred, is unity for ferri/ferrocyanide and F is Faraday's constant.

Following a similar approach to Strutwolf, who computed the response of rectangular microelectrodes,[16] dynamic adaptive mesh refinement (DAMR) was used to refine the current densities calculated from these simulations. In DAMR, the domain of interest is split into a grid of many individual elements, which is refined after each computation to increase grid detail, ensuring that the grid is densest at the electrode edges to accurately model the greatest rate of change of concentration gradients. The 'meshinit' option in COMSOL was selected to prevent physically unrealistic mesh overlap and five refinements were carried out for each computational step.

Results and discussion

Microsquare electrode fidelity

Fig. 4 shows a typical microsquare experimental cyclic voltammogram (CV) for ferricyanide reduction. As previously seen for microdiscs[17] and microsquares,[6] a sigmoidal wave is observed. This does not vary with sweep rate at these relatively low sweep rates, characteristic of a steady-state voltammetric response. Also, as with microdiscs, the mass-transfer corrected Tafel plot (Fig. 5) shows good straight lines for both the forward and the reverse scans of the CV, with gradients of 40 and 38 V^{-1} respectively. These are both in good agreement with the expected

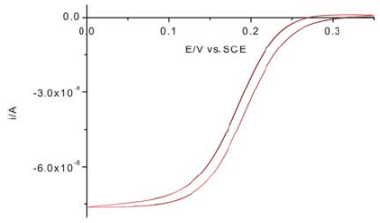

Fig. 4 Typical cyclic voltammogram obtained at a sweep rate of 5 $\mathrm{mV\ s^{-1}}$ from a microsquare platinum electrode (edge of 50 μm) in ferricyanide (10 mM) and KCl (0.1 M) background electrolyte. The potential was swept from +0.35 V to 0.00 V and then reversed.

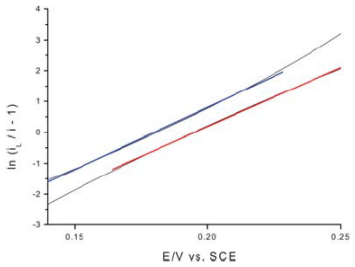

Fig. 5 Plot showing the corresponding modified Tafel plots generated from Fig. 4. The linear fits to the reducing (blue) and oxidising (red) data are shown. These give gradients of 40 and 38 V^{-1} respectively, in good agreement with the theoretical value of 40 V^{-1} for a fully reversible one electron reaction at 293 K.

value of $F/RT = 40\ V^{-1}$ at 293 K for a reversible one electron redox reaction, indicating the fabrication of clean platinum microelectrodes.

FEM simulation of microdisc and microsquare limiting currents

Fig. 6a shows the adapted microdisc mesh at the most dense refinement, typically produced after seven or eight computational steps, and Fig. 6b, the corresponding adapted mesh for a microsquare. The markedly increased mesh density at the electrode edge can clearly be seen in each case, and is consistent with the expectation of steep concentration gradients, large changes in these gradients and a large contribution of the edge current density to the overall limiting current. The largest microsquare mesh density is observed at the square corners, consistent with the largest current density. This is the most important difference between microdisc and microsquare, as these corners can be considered to introduce a nanoelectrode component, giving enhanced mass transport over microdisc and microsquare edge.

Fig. 7a and b show the corresponding calculated steady-state diffusive flux profiles for square and disc electrodes respectively. It is clear from these data that in each case the diffusion layers for the electrodes are similar and essentially hemispherical and do not extend to the box edge, confirming that the space domain is sufficiently large to ensure accurate simulation.

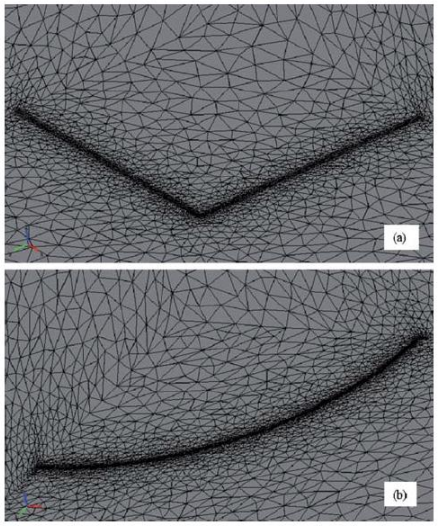

Fig. 6 The finite element mesh generated for (a) a quarter microsquare electrode simulation at a mesh density corresponding to 461 779 degrees of freedom (dof) shown with a vertical electrode x,y-plane orientation and (b) a quarter microdisc electrode simulation at a mesh density corresponding to 512 576 dof shown with a horizontal electrode x,y-plane orientation.

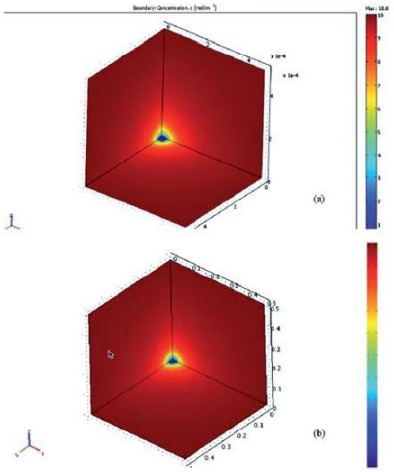

Fig. 7 Typical steady-state concentration profiles for (a) microsquare and (b) microdisc electrodes. The concentration of ferricyanide is shown in roygb format, with red corresponding to 10 mM (bulk) concentration and blue to 0 mM. The increasing depletion of ferricyanide can be clearly observed upon approaching the electrode surface.

Microelectrode response

Microdisc simulation. The well established analytical expression for the limiting current of a microdisc electrode[2,8,9] is:

$$i_L = 4nFDcr \qquad (4)$$

where r is the radius of the disc. The red circles in Fig. 8 show the limiting currents calculated for the microdisc ($r = 25.0$ μm) for successive computational steps with increasing number of mesh points. It is highly satisfying that these values asymptotically approach the established analytical value calculated from eqn (4), the red line in Fig. 8, which supports the accuracy of this method for calculations on electrodes of this dimension.

Microsquare measurement and simulation. The mass transport limiting current has been measured for ferricyanide reduction at 7 microsquare electrodes (at the most negative potentials in Fig. 3), with the mean values and standard deviation of these measurements shown as a blue line and bar respectively in Fig. 8. These data are seen to correspond well to the simulated value obtained for microsquares at higher degrees of freedom, which again confirms the accuracy of the COMSOL simulation in determining the limiting currents.

Previous analysis of the response of microsquare electrodes has used eqn (4), with $r = l/2$, where l is the edge length of the microsquare.[6] This is the red line in Fig. 8, which is systematically below both experimental and calculated values. An alternative that has also been postulated is again to use eqn (4), but rather to assume that the microsquare behaves like a microdisc of

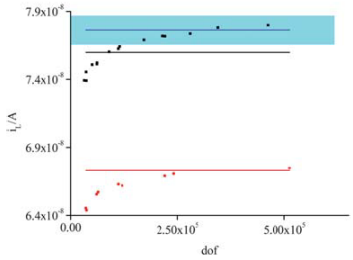

Fig. 8 Plot of COMSOL calculated limiting currents for simulated microdisc (r = 25.0 μm, red spots) and microsquare (l = 50.0 μm, black squares) at increasing degrees of freedom (dof). Also shown is the theoretical limiting microdisc current obtained from eqn (4) (red line). This is also the theoretical limiting current calculated for the microsquare from eqn (4) when using $r = l/2$,[6] whilst that using $r = l/\pi^{1/2}$ ref. 5 is shown as a black line. The blue line shows the average experimental current obtained for 7 microsquares, along with the standard deviation for these measurements (shaded blue box). These data are seen to be most consistent with the value obtained from microsquare simulation at high mesh density, rather than either theoretical microdisc value.

equivalent area,[5] with $r = (l/\sqrt{\pi})$. This value is the black line in Fig. 8, which is also below both mean experimental and calculated microsquare limiting current values. A recent paper by Amatore *et al.*[18] has demonstrated the influence of natural convection in increasing the observed current on the response of a large (250 μm radius) disc, in contrast to the insensitivity of the observed current to the effects of natural convection for a 12.5 μm radius microdisc. The close correspondence of simulated and experimental data for these microsquares indicates that as for this microdisc, which is comparable in dimension, the limiting current is controlled by diffusion, and that the effects of natural convection can be assumed to be negligible at this dimension.

Electrochemical impedance spectroscopy (EIS)

The question remains as to whether this deviation of microsquare limiting current response from microdisc analytical value is simply due to a difference in effective microelectrode area, as the previous treatments have assumed, or whether there is a fundamental difference between microsquare and microdisc electrode response, and the evolution of their diffusion layers with time (and hence diffusion layer thickness). EIS is a valuable method for probing this, as it measures electrode response as a function of frequency, which is inversely related to time and diffusion layer thickness. It is generally accepted that the EIS response of microdiscs can be closely approximated to the modified Randles circuit, shown in Fig. 9.[17,19,20]

Fig. 10 shows a typical impedance plot obtained from a platinum microsquare in aqueous ferricyanide solution, along with the corresponding fits to the Randles circuit of Fig. 9. It is reassuring that the charge transfer semicircle is extremely small on this scale, consistent with reversible electron transfer across the vast majority of the electrode surface, and the EIS response is

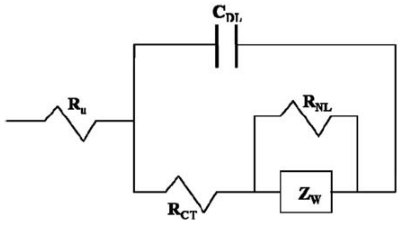

Fig. 9 Schematic representation of the modified Randles circuit, frequently used to model the EIS response of microdisc electrodes; R_u is the uncompensated (electrolyte) resistance, C_{DL} models the charging of the double layer, R_{CT} is the charge transfer resistance, Z_W is the Warburg impedance and R_{NL} models the non-linear resistance which corresponds to steady-state diffusion.

therefore dominated by the Warburg impedance, non linear resistance and double layer capacitance.

From fitting data at high and low frequencies, the values of the charge transfer (R_{CT}) and non-linear (R_{NL}) resistances can be obtained respectively. The variations of these values as a function of E_{dc} are shown in Fig. 11 and 12. Consistent with clean microsquare electrodes and the reversible nature of the one electron ferri/ferrocyanide couple, both sets of data fit best to the theoretical expression for charge transfer under thermodynamic control (eqn (5)) rather than kinetic control (eqn (6), for derivation see Appendix).

$$R_X = \frac{R_X^{min}}{4}\left[2 + \exp\left(\frac{F(E_{dc} - E^0)}{RT}\right) + \exp\left(\frac{F(E_{dc} - E^0)}{RT}\right)\right] \quad (5)$$

$$R_X = \frac{R_X^{min}}{2}\left(\exp\left(\frac{-\alpha_{ox}F(E_{dc} - E^0)}{RT}\right) + \left(\frac{(1-\alpha_{ox})F(E_{dc} - E^0)}{RT}\right)\right) \quad (6)$$

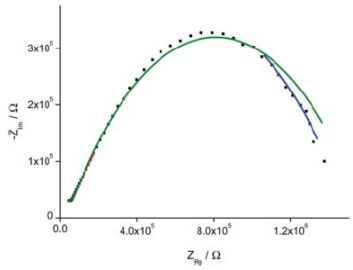

Fig. 10 A typical Nyquist plot for the EIS platinum microsquare response (l = 50.0 μm) in aqueous ferricyanide background electrolyte solution. The spectrum was measured at a dc potential, E_{dc} = +0.19 V, ac amplitude 10 mV rms and frequency range 1000 Hz (low Z_{Re}) to 0.01 Hz (high Z_{Re}). Fits using the modified Randles circuit (Fig. 9) are shown to the high frequency data (red line), the low frequency data (blue line) and all data (green line).

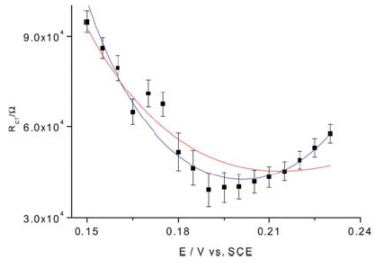

Fig. 11 Plot of the charge transfer resistances, R_{CT}, obtained from EIS fits at high frequency plotted against dc potential, E_{dc}. The curves are the best fits to the kinetic expression (eqn (6), red line) and the thermodynamic expression (eqn (5), blue line).

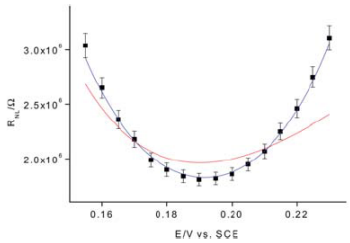

Fig. 12 Plot of the non-linear resistance, R_{NL}, obtained from EIS fits at low frequency plotted against dc potential, E_{dc}. The curves are best fits to the kinetic expression (eqn (6), red line) and the thermodynamic expression (eqn (5), blue line).

where X is CT or NL as appropriate, E^{θ} is the standard electrode potential, R and T are the gas constant and temperature respectively and α_{ox} is the transfer coefficient for oxidation, where $1 \geq \alpha_{ox} \geq 0$. From these data, values of R_{CT}^{min} and E^{θ} were obtained of 41 000 Ω and +0.195 V respectively.

Since in the reversible case, at high frequencies:

$$R_{CT}^{min} = \frac{4RTL}{ADF^2c} \quad (7)$$

one can obtain an estimate for L of around 650 nm. This is the thickness of the solution at the electrode surface where rapid thermodynamically controlled charge transfer occurs and Nernstian equilibrium is established (see Appendix). Given that at these high frequencies this layer thickness is small compared to the electrode dimensions, planar diffusion will be occurring, and A should simply be the area of the microsquare electrode. The good agreement with eqn (5) for the variation of R_{NL} (found at low frequency) with E_{dc} is satisfying and entirely consistent with the observation of reversible modified Tafel behaviour (Fig. 4), confirming that microsquare electrodes can be used to determine Tafel characteristics. However, the inability to fit EIS data accurately with this equivalent circuit across the whole frequency range for any E_{dc} is telling. It is clear that, if differences between the EIS microsquare electrode response and the microdisc response were simply due to differences in real or effective area, this circuit would fit these data at all frequencies and the systematic deviation seen at medium to low frequencies would not be found. Thus the evolution of the electrode response with time (or frequency) for a microsquare can be seen to be different to a microdisc.

In particular, the decrease in the value of the experimental resistance as the frequency tends to zero (obtained from the intercept of the blue line in Fig. 10 with the Z_{Re} axis) compared with that obtained from the fits to microdisc theory across all frequencies (obtained from the low frequency intercept of green line in Fig. 10 with the Z_{re} axis) is indicative of a greater steady-state current for a microsquare over a microdisc of equivalent area. This confirms the experimental observations in Fig. 8, again demonstrating a greater efficiency of diffusional transport across the diffusion layer at steady-state for a microsquare compared with a microdisc of equivalent area.

Conclusions

This study has demonstrated good agreement between FEM simulation and experiment, with both indicating that microsquare electrodes have increased mass transport limiting currents at steady-state compared with discs of comparable dimension, and hence that they have different limiting currents to those previously postulated theoretically. This is important to establish, given the potential prevalence of their use due to their relative ease of construction using pixellated photomasks. EIS experiments show that these differences are not simply due to a difference in actual or effective area, but that there is a distinct difference in the response of microdiscs and microsquares as a function of frequency, which indicates a difference in the evolution of the diffusion layer with time. This can be seen from simulation to be due to the effects of enhanced diffusion at microsquare corners, where the concentration gradients generated are seen to be at their largest. It is here that the current densities are therefore greatest and the diffusion layer is expected to increase most rapidly with time, faster than at the edge of a microdisc or long edge of a microsquare. Indeed, corner (and perhaps edge) diffusion may be sufficiently fast that the electron transfer rate for ferricyanide reduction may become rate limiting, even when diffusion control and reversible electron transfer are observed across most of the microsquare. As for the microdisc,[18] this could explain the slight separation of forward and reverse CV scans seen in Fig. 4.

These effects (and the initial symmetry) will preclude the exactly hemispherical and symmetrical growth in diffusion layer seen for microdiscs, and is likely to be at the heart of the observed differences in EIS response. This will also affect the response of arrays of microsquare electrodes compared to microdisc arrays, for which optimum electrode separation for electroanalytical detection has been established.[11] Therefore, we are currently developing the theoretical analysis of microsquare and microsquare array response.

Appendix

We have previously shown[21–24] for uniformly accessible electrodes that transmission line theory can be used to model the EIS

response of both modified electrodes and redox ions in solution at macroelectrodes. This theory produces a resistive rail, R_e, which models the transport of electrons in solution (in this case the transport of $Fe(CN_6)^{3-}$ and $Fe(CN_6)^{4-}$ through diffusion and electron exchange) and another resistive rail, R_X, which models the transport of electrolyte ions, coupled by a distributed capacitance, C, which ensures electroneutrality is maintained and generates the appropriate driving forces for charge movement (Fig. 13).

We have also demonstrated[24] that this reduces to the Randles equivalent circuit in the presence of an electrode double layer capacitance, C_{DL}, and electrode surface charge transfer resistance, R_{CT}, when $R_X \ll R_e$. This is the case in these experiments, as there is a high concentration of relatively mobile background electrolyte. In this case, $R_X \equiv R_u$ and the transmission line generates Z_W and R_{CT} in parallel with C_{DL}, giving the Randles circuit. We have previously[24] also treated the case when there is a kinetic limitation to charge injection into the R_e rail (in our case $Fe(CN_6)^{3-}/Fe(CN_6)^{4-}$ redox reaction at the electrode). For the general redox reaction:

$$A^+ + e^- \underset{k_{-1}}{\overset{k_1}{\rightleftharpoons}} B \tag{A1}$$

R_{CT} at the electrode surface is then given by:

$$R_{CT} = \frac{RT}{AF^2c}\left(\frac{1}{k_1} + \frac{1}{k_{-1}}\right) \tag{A2}$$

where c is the total concentration of redox active species (A and B) in solution. Since the electrochemical rate constants k_1 and k_{-1} are:

$$k_1 = k^\theta \exp\left(+\frac{\alpha_{ox}F(E - E^\theta)}{RT}\right) \tag{A3}$$

and

$$k_{-1} = k^\theta \exp\left(-\frac{(1-\alpha_{ox})F(E - E^\theta)}{RT}\right) \tag{A4}$$

by substitution

$$R_{CT} = \frac{RT}{k^\theta AF^2c}\left(\exp\left(\frac{-\alpha_{ox}F(E_{dc} - E^\theta)}{RT}\right) + \exp\left(\frac{(1-\alpha_{ox})F(E_{dc} - E^\theta)}{RT}\right)\right) \tag{A5}$$

When $E_{dc} = E^\theta$, $k_1 = k_{-1} = k^\theta$ and the minimum value of charge transfer resistance is given by:

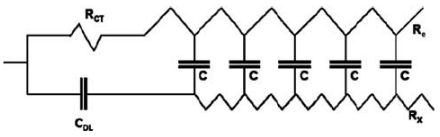

Fig. 13 Schematic diagram to represent the general transmission line which gives rise to the Randles equivalent circuit and the kinetic and thermodynamic fitting expressions.

$$R_{CT,K}^{min} = \frac{RT}{AF^2c}\left(\frac{2}{k^\theta}\right) \tag{A6}$$

substituting eqn (A6) into eqn (A5) then gives eqn (6).

If there is no kinetic limitation, C_{DL} will instead shunt the first part of the R_e rail at high frequency. This corresponds to a charge transfer resistance, R_{CT}, controlled by thermodynamics, with charge transfer being so rapid that in a thin layer of solution, L, at the electrode surface the Nernstian relationship between the concentrations of ferri/ferrocyanide and the applied potential applies even at these high frequencies. The mean concentrations of ferricyanide (b) and ferrocyanide (a) in this region are then given by:

$$E_{dc} = E^\theta + \frac{RT}{F}\ln\frac{\bar{b}}{\bar{a}} \tag{A7}$$

where $\bar{b} + \bar{a} = c$. This gives:

$$\frac{\bar{a}}{c} = \left(\frac{\exp\left(-\frac{(E_{dc} - E^\theta)F}{RT}\right)}{1 + \exp\left(-\frac{(E_{dc} - E^\theta)F}{RT}\right)}\right) \tag{A8}$$

and

$$\frac{\bar{b}}{c} = \left(\frac{\exp\left(\frac{(E_{dc} - E^\theta)F}{RT}\right)}{1 + \exp\left(\frac{(E_{dc} - E^\theta)F}{RT}\right)}\right) \tag{A9}$$

In this case R_{CT} is given by the established value for R_e[24] for a layer of thickness, L:

$$R_{CT} = \frac{RTL}{ADF^2}\left(\frac{c}{\bar{a}\bar{b}}\right) \tag{A10}$$

and by substitution with eqn (A9) and (A10)

$$R_{CT} = \frac{RTL}{ADF^2c}\left[2 + \exp\left(\frac{(E_{dc} - E^\theta)F}{RT}\right) + \exp\left(\frac{-(E_{dc} - E^\theta)F}{RT}\right)\right] \tag{A11}$$

at $E_{dc} = E^\theta$, R_{CT} is at its minimum value, equal to eqn (7). Substitution of eqn (7) into eqn (A11) then gives eqn (5). It has been established[19] that at the high frequencies where the resistive response is determined by R_{CT}, these equations should also apply to microdiscs.

The modified Randles circuit applied to a microdisc has an additional circuit element, R_{NL}, added to the Randles circuit to account for the effects at lower frequency of hemispherical diffusion and the lack of uniform accessibility characteristic of these micron scale disc electrodes; this enables the onset of a steady-state current at dc. We argue for a microelectrode of a given dimension that the potential dependence of charge transport in this resistive circuit element is driven by the same processes as in R_e in the macroelectrode. This means the same potential dependency of R_{NL} on E_{dc} as R_e is expected for both macro and microelectrodes of a given size, and those similar equations to eqn (5) and (6) will also apply to R_{NL}, with R_{NL} simply replacing R_{CT}. A constant value of R_{NL}^{min} will then be observed for microelectrodes of the same dimension, and

changes in R_{NL} as a function of electrode dimension will be reflected in changes in R_{NL}^{min}.

Acknowledgements

The authors thank Charlotte Brady and Dr Andrew Sherlock for their assistance with some cyclic voltammetry experiments and simulations respectively. The School of Chemistry at Edinburgh is part of the EaStCHEM joint chemistry research school with St Andrews. The Institute for Integrated Systems is part of the Edinburgh Research Partnership in Engineering and Mathematics (ERPem) with Heriot-Watt. Support from the Scottish Funding Council is acknowledged for the ERPem and EaStCHEM initiatives. HLW thanks EPSRC and the School of Chemistry at Edinburgh for financial support for her studentship.

References

1 R. J. Forster, *Chem. Soc. Rev.*, 1994, **23**, 289–297.
2 J. Heinze, *Angew. Chem., Int. Ed. Engl.*, 1993, **32**, 1268–1288.
3 K. Stulik, C. Amatore, K. Holub, V. Marecek and W. Kutner, *Pure Appl. Chem.*, 2000, **72**(8), 1483–1492.
4 J. A. Alden, J. Booth, R. G. Compton, R. A. W. Dryfe and G. H. W. Sanders, *J. Electroanal. Chem.*, 1995, **389**, 45–54.
5 M. Morita, M. L. Longmire and R. W. Murray, *Anal. Chem.*, 1988, **60**, 2770–2775.
6 A. Berduque, Y. H. Lanyon, V. Beni, G. Herzog, Y. E. Watson, K. Rodgers, F. Stam, J. Alderman and D. W. M. Arrigan, *Talanta*, 2007, **71**(3), 1022–1030.
7 S. L. Caston and R. McCarley, *J. Electroanal. Chem.*, 2002, **529**, 124–134.
8 D. Britz, K. Poulsen and J. Strutwolf, *Electrochim. Acta*, 2004, **50**(1), 107–113.
9 K. B. Oldham, *Electrochem. Commun.*, 2004, **6**(2), 210–214.
10 G. Schmitt, J. W. Schultze, F. Fassbender, G. Buss, H. Luth and M. J. Schoning, *Electrochim. Acta*, 1999, **44**(21–22), 3865–3883.
11 J. Guo and E. Lindner, *Anal. Chem.*, 2009, **81**(1), 130–138.
12 O. Koster, W. Schuhmann, H. Vogt and W. Mokwa, *Sens. Actuators, B*, 2001, **76**, 573–581.
13 T. J. Davies and R. G. Compton, *J. Electroanal. Chem.*, 2005, **502**, 177–187.
14 C. J. Amatore, M. Savéant and D. Tessier, *J. Electroanal. Chem.*, 1983, **147**, 39–51.
15 C. J. Amatore and B. Fosset, *Anal. Chem.*, 1996, **68**, 4377–4388.
16 J. Strutwolf, *Electroanalysis (N. Y.)*, 2005, **17**(2), 1547–1554.
17 P. Los, G. Zabinska, A. Kisza, L. Christie, A. Mount and P. G. Bruce, *Phys. Chem. Chem. Phys.*, 2002, **2**, 5449–5454.
18 C. Amatore, C. Pebay, L. Thouin and A. Wang, *Electrochem. Commun.*, 2009, **11**, 1269–1272.
19 P. Los and P. G. Bruce, *Pol. J. Chem.*, 1997, **71**(8), 1151–1159; P. Los, G. Zabinska, A. Kiska, L. Christie, A. Mount and P. G. Bruce, *Phys. Chem. Chem. Phys.*, 2000, **2**, 5449–5454.
20 M. Fleischmann, S. Pons and J. Daschbach, *J. Electroanal. Chem.*, 1991, **317**, 1–26.
21 W. J. Albery, Z. C. Benjamin, R. Horrocks, A. R. Mount, P. J. Wilson, D. Bloor, A. T. Monkman and C. M. Elliott, *Faraday Discuss. Chem. Soc.*, 1989, **88**, 247–259.
22 W. J. Albery and A. R. Mount, *J. Chem. Soc., Faraday Trans.*, 1993, **89**(14), 2487–2497.
23 W. J. Albery and A. R. Mount, *J. Chem. Soc., Faraday Trans.*, 1993, **89**(2), 327–331.
24 W. J. Albery and A. R. Mount, in *Electroactive Polymer Electrochemistry,Part 1: Fundamentals*, ed. M. E. G. Lyons, Plenum Press, New York, 1994.

Insert 1

List of Equations

Chapter 1

$$i_c = \frac{\Delta E}{R_U} \exp\left(\frac{-t}{R_U C_{CL}}\right) \quad \textbf{Eqn. 1.1}$$

Chapter 2

$$E = E^{\Theta\prime} + \frac{\mathbf{R}T}{n\mathbf{F}} ln \frac{c_O}{c_R} \quad \textbf{Eqn. 2.1}$$

$$[Fe(CN)_6]^{3-} + e^- \rightleftharpoons [Fe(CN)_6]^{4-} \quad \textbf{Eqn. 2.2}$$

$$A + e^- \underset{k_{ox}}{\overset{k_{red}}{\rightleftharpoons}} B \quad \textbf{Eqn. 2.3}$$

$$E_p^{ox} - E_p^{red} = 2.218 \frac{\mathbf{R}T}{n\mathbf{F}} \quad \textbf{Eqn. 2.4}$$

$$E_{1/2} = \frac{\left(E_p^{ox} - E_p^{red}\right)}{2} \quad \textbf{Eqn. 2.5}$$

$$E^{\Theta} = E_{1/2} + \frac{\mathbf{R}T}{n\mathbf{F}} ln \left(\frac{D_O}{D_R}\right)^{1/2} \quad \textbf{Eqn. 2.6}$$

$$i_p = 0.4663 A\mathbf{F} D^{1/2} v^{1/2} c^{\infty} \left(\frac{\mathbf{F}}{\mathbf{R}T}\right)^{1/2} \quad \textbf{Eqn. 2.7}$$

$$i_t = \frac{nA\mathbf{F}D^{1/2}c^{\infty}}{\pi^{1/2} t^{1/2}} \quad \textbf{Eqn. 2.8}$$

$$i_L = \frac{nA\mathbf{F}Dc^{\infty}}{r} \quad \textbf{Eqn. 2.9}$$

Insert 1

$$i = \frac{nAFD^{1/2}c^{\infty}}{\pi^{1/2}t^{1/2}} + \frac{nAFDc^{\infty}}{r}$$ **Eqn. 2.10**

$$\eta = a + b\log|i|$$ **Eqn. 2.11**

$$a = \frac{+2.3\mathbf{R}T}{\eta\alpha_{red}\mathbf{F}}\log i \quad \text{and} \quad b = \frac{+2.3\mathbf{R}T}{\eta\alpha_{red}\mathbf{F}}$$ **Eqn. 2.12**

$$J = k_{mt}(c^{\infty} - c^{0})$$ **Eqn. 2.13**

$$i = n\mathbf{F}AJ = n\mathbf{F}Ak_{mt}(c^{\infty} - c^{0})$$ **Eqn. 2.14**

$$i_L = n\mathbf{F}Ak_{mt}c^{\infty}$$ **Eqn. 2.15**

$$\left(\frac{i_L}{i} - 1\right) = \frac{n\mathbf{F}Ak_{mt}c^{\infty}}{n\mathbf{F}Ak_{mt}(c^{\infty} - c^{0})}$$ **Eqn. 2.16**

$$\left(\frac{i_L}{i} - 1\right) = \frac{c^{0}}{(c^{\infty} - c^{0})} = \frac{c^{0}}{c^{0}_{prod}}$$ **Eqn. 2.17**

$$E = E^{\theta} + \frac{\mathbf{R}T}{n\mathbf{F}}\ln\frac{c^{0}_{\mathrm{A}}}{c^{0}_{\mathrm{B}}}$$ **Eqn. 2.18**

$$E = E^{\theta} + \frac{\mathbf{R}T}{n\mathbf{F}}\ln\left(\frac{i_L}{i} - 1\right)$$ **Eqn. 2.19**

$$Z = \frac{E_{ac}}{i_{ac}}$$ **Eqn. 2.20**

$$Z(\omega) = Z_{\mathrm{Re}} - jZ_{Im}$$ **Eqn. 2.21**

$$Z_{\mathrm{W}} = \frac{\sigma}{\omega^{1/2}} - j\frac{\sigma}{\omega^{1/2}}$$ **Eqn. 2.22**

$$J_e = D_e\left\{\frac{\delta \mathrm{b}}{\delta \mathrm{z}} + \left[\frac{\mathrm{ab}}{\mathrm{a+b}}\right]\left(\frac{\mathbf{F}}{\mathbf{R}T}\right)\left(\frac{\delta E}{\delta z}\right)\right\}$$ **Eqn. 2.23**

Insert 1

$$E_N = E + \left(\frac{\mathbf{R}T}{\mathbf{F}}\right)\ln\left(\frac{\mathrm{a}}{\mathrm{b}}\right) \qquad \textbf{Eqn. 2.24}$$

$$J_{mx} = D_{mx}\left[\frac{\delta c}{\delta \mathrm{z}} \pm c\left(\frac{\mathbf{F}}{\mathbf{R}T}\right)\left(\frac{\delta E}{\delta z}\right)\right] \qquad \textbf{Eqn. 2.25}$$

$$E_D = E + \left(\frac{\mathbf{R}T}{\mathbf{F}}\right)\ln\left(\frac{\mathrm{a}}{\mathrm{s}}\right) \qquad \textbf{Eqn. 2.26}$$

$$E_N^* \approx E^* + \left(\frac{\mathbf{R}T}{\mathbf{F}}\right)\mathrm{a}^*\left[\left(\frac{1}{\bar{\mathrm{a}}}\right) + \left(\frac{1}{\bar{\mathrm{b}}}\right)\right] \qquad \textbf{Eqn. 2.27}$$

$$E_D^* \approx E^* - \left(\frac{\mathbf{R}T}{\mathbf{F}}\right)\frac{\mathrm{a}^*}{\bar{\mathrm{a}}} \qquad \textbf{Eqn. 2.28}$$

$$\frac{1}{\mathrm{C}_\Sigma} = \frac{1}{\mathrm{C}_\mathrm{N}} + \frac{1}{\mathrm{C}_\mathrm{D}} \qquad \textbf{Eqn. 2.29}$$

$$\mathrm{C}_\mathrm{N} = \left(\frac{ALF^2}{\mathbf{R}T}\right)\left(\frac{\bar{\mathrm{a}}\,\bar{\mathrm{b}}}{c}\right) \qquad \textbf{Eqn. 2.30}$$

$$\mathrm{C}_\mathrm{D} = \left(\frac{ALF^2}{\mathbf{R}T}\right)\bar{\mathrm{a}} \qquad \textbf{Eqn. 2.31}$$

$$R_e = \left(\frac{\mathbf{R}T}{\mathbf{F}^2}\right)\left(\frac{1}{\bar{\mathrm{a}}} + \frac{1}{\bar{\mathrm{b}}}\right)\left(\frac{L}{AD_e}\right) \qquad \textbf{Eqn. 2.32}$$

$$R_{MX} = \left(\frac{\mathbf{R}T}{\mathbf{F}^2}\right)\left(\frac{L}{AD_\chi \bar{a}}\right) \qquad \textbf{Eqn. 2.33}$$

$$\mathrm{R}_{\mathrm{CT,\,K}} = \frac{\mathbf{R}T}{A\mathbf{F}^2 c}\left(\frac{1}{k_{ox}} + \frac{1}{k_{red}}\right) \qquad \textbf{Eqn. 2.34}$$

Insert 1

$$k_{ox} = k^{\theta} \exp\left(\frac{\alpha_{ox} \mathrm{F}(E_{dc} - E^{\theta})}{\mathrm{R}T}\right) \quad \textbf{Eqn. 2.35}$$

$$k_{red} = k^{\theta} \exp\left(-\left(\frac{(1-\alpha_{ox})\mathrm{F}(E_{dc} - E^{\theta})}{\mathrm{R}T}\right)\right) \quad \textbf{Eqn. 2.36}$$

$$\mathrm{R}_{\mathrm{CT,\,K}} = \frac{\mathrm{R}T}{k^{\theta} A \mathrm{F}^2 c}\left[\exp\left(\frac{-\alpha_{ox}\mathrm{F}(E_{dc} - E^{\theta})}{\mathrm{R}T}\right) + \exp\left(\frac{(1-\alpha_{ox})\mathrm{F}(E_{dc} - E^{\theta})}{\mathrm{R}T}\right)\right] \quad \textbf{Eqn. 2.37}$$

$$\mathrm{R}^{\min}_{\mathrm{CT,\,K}} = \frac{\mathrm{R}T}{A\mathrm{F}^2 c}\left(\frac{2}{k^{\theta}}\right) \quad \textbf{Eqn. 2.38}$$

$$\mathrm{R}_{\mathrm{CT,\,K}} = \frac{\mathrm{R}^{\min}_{\mathrm{CT,\,K}}}{2}\left[\exp\left(\frac{-\alpha_{ox}\mathrm{F}(E_{dc} - E^{\theta})}{\mathrm{R}T}\right) + \exp\left(\frac{(1-\alpha_{ox})\mathrm{F}(E_{dc} - E^{\theta})}{\mathrm{R}T}\right)\right] \quad \textbf{Eqn. 2.39}$$

$$\mathrm{R}_{\mathrm{CT,e}} = \frac{\mathrm{R}TL}{A D_e \mathrm{F}^2 c}\left(\frac{c}{\bar{a}\,\bar{b}}\right) \quad \textbf{Eqn. 2.40}$$

$$\mathrm{R}_{\mathrm{CT,\,e}} = \frac{\mathrm{R}^{\min}_{\mathrm{CT,\,e}}}{4}\left[2 + \exp\left(\frac{\mathrm{F}(E_{dc} - E^{\theta})}{\mathrm{R}T}\right) + \exp\left(-\left(\frac{\mathrm{F}(E_{dc} - E^{\theta})}{\mathrm{R}T}\right)\right)\right] \quad \textbf{Eqn. 2.41}$$

$$\mathrm{R}_{\mathrm{NL}} = \frac{\mathrm{R}^{\min}_{\mathrm{NL}}}{4}\left[2 + \exp\left(\frac{\mathrm{F}(E_{dc} - E^{\theta})}{\mathrm{R}T}\right) + \exp\left(-\left(\frac{\mathrm{F}(E_{dc} - E^{\theta})}{\mathrm{R}T}\right)\right)\right] \quad \textbf{Eqn. 2.42}$$

$$|Z_{\mathrm{W}}| = \frac{\sqrt{2}\sigma}{\omega^{1/2}} \quad \textbf{Eqn. 2.43}$$

$$\sigma = \frac{\sigma^{\min}}{4}\left[2 + \exp\left(\frac{\mathrm{F}(E_{dc} - E^{\theta})}{\mathrm{R}T}\right) + \exp\left(-\left(\frac{\mathrm{F}(E_{dc} - E^{\theta})}{\mathrm{R}T}\right)\right)\right] \quad \textbf{Eqn. 2.44}$$

$$\mathrm{Y}_0 = \frac{\mathrm{Y}}{(j\omega)^{1/2}} \quad \textbf{Eqn. 2.45}$$

$$\sigma = \frac{1}{\sqrt{2}\cdot \mathrm{Y}_0} \quad \textbf{Eqn. 2.46}$$

Insert 1

$$n=\frac{1}{D-1} \qquad \textbf{Eqn. 2.47}$$

$$Z_{CPE} = \frac{1}{Q_0(\omega)^n}\exp\left(\frac{\pi}{2}nj\right) \qquad \textbf{Eqn. 2.48}$$

$$C = Q_0(\omega_{max})^{n-1} \qquad \textbf{Eqn. 2.49}$$

$$\frac{\delta c}{\delta t} = D\frac{\delta^2 c}{\delta x^2} \qquad \textbf{Eqn. 2.50}$$

$$\vec{c} = \vec{c}(t\vec{x}) \qquad \forall \vec{x} \in \Omega \qquad \textbf{Eqn. 2.51}$$

$$\vec{c} = D\nabla^2\vec{c} \qquad \textbf{Eqn. 2.52}$$

$$\vec{c}(t^0) = \vec{c}^{\infty} \qquad \textbf{Eqn. 2.53}$$

$$\nabla_n\vec{c}(t) = 0 \qquad \textbf{Eqn. 2.54}$$

$$\vec{c}(t^0) = \vec{c}^0 \qquad \textbf{Eqn. 2.55}$$

Chapter 3

$$C_{DL} = \frac{(Q_0 R_{CT})^{1/n}}{R_{CT}} \qquad \textbf{Eqn. 3.1}$$

$$\nabla\cdot(-D\nabla\vec{c}) = 0 \qquad \textbf{Eqn. 3.2}$$

$$\frac{\delta c}{\delta t} = -D\left(\frac{\delta^2}{\delta x^2}+\frac{\delta^2}{\delta y^2}+\frac{\delta^2}{\delta z^2}\right) = 0 \qquad \textbf{Eqn. 3.3}$$

Insert 1

$$JA = D\int_0^{l/2}\int_0^{l/2}\left.\frac{\delta c}{\delta z}\right|_{z=0}\delta y\delta x \qquad \textbf{Eqn. 3.4}$$

$$i_L = 4n\mathbf{F}JA \qquad \textbf{Eqn. 3.5}$$

$$i_L = 4n\mathbf{F}Dc^{\infty}r \qquad \textbf{Eqn: 3.6}$$

Chapter 4

$$i_L = 4n\mathbf{F}Dcrd \qquad \textbf{Eqn. 4.1}$$

$$H_2O \rightarrow \tfrac{1}{2}O_2 + 2H^+ + 2e^- \qquad \text{pH decreases} \qquad \textbf{Eqn. 4.2}$$

$$H_2O + e^- \rightarrow \tfrac{1}{2}H_2 + OH^- \qquad \text{pH increases} \qquad \textbf{Eqn. 4.3}$$

$$R_{CT,e}^{min} = \frac{4RTL}{AD\mathbf{F}^2c} \qquad \textbf{Eqn. 4.4}$$

$$i_L = 4n\mathbf{F}Dc\frac{l}{2} \qquad \textbf{Eqn. 4.5}$$

$$i_L = 4n\mathbf{F}Dc\frac{l}{\sqrt{\pi}} \qquad \textbf{Eqn. 4.6}$$

$$\sigma^{min} = \frac{\mathbf{R}T}{n^2\mathbf{F}^2A\sqrt{2}}\left(\frac{2}{D_O^{1/2}c^{\infty}} + \frac{2}{D_R^{1/2}c^{\infty}}\right) \qquad \textbf{Eqn. 4.7}$$

$$i_L = 3.46n\mathbf{F}Dcl \qquad \textbf{Eqn. 4.8}$$

Chapter 6

$$i_L = \frac{2\pi n\mathbf{F}Dc^{\infty}l}{\ln\left[\frac{4(Dt)}{r^2}\right]} \qquad \textbf{Eqn. 6.1}$$

Insert 1

$$|i_L| = \frac{2\pi nFD\, c^{\infty} l}{\ln\left[\frac{K(Dt)}{w^2}\right]} \qquad \textbf{Eqn. 6.2}$$

$$|i_L|^{-1} = \left(\frac{2\pi nDAF\, c^{\infty}}{w}\right)^{-1} \left\{\ln\left(\frac{KD}{w^2}\right) + \ln t\right\} \qquad \textbf{Eqn. 6.3}$$

$$|i|^{-1} = \left(\frac{2\pi nDAF\,(c^{\infty} - c^{0})}{w}\right)^{-1} \left\{\ln\left(\frac{KD}{w^2}\right) + \ln t\right\} \qquad \textbf{Eqn. 6.4}$$

$$L = (\pi Dt)^{1/2} \qquad \textbf{Eqn. 6.5}$$

$$|i_L|^{-1} = \left(\frac{2\pi DAFc^{\infty}}{w}\right)^{-1} \{B - \ln v\} \qquad \textbf{Eqn. 6.6}$$

$$|i_L|^{-1} = \left(\frac{2\pi DAFc^{\infty} - c^{0}}{w}\right)^{-1} \{B - \ln v\} \qquad \textbf{Eqn. 6.7}$$

Chapter 7

$$E(t) = E_{dc} + \Delta E cos(\omega t) \qquad \textbf{Eqn. 7.1}$$

$$Z_{Re} = \frac{X + Y\sqrt{\frac{\omega}{2}}}{\left(X + Y\sqrt{\frac{\omega}{2}}\right)^2 + \left(Y\frac{\sqrt{\omega}}{2}\right)^2} \qquad \textbf{Eqn. 7.2}$$

$$Z_{Im} = \frac{Y\sqrt{\frac{\omega}{2}}}{\left(X + Y\sqrt{\frac{\omega}{2}}\right)^2 + \left(Y\frac{\sqrt{\omega}}{2}\right)^2} \qquad \textbf{Eqn. 7.3}$$

$$X = \frac{\alpha'}{M} \qquad \textbf{Eqn. 7.4}$$

Insert 1

$$Y = \frac{\alpha' \gamma' \pi^{1/2}}{M} \qquad \textbf{Eqn. 7.5}$$

$$M = 4\left(\frac{\mathrm{R}T}{n\mathrm{F}}\right)\cosh^2\left(\frac{\theta}{2}\right) \qquad \textbf{Eqn. 7.6}$$

$$\theta = \left(\frac{nF}{RT}\right)[E_{dc} - \mathrm{E}^{\theta}] \qquad \textbf{Eqn. 7.7}$$

$$\frac{1}{Z} = \frac{1}{Z_W} + \frac{1}{Z_{\mathrm{R_{NL}}}} \qquad \textbf{Eqn. 7.8}$$

$$Z_W = \frac{\sigma}{\omega^{1/2}} - \frac{j\sigma}{\omega^{1/2}} \qquad \textbf{Eqn. 7.9}$$

$$Z_{\mathrm{R_{NL}}} = \mathrm{R_{NL}} \qquad \textbf{Eqn. 7.10}$$

$$\frac{1}{Z} = \frac{1}{\left(\frac{\sigma}{\omega^{1/2}} - \frac{j\sigma}{\omega^{1/2}}\right)} + \frac{1}{\mathrm{R_{NL}}} \qquad \textbf{Eqn. 7.11}$$

$$\frac{\sigma}{\omega^{1/2}} = \mathrm{A} \qquad \textbf{Eqn. 7.12}$$

$$\frac{1}{\mathrm{Z}} = \frac{1}{\mathrm{A} - j\mathrm{A}} + (\mathrm{R_{NL}})^{-1} \qquad \textbf{Eqn. 7.13}$$

$$\frac{1}{\mathrm{Z}} = \frac{1}{2\mathrm{A}}(1 + j) + (\mathrm{R_{NL}})^{-1} \qquad \textbf{Eqn. 7.14}$$

$$\mathrm{Z} = \left(\frac{1}{2\mathrm{A}}(1 + j) + (\mathrm{R_{NL}})^{-1}\right) \qquad \textbf{Eqn. 7.15}$$

$$\mathrm{Z} = \frac{\left(\frac{1}{2\mathrm{A}} + \frac{1}{\mathrm{R_{NL}}} - \frac{j}{2\mathrm{A}}\right)}{\left(\frac{1}{2\mathrm{A}} + \frac{1}{\mathrm{R_{NL}}}\right)^2 + \frac{1}{4\mathrm{A}^2}} \qquad \textbf{Eqn. 7.16}$$

Insert 1

$$Z = \frac{\left(\frac{\omega^{1/2}}{2\sigma} + \frac{1}{R_{NL}} - \frac{j\omega^{1/2}}{2\sigma}\right)}{\left(\left(\frac{\omega^{1/2}}{2\sigma} + \frac{1}{R_{NL}}\right)^2 + \frac{\omega}{4\sigma^2}\right)} \quad \textbf{Eqn. 7.17}$$

$$Z_{Re} = \frac{\left(\frac{\omega^{1/2}}{2\sigma} + \frac{1}{R_{NL}}\right)}{\left(\frac{\omega^{1/2}}{2\sigma} + \frac{1}{R_{NL}}\right)^2 + \frac{\omega}{4\sigma^2}} \quad \textbf{Eqn. 7.18}$$

$$Z_{Re} = \frac{\left(\frac{\omega^{1/2}}{2\sigma}\right)}{\left(\frac{\omega^{1/2}}{2\sigma} + \frac{1}{R_{NL}}\right)^2 + \frac{\omega}{4\sigma^2}} \quad \textbf{Eqn. 7.19}$$

$$X = \frac{1}{R_{NL}} \quad \textbf{Eqn. 7.20}$$

$$Y = \frac{1}{\sqrt{2}\sigma} \quad \textbf{Eqn. 7.21}$$

$$R_{CT}^{min} = \frac{RT}{AF^2 c}\left(\frac{2}{k^{\theta}}\right) \quad \textbf{Eqn. 7.22}$$

Chapter 8

$$i_L = 4nF\mathbf{D}c\frac{2l}{\pi} \quad \textbf{Eqn. 8.1}$$

Appendix A1

$$E_{dc} = E^{\theta} + \frac{RT}{F}\ln\frac{\bar{b}}{\bar{a}} \quad \textbf{Eqn. A1.1}$$

$$\frac{\bar{a}}{\bar{b}} = \exp\left(\frac{\left(E_{dc} - E^{\theta}\right)}{RT}\mathbf{F}\right) \quad \textbf{Eqn. A1.2}$$

Insert 1

$$\frac{\bar{a}}{c-\bar{a}} = \exp\left(\frac{(E_{dc}-E^{\theta})}{RT}\mathbf{F}\right) \qquad \textbf{Eqn. A1.3}$$

$$\bar{a}\left(\exp\left(\frac{(E_{dc}-E^{\theta})}{RT}\mathbf{F}\right)\right) = c\left(\exp\left(\frac{(E_{dc}+E^{\theta})}{RT}\mathbf{F}\right)\right) \qquad \textbf{Eqn. A1.4}$$

$$\frac{\bar{a}}{c} = \left(\frac{\exp(N)}{1+\exp(N)}\right) \qquad \textbf{Eqn. A1.5}$$

$$\frac{\bar{b}}{c} = \left(\frac{\exp(-N)}{1+\exp(-N)}\right) \qquad \textbf{Eqn. A1.6}$$

$$R_{CT,e} = \frac{RTl}{AD_e\mathbf{F}^2c}\left[\left(\frac{1+\exp(N)}{\exp(N)}\right)\left(\frac{1+\exp(-N)}{\exp(-N)}\right)\right] \qquad \textbf{Eqn. A1.7}$$

$$R_{CT,e} = \frac{RTl}{AD_e\mathbf{F}^2c}[2+\exp(N)+\exp(-N)] \qquad \textbf{Eqn. A1.8}$$

$$R_{CT,e}^{min} = \frac{4RTL}{AD\mathbf{F}^2c} \qquad \textbf{Eqn. A1.9}$$

$$R_{CT,e} = \frac{R_{CT,e}^{min}}{4}[2+\exp(N)+\exp(-N)] = R_{CT,e}^{min}\left(cosh^2\left(\frac{N}{2}\right)\right) \qquad \textbf{Eqn. A1.10}$$

$$\sigma = \frac{RT}{\mathbf{F}^2A\sqrt{2}}\left(\frac{1}{D_O^{1/2}a^{\infty}} + \frac{1}{D_R^{1/2}b^{\infty}}\right) \qquad \textbf{Eqn. A1.11}$$

$$\sigma = \frac{RT}{\mathbf{F}^2A\sqrt{2}}\left(\frac{1}{a^{\infty}} + \frac{1}{b^{\infty}}\right) \qquad \textbf{Eqn. A1.12}$$

$$\sigma = \frac{RT}{\mathbf{F}^2A\sqrt{2}c}\left(\frac{c^2}{\bar{a}\bar{b}}\right) \qquad \textbf{Eqn. A1.13}$$

Insert 1

$$\sigma = \frac{RT}{AD\mathrm{F}^2\sqrt{2}c}[2 + \exp(N) + \exp(-N)] \qquad \textbf{Eqn. A1.14}$$

$$\sigma^{\min} = \frac{4RT}{AD\mathrm{F}^2\sqrt{2}c} \qquad \textbf{Eqn. A1.15}$$

$$\sigma = \frac{\sigma^{\min}}{4}[2 + \exp(N) + \exp(-N)] = \sigma^{\min} cosh^2\left(\frac{N}{2}\right) \qquad \textbf{Eqn. A1.16}$$

Appendix A3

$$\ln\left(\frac{i_L}{i} - 1\right) = \frac{n\mathrm{F}(E - E_{1/2})}{RT} \qquad \textbf{Eqn. A3.1}$$

$$\ln\left(\frac{i_L}{i_1} - 1\right) = \frac{n\mathrm{F}(E_1 - E_{1/2})}{RT} \qquad \textbf{Eqn. A3.2}$$

$$\ln\left(\frac{i_L}{i_2} - 1\right) = \frac{n\mathrm{F}(E_2 - E_{1/2})}{RT} \qquad \textbf{Eqn. A3.3}$$

$$\left(\frac{i_L}{i_1} - 1\right) = e\left(\frac{n\mathrm{F}(E_1 - E_{1/2})}{RT}\right) \qquad \textbf{Eqn. A3.4}$$

$$\left(\frac{i_L}{i_2} - 1\right) = e\left(\frac{n\mathrm{F}(E_2 - E_{1/2})}{RT}\right) \qquad \textbf{Eqn. A3.5}$$

$$\left(\frac{i_L}{i_1} - 1\right) = e\left(\frac{n\mathrm{F}(P + \Delta E)}{RT}\right) \qquad \textbf{Eqn. A3.6}$$

$$\left(\frac{i_L}{i_2} - 1\right) = e\left(\frac{n\mathrm{F}(P)}{RT}\right) \qquad \textbf{Eqn. A3.7}$$

$$\left(\frac{i_L}{i_1} - 1\right) - \left(\frac{i_L}{i_2} - 1\right) = e\left(\left(\frac{n\mathrm{F}(P + \Delta E)}{RT}\right) - \left(\frac{n\mathrm{F}(P)}{RT}\right)\right) \qquad \textbf{Eqn. A3.8}$$

$$\left(\frac{i_L}{i_1} - 1\right) - \left(\frac{i_L}{i_2} - 1\right) = e\left(\frac{n\mathrm{F}(P)}{RT}\right) \cdot e\left(\frac{n\mathrm{F}\Delta E}{RT} - 1\right) \qquad \textbf{Eqn. A3.9}$$

Insert 1

$$\left(\frac{i_L}{i_1}-1\right)-\left(\frac{i_L}{i_2}-1\right)=e\left(\frac{n\mathrm{F}(P)}{\mathrm{R}T}\right)\cdot\left(\frac{n\mathrm{F}\Delta E}{\mathrm{R}T}\right) \quad \textbf{Eqn. A3.10}$$

$$\left(\frac{i_L(i_2-i_1)}{i_2 i_1}\right)=e\left(\frac{n\mathrm{F}(P)}{\mathrm{R}T}\right)\cdot\left(\frac{n\mathrm{F}\Delta E}{\mathrm{R}T}\right) \quad \textbf{Eqn. A3.11}$$

$$\left(-\frac{i_L(\Delta i)}{i_2 i_1}\right)=e\left(\frac{n\mathrm{F}(P)}{\mathrm{R}T}\right)\cdot\left(\frac{n\mathrm{F}\Delta E}{\mathrm{R}T}\right) \quad \textbf{Eqn. A3.12}$$

$$Z=-\frac{\mathrm{R}T i_L}{n\mathrm{F}i_2 i_1}e\left(-\frac{n\mathrm{F}P}{\mathrm{R}T}\right) \quad \textbf{Eqn. A3.13}$$

$$i=i_L\left(\frac{1}{e\left(\frac{E-E_{1/2}n\mathrm{F}}{\mathrm{R}T}\right)+1}\right) \quad \textbf{Eqn. A3.14}$$

$$i_2 i_1={i_L}^2\left(\frac{1}{e\left(\frac{Pn\mathrm{F}}{\mathrm{R}T}\right)+1}\right)\left(\frac{1}{e\left(\frac{(P+\Delta E)n\mathrm{F}}{\mathrm{R}T}\right)}\right)\approx {i_L}^2\left(\frac{1}{e\left(\frac{Pn\mathrm{F}}{\mathrm{R}T}\right)+1}\right)^2 \quad \textbf{Eqn. A3.15}$$

$$Z=-\frac{\mathrm{R}T}{n\mathrm{F}i_L}e\left(-\frac{n\mathrm{F}P}{\mathrm{R}T}\right)\left(e\left(\frac{n\mathrm{F}P}{\mathrm{R}T+1}\right)\right)^2 \quad \textbf{Eqn. A3.16}$$

$$Z=-\frac{\mathrm{R}T}{n\mathrm{F}i_L}\left(e\left(\frac{n\mathrm{F}P}{\mathrm{R}T+1}\right)\right)\left(1+e\left(-\frac{n\mathrm{F}P}{\mathrm{R}T}\right)\right) \quad \textbf{Eqn. A3.17}$$

$$Z_{R_{NL}}=-\frac{\mathrm{R}T}{n\mathrm{F}i_L}\left(2+e\left(\frac{n\mathrm{F}P}{\mathrm{R}T}\right)\right)+\left(e\left(-\frac{n\mathrm{F}P}{\mathrm{R}T}\right)\right) \quad \textbf{Eqn. A3.18}$$

$$Z_{R_{NL}}=\frac{\mathrm{R}T}{n\mathrm{F}|i_L|}\left(2+e\left(\frac{n\mathrm{F}P}{\mathrm{R}T}\right)\right)+\left(e\left(-\frac{n\mathrm{F}P}{\mathrm{R}T}\right)\right) \quad \textbf{Eqn. A3.19}$$

$$i_{L=}=\frac{4\mathrm{R}T}{n\mathrm{F}R_{NL}} \quad \textbf{Eqn. A3.20}$$

Insert 2

Equivalent Circuit Models

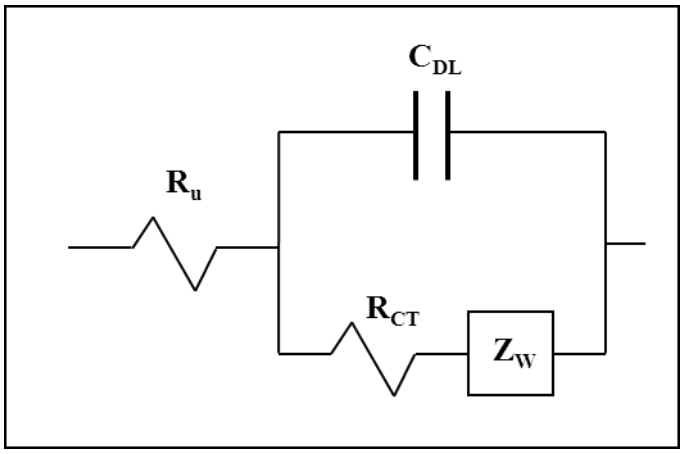

Figure 2.11: Schematic diagram representing Randles equivalent electrical circuit used to describe redox active electrochemical systems; R_u is the uncompensated electrolyte resistance, R_{CT} is the charge transfer resistance, Z_W is the Warburg impedance and C_{DL} is the double layer capacitance.

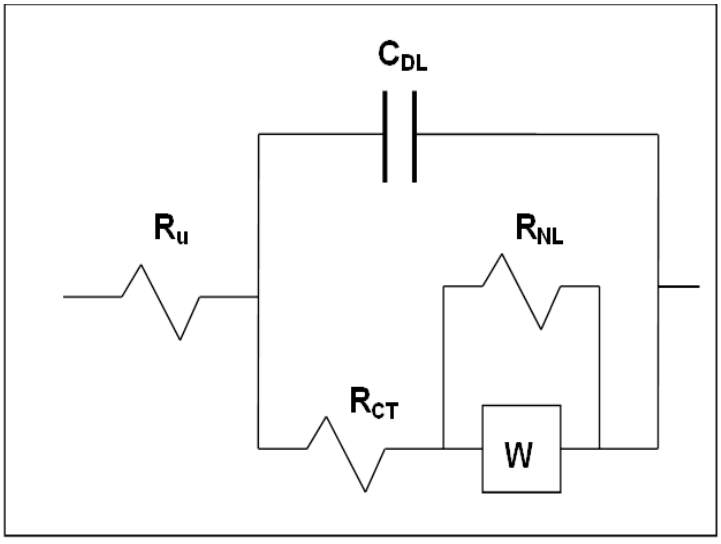

Figure 2.13: Schematic representation of the modified Randles' Circuit frequently used to model the EIS response of microdisc electrodes; R_u is the uncompensated (electrolyte) resistance, C_{DL} models the charging of the double layer, R_{CT} is the charge transfer resistance, Z_W is the Warburg impedance and R_{NL} models the non-linear resistance which corresponds to steady-state diffusion.

Insert 2

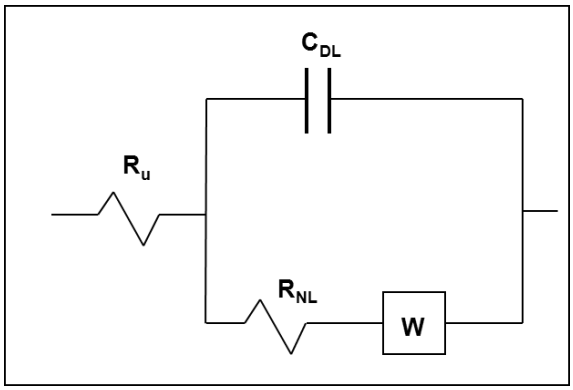

Figure 7.4: Schematic representation of the equivalent Circuit used to model the frequencies from 0.687 Hz to 0.01 Hz, which models a part of the microsquare non-linear resistance and the Warburg impedance associated with the overlapping microsquares in the array.

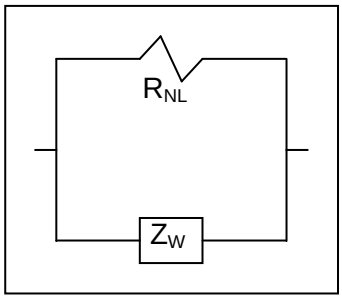

Figure 7.18: Equivalent circuit, representing the EIS response of a single nanoband electrode.

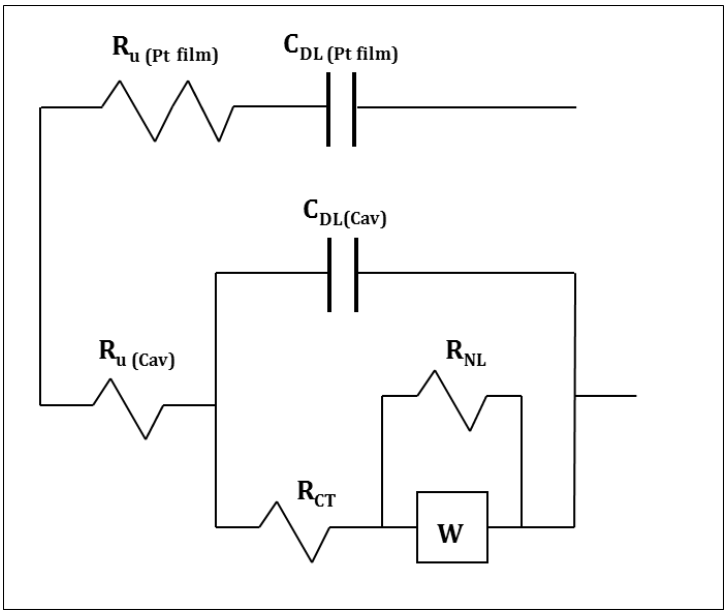

Figure 7.24: Schematic representation of the postulated equivalent circuit required to model the high frequency C30µ3d EIS data.